Flows of some non-Newtonian fluids due to oscillatory stretching boundaries

By

Sami Ullah Khan

Reg. No. 07-FBAS/PhDMA/S-12

Department of Mathematics and Statistics

Faculty of Basic and Applied Sciences

International Islamic University, Islamabad,

Pakistan

2016

Flows of some non-Newtonian fluids due to oscillatory stretching boundaries

By

Sami Ullah Khan

Reg. No. 07-FBAS/PhDMA/S-12

Supervised by

Dr. Nasir Ali

Co-Supervised by

Dr. Zaheer Abbas

Department of Mathematics and Statistics

Faculty of Basic and Applied Sciences

International Islamic University, Islamabad, Pakistan

2016

Flows of some non-Newtonian fluids due to oscillatory stretching boundaries

By

Sami Ullah Khan

A dissertation

submitted in the partial fulfillment of the

requirements for the degree of

DOCTOR OF PHILOSOPHY
IN
MATHEMATICS

Supervised by

Dr. Nasir Ali

Co-Supervised by

Dr. Zaheer Abbas

(Department of Mathematics, The Islamia University of Bahawalpur, Bahawalpur 63100, Pakistan)

Department of Mathematics and Statistics

Faculty of Basic and Applied Sciences

International Islamic University, Islamabad,

Pakistan

2016

Certificate

Flows of some non-Newtonian fluids due to oscillatory stretching boundaries

By

Sami Ullah Khan

A THESIS SUBMITTED IN THE PARTIAL FULFILLMENT OF THE REQUIREMENTS FOR THE DEGREE OF THE
DOCTOR OF PHILOSOPHY IN MATHEMATICS

We accept this thesis as conforming to the required standard

1. **Prof. Dr. Muhammad Ayub**
External Examiner

2. **Prof. Dr. Malik. M. Yousaf**
External Examiner

3. **Dr. Tariq Javed**
Internal Examiner

4. **Dr. Nasir Ali**
Supervisor

5. **Dr. Zaheer Abbas**
Co-Supervisor

6. **Prof. Dr. M. Arshad Zia**
Chairman

Department of Mathematics and Statistics
Faculty of Basic and Applied Sciences
International Islamic University, Islamabad
Pakistan
2016

Declaration

I, hereby declare that this dissertation, neither as a whole nor as a part there of, has been copied out from any source. It is further that I have prepared this dissertation entirely on the basses of my personal effort made under the sincere guidance o f my supervisor. No portion of the work, presented in this dissertation, has been submitted in support of any application of any degree or qualification of this or any other university or institute of learning.

Name and signature of student _____

Sami Ullah Khan (PhD Mathematics)

Dedicated to

My beloved Parents

&

Respected Supervisor

Dr. Nasir Ali

(May God shines His blessings upon him and fulfill all his wishes and dreams)

Acknowledgements

Foremost, I am always grateful to Almighty ALLAH, who made human being, the best creation o f all the living species and made them understand to write with pen. He provided me the boldness and capability to achieve this task. I offers countless Darood and Salaams to my beloved Holy Prophet Hazrat Muhammad (PBUH), for whom this universe has been manifested. ALLAH has shown His existence and ones by sending him as a messenger o f Islam and born me as a Muslim.

My respected supervisor **Dr. Nasir Ali**, a great teacher and a great human, is the man with the characteristic of turning nothing to something. For me he is a guidebook to lead my professional as well as my daily life. His dedication and his hard work impressed me a lot and his style of research will help me to conduct quality research in future. His quality time and discussions with me make me able to talk confidently about the subject of fluid mechanics. May Allah bless him with long and healthy life. I express my co-supervisor **Dr. Zaheer Abbas** for his knowledgeable discussions, valuable guidance and inexhaustible inspiration throughout my research time. Its great honor for me to acknowledge my respected teacher **Prof. Dr. Muhammad Sajid** for his valuable and intellectual suggestions, nice guidance, beneficial remarks and constructive criticism. I feel lucky to work with such a professional scientist. I am also grateful to my honorable teacher **Dr. Tariq Javed** who helped me in understanding the basics of homotopy analysis method. I would like to acknowledge the moral support and encouragement from my worthy teachers Prof. Dr. Muhammad Arshad Zia, Dr Ahmer Mahmood, Dr. Ahmed Zeeshan, Dr. Nayyar Mahmood and Dr. Tahir Mehmood. I gratefully thank HEC for providing financial help under Indigenous PhD Fellowships for 5000 Scholars, HEC (Phase-II) **(PIN No. 112-24531-2PS1-532)** to undertake my studies.

I would like to express my heartiest gratitude to Chairman Department **Dr. Waqar Adil Syed** who provides me a chance to teach various courses in Department of Physics. His kind support during my PhD is made my life prosperous. He provided me with all the moral support I needed during my PhD studies.

I also offer special thanks to all my friends Asif Javed, Dr. Akbar Zaman, Raheel, Khalid Mahmood, Zaheer Asghar, Khuram, Shani Zeeshan, Prof. Abid Majeed, Abuzar, Mudassar, Iftikhar Sahb and Usman for their nice wishes.

I extend my gratitude to my family for encouragement and support, even in the gloomiest of times. I cannot express enough love and appreciation to my father and mother who showered their everlasting love, care and support throughout their life trying to remove the hurdles of my life. The moral support provided by my brothers Shafa Ullah Khan, Hafeez and sisters is matchless. I express my indebtedness, appreciation and love for my wife Masoomah and cute daughter Dua who sacrificed during my studies, prayed for me and managed to support me.

Sami Ullah Khan

October 31, 2016

Preface

The analysis of non Newtonian fluids has gained the attention of engineers and scientist in recent times due to their important application in various branches of science and engineering. The non-Newtonian fluids are important in chemical and nuclear industries, material processing, geophysics and bio-engineering. The flow of such non-Newtonian fluids with heat transfer over a stretching surface has tremendous applications in the field of many industrial processes like manufacturing of plastic sheets, artificial fibers and polymeric sheets, plastic foam processing, extrusion of polymer sheet from a die, heat materials travelling between a feed roll and many others. The literature survey indicates that in the general, the stretching sheet is assumed non-oscillatory. However, the situation can arise where sheet may stretch and oscillate at the same time. The flow induced by such stretching surface is inherently unsteady. The combined heat and mass transfer effects on the flow due to oscillatory stretching surface is also an interesting area of research because of its valuable applications in industries and technology. Moreover, the governing equations of problems are highly nonlinear partial differential equations which always pose challenges for mathematicians to compute analytic and numerical solutions of these equations. In this thesis, we investigate the flow of various non-Newtonian fluids like second grade fluid, third grade fluid, Maxwell fluid, Couple stress fluid and Eyring-Powel fluid with heat/mass transfer over an oscillatory stretching surface. Moreover, flow features in the presence of saturated porous media and suction/injection phenomenon has also been discussed comprehensively. The heat transfer analysis incorporating the effects of radiation, heat absorption/generation, Cattaneo-Christov heat flux model and convective boundary condition is also presented. The resulting partial differential equations are highly nonlinear in nature. The analytical and numerical solutions of highly nonlinear partial differential equations are computed by using homotopy analysis method and an implicit finite difference scheme.

Chapter one consists of brief introduction and some basic definitions. Various types of viscoelastic constitutive equations have been discussed. Some details about finite difference scheme and homotopy analysis method are also included in this chapter.

Chapter 2 investigates the slip effects on the hydromagnetic flow of a viscoelastic second grade fluid through porous medium over a porous oscillatory stretching sheet. It is assumed that sheet is oscillating back and forth in its own plane and stretched linearly in $\bar{x}-$direction. The solution

of the problem is obtained numerically using finite difference method. The effects of viscoelastic parameter, combined parameter, ratio of oscillating frequency to stretching rate parameter, suction parameter and slip length on velocity and skin-friction coefficient are discussed. The study reveals that an oscillatory sheet embedded in a fluid-saturated porous medium generates oscillatory motion in the fluid. The amplitude and phase of oscillations depends on the involved parameters. Moreover, the results also predict a reduction in the amplitude of skin friction coefficient by increasing slip at the stretching surface. **The results of this chapter are accepted for publication in "Journal of Porous Media".**

Chapter 3 illustrates the boundary layer flow and heat transfer of an electrically conducting viscoelastic fluid (second grade fluid) over a porous oscillating stretching surface. The reduced partial differential equations in the normalized variables and have been solved numerically by using an implicit finite difference scheme. It is found that amplitude of flow velocity increases with increasing viscoelastic and mass suction/injection parameters. However, it decreases with increasing the strength of the applied magnetic field. Moveover, the temperature of fluid is a decreasing function of viscoelastic parameter, mass suction/injection parameter and Prandtl number. **The contents of this chapter have been published in "PLOS ONE, 2015; 10(12): e0144299.**

Chapter 4 extends the results of chapter 2 by including the Soret, Dufour and thermal radiation effects. The dimensionless partial differential equations are solved analytically by using homotopy analysis method. The variations of the velocity, temperature and concentration profiles for different values of emerging parameters are shown graphically and discussed in detail. It is observed that temperature decreases by an increase in the effective Prandtl number and the viscoelastic parameter. The concentration field increases by increasing the porosity parameter and the Soret number while it decreases by increasing the viscoelastic parameter and the Schmidt number. **The contents of this chapter are available online in "Journal of the Brazilian Society of Mechanical Sciences and Engineering" DOI: 10.1007/s40430-016-0506-x.**

Chapter 5 presents analysis of the boundary layer flow of a third grade fluid over an oscillatory stretching sheet. The heat transfer analysis has been performed in presence of the thermal radiation and the convective boundary conditions. The transformed set of governing equations is

solved by homotopy analysis method. It is concluded that the amplitude of velocity increases by increasing third grade fluid parameter while it decreases by increasing Hartmann number and ratio of the oscillation frequency of the sheet to its stretching rate parameter. The temperature profile increases by increasing thermal Biot number while decreases by increasing third grade fluid parameter. Moreover, the amplitude of skin friction coefficient decreases by increasing Reynolds number and third grade parameter. **These observations are published in "Nonlinear Engineering, 2015; 4(4): 223–236."**

Chapter 6 deals with the hydromagnetic flow and heat transfer of an electrically conducting Jeffrey fluid over an oscillatory stretching surface. Series solutions of the problem have been computed by using homotopy analysis methods while an implicit finite difference scheme is employed for numerical solutions. The results show that HAM solution at the higher order of approximation is in great agreement with the numerical solution. It is noted that the velocity increases by increasing Deborah number and decreases by increasing the ratio of relaxation to retardation time parameter. The amplitude of oscillation of the skin friction coefficient increases by increasing both Deborah number and the ratio of relaxation to retardation time parameter. The temperature increases by increasing ratio of relaxation to retardation time parameter and Hartmann number. **These results are published in "Zeitschrift für Naturforschung A, 2015; 70(7)a: 567–576".**

Chapter 7 presents the hydromagnetic flow and heat transfer of a couple stress fluid over a porous oscillatory stretching surface in the presence of heat source/sink. The unsteady flow problem is reduced into two coupled partial differential equations using dimensionless variables. Homotopy analysis method is employed to obtain the solution of these equations. Based on the solution an extensive analysis is performed to investigate the effects of various flow parameters on the velocity, temperature, skin friction coefficient and Nusselt number. It is found that the presence of couple stress in viscous fluid increases the amplitude of oscillations in the velocity and the skin friction coefficient. It is also noticed that the temperature increases by increasing heat source parameter. Moreover, the numerical values of the local Nusselt number are calculated and shown in tabular form. It is found that the Nusselt number increases by increasing Prandtl number while it decreases by increasing couple stress parameter. **These findings are published in "Alexandria Engineering Journal, 2016; 55: 915-924.**

Chapter 8 highlights the Soret and Dufour effects on hydromagnetic flow of Eyring-Powell fluid over an oscillatory stretching surface in the presence of heat generation/ absorption and chemical reaction. The convective boundary conditions are imposed on the energy equation. The governing equations are solved by using homotopy analysis method. It is observed that velocity increases with the increase of Eyring-Powell fluid parameter. The temperature increases with increasing Dufour number, heat source parameter and thermal Biot number. Moreover, concentration profile decreases with chemical reaction parameter. **The results of this chapter are accepted for publication in "Thermal Science Journal".**

Chapter 9 deals with combined heat and mass transfer effects in the unsteady flow of Walters' B Nanofluid over an oscillatory stretching surface. The effects of thermal radiation and heat absorption/generation are also considered in the energy equation. The study shows that the velocity of the fluid decreases by increasing viscoelastic fluid parameter. It is noted that the temperature increases by increasing thermal Biot number, Hartmann number, Brownian force parameter, thermophoresis parameter and heat source parameter. The concentration decreases with increase in Schmidt number and Brownian force parameter The effect of Prandtl number on the concentration profile is marginal. The amplitude of the skin friction increases by increasing viscoelastic parameter and Hartmann number. **These findings have been accepted for publication in "Journal of Computational and Theoretical Nanoscience".**

In Chapter 10, the hydromagnetic flow and heat transfer of a Maxwell fluid is analyzed. The boundaries are assumed to be oscillatory. The energy equation based on the Cattaneo-Christov heat flux model is used for heat transfer analysis. The system of nonlinear equations solved by means of the homotopy analysis method (HAM). It is found that Hartmann and Deborah numbers suppress the velocity. On the other hand, the velocity increases by increasing ratio of oscillation frequency to stretching rate. A reverse flow occurs in the central region of the channel which is found to decrease by increasing Hartmann and Deborah numbers. The temperature inside the channel predicted on the basis of Cattaneo-Christov heat flux model is less when compared with the temperature obtained on the basis of Fourier law. **Such findings are submitted in Proceedings of the National Academy of Sciences, India Section A: Physical Sciences.**

Contents

Nomenclature

$\mathbf{V}$	Velocity field
t	Time
$\frac{\partial}{\partial t}$	Partial derivative w.r.t time
ρ	Density
$\bar{x}, \bar{y}$	Cartesian coordinates
∇	Operator
τ	Cauchy stress tensor
u, v	Velocity components
C	Concentration
D	Diffusion coefficient
k_n	Chemical reaction constant
k_1	Thermal conductivity
c_p	Specific heat
T	Temperature
$(\rho c)_f$	Heat capacitance of the base fluid
$(\rho c)_p$	Heat capacitance of the nanoparticles
α	Thermal diffusivity
D_B	Brownian diffusion coefficient
D_T	Thermophoretic diffusion coefficient
T_∞	Ambient temperature
p	Pressure
$\hat{p}$	Modified pressure
$\mathbf{S}$	Extra stress tensor
$\mathbf{I}$	Identity tensor
μ	Dynamic viscosity

α_1, α_2	Material modulli
$\mathbf{A}_1$, $\mathbf{A}_2$	Rivlin Ericksen tensors
$\beta_1, \beta_2, \beta_3$	Material constants
N	Slip factor
λ	Ratio of relaxation to retardation time
λ_1	Retardation parameter
B_1, c	Eyring fluid parameters
h	Convergence parameter
p	Embedding parameter
$\pounds$	Operator
i, j	Grid points
K	Viscoelastic parameter
S	Ratio of the oscillation frequency to stretching rate
v_w	Wall mass transfer velocity
k^*	Permeability of porous medium
φ	Porous medium
γ	Suction/injection parameter
T_w	Ambient fluid temperature
T_∞	Free stream temperature
ω	Oscillation frequency
b	Stretching rate
Pr	Prandtl number
B	Porosity parameter
β	Combined parameter
τ_w	Shear stress
q_w	Heat flux at wall
σ	Electrical conductivity

C_f	Skin friction coefficient
Nu_x	Local Nusselt number
Re_x	Local Reynolds number
Pr	Prandtl number
C_w	Surface concentration
C_∞	Ambient concentration
α	Thermal diffusivity
D_m	Molecular diffusivity of the species concentration
k_T	Thermal diffusion ratio
k_m	Wall mass transfer coefficient
c_s	Concentration susceptibility
T_m	Mean fluid temperature
q_r	Radiative heat flux
σ^*	Stefan-Boltzmann constant
κ^*	Mean absorption coefficient
Sc	Schmidt number
Du	Dufour number
Sr	Soret number.
N_r	Radiation parameter
Pr_{eff}	Effective Prandtl number
q_m	Surface mass flux
Q	Heat source coefficient
h_m	Heat transfer coefficient
β^*	Third grade fluid parameter
λ	Heat source and heat sink parameter
γ_1	Thermal Biot number

De	Deborah number
K^*	Couple stress parameter
ρ_f	Density of base fluid
τ'	Ratio between heat capacity of nanoparticle material to heat capacity
D_B	Brownian diffusion coefficient
D_T	Thermophoretic diffusion coefficient.
γ_2	Concentration Biot number
Nb	Brownian motion parameter
Nt	Thermophoresis parameter

Chapter 1

Introduction

Aim of this chapter is to introduce the readers with classical and recent literature for the boundary layer flows of Newtonian and non-Newtonian fluids over a stretching surface. The incorporated literature includes research work relating to viscous and viscoelastic fluids, flow through porous media, flow of electrically conducting fluids, radiation phenomena in heat transfer and flow of nanofluids due to a stretching sheet. The constitutive relationships of non-Newtonian fluids including second grade, third grade, Jeffrey and Eyring-Powell fluids are also presented. In the later part of the chapter, the details of the analytic technique, namely, homotopy analysis method and numerical technique, namely, the implicit finite difference scheme are included.

1.1 Literature review

The theoretical and experimental evidences established the fact that fluids in industrial and technological applications obey nonlinear constitutive relationship between shear stress and rate of deformation. The dynamics of non-Newtonian fluids is entirely different from Newtonian fluids and such fluids have important practical applications in the industrial and technological processes. The constitutive relationships of non-Newtonian fluids exhibit important characteristics such as shear-thinning or thickening, yield stress, Weissenberg effects, fluid memory and die swelling, which cannot be explained using Newtonian fluids. The examples of non-Newtonian fluids in daily life are liquid crystals, foams, slurries, paints, polymer solutions, melts and many more. Many biological fluids like blood, spermatic fluid, chime and respiratory mucus are also modeled as non-Newtonian fluids. The diverse characteristics and applications of non-Newtonian fluids encouraged the rheologists to propose several constitutive relationships in the literature [1-10].

Analysis for the two-dimensional flow of Newtonian and non-Newtonian fluids over a stretching surface has attained a remarkable interest of the researchers in the past few decades. In fact, the stretching phenomenon has considerable importance in determining the quality of final product in the manufacturing processes of sheets and films. In stretching phenomenon when fluid

interacts with the solid surface the viscous forces are dominant in a thin region near the surface and have no significance far away from the surface. This emphasizes the role of boundary layer theory in deriving the governing equations for stretching flow problems. Apart from that, the boundary layer theory has numerous applications in industrial processes like metal spinning, metal extrusion, glass blowing, artificial fibers, continuous stretching of plastic films, filaments and wires and many more. The concept of boundary layer theory was presented by Prandtl [11] in early 20^{th} century which has been great impetus in the modern fluid mechanics. The boundary layer approximations are valid for the flow past solid boundaries at high Reynolds number. The earlier studies carried out by Prandtl and Blasius [12] deal with flow past a stationary boundary. In 1960, Sakiadis [13,14] originated the study of the boundary layer flow over a moving surface. He presented most interesting and important problem regarding the flow of a viscous fluid over a moving flat surface with constant velocity. Crane [15] investigated two-dimensional, steady flow of viscous fluid over a moving stretching surface and provided a closed form solution of the problem. Crane's problem motivated many researchers to study the flow of viscous and viscoelastic fluids over stretching surfaces. Wang [16] extended the Crane's problem for three dimensional flow. He provided exact similar solution of the problem successfully. Rajeswari and Nath [17] studied the numerical solution of problem regarding boundary layer flow and heat transfer of rotating viscous fluid over a stretching surface. They claimed that the temperature and the skin friction coefficient increase by increasing the rotation parameter. Ariel [18] provided exact numerical solution of axisymmetric flow of a viscoelastic fluid (second grade fluid) over a stretching sheet. His results were excellent agreement with existing literature. Sajid and Hayat [19] studied boundary layer flow of a third grade fluid over a stretching sheet. They discussed non-similar solutions of the problem by using homotopy analysis method. Mahapatra et al. [20] discussed the laminar flow and heat transfer of an incompressible viscoelastic fluid past a permeable stretching surface near an oblique stagnation point analytically by using perturbation technique. Javed et al. [21] developed the boundary layer equations for two-dimensional flow of Eyring-Powell fluid and discussed the stretching flow. They obtained numerical solutions using Keller-Box scheme to analyze the locally similar solutions of the boundary value problem. Their study reveals that the velocity of fluid increases by increasing the material parameter. Sajid et al. [22] implemented finite difference scheme to investigate two-dimensional flow of an Oldroyd-B

fluid over a stretching surface. Nadeem et al. [23] used homotopy analysis method to investigate boundary layer flow of a Williamson fluid over a stretching surface. Bhattacharyya et al. [24] showed that closed form solutions can be obtained in both stretching and shrinking cases. Furthermore dual solutions exist in the case of shrinking flow. Three-dimensional flow of a Maxwell fluid over a stretching surface is analyzed by Awais et al. [25].

The study of flow of electrically conducting fluid under the influence of a constant magnetic field is another topic of interest for scientists and engineers because of its promising applications in physics, engineering, chemistry, polymer industry and metallurgy. The cooling process is an important feature in many industrial processes. The MHD effects are important in controlling the cooling and boundary layer thickness. The desired cooling rate can be achieved by drawing a strip in magnetohydrodynamic fluid to obtain the end product of the desired quality. The problem regarding magnetohydrodynamic (MHD) flows are also encountered in various physiological fluids, for instance, blood plasma and blood pump machines. Keeping all these numerous applications in mind, many researchers studied the effects of transverse magnetic field on stretching flows under various configurations. Ariel [26] studied the effects of an applied magnetic field in the boundary layer flow of a viscoelastic fluid over a stretching sheet. He presented exact analytic solution of the problem and claimed that in the case of suction, the solution is possible for some critical values of viscoelastic parameter. Anderson [27] provided an exact solution of the MHD flow of a Walter's B over a stretching surface. He concluded that increase of magnetic field and voscoelasticity has same effects on the velocity profile. Kumari and Nath [28] analyzed the magnetohydrodynamic phenomenon in a power law fluid flow over a moving stretching surface numerically by using an implicit finite difference scheme. Hayat et al. [29] investigated the hydromagnetic flow of an Oldroyd-B fluid. Noor et al. [30] presented series solution by using well known analytic technique namely Adomian decomposition method for studying the magnetohydrodynamic flow of a viscous fluid flow due to a shrinking surface. Motsa et al. [31] used spectral-homotopy analysis technique to investigate the effects of an applied magnetic field in a Jeffery–Hamel problem. There results show that solution obtained by using this technique converges rapidly as compared to classical homotopy analysis solution. The hydromagnetic boundary layer flow of rotating viscous fluid over a shrinking surface was analyzed by Sajid et al. [32].

The flow analysis through saturated porous media is an important phenomenon and has major applications in technology and geothermal energy recovery. Some sophisticated applications of porous media have also been reported in the literature. Examples may include the usage of shear-thinning solutions to enhance oil recovery, the involvement of inline filtration of fluids with complex rheological properties in many processes in food and chemical industry, distillation towers and fixed bed reactor, biomedical separation devices etc. [33]. Chauhan and Agrawal [34] studied the flow of electrically conducting viscous fluid through a porous medium over a stretching sheet. Ishaq and Nazar [35] investigated the steady and unsteady flow of viscous fluid over a vertical stretching surface in a porous medium using Darcy-Brinkman equation model. Kumaran and Tamizharasi [36] computed the analytic solution for flow of a incompressible viscous over a stretching sheet in a presence of porous medium. Three dimensional boundary layer flow of Casson fluid over a stretching surface embedded in a saturated porous media was analyzed numerically by Nadeem et al. [37]. Sajid et al. [38] discussed the flow of viscous fluid over a stretching surface in presence of porous medium of uniform permeability. They obtained the exact solution of the problem.

The heat transfer is one of the important features in many industrial and technological processes. In many industrial processes like oil and gas processing and refining, the role of heat transfer cannot be neglected. Besides, the effects of heat transfer in the boundary layer flows due to stretching surfaces have applications in industrial and metallurgical processes. These applications include the manufacture of plastic and rubber sheets, annealing and thinning of copper wires, continuous cooling of fiber spinning etc. The primary interest of such investigations is to predict the variation of skin friction coefficient and local Nusselt number with non-Newtonian fluid parameters. The literature survey indicates that a number of studies are carried out in this direction. For instance, Vajravelu and Rollins [39] discussed the effects of heat transfer in the boundary layer flow of a viscoelastic fluid over a stretching sheet for prescribed surface temperature and heat flux cases. Their analysis showed that thermal boundary layer thickness is inversely proportional to the square root of the Prandtl number for both cases. Subhas and Veena [40] performed similar analysis by considering prescribed surface temperature and wall heat flux over a porous stretching surface. Massoudi and Maneschy [41] discussed the numerical solution of a viscoelastic second grade fluid by using quasi-linearization method.

Cortell [42] implemented an implicit finite difference scheme to discuss heat transfer phenomenon in the hydromagnetic flow of a viscoelastic fluid (second grade fluid) with mass suction. Abel et al. [43] presented analytic solution for the flow and heat transfer of a second grade fluid over a permeable stretching surface in the presence of heat absorption/generation. In this study blood is considered as a viscoelastic fluid obeying the constitutive equations of a second grade fluid. Analysis for the unsteady boundary layer flow of a Jeffrey fluid over a stretching surface was carried out by Hayat et al. [44]. Homotopy analysis method is adopted in [44] to obtain series solution of the resulting system of partial differential equations. Ibrahim and Shanker [45] used Keller-box scheme to discuss the heat transfer characteristics in a hydromagnetic flow of a viscous fluid in the presence of heat source/sink. Hayat et al. [46] investigated the slip flow of a second grade fluid over a porous stretching sheet. The unsteady stagnation boundary layer flow and heat transfer of a viscous fluid over a stretching surface was analyzed numerically by Bhattacharyya et al. [47]. Elbashbeshy and. Bazid [48] discussed the two-dimensional flow and heat transfer of a viscous fluid over unsteady stretching sheet by Runge-Kutta-Merson method. The stagnation-point flow and heat transfer of a Couple stress fluid with melting heat transfer over stretching sheet was analyzed by Hayat et al. [49].

Heat transfer in the presence of thermal radiation is another interesting feature in modern physics and engineering. In fact, at high temperatures, the thermal radiation effects are quit prominent and have applications in nuclear industry, power generation, astrophysical flows, solar power technology missiles, satellites and semiconductor wafers etc. Raptis et al. [50] presented most interesting result regarding heat transfer phenomenon in the presence of thermal radiation for an asymmetric flow of a viscous fluid under the influence of a transverse magnetic field. This problem encourages the researchers to discuss the effects of thermal radiation in the heat transfer analysis using various fluid models [51-54]. Later, Magyari and Pantokratoras [55] commented on thermal radiation effects under the linearized Rosseland approximation in boundary layer flows. They proved that heat transfer analysis with and without thermal radiation is exactly the same task. They further emphasized that the radiation problem admits the same solution for infinite set of parameter values (Nr, Pr) that corresponds to some effective Prandtl number.

In these studies the phenomenon of heat transfer is modeled using Fourier law of heat conduction [56] which states that heat transfer is proportional to temperature gradient. Fourier

law of heat conduction is applicable to macroscopic systems where time scale of the system is higher than average relaxation time. Based on this fact, Cattaneo [57] proposed a modification in the Fourier's law by adding a relaxation time term. In 2009, Christov [58] derived relations for invariant version of Maxwell-Cattaneo law by using Oldroyed upper convective derivative [59]. Pranesh et al. [60] implemented Maxwell-Cattaneo law of heat conduction to study the Rayleigh-Bénard magneto convection in a micropolar fluid. Tibullo et al. [61] validated the uniqueness and structural stability of the solutions obtained by using Cattaneo-Christov heat flux model. The effects of thermal convection using Cattaneo-Christov heat flux model has been discussed by Straughan [62] through Chebyshev-tau numerical method. Thermal instability for an incompressible viscous fluid in a Brinkman porous media using Cattaneo-Christov heat flux model was investigated by Haddad [63]. Recently, Han et al. [64] studied the effects of heat transfer in steady upper-convected Maxwell fluid over a stretching plate using Cattaneo-Christov heat flux model [58]. They solved nonlinear ordinary differential equations using HAM.

In last few decades, the combined heat and mass transfer in the boundary layer flow of various fluids over stretching surface is the topic of interest because of its tremendous applications in many engineering and industrial processes. The mathematical equivalence of the thermal boundary layer problem with the concentration analogue has provided the liberty to use the results obtained for heat transfer to the case of mass transfer by replacing the Prandtl number by Schmidt number. However, such equivalence is not possible when chemical reaction term is introduced in the mass diffusion equation. In such cases, the mass transfer equations must be solved along with momentum and energy equation to analyze the concentration field. Sanjayanand and Khan [65] presented analytic solution for the two-dimensional boundary layer flow and heat/mass transfer of a viscoelastic fluid over a an elastic stretching sheet. Alharbi et al. [66] studied the combined heat and mass transfer characteristics in the steady flow of a viscoelastic fluid over a stretching sheet. The effects of heat and mass transfer with chemical reaction for the flow of a second grade fluid have been analyzed by Hayat et al. [67] by using homotopy analysis method. Veena et al. [68] discussed the non-similar solutions of viscoelastic fluid flow with heat and mass transfer over a porous stretching sheet. The analysis of heat and mass transfer in the presence of transverse magnetic field and slip at the surface was studied by Turkyilmazoglu [69]. Moreover, Turkyilmazoglu successfully specified and defined the region

of existence or non-existence of the unique/multiple solutions. The phenomenon of heat and mass transfer in the stagnation-point flow of a viscous fluid over a porous stretching sheet with suction and blowing was analyzed by Layek et al. [70].

In some cases, heat and mass transfer occur simultaneously in moving fluid, then it is often observed that heat flux can be generated not only by temperature gradients but also by concentration gradients. The phenomenon of Soret (thermal diffusion) is occurrence of diffusion flux due to temperature gradient. The reciprocal of Soret effect is known as Dufour effect, the occurrence of energy flux due to chemical potential gradient. Soret and Dufour effects play a vital role in geoscience and chemical engineering. Anghel [71] analyzed Soret and Dufour effects for the free convection boundary layer flow over a vertical surface embedded in a porous medium. Postelnicu [72] investigated the phenomenon of heat and mass transfer by natural convection from a vertical surface embedded in a saturated porous medium by considering Soret and Dufour effects. Srinivasacharya et al. [73] studied mixed convection in a viscous fluid over an exponentially stretching vertical surface subject to Soret and Dufour effects. Beg et al. [74] focused their research to investigate Soret and Dufour effects for laminar magnetohydrodynamic flow of a viscous fluid. Soret and Dufour effects in Hiemenz flow through a porous medium over a stretching surface were investigated by Tsai [75]. Ahmed [76] reported the influence of Soret and Dufour effects by analyzing the similarity solution for free convection heat and mass transfer over a permeable stretching surface. Bazid et al. [77] presented the numerical solution for the stagnation point flow towards a stretching surface in the presence of buoyancy force, Soret and Dufour effects. Pal et al. [78] discussed the Soret and Dufour effects for MHD non-Darcian mixed convection heat and mass transfer over a stretching sheet with non-uniform heat source/sink. Nayak [79] discussed the Soret and Dufour effects on mixed convection unsteady boundary layer flow over a stretching sheet in a porous medium by using Runge-Kutta method with shooting technique. Hayat et al. [80] analyzed combined heat and mass transfer characteristics in the boundary layer flow of a viscoelastic fluid over a linearly stretching vertical surface by using homotopy analysis method. Turkyilmazoglu [81] computed exact solution hydromagnetic flow of a viscoelatic fluid in the presence of Soret and Dufout effects. His results show an excellent agreement with the results of Hayat et al. [80].

The tremendous physio-chemical properties of nanofluid such as higher electrical conductivities, higher stability and rheological characteristics have enormous applications in nano-micro electronic devices, refrigerators, coolants, power generators, solar water heaters, transformers, nuclear reactors, antibacterial agents, spaceships and nanotherapeutics [82, 83]. The nanofluids play a key role to increase the thermal conductivity of the base fluid because in many industrial processes simple base fluids do not meet the cooling requirements. For instance, many conventional fluids like water, oil, bio-fluids, ethylene glycol and organic liquids have low thermal conductivities and therefore cannot reach high heat exchange rates in many engineering equipments. To overcome this problem, Choi [84] was the first who suggested that effective thermal conductivity of these base fluids can be enhanced if nano-sized particles (1–100 nm) are merged in these conventional base fluids. This investigation leads many researchers to analyze the flow of base fluid in the presence of various nanoparticles. For instance, Kuznetsov et al. [85] presented similarity solution for natural convection boundary layer flow in the presence of nanoparticlesover over a vertical plate. Khan and Pop [86] presented first problem regarding boundary layer flow of viscous nanofluids over a stretching sheet. They used finite difference scheme to provide the similarity solution of the problem. Mustafa et al. [87] used convective boundary conditions to investigate heat and mass transfer in the boundary layer flow of a nanofluid over an exponentially stretching sheet. Turkyilmazoglu [88] obtained the analytical solutions for the flow of a nanofluid over a stretching/shrinking surface. Three-dimensional boundary layer flow of Maxwell nanofluid over a stretching sheet has been investigated by Hayat et al. [89]. Two-dimensional boundary layer flow of a viscous nanofluid has been examined by Shehzad et al. [90]. Das et al. [91] used Runge–Kutta–Fehlberg method to investigate the unsteady flow of a nanofluid over a stretching sheet. Nazar et al. [92] analyzed the stagnation point flow of a nanofluid over a stretching sheet. The effects of transverse magnetic field along with slip and thermal radiation for the boundary layer flow of a nanofluid over a permeable stretching sheet was investigated by Ibrahim and Shankar [93]. The effects of homogeneous-hetrogeneous chemical reaction on nanofluid flow over a porous stretching surface was analyzed by Kameswaran et al. [94]. Gayal and Bhargava [95] used finite element method to investigate the slip effects for the boundary layer flow of a viscoelastic nanofluid over a stretching sheet. Hamad et al. [96] considered free convection flow of nanofluids over a vertical flat plate. Din et

al. [97] presented group analysis for the flow of non-Newtonian naofluid with slip effects over a permeable stretching sheet. The effects of buoyancy force and Navier slip in the hydromagnetic flow of a nanofluid over a vertical porous plate was analyzed by Njane and Makinde [98]. Pal et al. [99] used Runge-Kutta-Fehlberg to investigate effects of heat generation/absorption in mixed convection stagnation-point flow of nanofluids over a porous stretching/shrinking.

In all above mentioned studies the stretching imposed at the surface may be linear, power law or exponential type. However, there are situations where the sheet is stretched as well as oscillate periodically in its own plane. Wang [100] was first who analyzed the unsteady boundary layer flow of a viscous fluid over an oscillatory stretching surface. A perturbation solution is presented in [100]. The analysis of Wang was extended by Saddipa et al. [101] for Walter's B fluid. Rajagopal et al. [102] examined the effects of suction and blowing in oscillatory motion of a viscoelastic fluid over a stretching sheet in the presence of saturated porous medium. Abbas et al. [103] complemented the Wang's analysis by including the slip effects and performing the heat transfer analysis. In another paper, Abbas et al. [104] discussed boundary layer flow of a second grade fluid over an oscillatory stretching surface by using homotpy analysis method and finite difference scheme. Zheng et al. [105] provided an analysis of the unsteady heat and mass transfer in MHD flow over an oscillatory stretching sheet with Soret and Dufour effects. They have employed homotopy analysis method and delineated the effects of various emerging parameters on the flow and heat transfer characteristics. Their study indicates a decrease in the velocity of the fluid by increasing unsteady parameter, magnetic parameter and suction/injection parameter. The heat transfer analysis in a channel with oscillatory stretching walls for a viscoelastic fluid was also analyzed by Misra et al. [106].

1.2 Some basic laws

1.2.1 Law of conservation of mass

The law of conservation of mass provides the following partial differential equation

$$\frac{\partial \rho}{\partial t} + \nabla \cdot (\rho \mathbf{V}) = 0, \tag{1.1}$$

where ρ is the density and $\mathbf{V}$ the velocity of the fluid. For incompressible flow, Eq. (1.1) becomes

$$\nabla \cdot \mathbf{V} = 0. \tag{1.2}$$

1.2.2 Law of conservation of linear momentum

The motion of fluids is governed by the equation

$$\rho \frac{d\mathbf{V}}{dt} = \nabla \cdot \boldsymbol{\tau} + \rho \mathbf{b}. \tag{1.3}$$

In above equation d/dt represents material derivative, $\boldsymbol{\tau}$ is the Cauchy stress tensor and $\mathbf{b}$ is the body force per unit mass. The velocity field for unsteady two-dimensional flow is

$$\mathbf{V} = [u(\bar{x}, \bar{y}, t), v(\bar{x}, \bar{y}, t), 0], \tag{1.4}$$

where u and v are the velocity components along $\bar{x}$ and $\bar{y}$ directions, respectively. The component form of the Eq. (1.3) for two-dimensional flow is given by

$$\rho\left(\frac{\partial u}{\partial t} + u\frac{\partial u}{\partial \bar{x}} + v\frac{\partial u}{\partial \bar{y}}\right) = \frac{\partial \tau_{xx}}{\partial \bar{x}} + \frac{\partial \tau_{xy}}{\partial \bar{y}} + \rho b_x, \tag{1.5}$$

$$\rho\left(\frac{\partial v}{\partial t} + u\frac{\partial v}{\partial \bar{x}} + v\frac{\partial v}{\partial \bar{y}}\right) = \frac{\partial \tau_{yx}}{\partial \bar{x}} + \frac{\partial \tau_{yy}}{\partial \bar{y}} + \rho b_y, \tag{1.6}$$

where $\tau_{xx}, \tau_{yx}, \tau_{yy}$ are the components of Cauchy stress tensor and $\rho b_x, \rho b_y$ are components of body force.

1.2.3 Law of conservation of energy

The energy equation for fluids in motion is

$$\rho c_p \frac{dT}{dt} = \boldsymbol{\tau} : \nabla \mathbf{V} + k_1 \nabla^2 T, \tag{1.7}$$

where c_p is the specific heat, T is the temperature, k_1 is the thermal conductivity and $\boldsymbol{\tau} : \nabla \mathbf{V}$ represents the viscous dissipation function.

1.2.4 Concentration equation

According to Fick's law, at constant diffusivity, the rate of change in concentration with time, is directly proportional to the rate at which the concentration gradient changes with distance in a given direction, i.e.,

$$\frac{dC}{dt} = D_m\left(\nabla^2 C\right), \tag{1.8}$$

where C denoted concentration and D_m is the diffusion coefficient. Eq. (1.8) in presence of chemical reaction is

$$\frac{dC}{dt} = D_m\left(\nabla^2 C\right) - k_n C^m, \tag{1.9}$$

where K_n is the reaction constant and m represents the order of the chemical reaction.

1.3 Governing Equations for nanofluid

The energy and concentration equations for nanofluid are

$$(\rho c)_f\left(\frac{\partial T}{\partial t} + \mathbf{V}.\nabla T\right) = k_1\nabla^2 T + (\rho c)_p\left[D_B \nabla C.\nabla T + \left(\frac{D_T}{T_\infty}\right)\nabla T.\nabla T\right], \tag{1.10}$$

$$\frac{\partial C}{\partial t} + \mathbf{V}.\nabla C = D_B\nabla^2 C + \left(\frac{D_T}{T_\infty}\right)\nabla^2 T, \tag{1.11}$$

In above equations $(\rho c)_f$ is the heat capacitance of the base fluid, $(\rho c)_p$ is the heat capacitance of the nanoparticles, $\alpha = k/(\rho c)_f$ is the thermal diffusivity of nanofluid, D_B is the Brownian diffusion coefficient and D_T is the thermophoretic diffusion coefficient.

1.4 Constitutive equations

The constitutive equation provides a relationship between the shear stress and rate of deformation. In the subsequent subsection, we introduce the readers with the constitutive equations of second grade, third grade, Jeffrey and Eyring-Powell fluids and corresponding boundary layer equations for unsteady two-dimensional flow of these fluids.

1.4.1 Boundary layer equation for Second grade fluid

The Cauchy stress tensor for a second grade fluid is given by [1]

$$\boldsymbol{\tau} = -p\mathbf{I} + \mu\mathbf{A}_1 + \alpha_1\mathbf{A}_2 + \alpha_2\mathbf{A}_1^2, \tag{1.12}$$

where p is the pressure, $\mathbf{I}$ is the identity tensor, μ represent the dynamic viscosity, α_1 and α_2 are the material modulli parameters and $\mathbf{A}_1$ and $\mathbf{A}_2$ are the Rivlin Ericksen tensors given by

$$\mathbf{A}_1 = \mathbf{L} + \mathbf{L}^t, \quad \mathbf{L} = \nabla \mathbf{V}, \tag{1.13}$$

$$\mathbf{A}_2 = \frac{d\mathbf{A}_1}{dt} + \mathbf{A}_1\mathbf{L} + \mathbf{L}^t\mathbf{A}_1 \ . \tag{1.14}$$

Using velocity profile (1.4) and utilizing (1.11)-(1.13) in Eq. (1.3), we get the following equations

$$\begin{aligned}
&\frac{\partial u}{\partial t} + u\frac{\partial u}{\partial \bar{x}} + v\frac{\partial u}{\partial \bar{y}} = -\frac{1}{\rho}\frac{\partial p}{\partial \bar{x}} + \nu\left(2\frac{\partial^2 u}{\partial \bar{x}^2} + \frac{\partial^2 u}{\partial \bar{y}^2} + \frac{\partial^2 v}{\partial \bar{y}\partial \bar{x}}\right) + \frac{\alpha_1}{\rho}\left(\frac{\partial u}{\partial \bar{y}}\frac{\partial^2 v}{\partial \bar{x}^2} + 2\frac{\partial u}{\partial \bar{x}}\frac{\partial^2 v}{\partial \bar{x}^2} + \frac{\partial v}{\partial \bar{x}}\frac{\partial^2 u}{\partial \bar{y}\partial \bar{x}} + 2\frac{\partial^3 u}{\partial t\partial \bar{x}^2}\right.\\
&+2\frac{\partial u}{\partial \bar{x}}\frac{\partial^2 u}{\partial \bar{x}^2} + 2u\frac{\partial^3 u}{\partial \bar{x}^3} + 2v\frac{\partial^3 u}{\partial \bar{y}\partial \bar{x}^2} + \frac{\partial^3 u}{\partial t\partial \bar{y}^2} + u\frac{\partial^3 u}{\partial \bar{x}\partial \bar{y}^2} + v\frac{\partial^3 u}{\partial \bar{y}^3} + \frac{\partial^3 v}{\partial t\partial \bar{x}\partial \bar{y}} + u\frac{\partial^3 v}{\partial \bar{x}^2\partial \bar{y}} + 2\frac{\partial v}{\partial \bar{y}}\frac{\partial^2 v}{\partial \bar{y}\partial \bar{x}} + v\frac{\partial^3 v}{\partial \bar{x}\partial \bar{y}^2}\\
&\left.+\frac{\partial u}{\partial \bar{x}}\frac{\partial^2 u}{\partial \bar{y}^2} - \frac{\partial u}{\partial \bar{y}}\frac{\partial^2 v}{\partial \bar{y}^2} - \frac{\partial u}{\partial \bar{x}}\frac{\partial^2 v}{\partial \bar{y}\partial \bar{x}} + \frac{\partial v}{\partial \bar{x}}\frac{\partial^2 v}{\partial \bar{y}^2}\right) + \frac{2\alpha_2}{\rho}\left[4\frac{\partial u}{\partial \bar{x}}\frac{\partial^2 u}{\partial \bar{x}^2} + \frac{\partial u}{\partial \bar{y}}\left(\frac{\partial^2 u}{\partial \bar{x}\partial \bar{y}} + \frac{\partial^2 v}{\partial \bar{x}^2}\right) + \frac{\partial v}{\partial \bar{x}}\left(\frac{\partial^2 u}{\partial \bar{x}\partial \bar{y}} + \frac{\partial^2 v}{\partial \bar{x}^2}\right)\right],
\end{aligned} \tag{1.15}$$

$$\begin{aligned}
&\frac{\partial v}{\partial t} + u\frac{\partial v}{\partial \bar{x}} + v\frac{\partial v}{\partial \bar{y}} = -\frac{1}{\rho}\frac{\partial p}{\partial \bar{y}} + \nu\left(\frac{\partial^2 v}{\partial \bar{x}^2} + 2\frac{\partial^2 v}{\partial \bar{y}^2} + \frac{\partial^2 u}{\partial \bar{y}\partial \bar{x}}\right) + \frac{\alpha_1}{\rho}\left(\frac{\partial^3 u}{\partial t\partial \bar{x}\partial \bar{y}} + 2\frac{\partial u}{\partial \bar{x}}\frac{\partial^2 u}{\partial \bar{y}\partial \bar{x}} + u\frac{\partial^3 u}{\partial \bar{y}\partial \bar{x}^2} + \frac{\partial v}{\partial \bar{x}}\frac{\partial^2 u}{\partial \bar{y}^2}\right.\\
&+v\frac{\partial^3 u}{\partial \bar{x}\partial \bar{y}^2} + \frac{\partial^3 v}{\partial t\partial \bar{x}^2} + u\frac{\partial^3 v}{\partial \bar{x}^3} + v\frac{\partial^3 v}{\partial \bar{x}^2\partial \bar{y}} + \frac{\partial^2 u}{\partial \bar{x}^2}\frac{\partial u}{\partial \bar{y}} - \frac{\partial^2 u}{\partial \bar{x}^2}\frac{\partial v}{\partial \bar{x}} - \frac{\partial v}{\partial \bar{y}}\frac{\partial^2 u}{\partial \bar{y}\partial \bar{x}} + \frac{\partial v}{\partial \bar{y}}\frac{\partial^2 v}{\partial \bar{x}^2} + 2\frac{\partial u}{\partial \bar{y}}\frac{\partial^2 u}{\partial \bar{y}^2} + 2\frac{\partial^3 v}{\partial t\partial \bar{y}^2}\\
&\left.+\frac{\partial u}{\partial \bar{y}}\frac{\partial^2 v}{\partial \bar{y}\partial \bar{x}} + 2u\frac{\partial^3 v}{\partial \bar{x}\partial \bar{y}^2} + v\frac{\partial^3 v}{\partial \bar{y}^3} + \frac{\partial u}{\partial \bar{y}}\frac{\partial^2 v}{\partial \bar{y}^2}\right) + \frac{2\alpha_2}{\rho}\left[4\frac{\partial u}{\partial \bar{y}}\frac{\partial^2 v}{\partial \bar{y}^2} + \frac{\partial u}{\partial \bar{y}}\left(\frac{\partial^2 v}{\partial \bar{x}\partial \bar{y}} + \frac{\partial^2 u}{\partial \bar{y}^2}\right) + \frac{\partial v}{\partial \bar{x}}\left(\frac{\partial^2 v}{\partial \bar{x}\partial \bar{y}} + \frac{\partial^2 u}{\partial \bar{y}^2}\right)\right],
\end{aligned} \tag{1.16}$$

Employing the order and magnitude analysis by considering [107]

$$u = O(1), v = O(\delta), x = O(1), y = O(\delta), \tag{1.17}$$

Eqs. (1.15) and (116) yield [103]

$$\frac{\partial u}{\partial t} + u\frac{\partial u}{\partial \bar{x}} + v\frac{\partial u}{\partial \bar{y}} = -\frac{1}{\rho}\frac{\partial \hat{p}}{\partial \bar{x}} + \nu\frac{\partial^2 u}{\partial \bar{y}^2} + \frac{\alpha_1}{\rho}\left[\frac{\partial^3 u}{\partial t\partial \bar{y}^2} + \frac{\partial}{\partial \bar{x}}\left(u\frac{\partial^2 u}{\partial \bar{y}^2}\right) + \frac{\partial u}{\partial \bar{y}}\frac{\partial^2 v}{\partial \bar{y}^2} + v\frac{\partial^3 u}{\partial \bar{y}^3}\right], \tag{1.18}$$

$$\frac{\partial \hat{p}}{\partial \bar{y}} = 0, \tag{1.19}$$

where $\hat{p}$ is the modified pressure defined as

$$\hat{p} = p - (2\alpha_1 + \alpha_2)\left(\frac{\partial u}{\partial \bar{y}}\right)^2. \tag{1.20}$$

Equation (1.18) is the boundary layer equation for flow of a second grade fluid.

1.4.2 Constitutive equations for third grade fluid

The constitutive relationship for a third grade fluid is [2]

$$\tau = -P\mathbf{I} + \mu\,\mathbf{A}_1 + \alpha_1\mathbf{A}_2 + \alpha_2\mathbf{A}_1^2 + \beta_3(tr\mathbf{A}_1^2)\mathbf{A}_1, \tag{1.21}$$

where β_3 is the material constant. This model parameters must satisfy the following constraints

$$\mu \geq 0,\ \ \alpha_1^* \geq 0,\ \ \beta_1 = \beta_2 = 0,\ \ \beta_3 \geq 0,\ \alpha_1^* + \alpha_2^* \leq \sqrt{24\mu\beta_3}. \tag{1.22}$$

Using Eq. (1.4) and (1.21) in (1.3), we get the following equations

$$\begin{aligned}
&\frac{\partial u}{\partial t}+u\frac{\partial u}{\partial x}+v\frac{\partial u}{\partial y}=-\frac{1}{\rho}\frac{\partial p}{\partial x}+\nu\left(\frac{\partial^2 u}{\partial x^2}+\frac{\partial^2 u}{\partial y^2}\right)+\frac{\alpha_1}{\rho}\left[2\frac{\partial^3 u}{\partial x^2\partial t}+\frac{\partial^3 u}{\partial y^2\partial t}+\frac{\partial^3 v}{\partial x\partial y\partial t}+\frac{\partial u}{\partial x}\left(13\frac{\partial^2 u}{\partial x^2}+\frac{\partial^2 u}{\partial y^2}\right)+u\left(\frac{\partial^3 u}{\partial x^3}+\frac{\partial^3 u}{\partial y^2\partial x}\right)\right]\\
&+\nu\left(\frac{\partial^3 u}{\partial y^3}+\frac{\partial^3 u}{\partial x^2\partial y}\right)+2\frac{\partial v}{\partial x}\left(\frac{\partial^2 v}{\partial x^2}+\frac{\partial^2 u}{\partial x\partial y}\right)+3\frac{\partial u}{\partial y}\left(\frac{\partial^2 u}{\partial x\partial y}+\frac{\partial^2 v}{\partial x^2}\right)+\frac{2\alpha_2}{\rho}\left[4\frac{\partial u}{\partial x}\frac{\partial^2 u}{\partial x^2}+\left(\frac{\partial u}{\partial y}+\frac{\partial v}{\partial x}\right)\left(\frac{\partial^2 u}{\partial x\partial y}+\frac{\partial^2 v}{\partial x^2}\right)\right]\\
&+\frac{\beta_3}{\rho}\left[8\frac{\partial u}{\partial x}\frac{\partial u}{\partial y}\frac{\partial^2 v}{\partial x^2}+24\frac{\partial u}{\partial x}\frac{\partial u}{\partial y}\frac{\partial^2 u}{\partial x\partial y}+12\frac{\partial u}{\partial y}\frac{\partial v}{\partial x}\frac{\partial^2 u}{\partial y^2}+24\frac{\partial u}{\partial x}\frac{\partial v}{\partial x}\frac{\partial^2 u}{\partial x\partial y}+6\left(\frac{\partial v}{\partial x}\right)^2\frac{\partial^2 u}{\partial y^2}+8\left(\frac{\partial u}{\partial x}\right)^2\frac{\partial^2 u}{\partial y^2}\right.\\
&\left.+40\left(\frac{\partial u}{\partial x}\right)^2\frac{\partial^2 u}{\partial x^2}+6\left(\frac{\partial u}{\partial y}\right)^2\frac{\partial^2 u}{\partial y^2}+8\frac{\partial u}{\partial x}\frac{\partial v}{\partial x}\frac{\partial^2 u}{\partial x^2}-2\left(\frac{\partial u}{\partial y}\right)^2\frac{\partial^2 u}{\partial x^2}-2\left(\frac{\partial v}{\partial x}\right)^2\frac{\partial^2 u}{\partial y^2}-4\frac{\partial u}{\partial y}\frac{\partial v}{\partial x}\frac{\partial^2 u}{\partial x^2}\right],
\end{aligned} \tag{1.23}$$

$$\begin{aligned}
&\frac{\partial v}{\partial t}+u\frac{\partial v}{\partial x}+v\frac{\partial v}{\partial y}=-\frac{1}{\rho}\frac{\partial p}{\partial y}+\nu\left(\frac{\partial^2 v}{\partial x^2}+\frac{\partial^2 v}{\partial y^2}\right)+\frac{\alpha_1}{\rho}\left[2\frac{\partial^3 u}{\partial x\partial y\partial t}+\frac{\partial^3 v}{\partial x^2\partial t}+2\frac{\partial^3 v}{\partial y^2\partial t}+\frac{\partial v}{\partial y}\left(\frac{\partial^2 v}{\partial x^2}+13\frac{\partial^2 v}{\partial y^2}\right)\right.\\
&\left.+u\left(\frac{\partial^3 v}{\partial x^3}+\frac{\partial^3 v}{\partial y^2\partial x}\right)+v\left(\frac{\partial^3 v}{\partial y^3}+\frac{\partial^3 v}{\partial x^2\partial y}\right)+2\frac{\partial u}{\partial y}\left(\frac{\partial^2 u}{\partial y^2}+\frac{\partial^2 v}{\partial y\partial x}\right)+3\frac{\partial u}{\partial x}\left(\frac{\partial^2 v}{\partial x\partial y}+\frac{\partial^2 u}{\partial y^2}\right)\right]\\
&+\frac{2\alpha_2}{\rho}\left[4\frac{\partial v}{\partial y}\frac{\partial^2 v}{\partial y^2}+\left(\frac{\partial u}{\partial y}+\frac{\partial v}{\partial x}\right)\left(\frac{\partial^2 v}{\partial x\partial y}+\frac{\partial^2 u}{\partial y^2}\right)\right]+\frac{\beta_3}{\rho}\left[40\left(\frac{\partial v}{\partial y}\right)^2\frac{\partial^2 v}{\partial y^2}+6\left(\frac{\partial u}{\partial y}\right)^2\frac{\partial^2 v}{\partial x^2}-2\left(\frac{\partial u}{\partial x}\right)^2\frac{\partial^2 v}{\partial y^2}\right.\\
&-2\left(\frac{\partial u}{\partial y}\right)^2\frac{\partial^2 v}{\partial y^2}+12\frac{\partial u}{\partial y}\frac{\partial v}{\partial x}\frac{\partial^2 v}{\partial x^2}+8\frac{\partial u}{\partial y}\frac{\partial v}{\partial y}\frac{\partial^2 u}{\partial y^2}+8\frac{\partial v}{\partial x}\frac{\partial v}{\partial y}\frac{\partial^2 u}{\partial y^2}+24\frac{\partial v}{\partial x}\frac{\partial v}{\partial y}\frac{\partial^2 v}{\partial x\partial y}+8\left(\frac{\partial v}{\partial y}\right)^2\frac{\partial^2 v}{\partial x^2}\\
&\left.+24\frac{\partial u}{\partial y}\frac{\partial v}{\partial y}\frac{\partial^2 v}{\partial x\partial y}+6\left(\frac{\partial v}{\partial x}\right)^2\frac{\partial^2 v}{\partial x^2}-4\frac{\partial u}{\partial y}\frac{\partial v}{\partial x}\frac{\partial^2 v}{\partial y^2}\right].
\end{aligned} \tag{1.24}$$

Using boundary layer approximations as defined in (1.17), we find the boundary layer equation for a third grade fluid as[107]

$$\frac{\partial u}{\partial t}+u\frac{\partial u}{\partial x}+v\frac{\partial u}{\partial y}=-\frac{1}{\rho}\frac{\partial \hat{p}}{\partial x}+\nu\frac{\partial^2 u}{\partial y^2}+\frac{\alpha_1}{\rho}\left[\frac{\partial^3 u}{\partial t\partial y^2}+v\frac{\partial^3 u}{\partial y^3}+\frac{\partial u}{\partial x}\frac{\partial^2 u}{\partial y^2}+u\frac{\partial^3 u}{\partial x\partial y^2}+\frac{\partial u}{\partial y}\frac{\partial^2 v}{\partial y^2}\right]+\frac{6\beta_3}{\rho}\left(\frac{\partial u}{\partial y}\right)^2\frac{\partial^2 u}{\partial y^2}, \quad (1.25)$$

$$\frac{\partial \hat{p}}{\partial y}=0. \quad (1.26)$$

1.4.3 Constitutive equations for Jeffrey fluid

The constitutive relationship for a Jeffrey fluid is [3]

$$\mathbf{S}=\frac{\mu}{1+\lambda}\left[\mathbf{A}_1+\lambda_1\left(\frac{\partial}{\partial t}+\mathbf{V}.\nabla\right)\mathbf{A}_1\right], \quad (1.27)$$

where λ is the ratio of relaxation to retardation time (ratio parameter) and λ_1 is the retardation time. The equation of motion (1.3) gives

$$\frac{\partial u}{\partial t}+u\frac{\partial u}{\partial x}+v\frac{\partial u}{\partial y}=-\frac{1}{\rho}\frac{\partial p}{\partial x}+\frac{\nu}{1+\lambda}\left[\frac{\partial^2 u}{\partial x^2}+\frac{\partial^2 u}{\partial y^2}+\lambda_1\left(\begin{array}{l}\frac{\partial^3 u}{\partial y^2\partial t}+\frac{\partial^3 u}{\partial x^3}+3\frac{\partial u}{\partial x}\frac{\partial^2 u}{\partial x^2}+v\frac{\partial^3 u}{\partial x^2\partial y}+2\frac{\partial v}{\partial x}\frac{\partial^2 u}{\partial x\partial y}\\ +\frac{\partial u}{\partial y}\frac{\partial^2 u}{\partial x\partial y}+\frac{\partial u}{\partial y}\frac{\partial^2 v}{\partial x^2}-\frac{\partial v}{\partial x}\frac{\partial^2 u}{\partial y^2}+v\frac{\partial^3 v}{\partial x\partial y^2}\end{array}\right)\right], \quad (1.28)$$

$$\frac{\partial v}{\partial t}+u\frac{\partial v}{\partial x}+v\frac{\partial v}{\partial y}=-\frac{1}{\rho}\frac{\partial p}{\partial y}+\frac{\nu}{1+\lambda}\left[\frac{\partial^2 v}{\partial x^2}+\frac{\partial^2 v}{\partial y^2}+\lambda_1\left(\begin{array}{l}v\frac{\partial^3 v}{\partial x^3}+3\frac{\partial u}{\partial x}\frac{\partial^2 u}{\partial x\partial y}-v\frac{\partial^3 u}{\partial x\partial y^2}+\frac{\partial u}{\partial x}\frac{\partial^2 v}{\partial x^2}+\frac{\partial v}{\partial x}\frac{\partial^2 u}{\partial x^2}\\ -u\frac{\partial^3 u}{\partial x^2\partial y}-\frac{\partial v}{\partial x}\frac{\partial^2 u}{\partial y^2}-v\frac{\partial^3 v}{\partial x^3}-2\frac{\partial u}{\partial y}\frac{\partial^2 u}{\partial x^2}\end{array}\right)\right], \quad (1.29)$$

Employing boundary layer approximations, we get the following equation

$$\frac{\partial u}{\partial t}+u\frac{\partial u}{\partial x}+v\frac{\partial u}{\partial y}=-\frac{1}{\rho}\frac{\partial p}{\partial x}+\frac{\nu}{1+\lambda}\left[\frac{\partial^2 u}{\partial y^2}+\lambda_1\left(\frac{\partial^3 u}{\partial y^2\partial t}+u\frac{\partial^3 u}{\partial x\partial y^2}-\frac{\partial u}{\partial x}\frac{\partial^2 u}{\partial y^2}+\frac{\partial u}{\partial y}\frac{\partial^2 u}{\partial x\partial y}+v\frac{\partial^3 u}{\partial y^3}\right)\right], \quad (1.30)$$

$$\frac{\partial p}{\partial y}=0, \quad (1.31)$$

as boundary layer equations for flow of a Jeffrey fluid.

1.4.4 Constitutive equations for Eyring-Powell Fluid

The extra stress tensor for an Eyring-Powell fluid is [5]

$$\mathbf{S}=\left[\mu+\frac{1}{B_1\dot{\gamma}}\sinh^{-1}\left(\frac{1}{c}\dot{\gamma}\right)\right]\mathbf{A}_1, \tag{1.32}$$

in which

$$\dot{\gamma}=\sqrt{\frac{1}{2}tr(\mathbf{A}_1)^2}, \tag{1.33}$$

The second order approximation of $\sinh^{-1}$ function is

$$\sinh^{-1}\left(\frac{1}{c}\dot{\gamma}\right)\cong\frac{\dot{\gamma}}{c}-\frac{\dot{\gamma}^3}{6c^3},\ \text{with}\ \ \frac{\dot{\gamma}^5}{c^5}<<<1. \tag{1.35}$$

where B_1 and c are the fluid parameters of the Eyring-Powell model. Using (1.32)-(1.35) in Eq. (1.3), one finds

$$\frac{\partial u}{\partial t}+u\frac{\partial u}{\partial x}+v\frac{\partial u}{\partial y}=-\frac{1}{\rho}\frac{\partial p}{\partial x}+\left(\nu+\frac{1}{\rho B_1 c}\right)\left(\frac{\partial^2 u}{\partial x^2}+\frac{\partial^2 u}{\partial y^2}\right)-\frac{1}{3\rho B_1 c^3}\frac{\partial}{\partial x}\left[2\left(\frac{\partial u}{\partial x}\right)^2+2\left(\frac{\partial v}{\partial y}\right)^2+\left(\frac{\partial u}{\partial y}+\frac{\partial v}{\partial x}\right)^2\right]\left(\frac{\partial u}{\partial x}\right) \tag{1.36}$$
$$-\frac{1}{6\rho B_1 c^3}\frac{\partial}{\partial y}\left[2\left(\frac{\partial u}{\partial x}\right)^2+2\left(\frac{\partial v}{\partial y}\right)^2+\left(\frac{\partial u}{\partial y}+\frac{\partial v}{\partial x}\right)^2\right]\left(\frac{\partial u}{\partial y}+\frac{\partial v}{\partial x}\right),$$

$$\frac{\partial v}{\partial t}+u\frac{\partial v}{\partial x}+v\frac{\partial v}{\partial y}=-\frac{1}{\rho}\frac{\partial p}{\partial y}+\left(\nu+\frac{1}{\rho B_1 c}\right)\left(\frac{\partial^2 v}{\partial x^2}+\frac{\partial^2 v}{\partial y^2}\right)-\frac{1}{6\rho B_1 c^3}\frac{\partial}{\partial x}\left[2\left(\frac{\partial u}{\partial x}\right)^2+2\left(\frac{\partial v}{\partial y}\right)^2+\left(\frac{\partial u}{\partial y}+\frac{\partial v}{\partial x}\right)^2\right]\left(\frac{\partial u}{\partial y}+\frac{\partial v}{\partial x}\right) \tag{1.37}$$
$$-\frac{1}{3\rho B_1 c^3}\frac{\partial}{\partial y}\left[2\left(\frac{\partial u}{\partial x}\right)^2+2\left(\frac{\partial v}{\partial y}\right)^2+\left(\frac{\partial u}{\partial y}+\frac{\partial v}{\partial x}\right)^2\right]\frac{\partial v}{\partial y},$$

Using boundary layer approximations, we get

$$\frac{\partial u}{\partial t}+u\frac{\partial u}{\partial x}+v\frac{\partial u}{\partial y}=-\frac{1}{\rho}\frac{\partial p}{\partial x}+\left(\nu+\frac{1}{\rho B_1 c}\right)\frac{\partial^2 u}{\partial y^2}-\frac{1}{2\rho B_1 c^3}\left[\left(\frac{\partial u}{\partial y}\right)^2\frac{\partial^2 u}{\partial y^2}\right], \tag{1.38}$$

$$\frac{\partial p}{\partial y}=0. \tag{1.39}$$

1.5 Homotopy

The word homotopy is a topological term. Two functions are said to be homotopic if one function can be deformed continuously into other function. Assuming f_1 and f_2 represents two

continuously mapping from one topological space X into the topological space Y then f_1 is homotopic to f_2 if exist a continuous map F such that for each $x \in X$

$$F : X \times [0,1] \to Y, \tag{1.40}$$

$$F(x,0) = f_1(x), F(x,1) = f_2(x) \tag{1.41}$$

The map F is called the homotopy between f_1 and f_2.

1.6 Homotopy analysis method

In many physical problems, the resulted differential equations are highly non-linear nature. The solution of these nonlinear equations always provides a challenge to mathematician to compute solution of the equations. For this purpose various analytic method has been proposed in the literature. The perturbation technique is one such analytic method. However, this method is valid only for small choice of parameter. To overcome this issue, Liao [108] developed a new analytic method which is independedt of any small or large parameter. Later on, many researchers used this method to solve various nonlinear problems in various disciplines of science and engineering [109-112]. It has been emphasized by Liao that the series solution obtained by HAM is purely analytic and he demonstrated this fact in number of articles for instance [113,114]. Moreover, it has been proved by Turkyilmazoglu [115] that HAM can handle any type of nonlinearity by a suitable HAM formulation.

Let us assume nonlinear differential equation

$$N[u(r,t)] = 0, \tag{1.42}$$

Where, N is an non-linear operator, $u(r,t)$ is an unknown function and r and t denote spatial and temporal indepent variable, respectively. Using homotopy concept, Liao [107] constructed zeroth-order deformation equation

$$(1-q)L[\Phi(r,t,q) - u_0(r,t)] = q\hbar H(r,t) N[\Phi(r,t,q)], \tag{1.43}$$

In which $q \in [0,1]$ is an embedding parameter, $u_0(r,t)$ denotes the initial guess, $h \neq 0$ is the auxiliary parameter, $H(r,t) \neq 0$ is an auxiliary function, $\Phi(r,t,q)$ is unknown function. The auxiliary property with property

$$\Phi(r,t,0) = u_0(r,t), \tag{1.44}$$

$$\Phi(r,t,1)=u(r,t), \tag{1.45}$$

It is remarked that q varies towards the final solution $w(x)$ when q tends 0 to 1. We expand $\hat{w}(x,q)$ about q using Taylor series

$$\Phi(r,t,q)=u_0(r,t)+\sum_{m=1}^{\infty}u_m(r,t)q^m, \tag{1.46}$$

where

$$u_m(r,t)=\frac{1}{m!}\frac{\partial^m\Phi(r,t,q)}{\partial q^m}\bigg|_{q=0}, \tag{1.47}$$

with property of linear operator, $h, H(r,t)$ the series (1.46) will converges at $q=1$ and power series (3) becomes

$$u(r,t)=u_0(r,t)+\sum_{m=1}^{\infty}u_m(r,t), \tag{1.48}$$

which must be one of the solutions of $N[u(r,t)]=0$. In short, defining a vector

$$\vec{u}_n=\{u_0(r,t),u_0(r,t),...,u_n(r,t)\}. \tag{1.49}$$

According to definition of $u_m(r,t)$, it can be derive from zeroth-order equation (1.43), differentiating the equation (1.43) m-times respective to q and then dividing it by $m!$ and finally setting $m=0$, we have the so-called mth-order deformation equation

$$L[u_m(r,t)-\chi_m u_{m-1}(r,t)]=\hbar H(r,t)R_m(\vec{u}_{m-1},r,t), \tag{1.50}$$

where

$$\chi_m=\begin{cases}0, m\le 1,\\ 1, m>1,\end{cases} \tag{1.51}$$

and

$$R_m(\vec{u}_{m-1},r,t)=\frac{1}{(m-1)!}\frac{\partial^{m-1}N[\Phi(r,t,q)]}{\partial q^{m-1}}\bigg|_{q=0} \tag{1.52}$$

Clearly, Eq. (1.50) is a linear one. Therefore a nonlinear equation could be transformed to a system of linear ones which can be easily solved using an iterative procedure and this is the main consequence of the HAM.

1.7 Implicit Finite Deference Method [11]

The finite difference is one of the simplest and the oldest methods to solve various highly nonlinear ordinary as well as partial differential equations. This method was introduced in the early 1950s and its development was stimulated after the emergence of computers that offered a convenient framework for dealing with complex problems of science and technology. To compute the numerical solution of nonlinear differential equations, the space derivatives of differential equations are replaced by central difference approximations while time derivatives by forward difference approximations.

For implementation of implicit finite difference scheme, let us consider the differential equation [116]

$$\frac{\partial T}{\partial t}=\alpha\frac{\partial^2 T}{\partial x^2}. \tag{1.53}$$

We replace the time derivative by forward/backward difference approximation and space derivatives by central difference approximation. Thus using BTCS approximation, the differential equation evaluated at $(i,n+1)$ grids namely

$$\left(\frac{\partial T}{\partial t}\right)_i^{n+1}=\alpha\left(\frac{\partial^2 T}{\partial x^2}\right)_i^{n+1}, \tag{1.54}$$

gives

$$\frac{T_i^{n+1}-T_i^n}{\Delta t}=\alpha\left(\frac{T_{i+1}^{n+1}-2T_i^{n+1}+T_{i-1}^{n+1}}{(\Delta x)^2}\right). \tag{1.55}$$

On simplification, we get following finite difference scheme

$$-rT_{i-1}^{n+1}+(1+2r)T_i^{n+1}-rT_{i+1}^{n+1}=T_i^n \tag{1.56}$$

For $i=1,2,3,...,N-1$, the number of unknown in $x-$direction. The equation is implicit in the sense that there are three unknown values of T at $(n+1)th$ time level. For $n=0$, Eq. (1.56) gives $(N-1)$ simultaneous linear algebraic equations for $(N-1)$ unknown value of T at internal grid points at time level zero in term of unknown initial and boundary values. These equations can be solved to get each values of T_i^1, for $i=1,2,...,N-1$. Similarly for $n=1$, we get

$(N-1)$ unknown value of T at second time level in term of boundary values and recently computed values of T at first step level and so on. For $i=1,2,...,N-1$ in Eq. (1.56), we get following simultaneous algebraic equations in tridiagonal form as given below

$$(1+2r)T_1^{n+1} - rT_2^{n+1} = d_1^n \tag{1.57}$$

$$-rT_1^{n+1} + (1+2r)T_2^{n+1} - rT_3^{n+1} = d_2^n \tag{1.58}$$

$$-rT_2^{n+1} + (1+2r)T_3^{n+1} - rT_4^{n+1} = d_3^n \tag{1.59}$$

$$\vdots$$

$$-rT_{N-2}^{n+1} + (1+2r)T_{N-1}^{n+1} = d_{N-1}^n \tag{1.60}$$

where

$$d_1^n = T_1^n + rT_0^{n+1}, d_i^n = T_i^n, i = 1,2,3,...N-1. \tag{1.61}$$

This system of these differential equations is converted into a system of algebraic equations which are further solved by Gaussian elimination method.

Chapter 2

Slip effects in the hydromagnetic flow of a viscoelastic fluid through porous medium over a porous oscillatory stretching sheet

In this chapter, the hydromagnetic flow of a viscoelastic second grade fluid through porous medium over porous oscillatory stretching sheet is considered. It is assumed that sheet is oscillating back and forth in its own plane and stretched linearly in $\bar{x}-$direction. The similarity flow is governed by nonlinear partial differential equation and nonlinear boundary conditions. The solution of the problem is obtained numerically using finite difference method. The effects of viscoelastic parameter, combined magnetic and porosity parameter, ratio of oscillating frequency to stretching rate parameter, suction parameter and slip length on velocity and skin-friction coefficient are discussed.

2.1 Mathematical Formulation

Consider an unsteady, two-dimensional, magnetohydrodynamic and incompressible flow of a second grade fluid through a porous medium over a porous oscillating stretching sheet. The plate coincides with the $\bar{x}\ \bar{z}-$plane and fluid occupies the space $\bar{y}>0$. The sheet performs periodic oscillations back and forth and stretched with a velocity $u_w=b\bar{x}\sin\omega t$ where b is the stretching rate and ω represents angular frequency. A magnetic field of strength B_0 is applied along $\bar{y}$ direction. In present case, we are interested in studying the effects of applied magnetic field on the fluid motion and not the vice versa. Hence the diffusion of magnetic field is important and thus magnetic susceptibility is large which results in a small magnetic Reynolds number. In the small magnetic Reynolds number limit, the induced magnetic field and electric currents are neglected in comparison to the applied magnetic field and current density, respectively.

According to the Hayat et al. [117], the Darcy resistance for second grade fluid flowing through a porous medium is

$$\mathbf{R}=-\frac{\varphi}{k^*}\left[\mu+\alpha_1\frac{\partial}{\partial t}\right]\mathbf{V}, \tag{2.1}$$

where φ is the porosity and k^* is the permeability of the porous medium. Under the assumption of very large magnetic diffusivity, the induced magnetic field is neglected.

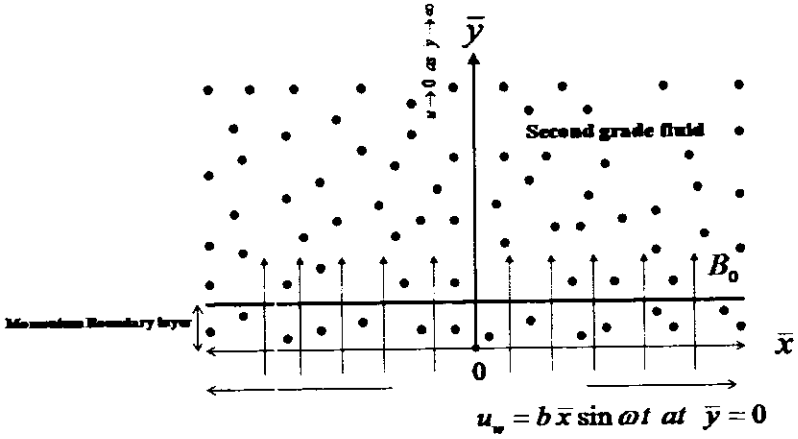

Fig. 2.1: Geometry of the problem

In the presence of porous medium and magnetic field, Eq. (1.1) and Eq. (1.18) after employing the boundary layer approximations reduce to

$$\frac{\partial u}{\partial \bar{x}} + \frac{\partial v}{\partial \bar{y}} = 0, \tag{2.2}$$

$$\frac{\partial u}{\partial t} + u\frac{\partial u}{\partial \bar{x}} + v\frac{\partial u}{\partial \bar{y}} = \nu\frac{\partial^2 u}{\partial \bar{y}^2} + \frac{\alpha_1}{\rho}\left[\frac{\partial^3 u}{\partial t \partial \bar{y}^2} + \frac{\partial}{\partial \bar{x}}\left(u\frac{\partial^2 u}{\partial \bar{y}^2}\right) + \frac{\partial u}{\partial \bar{y}}\frac{\partial^2 v}{\partial \bar{y}^2} + v\frac{\partial^3 u}{\partial \bar{y}^3}\right] - \frac{\sigma B_0^2}{\rho}u - \frac{\varphi}{\rho k^*}\left(\mu + \alpha_1\frac{\partial}{\partial t}\right)u. \tag{2.3}$$

The mass conservation equation (2.2) remains same throughout the thesis. Therefore, we shall not reproduce it in the subsequent chapters. The appropriate boundary conditions for the present slip flow are

$$u = u_w = b\bar{x}\sin\omega t + N^*\left[\frac{\partial u}{\partial \bar{y}} + \frac{\alpha_1}{\mu}\left(\frac{\partial^2 u}{\partial t \partial \bar{y}} + u\frac{\partial^2 u}{\partial \bar{x}\partial \bar{y}} + v\frac{\partial^2 u}{\partial \bar{y}^2} - 2\frac{\partial u}{\partial \bar{y}}\frac{\partial v}{\partial \bar{y}}\right)\right]_{\bar{y}=0}, \; v = -v_w \text{ at } \bar{y} = 0, \; t > 0 \tag{2.4}$$

$$u \to 0, \qquad \frac{\partial u}{\partial \bar{y}} \to 0 \qquad as \qquad \bar{y} \to \infty, \tag{2.5}$$

where N^* is the slip constant, ν is kinematic viscosity, v_w is the wall mass transfer velocity with $v_w < 0$ is for suction and $v_w > 0$ is for injection. The second condition in (2.5) is augmented boundary condition [103]. We remark here that such boundary condition for slip flow with wall mass transfer have been already used by several researchers (see refs. [48, 49, 69]).

The problem defined above can be normalized by defining the following variables [103]

$$y=\sqrt{\frac{b}{\nu}}\bar{y},\quad \tau=t\omega,\quad u=b\bar{x}f_{y}(y,\tau),\quad v=-\sqrt{\nu b}\,f(y,\tau). \tag{2.6}$$

In view of (2.6), the continuity equation (2.2) is satisfied identically and Eqs. (2.3)-(2.5) take the form

$$S(1+BK)f_{y\tau}+f_{y}^{2}-ff_{yy}+M^{2}f_{y}+Bf_{y}=f_{yyy}+K\left(Sf_{yyy\tau}+2f_{y}f_{yyy}-f_{yy}^{2}-ff_{yyyy}\right). \tag{2.7}$$

$$f_{y}(0,\tau)=\sin\tau+\varepsilon\left[f_{yy}(0,\tau)+K\left(3f_{y}f_{yy}(0,\tau)+Sf_{yy\tau}(0,\tau)-f(0,\tau)f_{yyy}(0,\tau)\right)\right],\ f(0,\tau)=\gamma, \tag{2.8}$$

$$f_{y}(\infty,\tau)=0,\ f_{yy}(\infty,\tau)=0. \tag{2.9}$$

In above equations $\gamma=v_{w}/\sqrt{\nu b}$ is the dimensionless suction $(\gamma>0)$ or injection $(\gamma<0)$ parameter, $M=\sqrt{\sigma B_{0}^{2}/\rho b}$ is the Hartmann number, $B=\nu\varphi/k^{*}b$ is the porosity/permeability parameter, $\varepsilon=N^{*}\sqrt{b/\nu}$ is the non-dimensional slip length, $K=b\alpha_{1}/\rho\nu$ is the viscoelastic parameter and $S=\omega/b$ is the ratio of the oscillating frequency to the stretching rate. The subscripts in Eqs. (2.7)-(2.9) indicate differentiation.

The formula of skin-friction coefficient C_{f} is

$$C_{f}=\frac{\tau_{w}}{\rho u_{w}^{2}}, \tag{2.10}$$

where τ_{w} is the shear stress at wall and is given by [103]

$$\tau_{w}=\mu\left(\frac{\partial u}{\partial\bar{y}}\right)_{\bar{y}=0}+\alpha_{1}\left(\frac{\partial^{2}u}{\partial t\partial\bar{y}}+u\frac{\partial^{2}u}{\partial\bar{x}\partial\bar{y}}+v\frac{\partial^{2}u}{\partial\bar{y}^{2}}-2\frac{\partial u}{\partial\bar{y}}\frac{\partial v}{\partial\bar{y}}\right)_{\bar{y}=0}. \tag{2.11}$$

The normalized version of Eq. (2.11) is

$$\mathrm{Re}_{x}^{1/2}\,C_{f}=\left[f_{yy}+K\left(3f_{y}f_{yy}+Sf_{yy\tau}-ff_{yyy}\right)\right]_{\bar{y}=0}, \tag{2.12}$$

where $\mathrm{Re}_{x}=u_{w}\bar{x}/\nu$ is the local Reynolds number.

initial conditions for velocity field is

$$f(\eta,\tau=\tau'=0)=0. \tag{2.18}$$

Following Abbas et al. [103] the time difference scheme is constructed for f as

$$\begin{aligned}
&S\left(1-6K\eta^2+BK\right)\frac{1}{\Delta\tau}\left(\frac{\partial f^{(n+1)}}{\partial\eta}-\frac{\partial f^{(n)}}{\partial\eta}\right)-SK\eta^4\frac{1}{\Delta\tau}\left(\frac{\partial^3 f^{(n+1)}}{\partial\eta^3}-\frac{\partial^3 f^{(n)}}{\partial\eta^3}\right)-6SK\eta^3\frac{1}{\Delta\tau}\left(\frac{\partial^2 f^{(n+1)}}{\partial\eta^2}-\frac{\partial^2 f^{(n)}}{\partial\eta^2}\right)\\
&=\left(\eta^2-8K\eta^4\right)\left(\frac{\partial f^{(n)}}{\partial\eta}\right)^2+\left(6\eta^2-M^2-B\right)\frac{\partial f^{(n+1)}}{\partial\eta}+\left(24K\eta^3-2\eta\right)f^{(n)}\frac{\partial f^{(n)}}{\partial\eta}+6\eta^3\frac{\partial^2 f^{(n+1)}}{\partial\eta^2}\\
&+\left(36K\eta^4-\eta^2\right)f^{(n)}\frac{\partial^2 f^{(n)}}{\partial\eta^2}-8K\eta^5\frac{\partial f^{(n)}}{\partial\eta}\frac{\partial^2 f^{(n)}}{\partial\eta^2}+K\eta^6\left(\frac{\partial^2 f^{(n)}}{\partial\eta^2}\right)^2+\eta^4\frac{\partial^3 f^{(n+1)}}{\partial\eta^3}\\
&-2K\eta^6\frac{\partial f^{(n)}}{\partial\eta}\frac{\partial^3 f^{(n)}}{\partial\eta^3}+12K\eta^5 f^{(n)}\frac{\partial^3 f^{(n)}}{\partial\eta^3}+K\eta^6 f^{(n)}\frac{\partial^4 f^{(n)}}{\partial\eta^4}.
\end{aligned} \tag{2.19}$$

The advantage of above scheme is that only linear terms need to be considered at $(n+1)$ time step. It is important to mention that other choices of time differences are also possible. Using finite difference method above equations are converted into system of linear equations that can be solved by using Gaussian elimination method. This method has already been implemented by several authors to simulate other similar flows [103,104,118-121].

2.4 Numerical results and discussion

In order to study the influence of emerging parameters of interest on velocity and skin friction coefficient, the numerical technique described in previous section is implemented for solving Eq. (2.7) subject to the boundary conditions (2.8) and (2.9) with the initial conditions (2.18). The obtained results are displayed in **Figs. 2.2-2.8**. **Fig. 2.2** shows the effects of the viscoelastic parameter K (panel (a)), suction parameter γ (panel (b)), Hartmann number M (panel (c)), slip parameter ε (panel (d)) and porosity parameter B (panel (e)) on the velocity with time f' at a distance $y=0.25$ from sheet. It is expected that due to the oscillations of stretching sheet the velocity f' at a specific location from the sheet also oscillates but may not with the same amplitude and phase as that of the sheet. From **Fig. 2.2**, we observe that viscoelastic parameter K and suction parameter γ enhance the amplitude of oscillation in the time-series of f'. However, the amplitude of oscillations decrease with increasing slip parameter ε, Hartmann

number M and porosity parameter B. It is interesting to note that a phase difference is observed with increasing the viscoelastic parameter K. This phase shift is attributed to the increase in effective viscosity caused with an increase in K.

Fig. 2.3 illustrates the effects of viscoelastic parameter K on the f' at four different time instants $\tau = 8.5\pi, 9\pi, 9.5\pi$ and 10π with $S = 1.5$, $M = 12$, $\varepsilon = 0.01$, $B = 0.2$ and $\gamma = 0.2$. **Fig. 2.3(a)** shows that f' is an increasing function of K. It is also observed from this figure that there is no oscillation in velocity profile at this time instant. **Fig. 2.3(b)** is plotted to describe the behavior of velocity at $\tau = 9\pi$. This figure elucidates that at this time instant velocity oscillates near the boundary. The velocity profiles for other two times are shown in **Figs. 2.3(c)** and **2.3(d)**, respectively. Again at time instant $\tau = 9.5\pi$, there is no oscillation in the velocity while at $\tau = 10\pi$ the velocity oscillates inside the boundary layer. Moreover, due to introduction of slip at the wall, the velocity f' at the wall decreases with increasing viscoelastic parameter K at time instant $\tau = 8.5\pi, 9.5\pi$ and 10π. However, it increases by increasing K at time $\tau = 9\pi$. The boundary layer thickness is also found to increase with increasing K as evident from **Figs. 2.3(a-d)**. **Fig. 4** shows the influence of suction parameter on the velocity at four different time instants. It is evident that oscillations in f' occurs at $\tau = 9\pi$ and 10π. The velocity and boundary layer thickness increases with increasing suction for $\tau = 8.5\pi$ and the fact is evident from **Fig. 2.4(a)**. A similar behavior is noted form in **Fig. 2.4(c)** for $\tau = 9.5\pi$. For $\tau = 9\pi$ and $\tau = 10\pi$, the velocity oscillates inside the boundary layer as shown in **Figs. 2.4(b)** and **(d)**. **Fig. 2.4** further reveals that due to imposition of slip at the wall, the velocity f' decreases at the wall by increasing γ at time instants $\tau = 8.5\pi$ and 9π while it increases at the wall for $\tau = 9.5\pi$ and $\tau = 10\pi$. **Fig. 2.5** shows the effects of Hartmann number M on f' for four different times. It is observed that an increase in M both reduces velocity and boundary layer thickness. Hence an applied magnetic field can be used to control the boundary layer thickness. **Figure 2.6** illustrates the behavior of velocity under the influence of slip parameter ε. This figure depicts a decrease in f' at the wall for all the considered time instants except $\tau = 10\pi$.

Fig. 2.7 shows the effects of porosity parameter B on the velocity profile at four different times. **Fig. 2.7(a)** indicates a decrease in velocity near the wall at $\tau = 8.5\pi$. with increasing porosity

parameter. On contrary, an increase in velocity at the wall is observed at $\tau = 9\pi$ with increasing B. **Fig. 2.7(c)** and **(d)** show the similar behavior as observed in **Fig. 2.7(b)** and **2.7(a)**, respectively. A slight decrease in boundary layer thickness is also noted with increasing B at all considered time instant.

The variation skin friction coefficient against time is presented in **Fig. 2.8**. It is observed from **Figs. 2.8(a)-(e)** that the amplitude of skin friction increases with increasing viscoelastic parameter, suction parameter, Hartmann number and porosity parameter while it decreases with increasing slip parameter. We also note from this figure a phase shift in skin friction with increasing viscoelastic parameter.

2.5 Concluding remarks

An analysis for the hydromagnetic flow of viscoelastic second grade fluid through a porous medium under the influence of applied magnetic field and slip condition is carried out in this paper. The main objective of the paper is to highlight the influence of slip and porosity parameter on the fluid velocity and skin friction coefficient. To this end, the governing partial differential equations are solved numerically using a robust finite difference scheme. The results show that amplitude of oscillation in the time-series of velocity is an increasing function of viscoelastic, suction and porosity parameters. In contrast, the Hartmann number and slip parameter cause a damping in the amplitude of oscillation in the time-series of velocity. The transverse profiles of velocity indicate a reduction in the boundary layer thickness with increasing porosity parameter and Hartmann number. The results further indicate that skin friction coefficient is oscillatory in nature and its amplitude increases with increasing viscoelastic, porosity and suction parameters. On the contrary, the amplitude of skin friction coefficient decrease with increasing slip parameter.

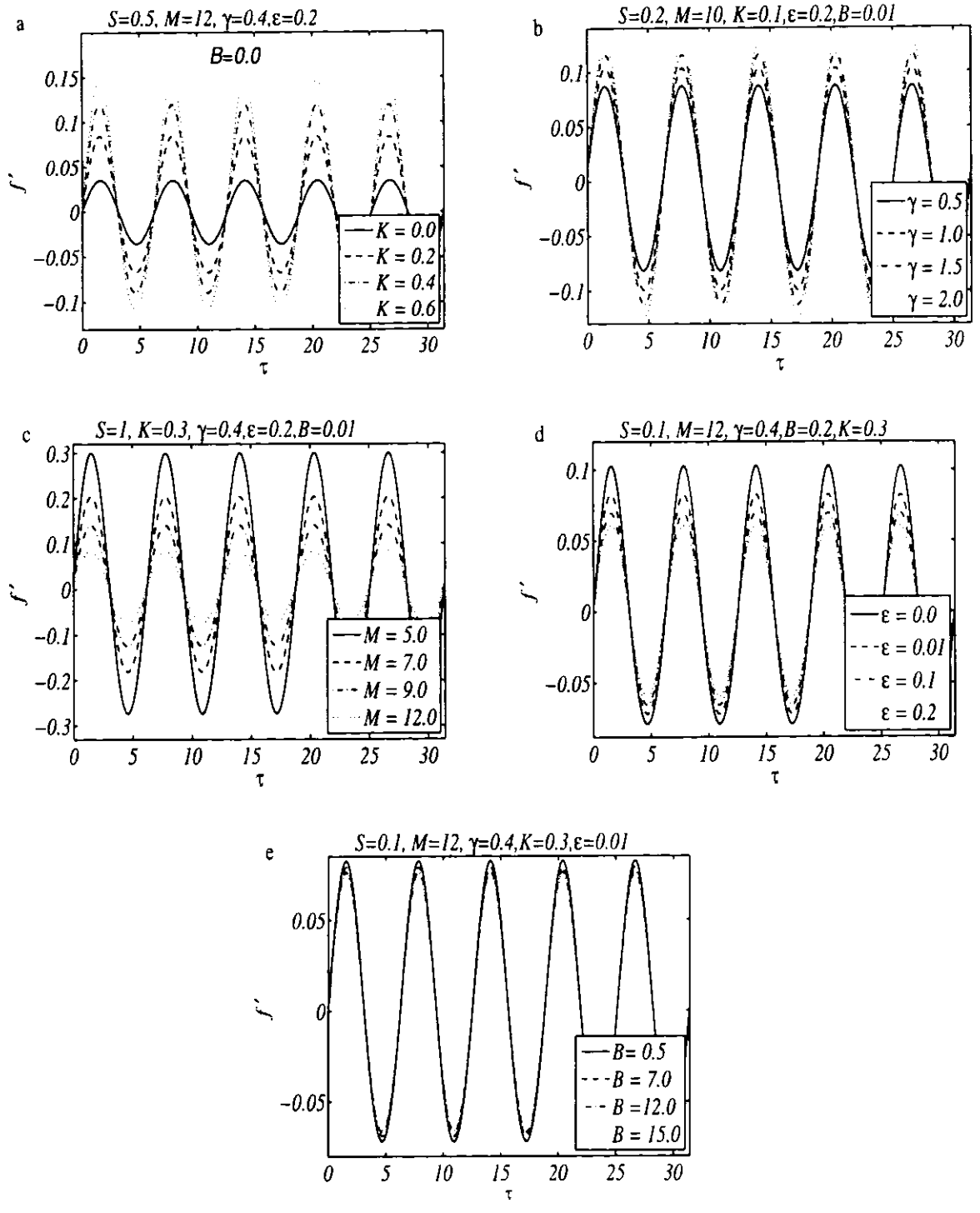

Fig. 2.2: Velocity profile f' as a function of time for different values (a) viscoelastic parameter K (b) suction parameter γ (c) Hartmann number M (d) slip parameter ε and (e) porosity parameter B.

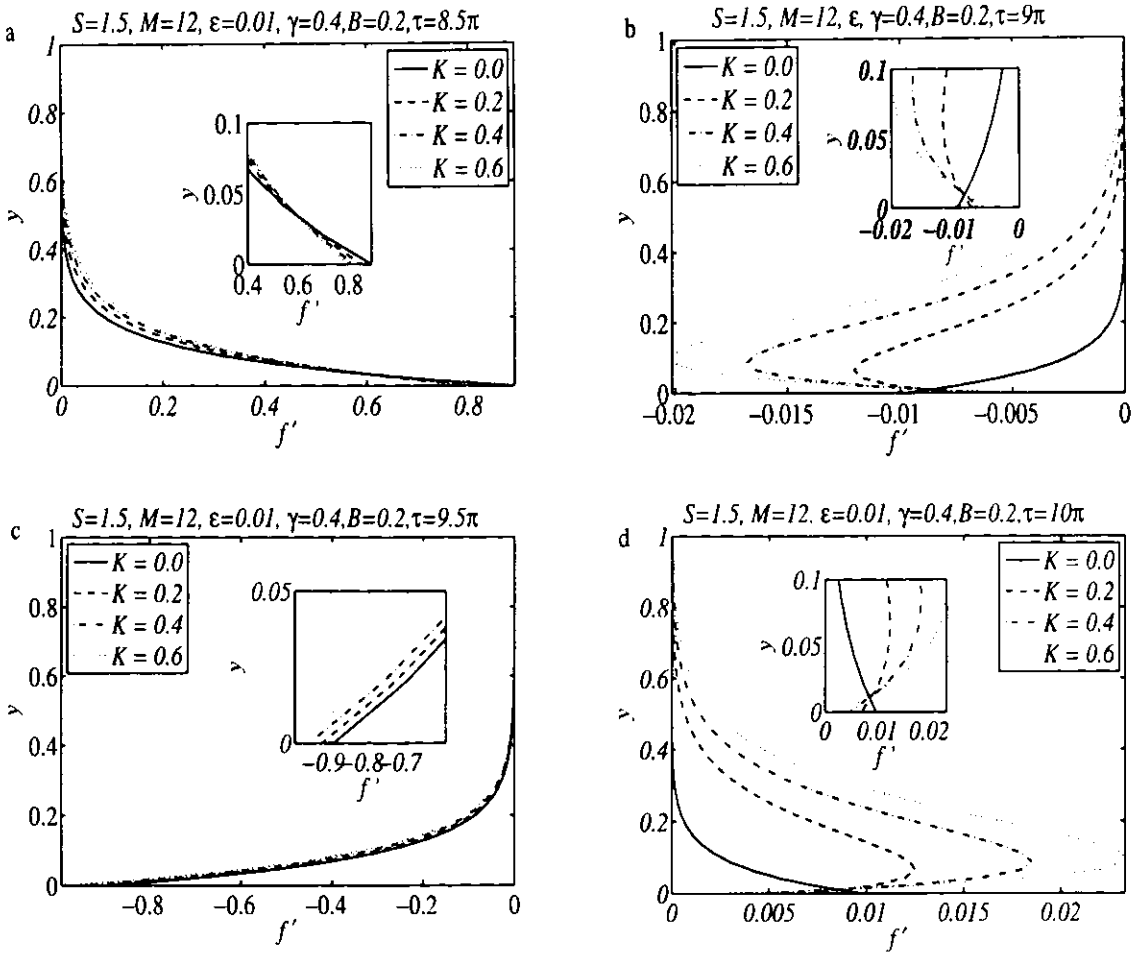

Fig. 2.3: Effects of K on transverse profile of velocity.

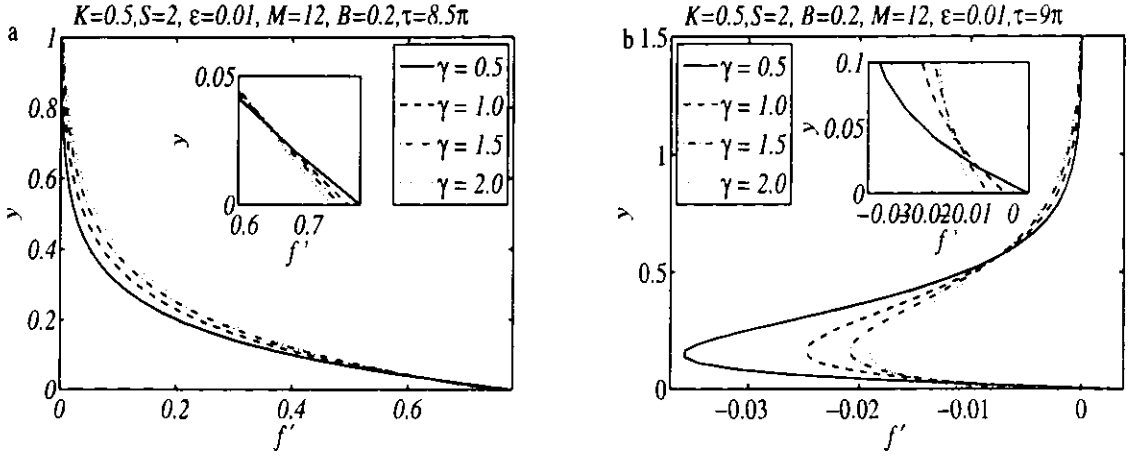

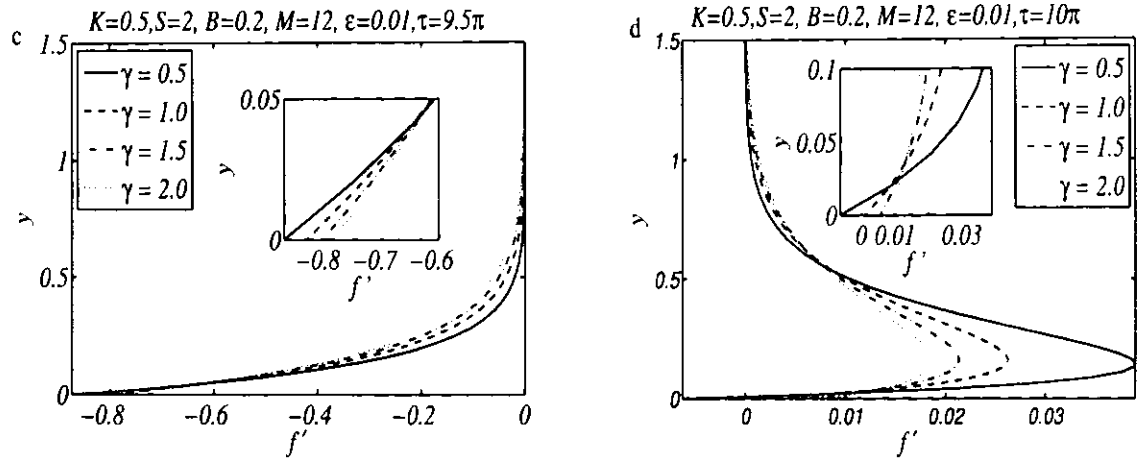

Fig. 2.4: Effects of γ on transverse profile of the velocity.

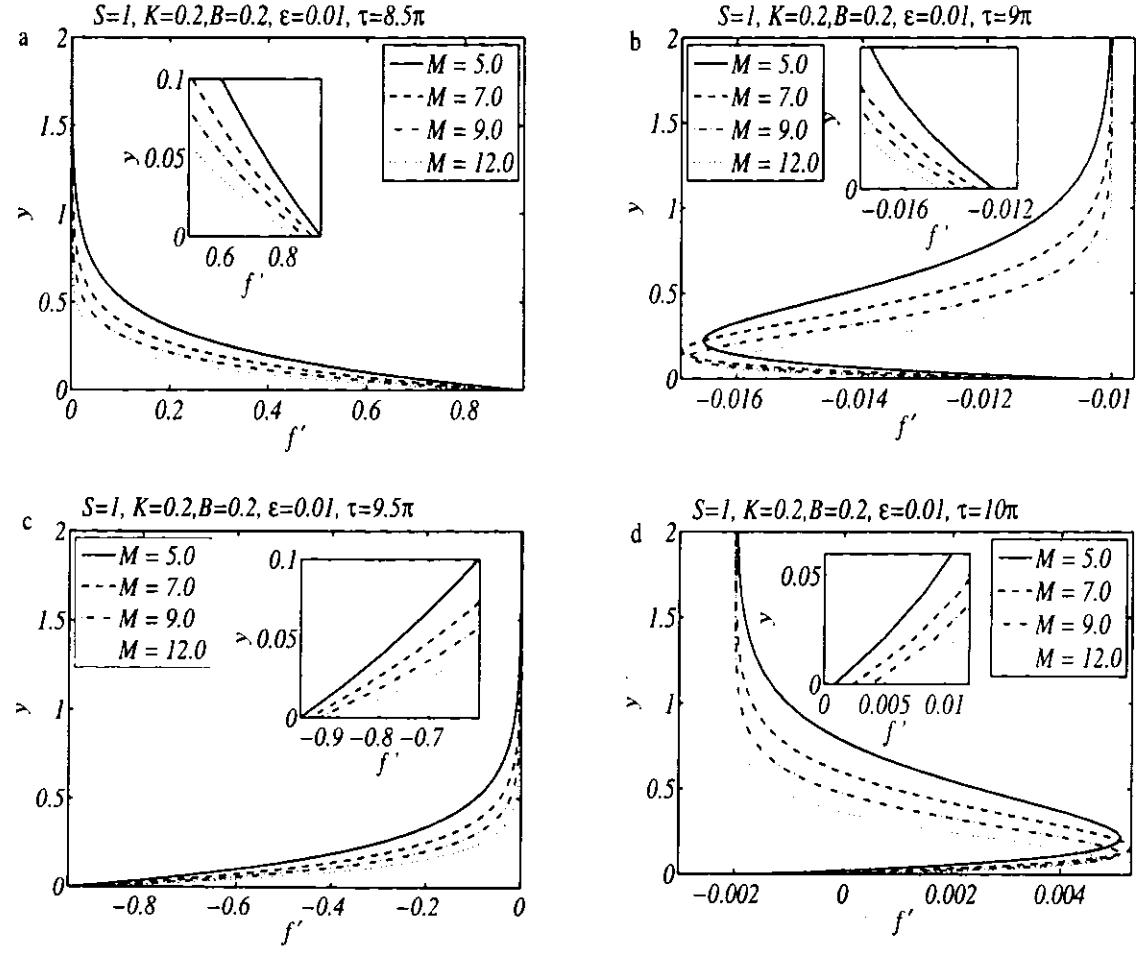

Fig. 2.5: Effects of M on transverse profile of the velocity.

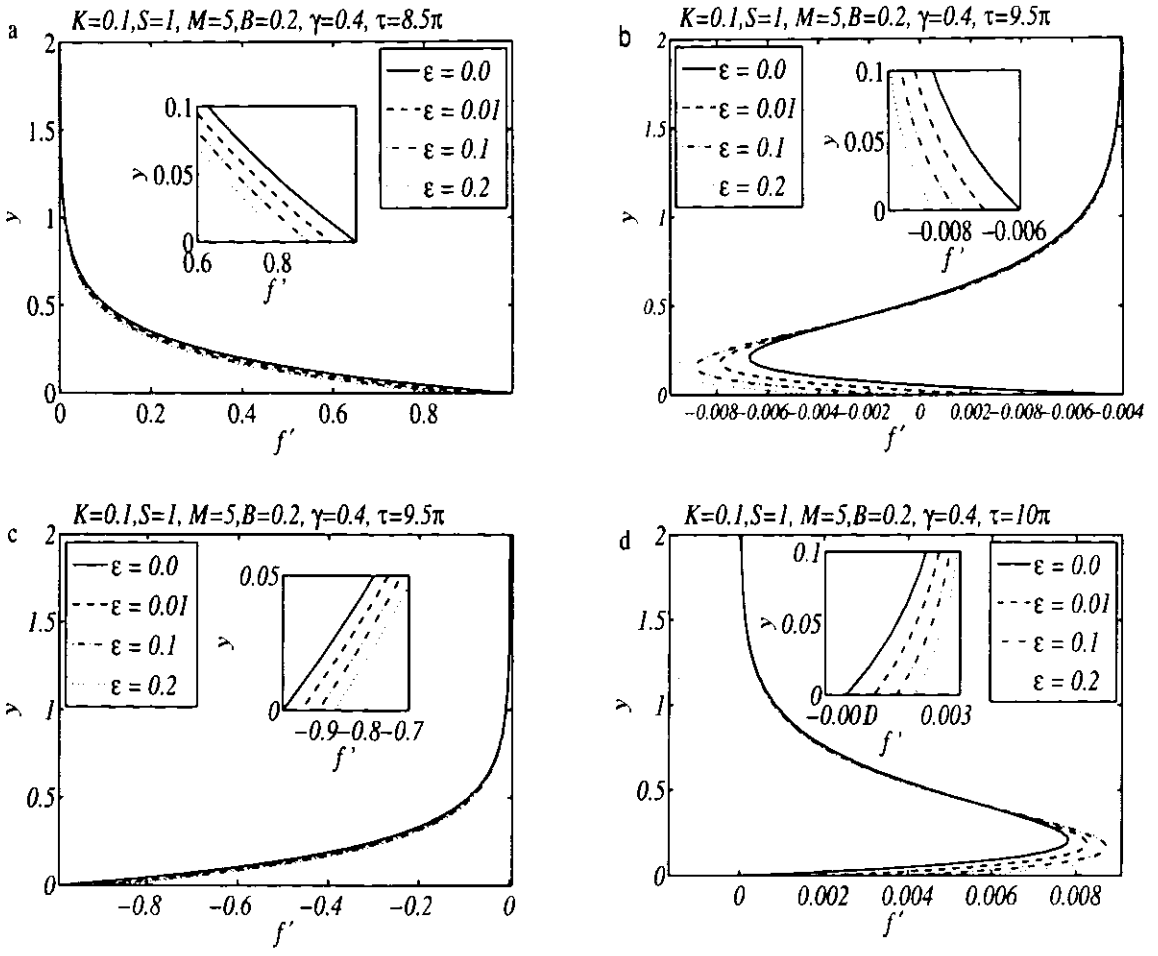

Fig. 2.6: Effects of ε on transverse profile of the velocity.

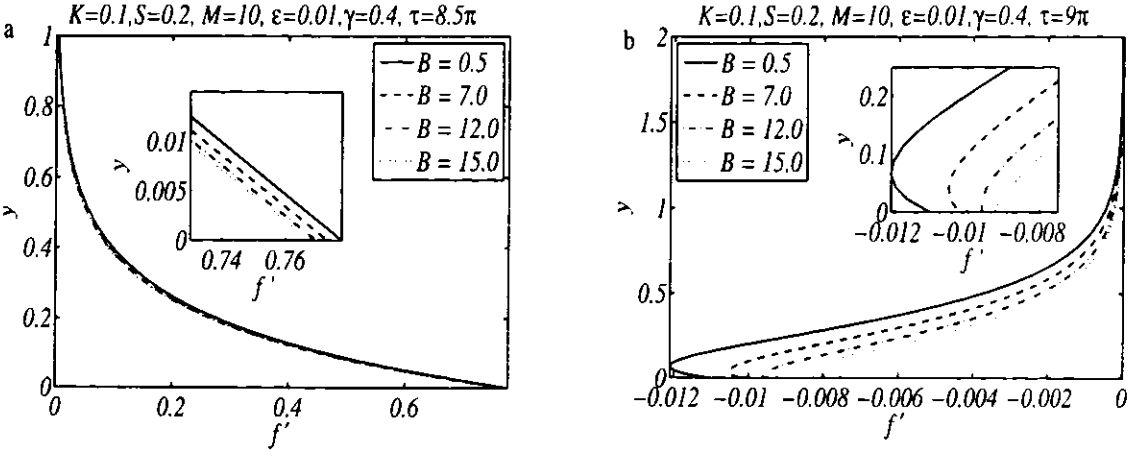

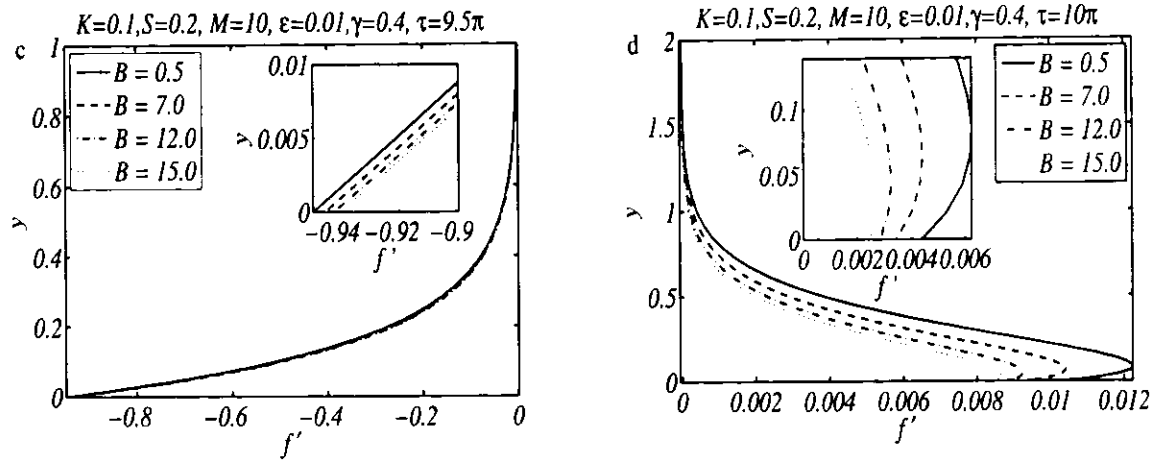

Fig. 2.7: Effects of B on transverse profile of the velocity.

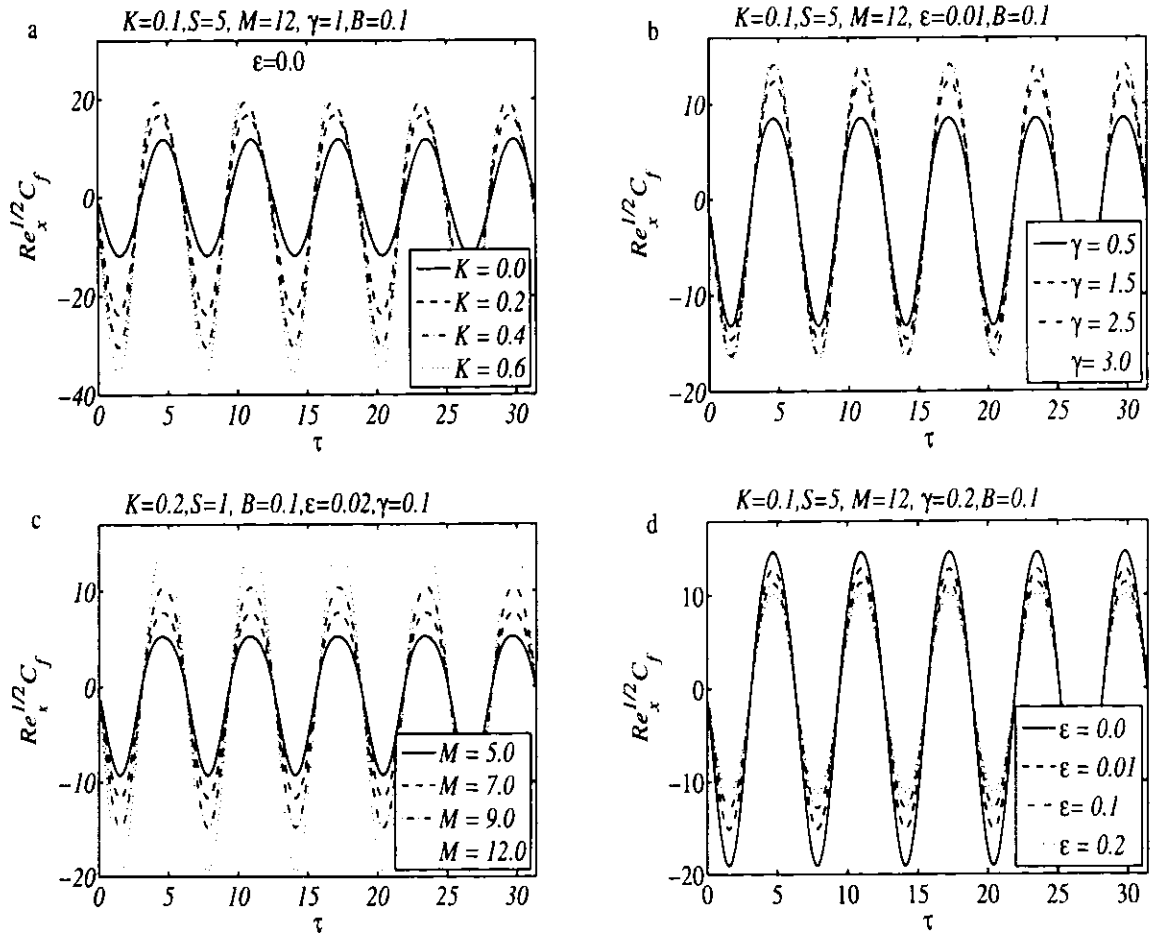

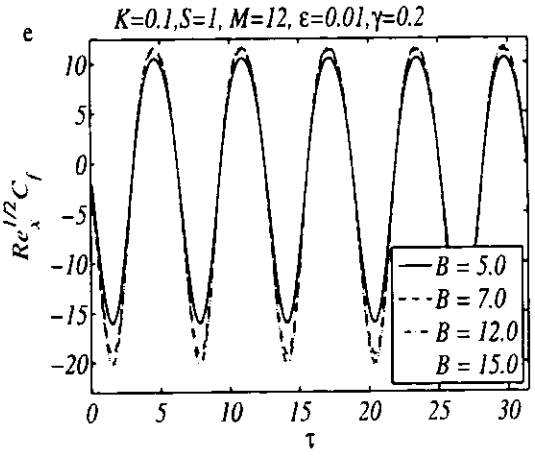

Fig. 2.8: Variation of Skin friction coefficient $\mathrm{Re}_x^{1/2} C_f$ with time (a) effects of K (b) effects of γ (c) effects of M (d) effects of ε and (e) effects of B.

Chapter 3

Hydromagnetic flow and heat transfer over a porous oscillating stretching surface in a viscoelastic fluid with porous medium

In this chapter an analysis is carried out to study the heat transfer for an unsteady two-dimensional magnetohydrodynamics boundary layer flow of a second grade fluid due to porous oscillating stretching surface embedded in a porous medium. The surface is elastic and is stretched periodically to produce flow phenomena. A system of non-linear partial differential equations is developed using suitable dimensionless variables. The semi-infinite domain is transformed to a finite domain and finite difference method is implemented to obtained the numerical solution of the considered flow and heat transfer problem. Fluid velocity, temperature, skin friction coefficient and local Nusselt number are evaluated and analyzed to see the influence of involved parameters.

3.1 Flow Analysis

Consider an unsteady, incompressible and two-dimensional magnetohydrodynamics (MHD) flow of a viscoelastic (second grade) fluid over a porous oscillatory stretching heated sheet embedded in a porous medium and coinciding with the plane $\bar{y}=0$. The temperature of the sheet is maintained as T_w and free stream temperature is T_∞, where $T_w > T_\infty$. A schematic of the flow geometry is illustrated in **Fig. 3.1**. Incorporating these assumptions along with the boundary layer approximations and neglecting viscous dissipation, the governing equations based on conservation momentum and energy in presence of porous medium and body force for unsteady two-dimensional flow are

$$\frac{\partial u}{\partial t}+u\frac{\partial u}{\partial \bar{x}}+v\frac{\partial u}{\partial \bar{y}}=\nu\frac{\partial^2 u}{\partial \bar{y}^2}+\frac{\alpha_1}{\rho}\left[\frac{\partial^3 u}{\partial t\partial \bar{y}^2}+\frac{\partial}{\partial \bar{x}}\left(u\frac{\partial^2 u}{\partial \bar{y}^2}\right)+\frac{\partial u}{\partial \bar{y}}\frac{\partial^2 v}{\partial \bar{y}^2}+v\frac{\partial^3 u}{\partial \bar{y}^3}\right]-\frac{\sigma B_0^2}{\rho}u-\frac{\nu\varphi}{k^*}u, \tag{3.1}$$

$$\rho c_p\left(\frac{\partial T}{\partial t}+u\frac{\partial T}{\partial \bar{x}}+v\frac{\partial T}{\partial \bar{y}}\right)=k_1\frac{\partial^2 T}{\partial \bar{y}^2}. \tag{3.2}$$

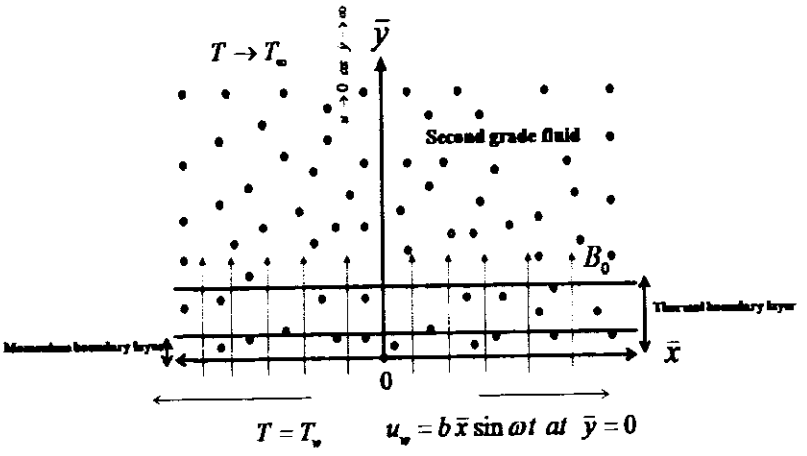

Fig. 3.1: Geometry of the problem.

The flow is subject to no-slip at the wall, therefore the appropriate boundary conditions on velocity components follows from (2.4) and (2.5) with $N^* = 0$. The boundary conditions on temperature field are

$$T = T_w \quad \text{at} \quad \bar{y} = 0, \ t > 0, \tag{3.3}$$

$$T \to T_\infty \quad \text{at} \quad \bar{y} \to \infty. \tag{3.4}$$

Using the non-dimensional variables in Eq. (2.6) along with additional dimensionless variable defined by

$$\theta(y,\tau) = \frac{T - T_\infty}{T_w - T_\infty}, \tag{3.5}$$

Eqs. (3.1) and (3.2) become

$$Sf_{y\tau} + f_y^2 - ff_{yy} + \beta f_y = f_{yyy} + K\left[Sf_{yyy\tau} + 2f_y f_{yyy} - f_{yy}^2 - ff_{yyyy}\right], \tag{3.6}$$

$$\theta_{yy} + \Pr\left(f\theta_y - S\theta_\tau\right) = 0. \tag{3.7}$$

where $\Pr = \mu c_p / k$ is the Prandtl number. The boundary conditions on velocity and temperature in terms of new variables are

$$f_y(0,\tau) = \sin\tau, \quad f(0,\tau) = \gamma, \qquad \theta(0,\tau) = 1, \tag{3.8}$$

$$f_y(\infty,\tau) = 0, \quad f_{yy}(\infty,\tau) = 0, \qquad \theta(\infty,\tau) = 0, \tag{3.9}$$

where $\beta = M^2 + B$ denotes combined parameter due to magnetic field and the porosity of the

porous medium. For non-conducting fluids, $\sigma = 0$ and thus $B = \nu\varphi / k^* b$ corresponds to the classical porosity/permeability parameter and by taking $k^* \to \infty$, as such M corresponds to the classical Hartmann number.

The physical quantities of interest are the skin-friction coefficient C_f and the local Nusselt number Nu_x. The skin-friction coefficient is defined through Eq. (2.12). The local Nusselt number is defined as

$$Nu_x = \frac{\bar{x} q_w}{k_1 (T_w - T_\infty)}, \tag{3.10}$$

where q_w is the heat flux at wall given by

$$q_w = -k_1 \left(\frac{\partial T}{\partial \bar{y}} \right)_{\bar{y}=0}. \tag{3.11}$$

In view of Eqs. (3.5) and (3.11), Eq. (3.10) gives

$$\mathrm{Re}_x^{-1/2} Nu_x = -\theta_\eta (0, \tau). \tag{3.12}$$

3.2 Numerical solution of the problem

In this section, we describe the procedure to obtain the solution of nonlinear boundary value problem consisting of Eqs. (3.6) and (3.7) with boundary conditions (3.8) and (3.9) using finite difference method. As a first step, the infinite domain $y \in [0, \infty)$ is transformed to a finite domain $\eta \in [0,1]$ using transformation (2.14). Equations (3.6) and (3.7) along with boundary conditions in the bounded domain are

$$\begin{aligned} & S(1 - 6K\eta^2) \frac{\partial^2 f}{\partial \eta \partial \eta} - SK\eta^4 \frac{\partial^4 f}{\partial \eta^3 \partial \tau} - 6SK\eta^3 \frac{\partial^3 f}{\partial \eta^2 \partial \tau} = (\eta^2 - 8K\eta^4) \left(\frac{\partial f}{\partial \eta} \right)^2 \\ & + (6\eta^2 - \beta + 24Kf\eta^3 - 2f\eta) \frac{\partial f}{\partial \eta} + \eta^4 \frac{\partial^3 f}{\partial \eta^3} + (6\eta^3 - f\eta^2 + 36Kf\eta^4) \frac{\partial^2 f}{\partial \eta^2} \\ & - 8K\eta^5 \frac{\partial f}{\partial \eta} \frac{\partial^2 f}{\partial \eta^2} + K\eta^6 \left(\frac{\partial^2 f}{\partial \eta^2} \right)^2 - 2K\eta^6 \frac{\partial f}{\partial \eta} \frac{\partial^3 f}{\partial \eta^3} + 12K\eta^5 f \frac{\partial^3 f}{\partial \eta^3} + K\eta^6 f \frac{\partial^4 f}{\partial \eta^4}, \end{aligned} \tag{3.13}$$

$$\eta^4 \frac{\partial^2 \theta}{\partial \eta^2} + 2\eta^3 \frac{\partial \theta}{\partial \eta} - \mathrm{Pr} \left(f\eta^2 \frac{\partial \theta}{\partial \eta} + S \frac{\partial \theta}{\partial \tau} \right) = 0, \tag{3.14}$$

$$f_\eta = 0,\ f_{\eta\eta} = 0,\quad \theta = 0 \quad \text{at} \quad \eta = 0, \tag{3.15}$$

$$f = \gamma,\quad f_\eta = -\sin\tau,\quad \theta = 1 \text{ at } \eta = 1. \tag{3.16}$$

The initial conditions for velocity field and temperature are

$$f(\eta, \tau = 0) = 0 \text{ and } \theta(\eta, \tau = 0) = 0. \tag{3.17}$$

The semi-implicit time difference versions of Eqs. (3.13)-(3.17) are

$$\begin{aligned} &S\left(1-6K\eta^2\right)\frac{1}{\Delta\tau}\left(\frac{\partial f^{(n+1)}}{\partial\eta}-\frac{\partial f^{(n)}}{\partial\eta}\right)-SK\eta^4\frac{1}{\Delta\tau}\left(\frac{\partial^3 f^{(n+1)}}{\partial\eta^3}-\frac{\partial^3 f^{(n)}}{\partial\eta^3}\right)-6SK\eta^3\frac{1}{\Delta\tau}\left(\frac{\partial^2 f^{(n+1)}}{\partial\eta^2}-\frac{\partial^2 f^{(n)}}{\partial\eta^2}\right)\\ &=\left(\eta^2-8K\eta^4\right)\left(\frac{\partial f^{(n)}}{\partial\eta}\right)^2+\left(6\eta^2-\beta\right)\frac{\partial f^{(n+1)}}{\partial\eta}+\left(24K\eta^3-2\eta\right)f^{(n)}\frac{\partial f^{(n)}}{\partial\eta}+6\eta^3\frac{\partial^2 f^{(n+1)}}{\partial\eta^2}\\ &+\left(36K\eta^4-\eta^2\right)f^{(n)}\frac{\partial^2 f^{(n)}}{\partial\eta^2}-8K\eta^5\frac{\partial f^{(n)}}{\partial\eta}\frac{\partial^2 f^{(n)}}{\partial\eta^2}+K\eta^6\left(\frac{\partial^2 f^{(n)}}{\partial\eta^2}\right)^2+\eta^4\frac{\partial^3 f^{(n+1)}}{\partial\eta^3}+\\ &-2K\eta^6\frac{\partial f^{(n)}}{\partial\eta}\frac{\partial^3 f^{(n)}}{\partial\eta^3}+12K\eta^5 f^{(n)}\frac{\partial^3 f^{(n)}}{\partial\eta^3}+K\eta^6 f^{(n)}\frac{\partial^4 f^{(n)}}{\partial\eta^4}, \end{aligned} \tag{3.18}$$

$$S\,\mathrm{Pr}\frac{\left(\theta^{(n+1)}-\theta^{(n)}\right)}{\Delta t}=\eta^4\frac{\partial^2\theta^{(n+1)}}{\partial\eta^2}+2\eta^3\frac{\partial\theta^{(n+1)}}{\partial\eta}-\mathrm{Pr}\,f^{(n)}\eta^2\frac{\partial\theta^{(n+1)}}{\partial\eta}. \tag{3.19}$$

$$f_\eta^{(n)} = 0,\ f_{\eta\eta}^{(n)} = 0,\ \theta^{(n)} = 0 \quad \text{at} \quad \eta = \eta_0 = 0, \tag{3.20}$$

$$f_\eta^{(n)} = \gamma,\ f_\eta^{(n)} = \sin\tau',\ \theta^{(n)} = 1 \quad \text{at} \quad \eta = \eta_{L+1} = 1. \tag{3.21}$$

Using finite difference method the above equations are converted into system of linear equations that can be solved by using Gaussian elimination method at each time step. The stability is solution is largely dependent on the choice of temporal and spatial time step sizes. For the present case, we choose $\Delta\tau = 0.025$ and $\Delta\eta = 0.018$.

3.3 Results and discussion

In this section graphical results based on the numerical solution of Eqs. (3.6) and (3.7) with boundary conditions (3.8) and (3.9) are shown using the numerical scheme described in the previous section. The transverse distributions and time-series for velocity and temperature fields

in the first five periods $\tau \in [0,10\pi]$ are plotted to analyze the influence of the various involved parameters. Furthermore, the values of the skin friction coefficient $\mathrm{Re}_x^{1/2} C_f$ and the local Nusselt number $\mathrm{Re}_x^{-1/2} Nu_x$ for different parameters and displayed both graphically and in tabular form.

Fig. 3.2 shows the velocity component f' against time in the first five periods $\tau \in [0,10\pi]$ for four different values of y (which correspond to different distances from the sheet) when $S = 2$, $\beta = 10$, $\gamma = 0.5$ and $K = 0.1$. It is evident from **Fig. 3.2(a)** that with the increase of distance from the oscillatory sheet, the amplitude of the velocity decreases. It is further noted that far away from the surface, the amplitude of the flow motion is almost negligible. We observe a similar phenomenon from **Fig. 3.2(b)** for $K = 0.5$. However, for $K = 0.5$ the amplitude of the flow motion is large in comparison to the corresponding amplitude for $K = 0.1$.

Fig. 3.3(a-c) illustrates the influence of viscoelastic parameter K, combined parameter β and the mass suction/injection parameter γ on the time-series f'. **Fig. 3.3(a)** shows the effect of the viscoelastic parameter K on the time-series of the velocity profile f' for $S = 2$, $\beta = 10$ and $\gamma = 0.5$. The amplitude of the velocity increases for larger value of K due to the increased effective viscosity and a phase shift occurs which increases with K. The variation of velocity with time for different values of β is shown in **Fig. 3.3(b)**. It is found that an increase in β results in the decrease of amplitude of the flow motion. In fact, an increase in β corresponds to either an increase in strength of the applied magnetic field or a decrease in the permeability of the porous medium. In either case, the resistance to flow is increased and as a result of that the amplitude of the flow velocity is suppressed. **Fig. 3.3(c)** shows the time-series for velocity field f' for different values of the mass suction/injection parameter γ. It is evident from this figure that the amplitude velocity is larger for the higher values of γ. It is also noted that a phase shift occurs which increases with the increase in γ.

Fig. 3.4 depicts the variation of the viscoelastic parameter K on the velocity f' for different values of $\tau = 8.5\pi, 9\pi, 9.5\pi$ and 10π in the fifth period $\tau \in [8\pi,10\pi]$ for which a periodic motion has been reached. At $\tau = 8.5\pi$, f' decays from unity at the surface to zero far away from the surface (**Fig. 3.4(a)**). Morevoer, there is no oscillation in the velocity and it is an

increasing function of the viscoelastic parameter K, i.e. by increasing the values of K. **Fig 3.4(b)** presents the velocity component f' at time instant $\tau = 9\pi$ for various values of K. At this time instant, velocity is zero both at the sheet and far away from the sheet. It is also observed that near the surface, there exists some oscillations in the velocity field and the amplitude of the these oscillations increases with K. These oscillations in the transverse profile is an evidence of a phase shift in the viscoelastic fluid $(K \neq 0)$ in contrast to the viscous fluid $(K = 0)$. **Fig. 3.4(c)-(d)** display the velocity field f' for others two time instants within the fifth periods. It is evident from **Figs. 3.4(c)-(d)** that the flow in the whole domain is almost in phase with the sheet oscillations in the case of Newtonian fluid $(K = 0)$, as shown from the solid lines displayed in **Figs. 3.4(a)-(d)**. Furthermore, we can see from **Fig. 3.4** that the boundary layer thickness is increased by increasing the value of K.

Fig. 3.5 illustrates the effect of the combined parameter β on the transverse profile of the velocity component f' for $\tau = 8.5\pi, 9\pi, 9.5\pi$ and 10π with $S = 1$, $\gamma = 2$ and $K = 0.2$. It is evident from this figure that an increase in the Hartmann number or permeability parameter causes a reduction in the velocity field and the boundary layer thickness (**Fig. 3.5(a)**). However, at $\tau = 9\pi$ (**Fig. 3.5(b)** and $\tau = 10\pi$ (**Fig. 3.5(d)**), there exist the oscillations with fairly small amplitudes in the transverse profiles of f' near the wall. It is also noted that with increase in combined parameter β, the phase difference in f' is almost invisible.

Fig. 3.6 presents the variation in the transverse profile of the velocity field f' for various values of mass suction/injection parameter γ at $\tau = 8.5\pi, 9\pi, 9.5\pi$ and 10π in the fifth period with $S = 2$, $\beta = 10$ and $K = 0.1$. The change in the velocity f' for different values of γ at time $\tau = 8.5\pi$ can be seen from **Fig. 3.6(a)**. It is found that $f' = 1$ at the sheet $y = 0$ and it approaches to zero far away from the sheet. Furthermore, the velocity profile is increased by increasing the value of the γ. The influence of γ on the velocity f' at the time $\tau = 9\pi$ is presented in **Fig. 3.6(b)**. It is evident that at this time point the velocity takes zero value both at the wall and far away from the surface. The amplitude of oscillations near the plate decreases with increasing γ. The velocity fields for other two time points within the fifth period are plotted in **Fig. 3.6(c)** and **(d)** with the similar results as observed in **Figs. 3.6(a)** and **3.6(b)**.

Fig. 3.7 shows the effects of the combined parameter β and the mass suction/injection parameter γ on the time-series of shear stress at the wall $\mathrm{Re}_x^{1/2} C_f$ for the first five periods $\tau \in [0, 10\pi]$. **Fig. 3.7(a)** gives the variation of the combined parameter β on the skin-friction coefficient $\mathrm{Re}_x^{1/2} C_f$. It is evident that skin friction coefficient is oscillatory in nature and amplitude of oscillations increases with increasing β. **Fig. 3.7(b)** displays the effects of γ on the skin-friction coefficient $\mathrm{Re}_x^{1/2} C_f$ with $S = 1$, $\beta = 12$ and $K = 0.2$. It is noted that the oscillation amplitude of the skin-friction coefficient $\mathrm{Re}_x^{1/2} C_f$ increases for large values of mass suction/injection parameter γ.

Fig. 3.8 displays the effect of the Prandtl number Pr, viscoelastic parameter K, parameter β and the mass suction/injection parameter γ on the transverse profile of the temperature θ for the time point $\tau = 8\pi$. **Fig. 3.8(a)** shows the variation of the transverse profile of the temperature distribution θ for different values of Pr at the time point $\tau = 8\pi$. This figure shows that thermal boundary layer thickness decreases with increasing Prandtl number. In fact the Prandtl number represents the ratio of momentum diffusivity to thermal diffusivity; larger values of Prandtl number correspond to fluids with weaker thermal diffusivity. Thus thermal boundary layer thickness in fluids with greater Prandtl number is small in comparison to the fluids having lower Prandtl number. In view of the above fact, it may be concluded that Prandtl number play a key role in the cooling process. In other words it may be used to control the thickness of the momentum and thermal boundary layers. **Fig. 3.8(b)** depicts the transverse profiles of temperature θ for different values of viscoelastic parameter K for the time point $\tau = 8\pi$. It is noticed from this figure that influence of viscoelastic parameter K is to decrease the temperature of the fluid. **Fig. 3.8(c)** illustrates temperature profile θ for various values of β at the time point $\tau = 8\pi$ by keeping all other parameters fixed. It is observed that as we increase the values of β, both temperature θ and thermal boundary layer thickness are increased. The influence of the mass suction/injection parameter γ on the temperature field θ can be seen from **Fig. 3.8(d)**. It is found from this figure that the temperature is a decreasing function of γ. The thermal boundary layer thickness also decreases by increasing γ.

Fig. 3.9 presents the results by varying Pr and γ on the time-series of the temperature distribution θ and the local Nusselt number $\mathrm{Re}_x^{-1/2} Nu_x$ in the first five periods $\tau \in [0, 10\pi]$ at a fixed distance $y = 0.25$ from the sheet. From **Fig. 3.9(a)**, it can be seen that with the increase of Prandtl number Pr, temperature decreases because of thermal diffusivity decreases. **Fig. 3.9(a)** also shows that the magnitude of the local Nusselt number $\mathrm{Re}_x^{-1/2} Nu_x$ is increased by increasing the values of Pr. **Fig. 3.9(b)** illustrates the effects of the mass suction/injection parameter γ on the temperature profile θ and the local Nusselt number $\mathrm{Re}_x^{-1/2} Nu_x$. It is noted from this figure that with the increase in the mass suction/injection parameter γ, the decrease in temperature θ with time becomes slower. Furthermore, a small oscillation, which is superimposed on the monotonically increasing temperature time-series, can be identified for large values of γ. It is further observed that local Nusselt number $\mathrm{Re}_x^{-1/2} Nu_x$ increases with γ. A common observation from **Fig. 3.9(a)-(b)** is that for $\tau = 0$, the local Nusselt number attains a maximum and then decreases monotonically because of the given initial conditions i.e., the temperature gradient at the sheet has its maximum initially which decreases with time.

Table 3.1 shows the numerical values of the skin friction coefficient $\mathrm{Re}_x^{1/2} C_f$ for various values of S, K, β and γ at $\tau = 1.5\pi, 5.5\pi$ and 9.5π. It is evident from this table that the values of skin friction coefficient for the three different time points $\tau = 1.5\pi$, $\tau = 5.5\pi$ and $\tau = 9.5\pi$ are almost identical. Furthermore, we can see that the periodic motion may be reached within the first period when the initial conditions are set up. However, the change in the skin friction coefficient from positive to negative by increasing the value of K indicates the large phase difference as K increases. It is also noted that the values of the skin friction coefficient $\mathrm{Re}_x^{1/2} C_f$ are increased as the relative frequency to the stretching rate S, combined parameter β and the mass suction/injection parameter γ are increased. **Table 3.2** gives the numerical values of the local Nusselt number for Pr, K, β and γ at the four different times points $\tau = 2\pi$, $\tau = 4\pi$, $\tau = 6\pi$ and $\tau = 8\pi$. It is concluded that the local Nusselt number increases by increasing the value of Pr, K and γ while it decreases by increasing β at all four times points $\tau = 2\pi, \tau = 4\pi, \tau = 6\pi$ and $\tau = 8\pi$. Moreover, the values of local Nusselt number are also decrease with time increase from

$\tau = 2\pi$ to $\tau = 8\pi$ due to the decrease in the rate of heat transfer near the sheet.

3.4 Concluding remarks

In chapter, we analyzed the MHD flow and heat transfer of a viscoelastic fluid due to the oscillation of an infinite porous stretching sheet with magnetic field in a porous medium. A coordinate transformation is used to transform the semi-infinite flow domain to a finite computational domain and a suitable finite difference method is used to solve the governing partial differential equations. The time-series of the flow velocity, the temperature, the structure of the boundary layer near the plate for different values of the involved parameters are graphically presented and discussed. The following observations are made on the basis of obtained numerical results:

- The flow field generated by flat sheet which is suddenly stretched periodically rapidly becomes periodic, at most after three or four periods.
- The amplitude of velocity time-series is suppressed for large values of the combined parameter. On the contrary, it increases with increasing the viscoelastic parameter.
- The flow exists only within a boundary layer near the plate, whilst the heat can be transferred to an infinitely large distance with the increase of time.
- The behavior of the temperature is monotonic with time rather than oscillatory.
- The temperature and thermal boundary layer thickness increase with increasing combined parameter while converse trend is noted with increasing viscoelastic parameter and mass suction/injection parameter.

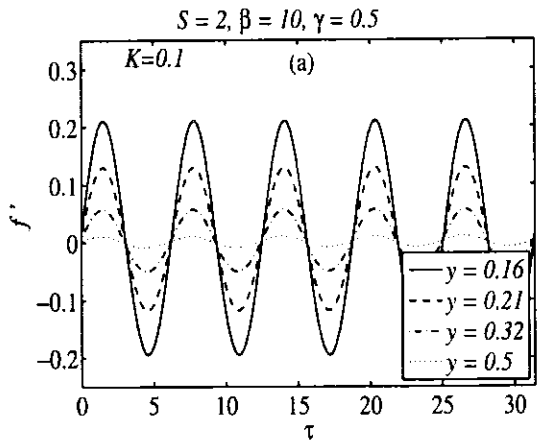

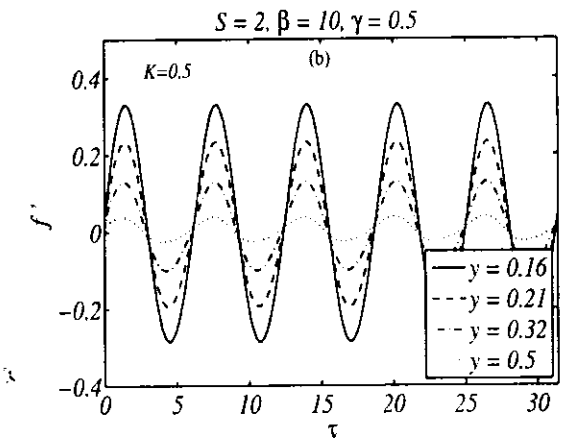

Fig. 3.2: Velocity profile as function of time at four different distances from the sheet $\tau \in [0, 10\pi]$

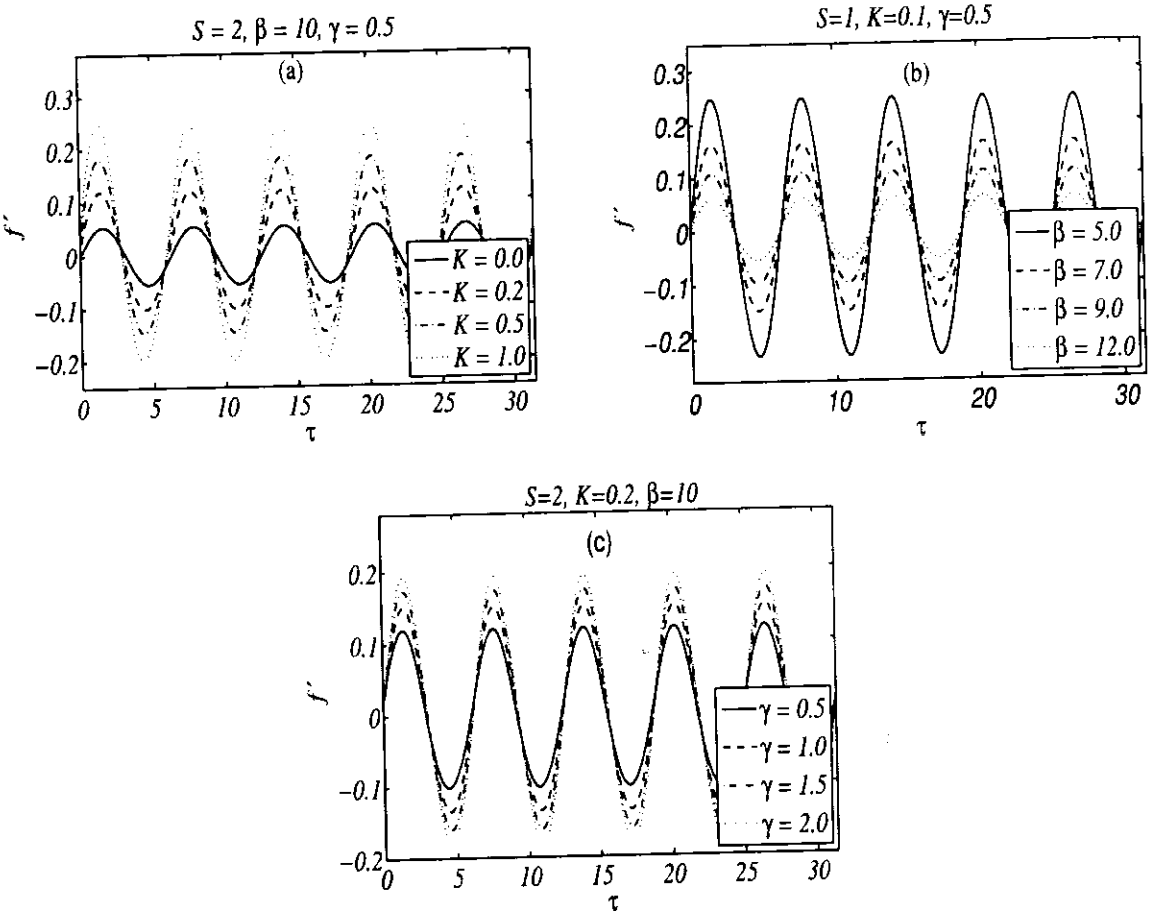

Fig. 3.3: Velocity profile as function of time (a) effects of viscoelastic parameter K (b) effects of β (c) effects of γ.

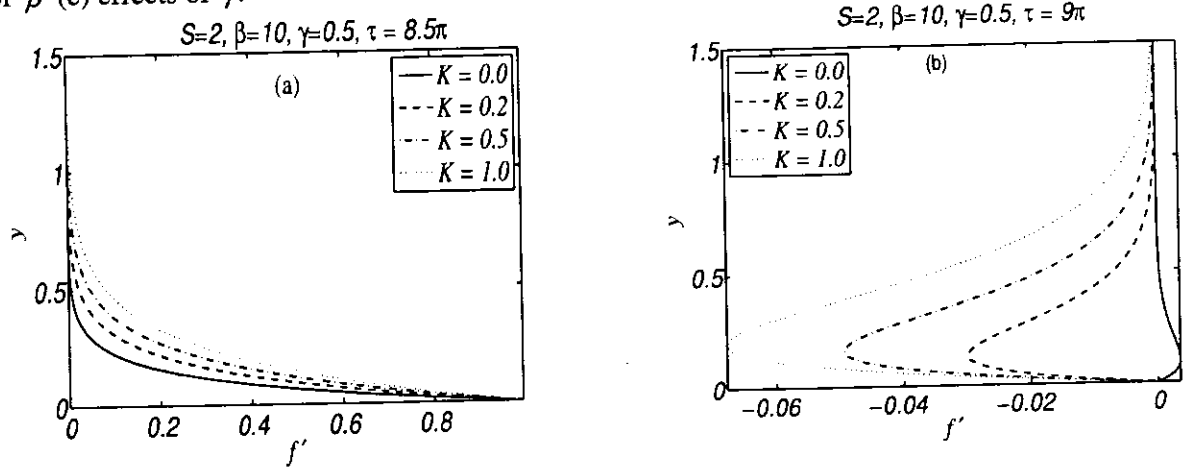

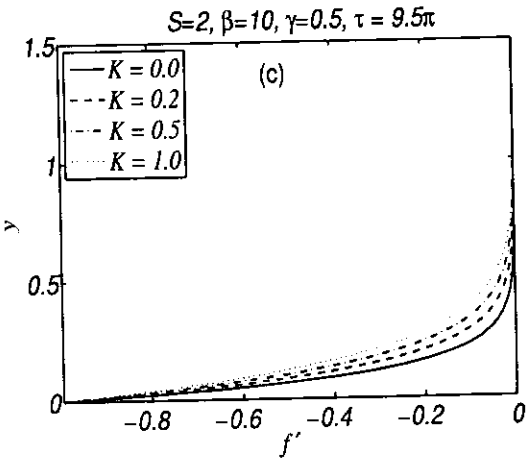

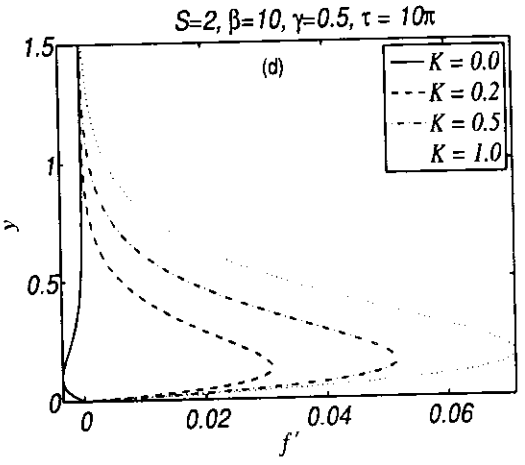

Fig. 3.4: Velocity profile for different values of K.

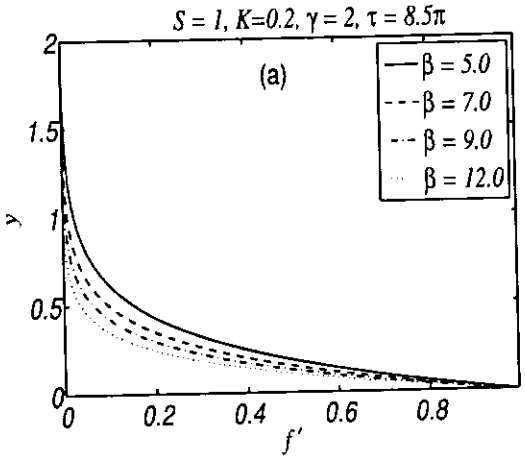

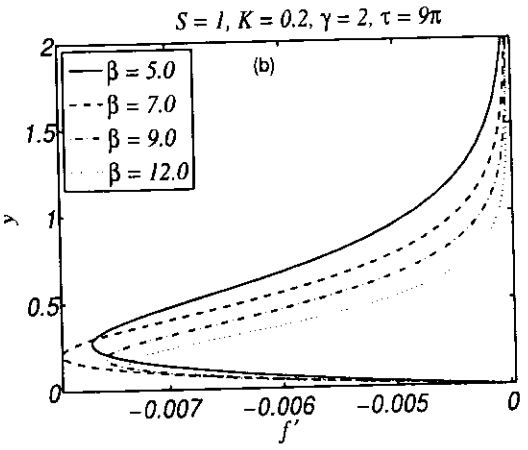

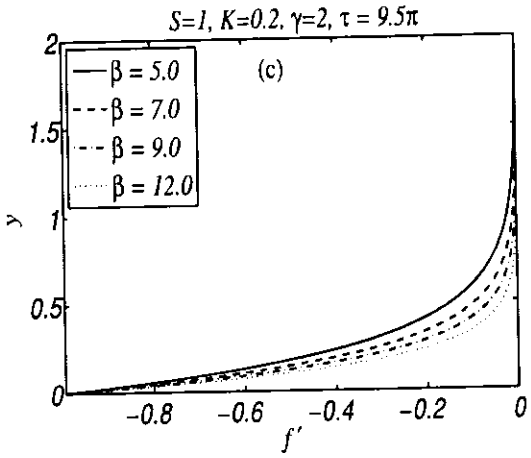

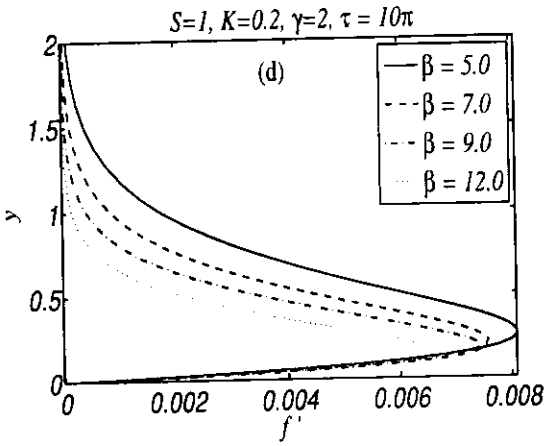

Fig. 3.5: Velocity profile for different values of β.

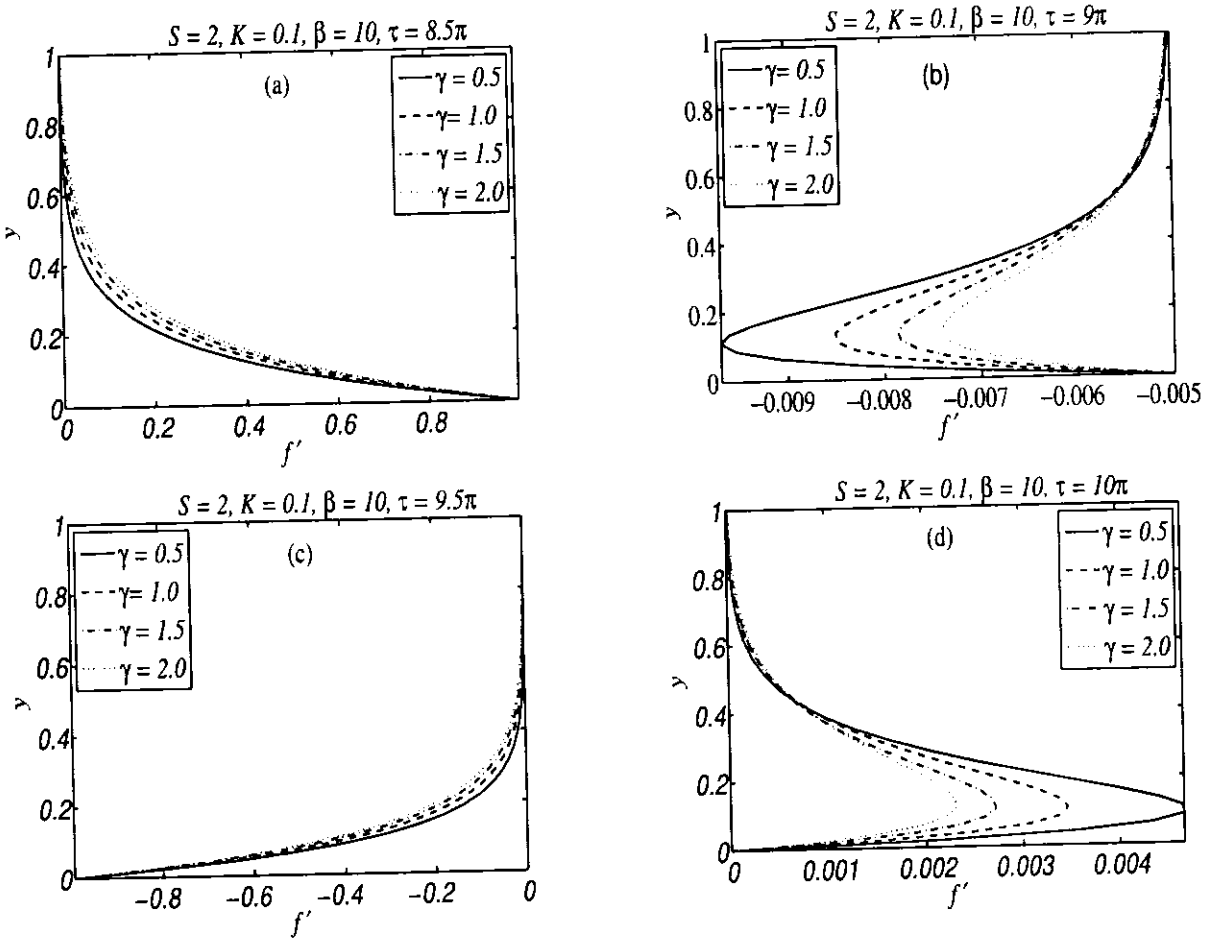

Fig. 3.6: Velocity profile for different values of different values of γ.

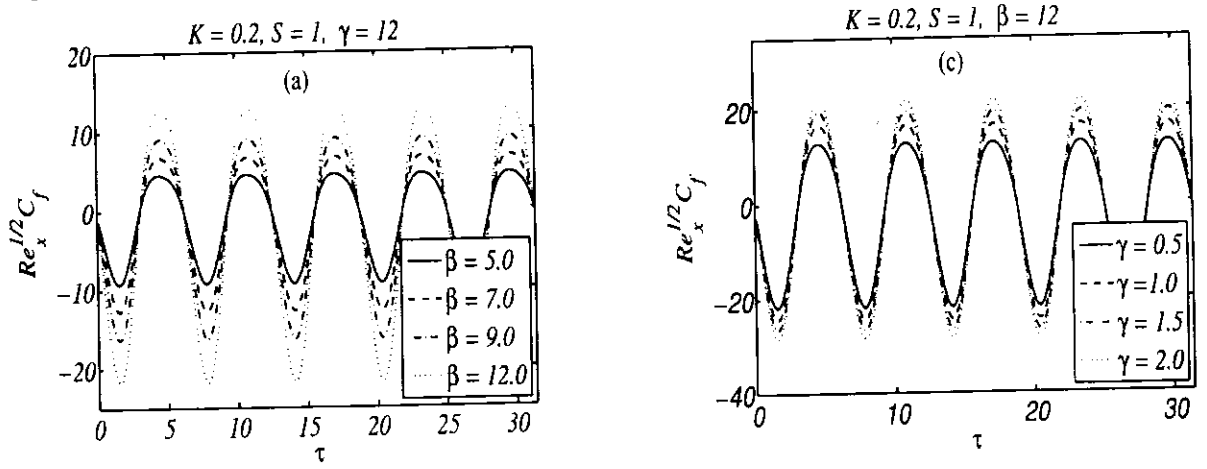

Fig. 3.7: Distribution of skin friction coefficient $\mathrm{Re}_x^{1/2} C_f$ with time (a) effects of β (b) effects of γ.

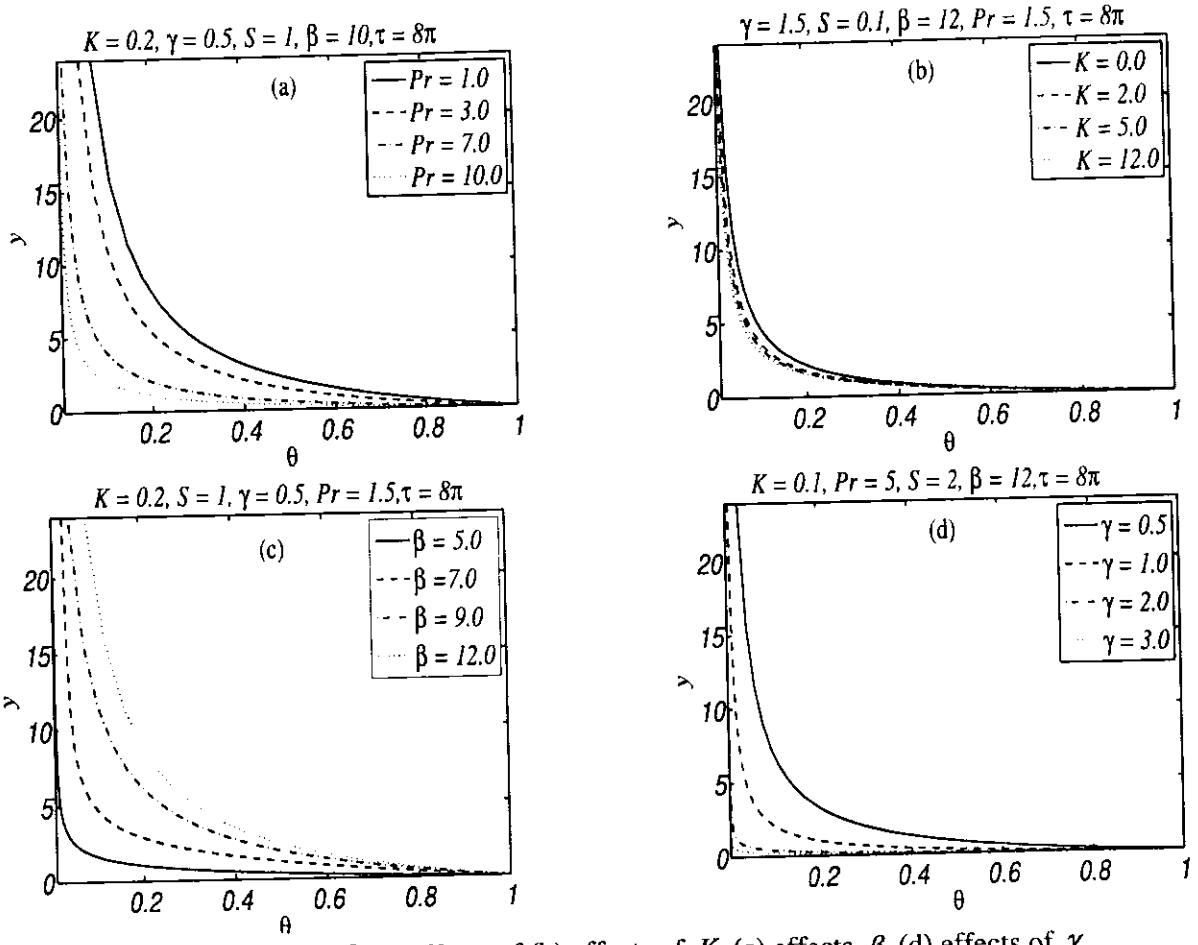

Fig. 3.8: Temperature field θ (a) effects of (b) effects of K (c) effects β (d) effects of γ.

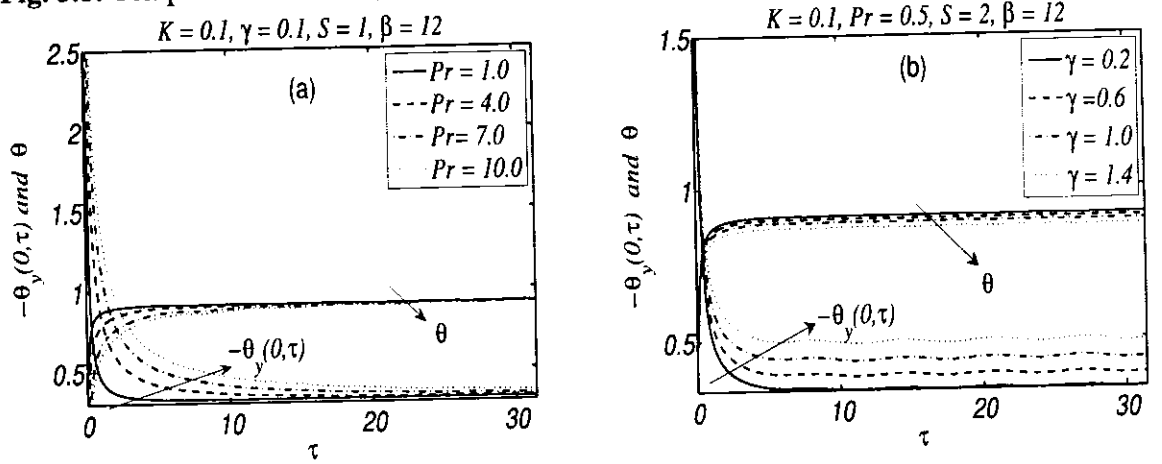

Fig. 3.9: Variation of Nusselt number $\mathrm{Re}_x^{-1/2} Nu_x$ with time and temperature profile θ with time (a) effects of Pr (b) effects of γ.

Table 3.1: Numerical values of the skin-friction coefficient $\mathrm{Re}_x^{1/2} C_f$ for different values of S, K, β and γ at three different time points $\tau = 1.5\pi$, 5.5π and 9.5π.

S	K	β	γ	$\tau = 1.5\pi$	$\tau = 5.5\pi$	$\tau = 9.5\pi$
0.5	0.2	12	0.1	7.712793	7.712849	7.712781
1.0				7.824557	7.824703	7.824677
2.0				8.146671	8.147018	8.146691
3.0				8.570725	8.570726	8.570721
4.0				9.065895	9.066202	9.066481
1.0	0.0			12.182205	12.182195	12.182195
	0.2			7.824557	7.824703	7.824677
	0.5			1.846781	1.846511	1.846236
	0.8			-3.577653	-3.577136	-3.577650
	1.0			-6.938216	-6.938253	-6.938675
	0.2	5.0		3.038148	3.038256	3.037955
		7.0		4.355440	4.355567	4.355471
		9.0		5.716519	5.716240	5.716628
		12.0		7.824557	7.824703	7.824677
		15.0		9.992332	9.992408	9.992349
		12.0	0.2	9.416449	9.416035	9.417047
			0.5	12.837937	12.839594	12.833545
			0.8	15.306652	15.294266	15.292671
			1.0	16.664039	16.656905	16.651919
			1.5	19.506594	19.486431	19.500553

Table 3.2: Numerical values of local Nusselt number $\mathrm{Re}_x^{-1/2} Nu_x$ for several values of parametrs Pr, K, β and γ at four different time points $\tau = 2\pi, 4\pi, 6\pi$ and $\tau = 8\pi$ when $S = 3$.

Pr	K	γ	β	$\tau = 2\pi$	$\tau = 4\pi$	$\tau = 6\pi$	$\tau = 8\pi$
0.3	0.1	0.1	12.0	3.286656	3.250347	3.246147	3.245864
0.5				3.442377	3.300958	3.280489	3.279686
1.0				3.949524	3.528154	3.414912	3.381638
2.0				5.049508	4.140732	3.838137	3.707441
3.0				6.127671	4.814339	4.339281	4.116033
1.0	0.0			3.929795	3.510038	3.396825	3.363732
	0.3			3.957418	3.536146	3.420409	3.387667
	0.8			3.975992	3.554076	3.435345	3.403153
	1.0			3.979141	3.557149	3.437445	3.405464
	1.5			3.981102	3.559297	3.437308	3.405878
	0.2	0.0		3.735224	3.325657	3.215876	3.183788
		0.5		4.967091	4.498941	4.368397	4.331065
		1.0		6.513363	5.997575	5.848653	5.807043
		1.5		8.396179	7.850689	7.687753	7.643900
		1.8		9.694819	9.142083	8.973502	8.929473
		0.1	9.0	3.969607	3.546253	3.434544	3.400663
			12.0	3.967523	3.544466	3.432311	3.398531
			15.0	3.963304	3.540774	3.427898	3.394361
			18.0	3.956978	3.535232	3.421240	3.388076
			20.0	3.945905	3.525353	3.409733	3.376938

Chapter 4

Soret and Dufour effects on hydromagnetic flow of viscoelastic fluid over porous oscillatory stretching sheet with thermal radiation

The aim of this chapter is to investigate the thermal-diffusion and diffusion-thermo effects on magnetohydrodynamics (MHD) viscoelastic second grade fluid due to a porous oscillatory stretching sheet with thermal radiation. The dimensionless nonlinear partial differential equations are solved by means of the homotopy analysis method. The effects of various parameters on velocity, temperature and concentration distributions are investigated and discussed in detail. The numerical values of effective local Nusselt number and Sherwood number are computed and expressed in tabular form.

4.1 Statement of the problem

Consider two-dimensional boundary layer flow of an incompressible electrically conducting second grade fluid over a permeable oscillatory stretching sheet embedded in a porous medium in the presence of Soret and Dufour effects. The effects of the thermal radiation are also incorporated. It is assumed that T_w is the temperature of the sheet and T_∞ denotes the ambient temperature in the free stream, while C_w and C_∞ correspond to surface and ambient concentration, respectively. The schematic diagram of the flow is shown in **Fig. 4.1**. The boundary layer equation in the presence of transverse magnetic field is

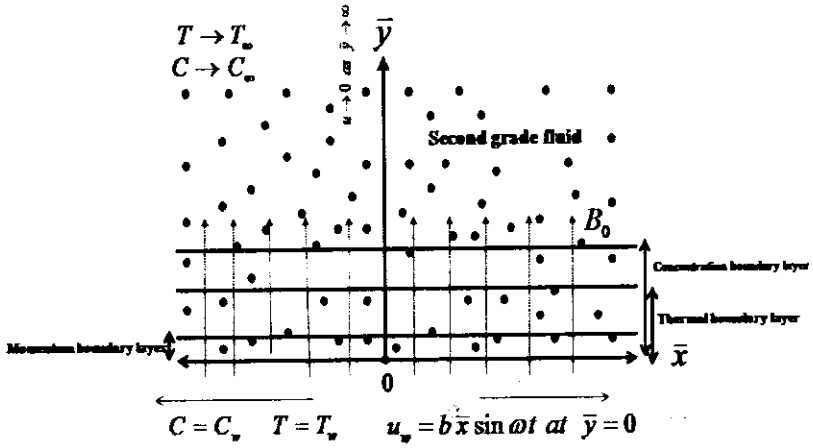

Fig. 4.1: Schematic diagram of the flow

$$\frac{\partial u}{\partial t}+u\frac{\partial u}{\partial x}+v\frac{\partial u}{\partial y}=\nu\frac{\partial^2 u}{\partial y^2}+\frac{\alpha_1}{\rho}\left[\frac{\partial^3 u}{\partial t\partial y^2}+\frac{\partial}{\partial x}\left(u\frac{\partial^2 u}{\partial y^2}\right)+\frac{\partial u}{\partial y}\frac{\partial^2 v}{\partial y^2}+v\frac{\partial^3 u}{\partial y^3}\right]-\frac{\sigma B_0^2}{\rho}u-\frac{\varphi}{\rho k^*}\left(\mu+\alpha_1\frac{\partial}{\partial t}\right)u. \quad (4.1)$$

The involved parameters in above equation are already defined in chapter 2. The energy and concentration equations in presence of thermal radiation, Soret and Dufour effects are

$$\frac{\partial T}{\partial t}+u\frac{\partial T}{\partial x}+v\frac{\partial T}{\partial y}=\alpha\frac{\partial^2 T}{\partial y^2}+\frac{D_m k_T}{c_s c_p}\frac{\partial^2 C}{\partial y^2}-\frac{1}{\rho c_p}\frac{\partial q_r}{\partial y}, \quad (4.2)$$

$$\frac{\partial C}{\partial t}+u\frac{\partial C}{\partial x}+v\frac{\partial C}{\partial y}=D_m\frac{\partial^2 C}{\partial y^2}+\frac{D_m k_T}{T_m}\frac{\partial^2 T}{\partial y^2}, \quad (4.3)$$

where α is the thermal diffusivity, D_m is the molecular diffusivity of the species concentration, k_T is the thermal diffusion ratio, c_s is the concentration susceptibility, T_m is the mean fluid temperature and q_r is the radiative heat flux. By using Rosseland approximation for radiation heat flux [50], we write

$$q_r=-\frac{4\sigma^*}{3\kappa^*}\frac{\partial T^4}{\partial y}, \quad (4.4)$$

where σ^* denotes Stefan-Boltzmann constant, κ^* is mean absorption coefficient. Using Taylor series expansion, one can get

$$T^4\cong 4TT_\infty^3-3T_\infty^4, \quad (4.5)$$

In view of Eqs. (4.4) and (4.5), Eq. (4.2) becomes

$$\frac{\partial T}{\partial t}+u\frac{\partial T}{\partial x}+v\frac{\partial T}{\partial y}=\left(\alpha+\frac{16\sigma^* T_\infty^3}{3k^*}\right)\frac{\partial^2 T}{\partial y^2}+\frac{D_m k_T}{c_s c_p}\frac{\partial^2 C}{\partial y^2}, \quad (4.6)$$

The corresponding initial and boundary conditions for velocity profile remain same as we have discussed in chapter 3 (Eqs. (3.3),(3.4)). The boundary conditions for temperature and concentration profiles are

$$T=T_w=T_\infty+A\bar{x},\ C=C_w=C_\infty+B\bar{x} \ \text{ at } \ \bar{y}=0,\ t>0, \quad (4.7)$$

$$T\to T_\infty,\ C\to C_\infty \quad \text{at} \quad \bar{y}\to\infty, \quad (4.8)$$

where A and B are constant. To non-dimentionalize the flow problem, we use dimensionless variable defined in Eqs. (2.6) and (3.5) along with

$$\phi(y,\tau)=\frac{C-C_\infty}{C_w-C_\infty}. \tag{4.9}$$

with the help of Eq. (2.6), (3.5) and (4.9), Eqs. (4.1), (4.2) and (4.6) reduces to

$$S(1+BK)f_{y\tau}+f_y^2-ff_{yy}+M^2f_y+Bf_y=f_{yyy}+K\left[Sf_{yyy\tau}+2f_yf_{yyy}-f_{yy}^2-ff_{yyyy}\right], \tag{4.10}$$

$$\frac{1}{\Pr}(1+N_r)\theta_{yy}+Du\phi_{yy}+f\theta_y-S\theta_\tau-\theta f_y=0, \tag{4.11}$$

$$\phi_{yy}+Sc\left(Sr\theta_{yy}+f\theta_y-S\theta_\tau-\theta f_y\right)=0. \tag{4.12}$$

In above equations $Sc=\nu/D_mSc$ is the Schmidt number, $Du=D_mk_T(C_w-C_\infty)/c_sc_p\nu(T_w-T_\infty)$ is the Dufour number, $Sr=D_mk_T(T_w-T_\infty)/T_m\nu(C_w-C_\infty)$ represents Soret number and $N_r=16\sigma^*T_\infty^3/3\alpha\kappa^*$ is the radiation parameter.

Following Magyari and Pantokratoras [55], we write Eq. (4.11) as

$$\frac{1}{\Pr_{eff}}\theta_{yy}+Du\phi_{yy}+f\theta_y-S\theta_\tau-\theta f_y=0. \tag{4.13}$$

The dimensionless effective Prandtl number is defined as $\Pr_{eff}=\Pr/(1+N_r)$. In fact, Magyari and Pantokratoras [55] pointed out that there is no need to solve energy equation (4.13) by using two parameter approach i.e. for different values of Pr and N_r. They showed that in fact the investigation of heat transfer characteristics with and without thermal radiation is exactly the same task. They further emphasized that the radiation problem admits the same solution for infinite set of parameter values $(N_r,\Pr)$ which corresponds to same effective Prandtl number. Following Magyari and Pantokratoras [55], we solve the Eq. (4.13) for various values of the effective Prandtl number.

The boundary conditions are

$$f_y(0,\tau)=\sin\tau,\quad f(0,\tau)=\gamma,\qquad \theta(0,\tau)=1, \tag{4.14}$$

$$f_y(\infty,\tau)=0,\quad f_{yy}(\infty,\tau)=0,\qquad \theta(\infty,\tau)=0. \tag{3.15}$$

The skin-friction coefficient C_f is defined in (2.12). We define local Nusselt number and local Sherwood number as

$$Nu=\frac{\bar{x}q_w}{k_1\left(T_f-T_\infty\right)},Sh=\frac{\bar{x}q_m}{D_B\left(C_f-C_\infty\right)}, \tag{4.16}$$

where q_w is the surface heat flux and q_m is the surface mass flux, which can be defined as

$$q_w=-k_1\left(1+\frac{16\sigma^*T_\infty^3}{3k^*}\right)\left(\frac{\partial T}{\partial \bar{y}}\right)_{\bar{y}=0},q_m=-D\left(\frac{\partial C}{\partial \bar{y}}\right)_{\bar{y}=0}, \tag{4.17}$$

In view of (2.6), (3.5) and Eq. (4.9), Eqs. (4.16) and (4.17) become

$$\mathrm{Re}_x^{-1/2}Nu_x^*=-\theta_y(0,\tau),\mathrm{Re}_x^{-1/2}Sh=-\phi_y(0,\tau), \tag{4.18}$$

where $Nu_x^*=Nu_x/(1+N_r)$ is the effective local Nusselt number.

4.2 Solution by homotopy analysis method

In view of boundary conditions, we choose the following initial guesses and linear operators for velocity, temperature and concentration fields

$$f_0(y,\tau)=\gamma+\sin\tau\left(1-\exp(-y)\right),\ \theta_0(y)=\exp(-y),\phi_0(y)=\exp(-y). \tag{4.19}$$

$$\pounds_f(f)=\frac{\partial^3 f}{\partial y^3}-\frac{\partial f}{\partial y},\ \pounds_\theta(f)=\frac{\partial^2 f}{\partial y^2}-f,\ \pounds_\phi(f)=\frac{\partial^2 f}{\partial y^2}-f, \tag{4.20}$$

Such that

$$\pounds_f\left[C_1+C_2\exp(y)+C_3\exp(-y)\right]=0, \tag{4.21}$$

$$\pounds_\theta\left[C_4\exp(y)+C_5\exp(-y)\right]=0, \tag{4.22}$$

$$\pounds_\phi\left[C_6\exp(y)+C_7\exp(-y)\right]=0, \tag{4.23}$$

where $C_i(i=1-5)$ are arbitrary constants.

We construct the following zeroth-order deformation problems

$$(1-p)\pounds_f\left[\hat{f}(y,\tau;p)-f_0(y,\tau)\right]=p\hbar_f N_f\left[\hat{f}(y,\tau;p)\right], \tag{4.24}$$

$$(1-p)\pounds_\theta\left[\hat{\theta}(y,\tau;p)-\theta_0(y,\tau)\right]=p\hbar_\theta N_\theta\left[\hat{\theta}(y,\tau;p),\hat{f}(y,\tau;p),\hat{\phi}(y,\tau;p)\right], \tag{4.25}$$

$$(1-p)\pounds_\phi\left[\hat{\phi}(y,\tau;p)-\phi_0(y,\tau)\right]=p\hbar_\phi N_\phi\left[\hat{\phi}(y,\tau;p),\hat{f}(y,\tau;p),\hat{\theta}(y,\tau;p)\right], \tag{4.26}$$

$$\hat{f}(y,\tau;p)\Big|_{y=0}=0,\ \left.\frac{\partial \hat{f}(y,\tau;p)}{\partial y}\right|_{y=0}=\sin\tau,\ \left.\frac{\partial \hat{f}(y,\tau;p)}{\partial y}\right|_{y=\infty}=0,\ \left.\frac{\partial^2 \hat{f}(y,\tau;p)}{\partial y^2}\right|_{y=\infty}=0. \tag{4.27}$$

$$\hat{\theta}(0,\tau;p)=1,\quad \hat{\theta}(\infty,\tau;p)=0, \tag{4.28}$$

$$\hat{\phi}(0,\tau;p)=1,\quad \hat{\phi}(\infty,\tau;p)=0, \tag{4.29}$$

where $p\in[0,1]$ is an embedding parameter and $\hbar_f,\hbar_\theta,\ \hbar_\phi$ are the auxiliary parameters. The nonlinear operators N_f, N_θ and N_ϕ are

$$N_f\left[\hat{f}(y,\tau;p)\right]=\frac{\partial^3 \hat{f}(y,\tau;p)}{\partial y^3}-S(1+BK)\frac{\partial^2 \hat{f}(y,\tau;p)}{\partial y\partial\tau}+\hat{f}(y,\tau;p)\frac{\partial^2 \hat{f}(y,\tau;p)}{\partial y^2}-\left(\frac{\partial \hat{f}(y,\tau;p)}{\partial y}\right)^2$$
$$-\left(M^2+B\right)\frac{\partial \hat{f}(y,\tau;p)}{\partial y}+K\left\{S\frac{\partial^4 \hat{f}(y,\tau;p)}{\partial y^3\partial\tau}+2\frac{\partial \hat{f}(y,\tau;p)}{\partial y}\frac{\partial^3 \hat{f}(y,\tau;p)}{\partial y^3}-\left(\frac{\partial \hat{f}(y,\tau;p)}{\partial y}\right)^2\right. \tag{4.30}$$
$$\left.-\hat{f}(y,\tau;p)\frac{\partial^4 \hat{f}(y,\tau;p)}{\partial y^4}\right\},$$

$$N_\theta\left[\hat{\theta}(y,\tau;p),\hat{f}(y,\tau;p)\right]=\frac{1}{\mathrm{Pr}_{eff}}\frac{\partial^2\hat{\theta}(y,\tau;p)}{\partial y^2}+\hat{f}(y,\tau;p)\frac{\partial\hat{\theta}(y,\tau;p)}{\partial y}-\hat{\theta}(y,\tau;p)\frac{\partial \hat{f}(y,\tau;p)}{\partial y} \tag{4.31}$$
$$+Du\frac{\partial^2\hat{\phi}(y,\tau;p)}{\partial y^2}-S\frac{\partial\hat{\theta}(y,\tau;p)}{\partial\tau}$$

$$N_\phi\left[\hat{\phi}(y,\tau;p),\hat{\theta}(y,\tau;p),\hat{f}(y,\tau;p)\right]=\frac{\partial^2\hat{\phi}(y,\tau;p)}{\partial y^2}+Sc\left(\hat{f}(y,\tau;p)\frac{\partial\hat{\phi}(y,\tau;p)}{\partial y}-\hat{\phi}(y,\tau;p)\frac{\partial \hat{f}(y,\tau;p)}{\partial y}\right. \tag{4.32}$$
$$\left.+Sr\frac{\partial^2\hat{\theta}(y,\tau;p)}{\partial y^2}-S\frac{\partial\hat{\phi}(y,\tau;p)}{\partial\tau}\right).$$

The solutions of above problems at $p=0$ and $p=1$ are

$$\hat{f}(y,\tau;0)=f_0(y,\tau),\hat{f}(y,\tau;1)=f(y,\tau), \tag{4.33}$$

$$\hat{\theta}(y,\tau;0)=\theta_0(y,\tau),\hat{\theta}(y,\tau;1)=\theta(y,\tau), \tag{4.34}$$

$$\hat{\phi}(y,\tau;0)=\phi_0(y,\tau),\hat{\phi}(y,\tau;1)=\phi(y,\tau). \tag{4.35}$$

Expanding $\hat{f}(y,\tau;p)$ $\hat{\theta}(y,\tau;p)$ and $\hat{\phi}(y,\tau;p)$ in a Taylor's series with respect to p, we get

$$\hat{f}(y,\tau;p)=f_0(y,\tau)+\sum_{m=1}^{\infty}f_m(y,\tau)\,p^m,\quad f_m(y,\tau)=\frac{1}{m!}\frac{\partial^m\hat{f}(y,\tau;p)}{\partial p^m},\tag{4.36}$$

$$\theta(y,\tau;p)=\theta_0(y,\tau)+\sum_{m=1}^{\infty}\theta_m(y,\tau)\,p^m,\quad \theta_m(y,\tau)=\frac{1}{m!}\frac{\partial^m\hat{\theta}(y,\tau;p)}{\partial p^m},\tag{4.37}$$

$$\hat{\phi}(y,\tau;p)=\phi_0(y,\tau)+\sum_{m=1}^{\infty}\phi_m(y,\tau)\,p^m,\quad \phi_m(y,\tau)=\frac{1}{m!}\frac{\partial^m\hat{\phi}(y,\tau;p)}{\partial p^m},\tag{4.38}$$

Using generalized Leibnitz formula, we take *mth* derivative of *zeroth*-order problem with respect to p and then set $p=0$ to get

$$\pounds_f\left[f_m(y,\tau)-\chi_m f_{m-1}(y,\tau)\right]=\hbar_f R_m^f(y,\tau),\tag{4.39}$$

$$\pounds_\theta\left[\theta_m(y,\tau)-\chi_m\theta_{m-1}(y,\tau)\right]=\hbar_\theta R_m^\theta(y,\tau),\tag{4.40}$$

$$\pounds_\phi\left[\phi_m(y,\tau)-\chi_m\phi_{m-1}(y,\tau)\right]=\hbar_\phi R_m^\phi(y,\tau),\tag{4.41}$$

$$f_m(0,\tau)=0,\ \frac{\partial f_m(0,\tau)}{\partial y}=0,\ \frac{\partial f_m(\infty,\tau)}{\partial y}=0,\frac{\partial^2 f_m(\infty,\tau)}{\partial y^2}=0,\tag{4.42}$$

$$\theta_m(0,\tau)=\theta_m(\infty,\tau)=0,\phi_m(0,\tau)=\theta_m(\infty,\tau)=0,\tag{4.43}$$

$$R_m^f(y,\tau)=\frac{\partial^3 f_{m-1}}{\partial y^3}-S(1+BK)\frac{\partial^2 f_{m-1}}{\partial y\partial\tau}-M^2\frac{\partial f_{m-1}}{\partial y}-B\frac{\partial f_{m-1}}{\partial y}+\sum_{k=0}^{m-1}\left(f_{m-1-k}\frac{\partial^2 f_k}{\partial y^2}-\frac{\partial f_{m-1-k}}{\partial y}\frac{\partial f_k}{\partial y}\right)$$
$$+KS\frac{\partial^4 f_{m-1}}{\partial y^3\partial\tau}+K\sum_{k=0}^{m-1}\left(2\frac{\partial f_{m-1-k}}{\partial y}\frac{\partial^2 f_k}{\partial y^2}-\frac{\partial^2 f_{m-1-k}}{\partial y^2}\frac{\partial^2 f_k}{\partial y^2}-f_{m-1-k}\frac{\partial^4 f_k}{\partial y^4}\right),\tag{4.44}$$

$$R_m^\theta(y,\tau)=\frac{1}{\mathrm{Pr}_{eff}}\frac{\partial^2\theta_{m-1}}{\partial y^2}+Du\left(\frac{\partial^2\theta_{m-1}}{\partial y^2}\right)-S\frac{\partial\theta_{m-1}}{\partial\tau}+\sum_{k=0}^{m-1}\left(f_{m-1-k}\frac{\partial\theta_k}{\partial y}-\theta_{m-1-k}\frac{\partial f_k}{\partial y}\right).\tag{4.45}$$

$$R_m^\phi(y,\tau)=\frac{\partial^2\phi_{m-1}}{\partial y^2}+Sc(Sr)\frac{\partial^2\theta_{m-1}}{\partial y^2}-Sc\left(S\frac{\partial\theta_{m-1}}{\partial\tau}\right)+Sc\sum_{k=0}^{m-1}\left(f_{m-1-k}\frac{\partial\phi_k}{\partial y}-\phi_{m-1-k}\frac{\partial f_k}{\partial y}\right).\tag{4.46}$$

$$\chi_m=\begin{cases}0, & m\le 1,\\ 1, & m>1.\end{cases}\tag{4.47}$$

The problems defined above are called *mth*-order deformation problems. The solution of above problems can be expressed as

$$f_m(y,\tau)=f_m^*(y,\tau)+C_1+C_2\exp(y)+C_3\exp(-y),\tag{4.48}$$

$$\theta_m(y,\tau)=\theta_m^*(y,\tau)+C_4\exp(y)+C_5\exp(-y). \tag{4.49}$$

$$\phi_m(y,\tau)=\phi_m^*(y,\tau)+C_4\exp(y)+C_5\exp(-y), \tag{4.50}$$

where $f_m^*(y,\tau),\theta_m^*(y,\tau)$ and $\phi_m^*(y,\tau)$ denote the particular solutions.

4.3 Convergence of HAM solution

We see that Eqs. (4.39)-(4.41) consist of nonzero auxiliary parameters $\hbar_f,\hbar_\theta$ and $\hbar_\phi$. The convergence of the obtained series solution can be controlled by proper choice of these auxiliary parameters. **Fig. 4.2(a-c)** are plotted to find the plausible values of $\hbar_f,\hbar_\theta$ and $\hbar_\phi$ at 10^{th} order of approximation. We note from these figures that for convergent solutions $-1\le\hbar_f<-0.1,-1.2\le\hbar_\theta<-0.1$ and $-1.3\le\hbar_\phi<-0.1$.

4.4 Analysis of obtained results

The main aim of this work is to investigate the effects of various parameters of interest on velocity, temperature and concentration. To this end **Fig. 4.3-4.19** have been plotted. **Figs. 4.3(a-d)** shows the effects of viscoelastic parameter K, Hartmann number M, porosity parameter B and suction/injection parameter γ on the time-series of velocity profile f' at fixed distance $y=0.25$ from the surface. From **Fig. 4.3(a)** it is noticed that amplitude of the velocity increases by increasing viscoelastic parameter K because of increased effective viscosity. Further, it can be seen that a phase shift occurs which increases with an increase in viscoelastic parameter K. **Fig. 4.3(b)** elucidate the variation of Hartmann number M on time-evolution of velocity profile when $S=1,K=0.1\ \gamma=3$ and $B=0.5$. This figure show that the amplitude of velocity is suppressed by increasing Hartmann number M. Since the magnetic lines of force behaves like elastic bands in the fluid motion therefore, fluid motion is suppressed and thus amplitude is reduced. The velocity as a function of time $f'(y,\tau)$ by keeping values of other parameters fixed is illustrated for different values of B in **Fig. 4.3(c).** We note that the influence of porosity parameter is similar to Hartmann number i.e., the amplitude of velocity decreases with increase of porosity parameter B, In fact, an increase in the porosity parameter decrease the permeability of the porous medium and hence increase the resistance to flow. The effects of suction/injection

parameter γ on f' are illustrated in **Fig. 4.3(d)**. In the case of suction $(\gamma>0)$, the amplitude of velocity decreases with time. However, in the case of injection $(\gamma<0)$ an opposite behavior is observed.

Figs. (4.4-4.7) demonstrate the effects of viscoelastic parameter K, Hartmann number M, suction/injection parameter γ and porosity parameter B on transverse profile of f' at a fixed time $\tau=8.5\pi$. **Fig. 4.4** shows the effects of viscoelastic parameter K on velocity profile f'. It is noted from this figure that f' increases with the increase of viscoelastic parameter K. The momentum boundary layer thickness also increases by increasing viscoelastic parameter. The dimensionless form of the viscoelastic parameter suggests that K is inversely proportional to the viscosity and thus increase in K reduces the viscosity as a result velocity is increased. **Fig. 4.5** shows a decrease in f' with the increase in the Hartmann number M. The momentum boundary layer thickness is suppressed for higher values of Hartmann number M. This is in accordance with the fact that a constant magnetic field suppresses the bulk motion and alters the boundary layers. The porous medium also offers resistance to the flow and thus **Fig. 4.6** depicts a decrease in velocity. **Fig. 4.7** shows the same behavior as observed in **Fig. 4.6** i.e. the velocity decreases significantly with the increase in the suction $(\gamma>0)$ while in the case of blowing $(\gamma<0)$ the velocity of fluid increases. It is also noted that in the case of wall suction $(\gamma>0)$, a decrease in momentum boundary layer thickness is observed.

The effects of effective Prandtl number Pr_{eff} viscoelastic parameter K, Dufour numbers Du, Hartmann number M, suction/injection parameter γ and porosity parameter B on the temperature profile are illustrated in **Figs. (4.8-4.13)**. It is observed from figure 8 that increase of effective Prandtl number Pr_{eff}, temperature and thermal boundary layer thickness decreases. An increase in effective Prandtl number means that thermal diffusivity is decreased and as a result temperature of the fluid decreases.

Fig. 4.9 depicts that with the increase of Dufour number Du, the thickness of thermal boundary layer enhanced. **Fig. 4.10** depicts that graph of the non-dimensional temperature profile $\theta(\eta)$ for different values of Hartmann number M. Increase of magnetic parameter means increase of

Lorentz force which creates enhancement in the dimensionless temperature and thermal boundary layer thickness. It is evident from this figure that temperature increase with the increase of Hartmann number M. **Figs. 4.11** shows that temperature decreases with the increase of viscoelastic parameter K. The effects of suction/injection parameter on $\theta(\eta)$ are illustrated in **Fig. 4.12**. Here a decrease in the temperature is noted with increasing suction velocity. In fact, the strong cross-stream flow velocity imposed at the plate prevents the thermal boundary layer to grow and as a result the temperature of the fluid is decreased.

The variation of the concentration field at $\tau = \pi/2$ is illustrated in **Figs. (4.13-4.19)** for various values of Schmidt number Sc, Soret number Sr, Hartmann number M, viscoelastic parameter K, porosity parameter B and suction/injection parameter γ.

Fig. 4.13 represents the effects of Schmidt number Sc on dimensionless concentration profile. The concentration profile as well as concentration boundary layer thickness decreases for higher values of Schmidt number. As Schmidt number Sc is the ratio of momentum to mass diffusivities, hence mass diffusivity decreases for higher values of Schmidt number Sc which leads to a decrease in the concentration profile. These effects may be attributable to the increase in the rate of solute transfer from the surface by increasing the Schmidt number. The influence of dimensionless Soret number Sr is presented in **Fig. 4.14**. This figure shows that concentration profile is an increasing function of Soret number. The variation of Hartmann number M on concentration field ϕ is shown in **Fig. 4.15**. Likewise temperature, the concentration increases with increase in Hartmann number M. **Fig. 4.16** demonstrates the effects of viscoelastic parameter K on dimensionless concentration profile. The concentration profile decreases with an increase in viscoelastic parameter K. The thickness of the concentration boundary layer also decreases for lager values of viscoelastic parameter. The variation of porosity parameter B on concentration profile is plotted in **Fig. 4.17**. An increase in porosity parameter B causes a rise in the concentration. The concentration boundary layer thickness increases with increasing porosity parameter B. **Fig. 4.18** displays the effects of suction/injection parameter on the concentration profile. The concentration decreases in case of suction while it increases in case of injection. The concentration boundary layer thickness is reduced because of the suction of decelerated fluid particles through the porous wall. In contrast, the concentration boundary layer thickness is higher in the case of injection.

The time-series of skin friction coefficient for different values of K and B is illustrated in **Figs. 4.19 (a-b)**. **Fig. 4.19(a)** shows that the skin friction coefficient oscillates with time and its amplitude raises with the increase of viscoelastic parameter K. **Fig. 4.19 (b)** depicts the influence of B on time-evolution of skin friction coefficient. It is observed that the amplitude of skin friction coefficient increases with increasing B. It is also noted that a phase shift occurs which increases for larger values of B.

Table 4.1 shows the numerical values of the effective local Nusselt number at fixed time $\tau = \pi/2$. It is observed from this table that effective local Nusselt number increases with an increase of Pr_{eff}, Sr, γ and K while it decrease with an increase in M, Sc, Du and B. The numerical values of the local Sherwood number are illustrated in **Table 4.2**. We observe that local Sherwood number increases with Sc, Du, K and γ while it shows opposite behavior by increasing Pr_{eff}, Sr, M and B.

4.5 Conclusions

The Soret and Dufour effects on unsteady boundary layer flow of a second grade fluid over a porous oscillatory stretching sheet have been investigated. Heat transfer analysis has been performed under influence of thermal radiation. The number of independent variables in governing equations has been reduced by using transformed dimensionless variables. Well known analytical technique namely, homotopy analysis method has been employed for solution. The solutions are illustrated through various plots. The main findings are:

- Increasing the viscoelastic parameter causes an increase of the amplitude of the flow velocity. The amplitude of the flow velocity decreases for larger values of Hartmann number, porosity parameter and suction/injection parameter.
- Velocity inside the boundary layer increases with the increase of viscoelastic parameter while it decreases with the increase of Hartmann number and porosity parameter.
- Suction at the sheet decreases the velocity inside the boundary layer.
- With the increase of the effective Prandtl number, the heat transfer from the plate to fluid becomes slower and the thermal boundary layer thickness decreases. However, an increase in Dufour number, porosity parameter and suction/injection parameter leads to rise in the fluid temperature.

- An enhancement in Hartmann number increases the temperature and concentration.
- Concentration is higher for larger values of Soret number while its magnitude is suppressed with an increase in the Schmidt number.
- The effective local Nusselt number is an increasing function of effective Prandtl number, Soret number, suction/injection and viscoelastic parameters while it shows opposite behavior by increasing Hartmann number, Schmidt number, Dufour number and porosity parameter.
- The local Sherwood number is found to be increase for higher values of Schmidt number, Dufour number and viscoelastic parameter while it decreases with the increase of effective Prandtl number, Soret number, porosity parameter and Hartmann number.
- The amplitude of skin friction coefficient increases by increasing viscoelastic and porosity parameters.

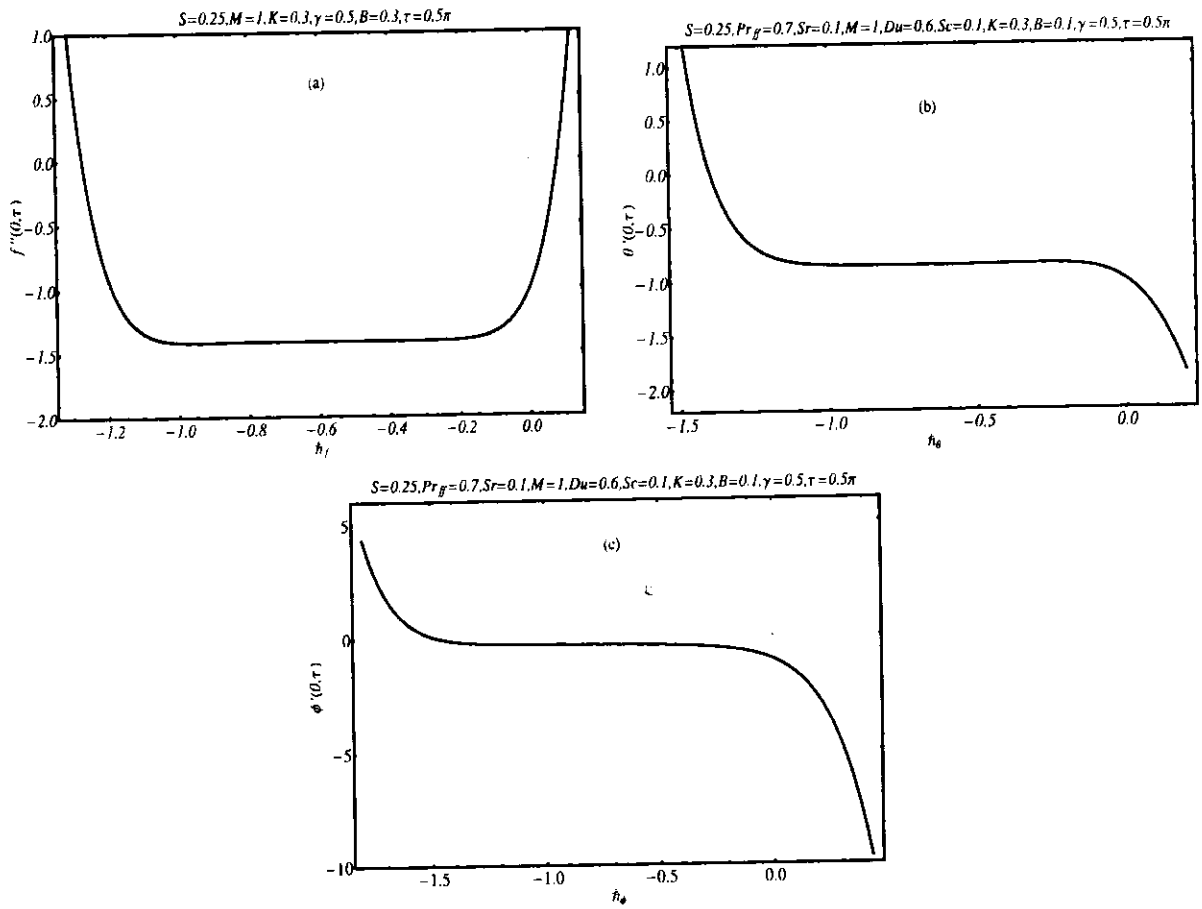

Fig. 4.2: The $\hbar$-curve at $10th$ order of approximation (a) for velocity (b) for temperature and (c) for concentration.

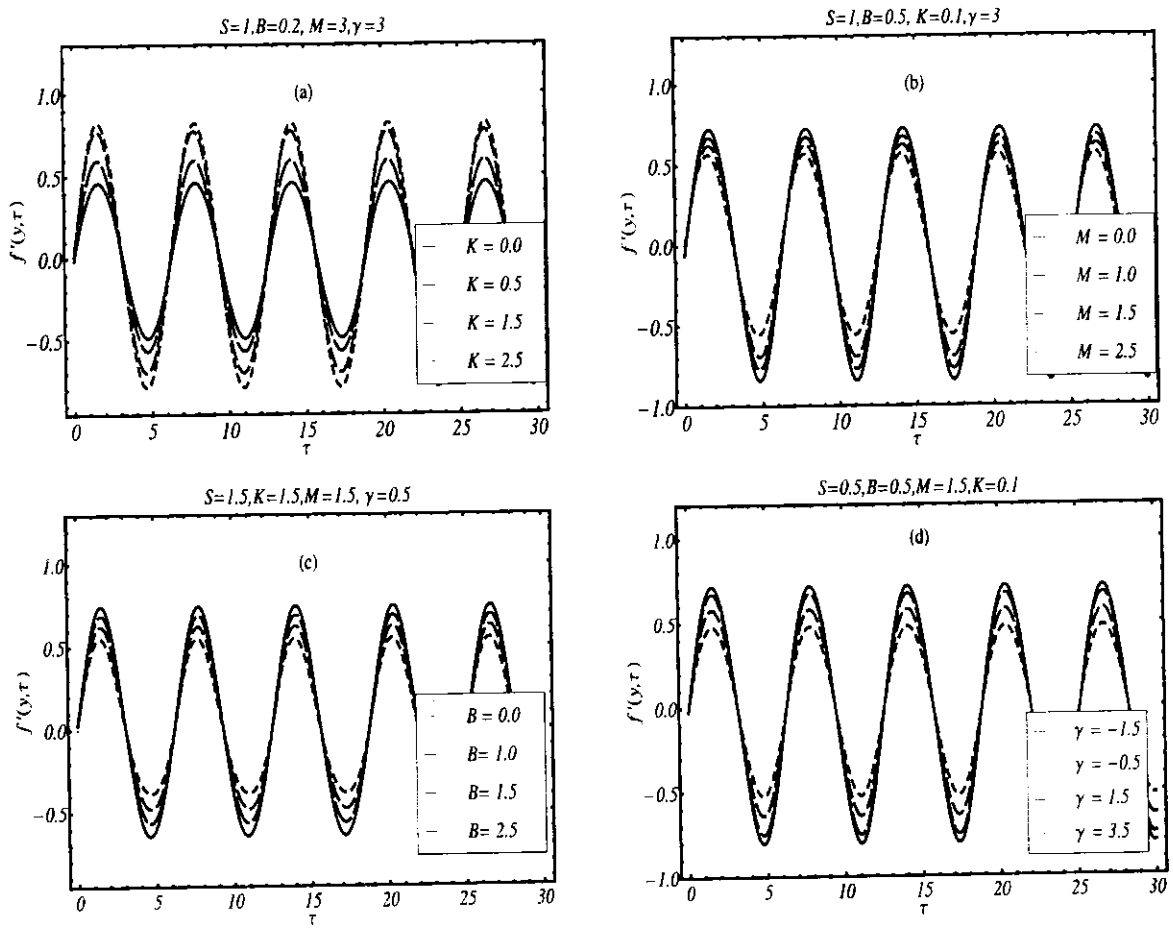

Fig. 4.3. Velocity as a function of time (a) influence of K (b) influence of M (c) influence of β and (d) influence of γ.

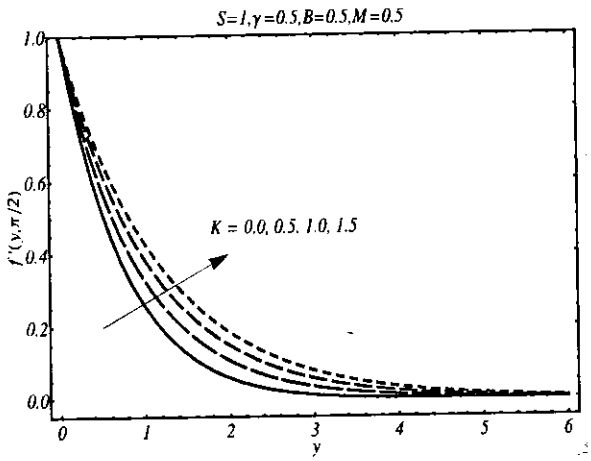

Fig. 4.4: Effects of K on velocity f'.

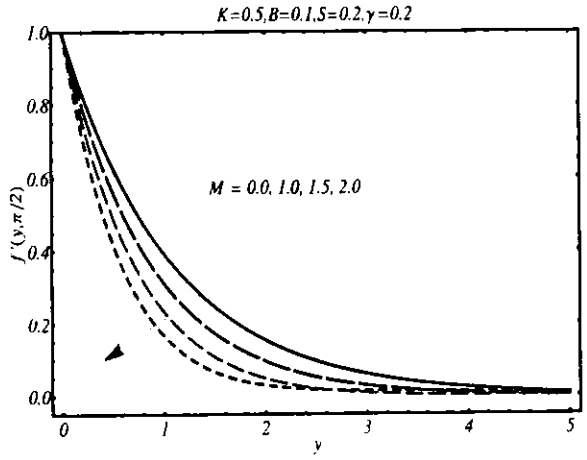

Fig. 4.5: Effects of M on velocity f'.

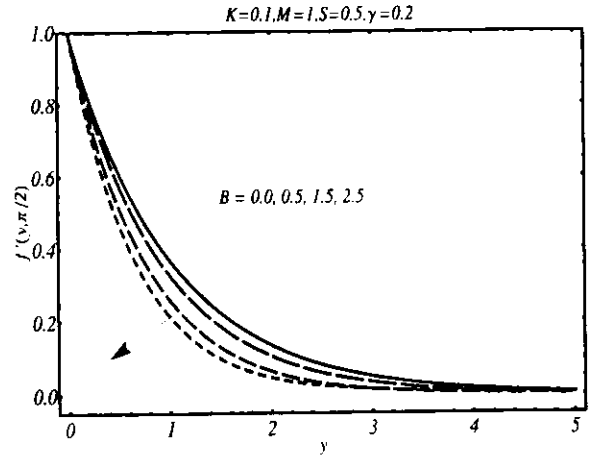

Fig. 4.6: Effects of B on velocity f'.

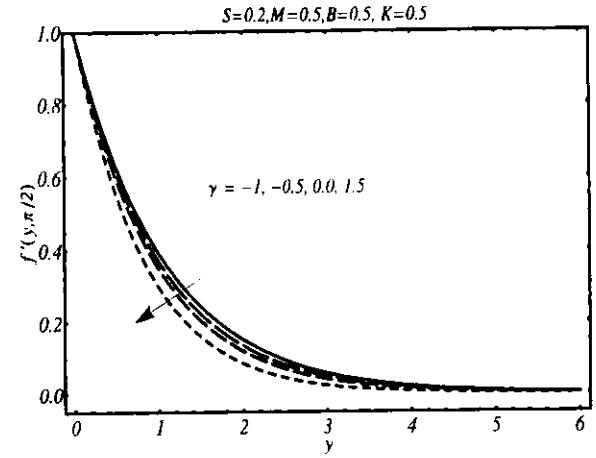

Fig. 4.7: Effects of γ on velocity f'.

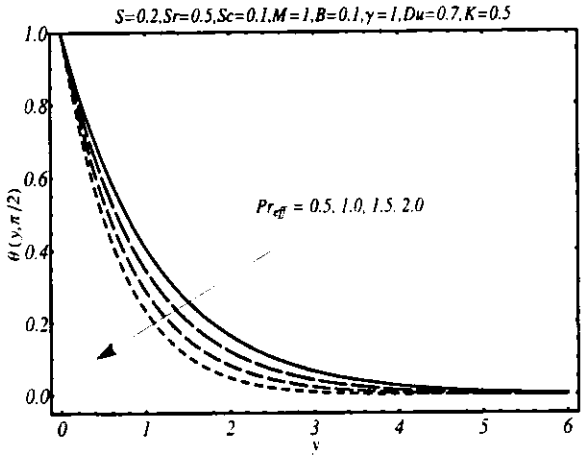

Fig. 4.8: Effects of Pr_{eff} on temperature θ.

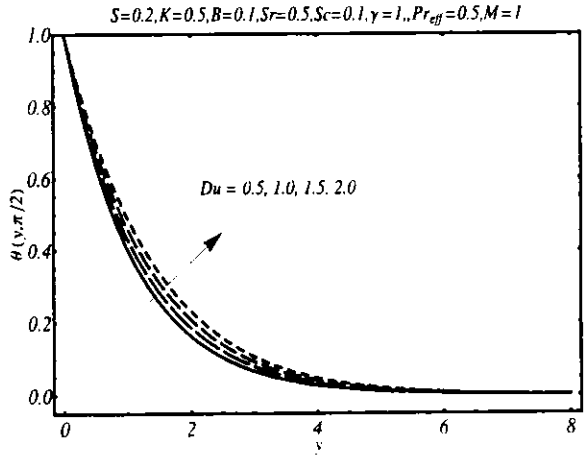

Fig. 4.9: Effects of Du on temperature θ.

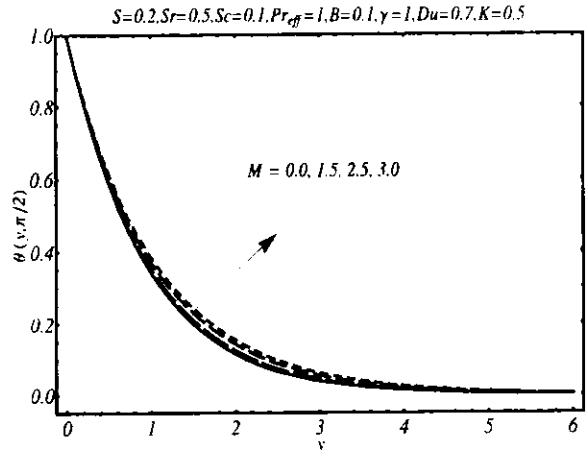

Fig. 4.10: Effects of M on temperature θ.

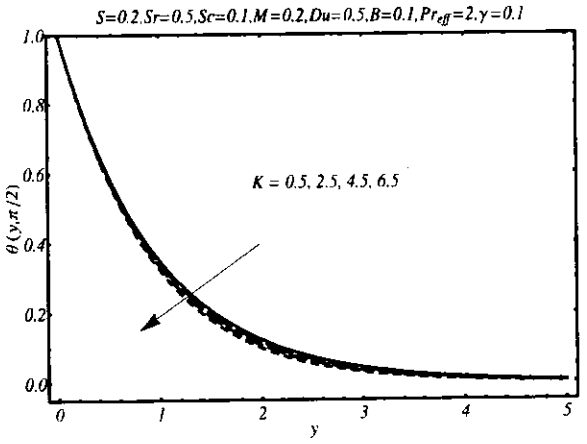

Fig. 4.11: Effects of K on temperature θ.

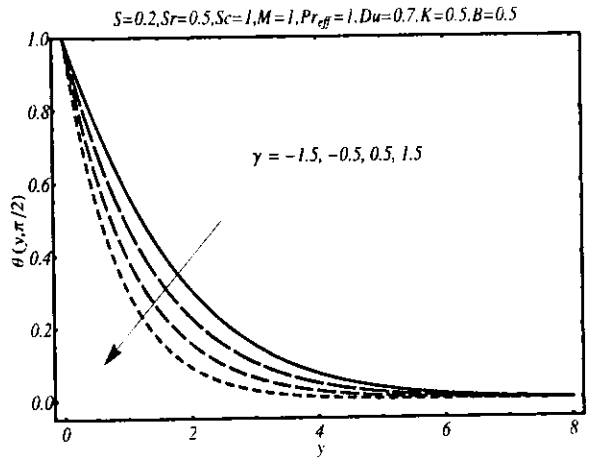

Fig. 4.12: Effects of γ on temperature θ.

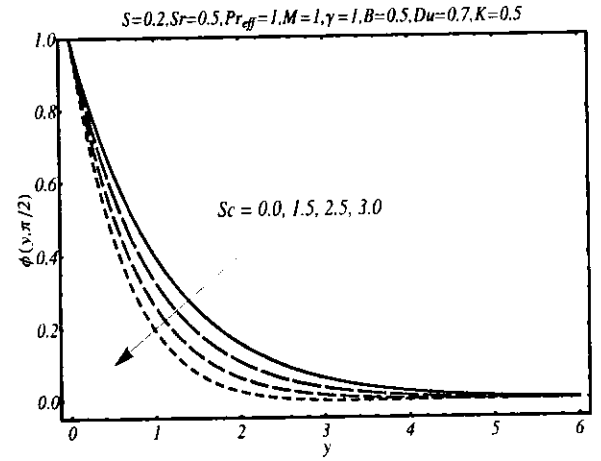

Fig. 4.13: Effects of Sc on concentration ϕ.

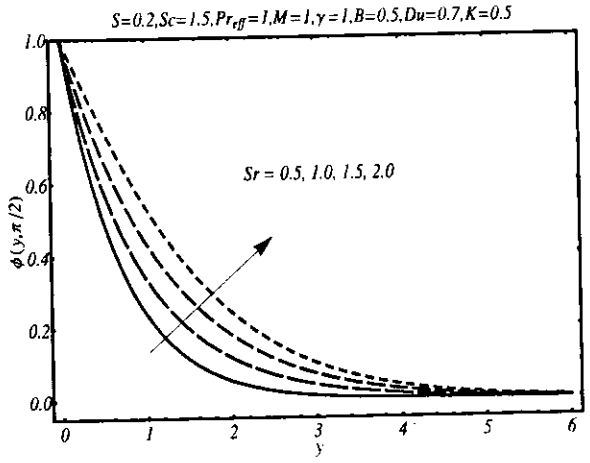

Fig. 4.14: Effects of Sr on concentration ϕ.

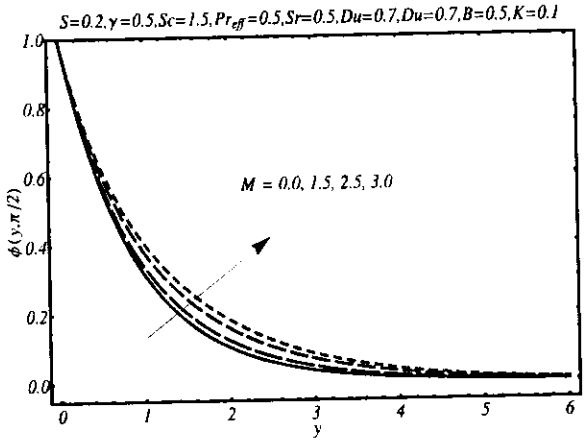

Fig. 4.15: Effects of M on concentration ϕ.

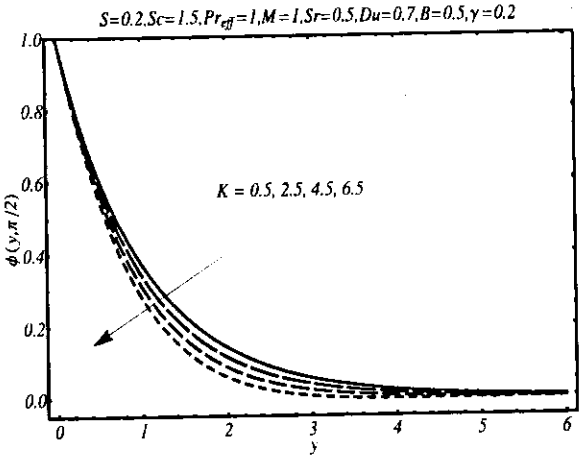

Fig. 4.16: Effects of K on concentration ϕ.

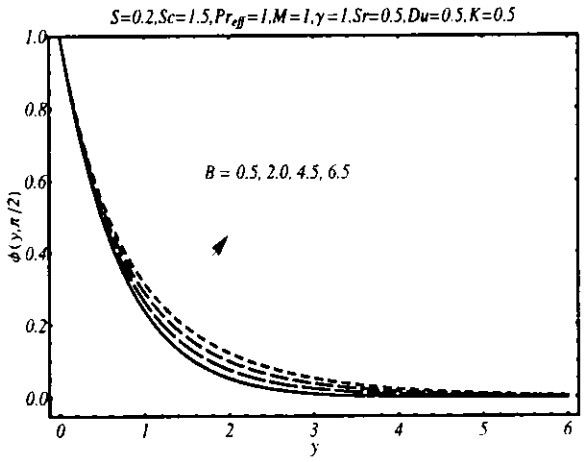

Fig. 4.17: Effects of B on concentration ϕ.

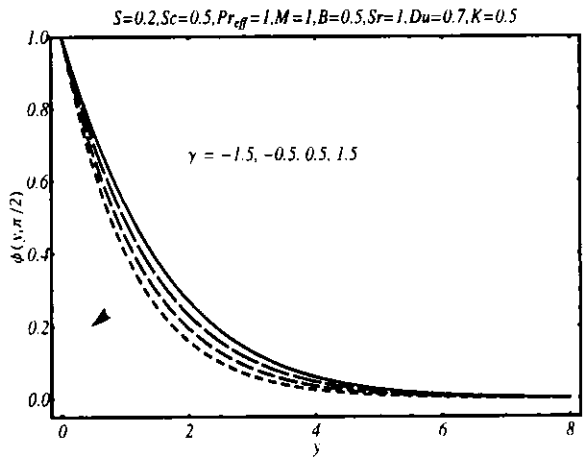

Fig. 4.18: Effects of γ on concentration ϕ.

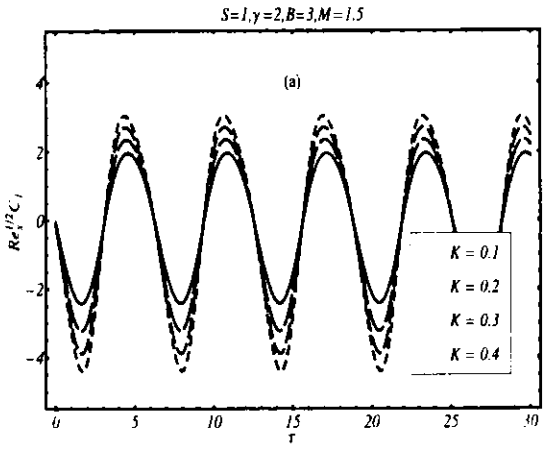

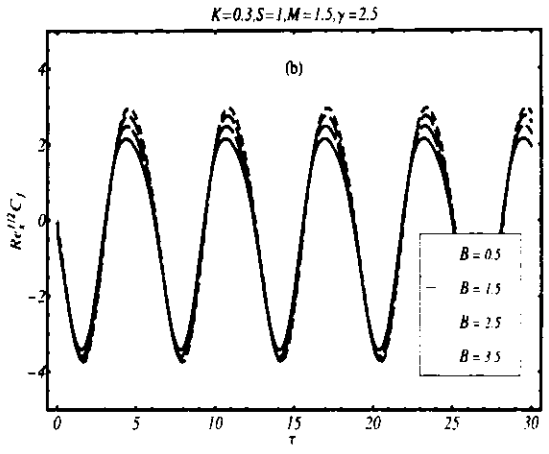

Fig. 4.19: Skin friction coefficient $\mathrm{Re}_x^{1/2} C_f$ as a function of time (a) influence of K (b) influence of B.

Table 4.1: Numerical values of effective local Nusselt number when $S = 0.5$ and $\tau = \pi/2$.

Pr_{eff}	M	Du	Sc	Sr	γ	B	K	$Re_x^{-1/2} Nu_x^*$
0.2	0.5	0.5	0.2	0.2	0.5	0.5	0.5	0.679021
0.4								0.764708
0.6								0.850813
0.2	0.5							0.679021
	1.5							0.660688
	2.5							0.654021
	0.5	0.5						0.679021
		1.0						0.645229
		1.5						0.611438
		0.2	0.5					0.675365
			1.5					0.669271
			2.5					0.663177
			0.5	0.5				0.676771
				1.5				0.681458
				2.5				0.686146
				0.5	0.5			0.676771
					1.5			0.747708
					2.0			0.784115
					0.5	0.5		0.676771
						1.5		0.672604
						3.5		0.664271
						0.5	0.5	0.676771
							2.5	0.689271
							3.5	0.695521

Table 4.2: Numerical values of the local Sherwood number $\mathrm{Re}_x^{-1/2} Sh$ when $S = 0.5$ and $\tau = \pi/2$.

Pr_{eff}	M	Du	Sc	Sr	γ	B	K	$\mathrm{Re}_x^{-1/2} Sh$
0.2	0.5	0.2	0.2	0.2	0.5	0.5	0.5	0.699296
0.5								0.697833
0.7								0.696858
0.1	0.5							0.699783
	1.5							0.69145
	2.5							0.674783
	0.5	0.1						0.699746
		0.7						0.699971
		1.5						0.700083
		0.2	0.2					0.699783
			0.4					0.806358
			0.6					0.913475
			0.5	0.1				0.706298
				0.3				0.693269
				0.6				0.673725
				0.5	0.5			0.699783
					1.0			0.737283
					1.5			0.775408
					0.5	0.3		0.700617
						0.6		0.699367
						0.9		0.698117
						0.5	0.5	0.699783
							1.5	0.706033
							2.5	0.712283

Chapter 5

Unsteady flow of third grade fluid over an oscillatory stretching sheet with thermal radiation and heat source/sink

The chapter aims to investigate the unsteady boundary layer flow and heat transfer analysis in a third grade fluid due an oscillatory stretching surface under the influence of thermal radiation and heat source/sink. The convective boundary condition at the sheet is imposed to determine the temperature distribution. Homotopy analysis method (HAM) is used to solve dimensionless nonlinear partial differential equations. The effects of involved parameters on both velocity and temperature distributions are illustrated in detail through various plots.

5.1 Mathematical model

We consider heat transfer in unsteady two-dimensional magnetohydrodynamic (MHD) laminar flow of an incompressible third grade fluid due to an oscillatory stretching sheet. The geometry of the problem is same as illustrated in **Fig. 3.1**. However, instead of specifying the wall temperature, the flux of temperature at the wall is specified in the term of convective fluid temperature T_f below the sheet. Moreover, in contrast to chapter 3, the effects of heat source/sink and thermal radiation are included in the present analysis. The boundary layer equation for third grade fluid under influence of transverse magnetic field is

$$\frac{\partial u}{\partial t}+u\frac{\partial u}{\partial \bar{x}}+v\frac{\partial u}{\partial \bar{y}}=-\frac{1}{\rho}\frac{\partial \hat{p}}{\partial \bar{x}}+\nu\frac{\partial^2 u}{\partial \bar{y}^2}+\frac{\alpha_1}{\rho}\left[\begin{array}{l}\dfrac{\partial^3 u}{\partial t\partial \bar{y}^2}+v\dfrac{\partial^3 u}{\partial \bar{y}^3}+\dfrac{\partial u}{\partial \bar{x}}\dfrac{\partial^2 u}{\partial \bar{y}^2}\\ +u\dfrac{\partial^3 u}{\partial \bar{x}\partial \bar{y}^2}+\dfrac{\partial u}{\partial \bar{y}}\dfrac{\partial^2 v}{\partial \bar{y}^2}\end{array}\right]+\frac{6\beta_3}{\rho}\left(\frac{\partial u}{\partial \bar{y}}\right)^2\frac{\partial^2 u}{\partial \bar{y}^2}-\frac{\sigma B_0^2}{\rho}u, \tag{5.1}$$

Similarly, the energy Eq. (3.2) defined in chapter 3 in presence of thermal radiation and heat source sink effects is

$$\rho c_p\left(\frac{\partial T}{\partial t}+u\frac{\partial T}{\partial \bar{x}}+v\frac{\partial T}{\partial \bar{y}}\right)=\left(k_1+\frac{16\sigma^* T_\infty^3}{3k^*}\right)\frac{\partial^2 T}{\partial \bar{y}^2}+Q(T-T_\infty). \tag{5.2}$$

The flow phenomenon is subject to same boundary conditions as given in chapter 3. The boundary conditions on energy equation are

$$-k_1\frac{\partial T}{\partial \bar{y}}=h_m\left(T_f-T\right) \quad \text{at} \quad \bar{y}=0,\ t>0, \tag{5.3}$$

$$T\to T_\infty \quad \text{at} \quad \bar{y}\to\infty. \tag{5.4}$$

The condition in (5.3) is known as the convective boundary condition in the literature. In Eq. (5.3), h_m denotes the heat transfer coefficient.

Utilizing the dimensionless variables given in Eq. (2.6) together with

$$\theta(y,\tau)=\frac{T-T_\infty}{T_f-T_\infty}, \tag{5.5}$$

Eqs. (5.1) and (5.2) take the following form

$$Sf_{y\tau}+f_y^2+M^2f_y-ff_{yy}=f_{yyy}+K\left[Sf_{yyy\tau}+2f_yf_{yyy}-ff_{yyyy}-f_{yy}^2\right]+6\beta^*\,\mathrm{Re}\,f_{yy}^2f_{yyy}, \tag{5.6}$$

$$\frac{1}{\mathrm{Pr}}(1+N_r)\theta_{yy}+f\theta_y-S\theta_\tau+\delta\theta=0. \tag{5.7}$$

In above equations $\beta^*=\beta_3b^2/\mu$ is the third grade fluid parameter, $\delta=Q/b\rho c_p$ is the heat source $(\delta>0)$ and heat sink for $(\delta<0)$ and $\gamma_1=(h/k)\sqrt{\nu/b}$ is the Biot number. Following Magyari and Pantokratoras [55], we write Eq. (5.7) as

$$\frac{1}{\mathrm{Pr}_{eff}}\theta_{yy}+f\theta_y-S\theta_\tau+\delta\theta=0. \tag{5.8}$$

The transformed boundary conditions are

$$f_y(0,\tau)=\sin\tau,\quad f(0,\tau)=0,\quad \theta_y(0,\tau)=-\gamma_1\left[1-\theta(0,\tau)\right], \tag{5.9}$$

$$f_y(\infty,\tau)=0,\quad f_{yy}(\infty,\tau)=0,\qquad \theta(\infty,\tau)=0. \tag{5.10}$$

The skin friction coefficient in present case is defined as

$$\mathrm{Re}_x^{1/2}C_f=\left[f_{yy}+K\left(Sf_{yy\tau}+3f_yf_{yy}-ff_{yyy}\right)+2\beta^*\,\mathrm{Re}\,f_{yyy}^3\right]_{y=0}. \tag{5.11}$$

The expression of effective local Nusselt number is same as defined in (4.18).

5.2 Homotopy analysis method

In this section homotopy analysis method (HAM) is employed to solve nonlinear partial differential equations (5.6) and (5.7) together with boundary conditions (5.9) and (5.10). In view

of boundary conditions, the appropriate initial guesses for $f(y,\tau)$ and $\theta(y,\tau)$ are

$$f_0(y,\tau)=\sin\tau\left(1-\exp(-y)\right),\ \theta_0(y,\tau)=\frac{\gamma_1\exp(-y)}{1+\gamma_1}. \tag{5.12}$$

Further we choose the following auxiliary linear operators for the velocity and temperature profiles

$$\pounds_f(f)=\frac{\partial^3 f}{\partial y^3}-\frac{\partial f}{\partial y},\quad \pounds_\theta(f)=\frac{\partial^2 f}{\partial y^2}-f, \tag{5.13}$$

satisfying

$$\pounds_f\left[C_1+C_2\exp(y)+C_3\exp(-y)\right]=0, \tag{5.14}$$

$$\pounds_\theta\left[C_4\exp(y)+C_5\exp(-y)\right]=0, \tag{5.15}$$

Zeroth-order deformation problems are

$$(1-p)\pounds_f\left[\hat{f}(y,\tau;p)-f_0(y,\tau)\right]=p\hbar_f N_f\left[\hat{f}(y,\tau;p)\right], \tag{5.16}$$

$$(1-p)\pounds_\theta\left[\hat{\theta}(y,\tau;p)-\theta_0(y,\tau)\right]=p\hbar_\theta N_\theta\left[\hat{f}(y,\tau;p),\hat{\theta}(y,\tau;p)\right], \tag{5.17}$$

$$\hat{f}(y,\tau;p)\Big|_{y=0}=0,\ \left.\frac{\partial\hat{f}(y,\tau;p)}{\partial y}\right|_{y=0}=\sin\tau,\ \left.\frac{\partial\hat{f}(y,\tau;p)}{\partial y}\right|_{y=\infty}=0,\ \left.\frac{\partial^2\hat{f}(y,\tau;p)}{\partial y^2}\right|_{y=\infty}=0. \tag{5.18}$$

$$\frac{\partial\hat{\theta}(0,\tau;p)}{\partial y}=-\gamma_1\left(1-\hat{\theta}(0,\tau;p)\right),\quad \hat{\theta}(\infty,\tau;p)=0, \tag{5.19}$$

The associated nonlinear operators are

$$N_f\left[\hat{f}(y,\tau;p)\right]=\frac{\partial^3\hat{f}(y,\tau;p)}{\partial y^3}-S\frac{\partial^2\hat{f}(y,\tau;p)}{\partial y\partial\tau}-M^2\frac{\partial\hat{f}(y,\tau;p)}{\partial y}-\left(\frac{\partial\hat{f}(y,\tau;p)}{\partial y}\right)^2$$

$$+\hat{f}(y,\tau;p)\frac{\partial^2\hat{f}(y,\tau;p)}{\partial y^2}+K\left[S\frac{\partial^4\hat{f}(y,\tau;p)}{\partial y^3\partial\tau}+2\frac{\partial\hat{f}(y,\tau;p)}{\partial y}\frac{\partial^3\hat{f}(y,\tau;p)}{\partial y^3}-\hat{f}(y,\tau;p)\frac{\partial^4\hat{f}(y,\tau;p)}{\partial y^4}\right. \tag{5.20}$$

$$\left.-\left(\frac{\partial^2\hat{f}(y,\tau;p)}{\partial y}\right)^2\right]+6\beta^*\,\mathrm{Re}\left(\frac{\partial\hat{f}(y,\tau;p)}{\partial y}\right)^2\frac{\partial^3\hat{f}(y,\tau;p)}{\partial y^3},$$

$$N_\theta\left[\hat{\theta}(y,\tau;p),\hat{f}(y,\tau;p)\right]=\frac{1}{\mathrm{Pr}_{eff}}\frac{\partial^2\hat{\theta}(y,\tau;p)}{\partial y^2}+\hat{f}(y,\tau;p)\frac{\partial\hat{\theta}(y,\tau;p)}{\partial y}-S\frac{\partial\hat{\theta}(y,\tau;p)}{\partial\tau}+\delta\theta. \tag{5.21}$$

Setting $p = 0$ and $p = 1$ in zeroth-order problems, we get

$$\hat{f}(y,\tau;0) = f_0(y,\tau), \hat{f}(y,\tau;1) = f(y,\tau), \tag{5.22}$$

$$\hat{\theta}(y,\tau;0) = \theta_0(y,\tau), \hat{\theta}(y,\tau;1) = \theta(y,\tau). \tag{5.23}$$

Expanding $\hat{f}(y,\tau;p)$ and $\hat{\theta}(y,\tau;p)$ using Taylor's series, one gets

$$\hat{f}(y,\tau;p) = f_0(y,\tau) + \sum_{m=1}^{\infty} f_m(y,\tau)\, p^m, \quad f_m(y,\tau) = \frac{1}{m!}\frac{\partial^m \hat{f}(y,\tau;p)}{\partial p^m}, \tag{5.24}$$

$$\hat{\theta}(y,\tau;p) = \theta_0(y,\tau) + \sum_{m=1}^{\infty} \theta_m(y,\tau)\, p^m, \quad \theta_m(y,\tau) = \frac{1}{m!}\frac{\partial^m \hat{\theta}(y,\tau;p)}{\partial p^m}. \tag{5.25}$$

Setting $p = 0$ in Eqs. (5.27) and (5.28), we find

$$f(y,\tau;p) = f_0(y,\tau) + \sum_{m=1}^{\infty} f_m(y,\tau), \tag{5.26}$$

$$\theta(y,\tau) = \theta_0(y,\tau) + \sum_{m=1}^{\infty} \theta_m(y,\tau), \tag{5.27}$$

as solutions to the original equations (5.6) and (5.7). In Eqs. (5.26) and (5.27), f_m and θ_m can be computed through *mth*-order deformations problems given by

$$\pounds_f\left[f_m(y,\tau) - \chi_m f_{m-1}(y,\tau)\right] = \hbar_f R_m^f(y,\tau), \tag{5.28}$$

$$\pounds_\theta\left[\theta_m(y,\tau) - \chi_m \theta_{m-1}(y,\tau)\right] = \hbar_\theta R_m^\theta(y,\tau), \tag{5.29}$$

$$f_m(0,\tau) = 0, \ \frac{\partial f_m(0,\tau)}{\partial y} = 0, \ \frac{\partial f_m(\infty,\tau)}{\partial y} = 0, \frac{\partial^2 f_m(\infty,\tau)}{\partial y^2} = 0, \tag{5.30}$$

$$\frac{\partial \theta_m(0,\tau)}{\partial y} - \gamma_1 \theta_m(0,\tau) = \theta_m(\infty,\tau) = 0, \tag{5.31}$$

$$R_m^f(y,\tau) = \frac{\partial^3 f_{m-1}}{\partial y^3} - M^2\frac{\partial f_{m-1}}{\partial y} - \alpha_1 S\frac{\partial^4 f_{m-1}}{\partial y^3 \partial \tau} + K\sum_{k=0}^{m-1}\left(2\frac{\partial f_{m-1-k}}{\partial y}\frac{\partial^3 f_k}{\partial y^3} - f_{m-1-k}\frac{\partial^4 f_k}{\partial y^4} - \frac{\partial^2 f_{m-1-k}}{\partial y^2}\frac{\partial^2 f_k}{\partial y^2}\right) + \tag{5.32}$$

$$+6\beta^* \,\mathrm{Re}\sum_{k=0}^{m-1}\frac{\partial^2 f_{m-1-k}}{\partial y^2}\sum_{l=0}^{k}\frac{\partial^2 f_{k-l}}{\partial y^2}\frac{\partial^3 f_l}{\partial y^3},$$

$$R_m^\theta(y,\tau) = \frac{1}{\mathrm{Pr}_{eff}}\frac{\partial^2 \theta_{m-1}}{\partial y^2} - S\frac{\partial \theta_{m-1}}{\partial \tau} + \delta\theta_{m-1} + \sum_{k=0}^{m-1}\left(f_{m-1-k}\frac{\partial \theta_k}{\partial y}\right). \tag{5.33}$$

$$\chi_m = \begin{cases} 0, & m \le 1, \\ 1, & m > 1. \end{cases} \tag{5.34}$$

The general solution is of the form

$$f_m(y,\tau) = f_m^*(y,\tau) + C_1 + C_2 \exp(y) + C_3 \exp(-y), \tag{5.35}$$

$$\theta_m(y,\tau) = \theta_m^*(y,\tau) + C_4 \exp(y) + C_5 \exp(-y). \tag{5.36}$$

where $f_m^*(y,\tau)$ and $\theta_m^*(y,\tau)$ represents the particular solutions. In view of the boundary conditions (5.30) and (5.31), the constants $C_i (i=1,2...,5)$ are computed as follows

$$C_2 = C_4 = 0,\ C_3 = \frac{\partial f_m^*(0,\tau)}{\partial y},\quad C_1 = -C_3 - f_m^*(0,\tau),\quad C_5 = \frac{1}{\gamma_1 + 1}\left[\frac{\partial \theta_m^*(0,\tau)}{\partial y} - \gamma_1 \theta_m^*(0,\tau)\right]. \tag{5.37}$$

5.3 Convergence of the HAM solution

The proper choice of auxiliary parameters $\hbar_f$ and $\hbar_\theta$ plays prime role in convergent HAM solution. **Figs. 5.1** and **5.2** are plotted to see the appropriate regions indicating plausible values of $\hbar_f$ and $\hbar_\theta$. These figures clearly show that the for convergent solutions $\hbar_f$ and $\hbar_\theta$ must be in the range $-1 \le \hbar_f < 0$ and $-1.5 \le \hbar_\theta < -0.2$.

5.4 Results and discussion

Figs. (5.1)-(5.15) are displayed to reflect the behavior of velocity and temperature in response to the pertinent parameters. **Figs. 5.3 (a-c)** shows the effects of M, S and β^* on the time series of velocity profile f' when $y = 0.25$ from the surface of the sheet. **Fig. 5.3 (a)** illustrate that with an increase in Hartmann number M, the amplitude of the flow velocity decreases. This is due to the fact that magnetic field introduces a retarding force known as Lorentz force which is of resistive nature. The variation of ratio of the oscillation frequency to its stretching rate S on the time-evolution of the velocity profile f' is illustrated in **Fig. 5.3 (b)**. It is clear from this figure that the amplitude of flow motion decreases by increasing S. It is also observed that a phase shift occur with increasing S. **Fig. 5.3 (c)** elucidates that the amplitude of the velocity is an increasing function of third grade fluid parameter β^*. Physically, for non-zero values of β^*, the viscosity of the fluid increases with increasing the shear rate and as a result of that an acceleration in the

flow is observed.

Figs. **5.4 (a-d)** describe the variation of fluid parameter K on the transverse profiles of velocity field f' at time instants $\tau = 8.5\pi$, $\tau = 9\pi$, $\tau = 9.5\pi$ and $\tau = 10\pi$. Fig. **5.4(a)** shows the effects of parameter K at $\tau = 8.5\pi$. The velocity f' increases from unity to zero by increasing K. It is also observed that an increase in K results in an increase of the momentum boundary layer thickness. This increase in momentum boundary layer thickness is attributed to the increase in the effective viscosity and normal stress effect exhibited by third grade fluid for nonzero values of K. The effects of the velocity profile f' at time instant $\tau = 9\pi$ are shown in **Fig. 5.4(b)**. This figure reflects opposite effects, i.e., the velocity and momentum boundary layer decreases by increasing K at this time instant. At $\tau = 9.5\pi$, (**Fig. 5.4(c)**) the magnitude of the velocity f' is an increasing function of fluid parameter K. **Fig. 5.4(d)** indicates that f' decreases with K at time instant $\tau = 10\pi$. At this time instant, the velocity at the surface and for away from the surface is zero.

The variation of Hartmann number M at four time points is depicted in **Fig. 5.5(a-d)**. It is clear from these figures that the magnitude of the velocity decreases at all time instants except at $\tau = 9.5\pi$ where an increasing trend in magnitude is observed. **Fig. 5.6(a-d)** is plotted to see the effects of third grade fluid parameter β^* at different time instant. **Fig. 5.6(a)** shows that the magnitude of the velocity is an increasing function of β^*. Similar observations are made from **Fig. 5.6(b)** which is plotted at time instant $\tau = 9\pi$. **Fig. 5.6(c)** is sketched at time instant $\tau = 9.5\pi$ where again it is observed that the magnitude of the velocity increases with β^*. The influence of β^* on f' at time instant $\tau = 10\pi$ is similar to the influence of β^* on f' at the time instant $\tau = 9\pi$.

The time -evolution of skin friction coefficient for different values of M, S, β^* and Re are illustrated in **Figs. 5.7(a-d)**. **Fig. 5.7(a)** shows that skin friction coefficient oscillates with time due to oscillatory motion of the sheet. Moreover, the amplitude of oscillations increases with an increase in dimensionless Hartmann number M. The increase in the skin friction coefficient with increasing Hartmann number is expected because of flow suppression caused by Lorentz force. The effect of ratio of oscillation frequency of sheet to stretching rate S on the skin friction coefficient is similar to effects of M and shown in **Fig. 5.7(b)**. Further, it is observed that there

exists a phase shift for larger values of S. **Fig. 5.7(c)** depicts that for higher values of β^* amplitude of the skin friction coefficient decreases. This is perhaps due to result of flow acceleration observed for the larger values of β^*. The influence of Reynolds number Re the on skin friction coefficient is displayed in **Fig. 5.8(d)**, where it is observed that the skin friction coefficient decreases for large values of the Reynolds number Re.

Figs. (5.8-5.15) portray the effects of $\Pr$, $K, \beta^*, M, \gamma_1, \delta$ on the temperature profile θ at $\tau = 0.5\pi$. **Fig. 5.8** shows the effects of effective Prandtl number $\Pr_{eff}$ on temperature profile θ. It is evident from this figure that the temperature as well as thermal boundary layer thickness decreases by increasing effective Prandtl number $\Pr_{eff}$. This decrease in the temperature inside the boundary layer by increasing $\Pr_{eff}$ is a consequence of the fact that $\Pr_{eff}$ is directly proportional to Prandtl number $\Pr_{eff}$ and inversely proportional to radiation parameter. The effects of fluid parameters K and β^* on the temperature are shown in **Figs. (5.9)** and **(5.10)**, respectively. The temperature is found to be decrease with an increase in these fluid parameters. The decrease of the temperature also leads to decrease in the thermal boundary layer thickness. The influence of Hartmann number on temperature is shown in **Fig. 5.11**. This figure reveals that at an increase in Hartmann number M results in an increase in temperature. Moreover, it is found that the thermal boundary layer increases also increases. It can be justified physically because the Lorentz force opposes the fluid motion and increases the internal fluid friction, as a result of this increase the thermal boundary layer becomes thicker for strong larger values of magnetic field. The effects of heat source parameter on the temperature distribution are presented in **Fig. 5.12,** which indicates that temperature increases by increasing heat source strength. It is expected because more heat is added to the system results in the rise of the fluid temperature and the thermal boundary layer thickness. **Fig. 5.13** shows opposite effects i.e., the temperature and the thermal boundary layer thickness decreases with increase of the strength of the heat sink. This result is of key importance for the flows where heat transfer is of prime importance. The variation of Biot number γ_1 on the temperature profile θ is shown in **Fig. 5.14**. This figure elucidates that the temperature as well as the thermal boundary layer thickness increases by increasing Biot number γ_1. It is also observed from this figure that there is no heat transfer when

$\gamma_1 = 0$. Since thermal Biot number depends upon heat transfer coefficient h, therefore its higher values represent the case of enhanced heat transfer from stretching sheet to the fluid stream. This enhancement in heat transfer is responsible for increase in the temperature of fluid. **Fig. 5.15(a-c)** shows the effects of effective Prandtl number Pr_{eff}, Harmann number M and Reynolds number Re on the time-series of effective local Nusselt number $\mathrm{Re}_x^{-1/2} Nu_x^*$. It is observed that the effective local Nusselt number increases monotonically with time for large values of Pr_{eff}, Re while the effects of Hartmann number M are opposite. **Table 5.1** shows the numerical values of the effective local Nusselt number for different values of Pr_{eff}, β^*, γ_1 and Hartmann number M. From the table it is clear the larger values of the effective Prandtl number Pr_{eff} lead to an increase in the effective local Nusselt number. The effective local Nusselt number also increases by increasing fluid parameters K and β^*. However, this increase is marginal. **Table 5.1** also shows that heat transfer rate is zero when $\gamma_1 = 0$. Moreover, the effective local Nusselt number decreases with an increase in Hartmann number M and heat source parameter δ.

5.5 Concluding remarks

This study deals with the unsteady boundary layer flow of a third grade fluid over an oscillatory stretching surface in the presence of thermal radiation effects and heat source/sink. The dimensionless nonlinear partial differential equations are solved through homotopy analysis method (HAM). The main observations of the study are:

- The amplitude of the velocity f' increases by increasing fluid parameter β^* while it decreases by increasing Hartmann number M.
- Amplitude of the wall shear stress increases periodically with Hartmann number M while it shows opposite trend with third grade parameter β^* and Reynold number Re.
- The temperature and the thermal boundary layer thickness increases by increasing Hartmann number M, Biot number γ and heat source parameter δ while decreases by increasing all other parameters. Moreover, there is no heat transfer if $\gamma = 0$.
- The numerical values of the effective local Nusselt number increases by increasing effective

Prandtl number $\Pr_{eff}$, third grade parameter β^* and Biot number γ_1. However, the effective local Nusselt number decreases for large values of heat source parameter δ and Hartmann number M.

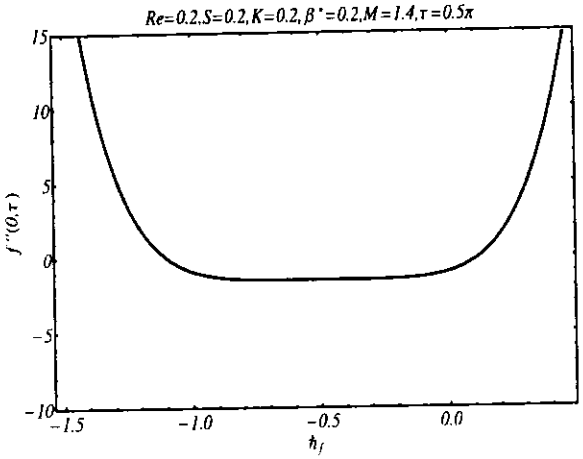

Fig. 5.1: $\hbar$-curve for $f''(0,\tau)$ at $6th$ order of approximation.

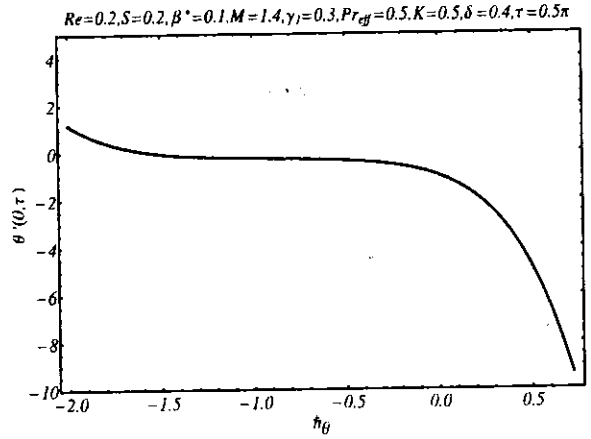

Fig. 5.2: $\hbar$-curve for $\theta'(0,\tau)$ at $6th$ order of approximation.

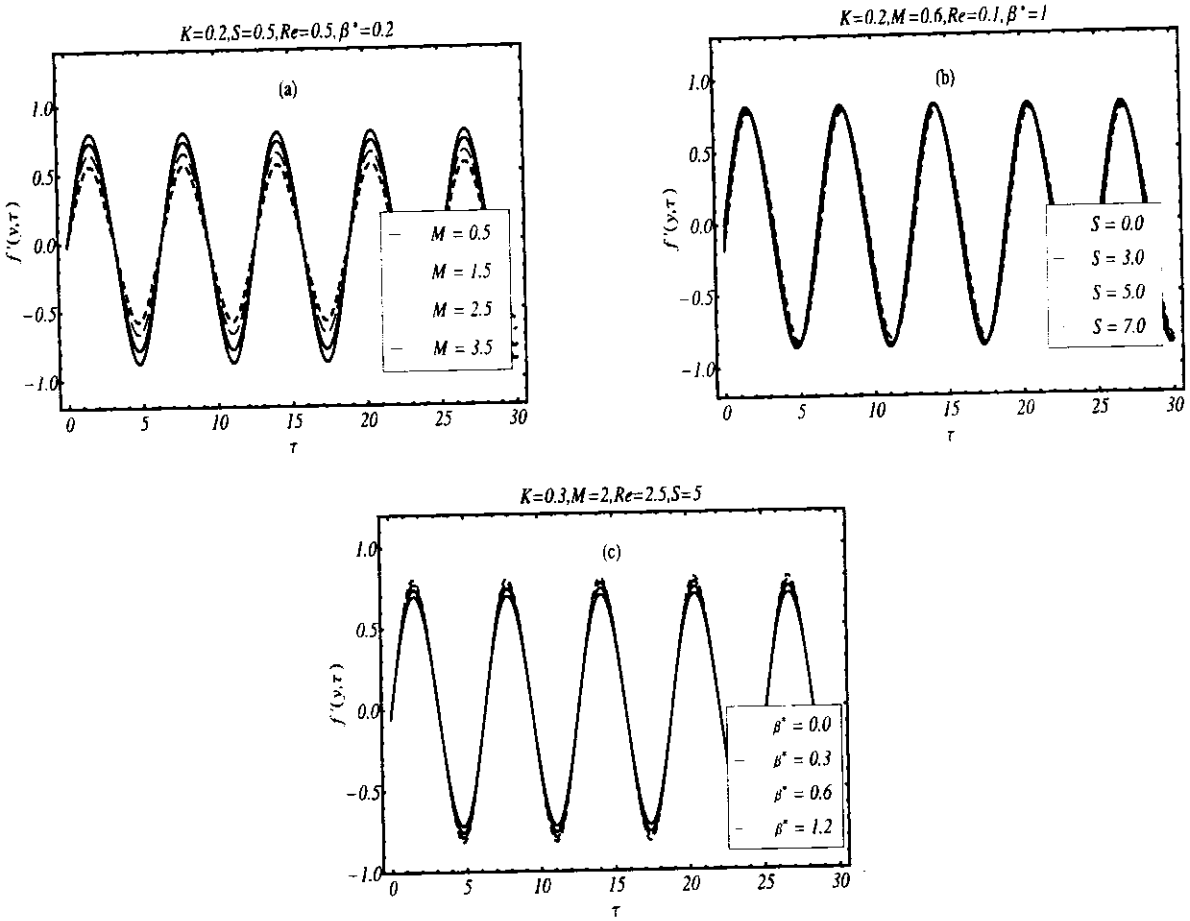

Fig. 5.3: Velocity as function of time (a) effects of M (b) effects of S (c) effects of β^*.

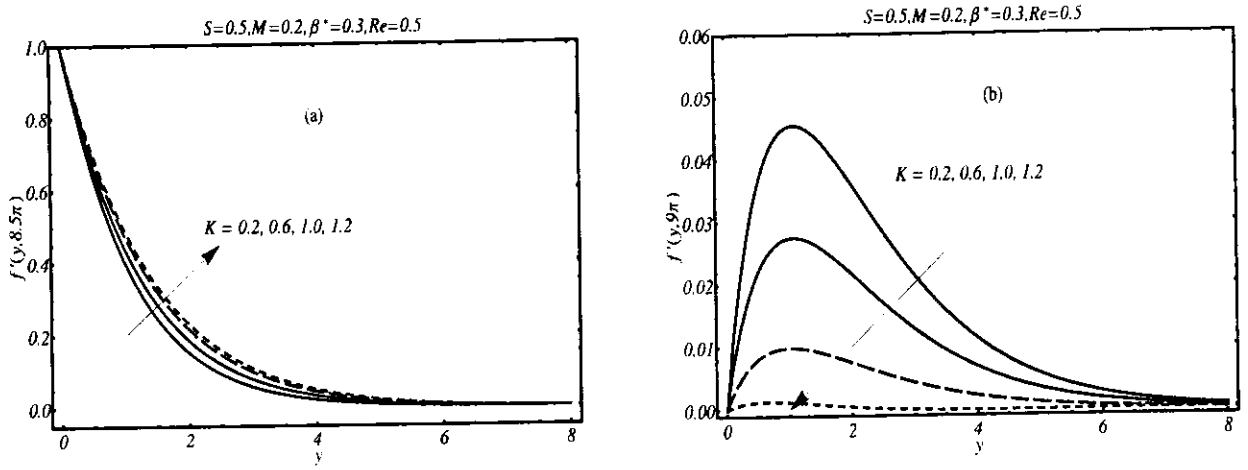

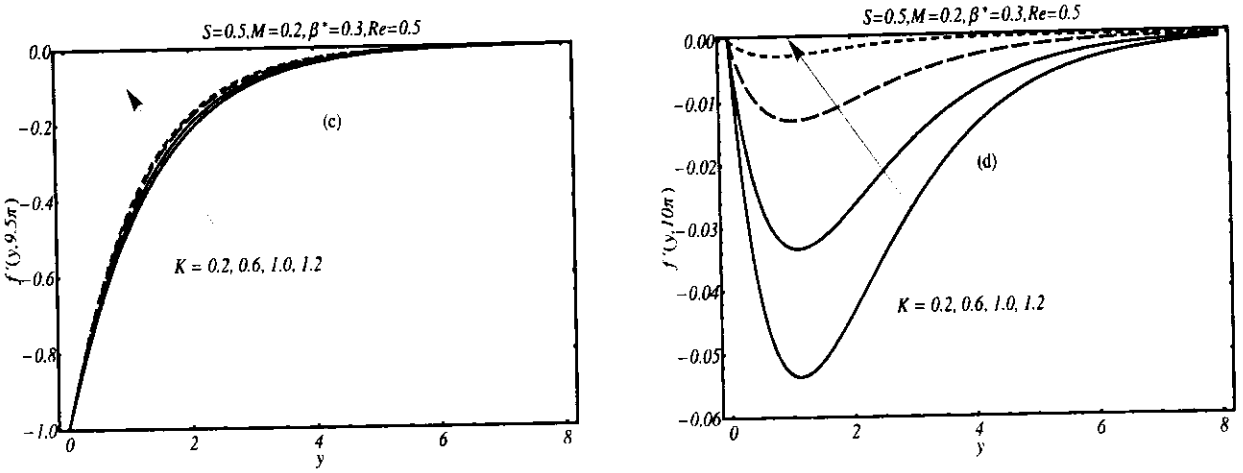

Fig. 5.4: Effects of K on velocity profile.

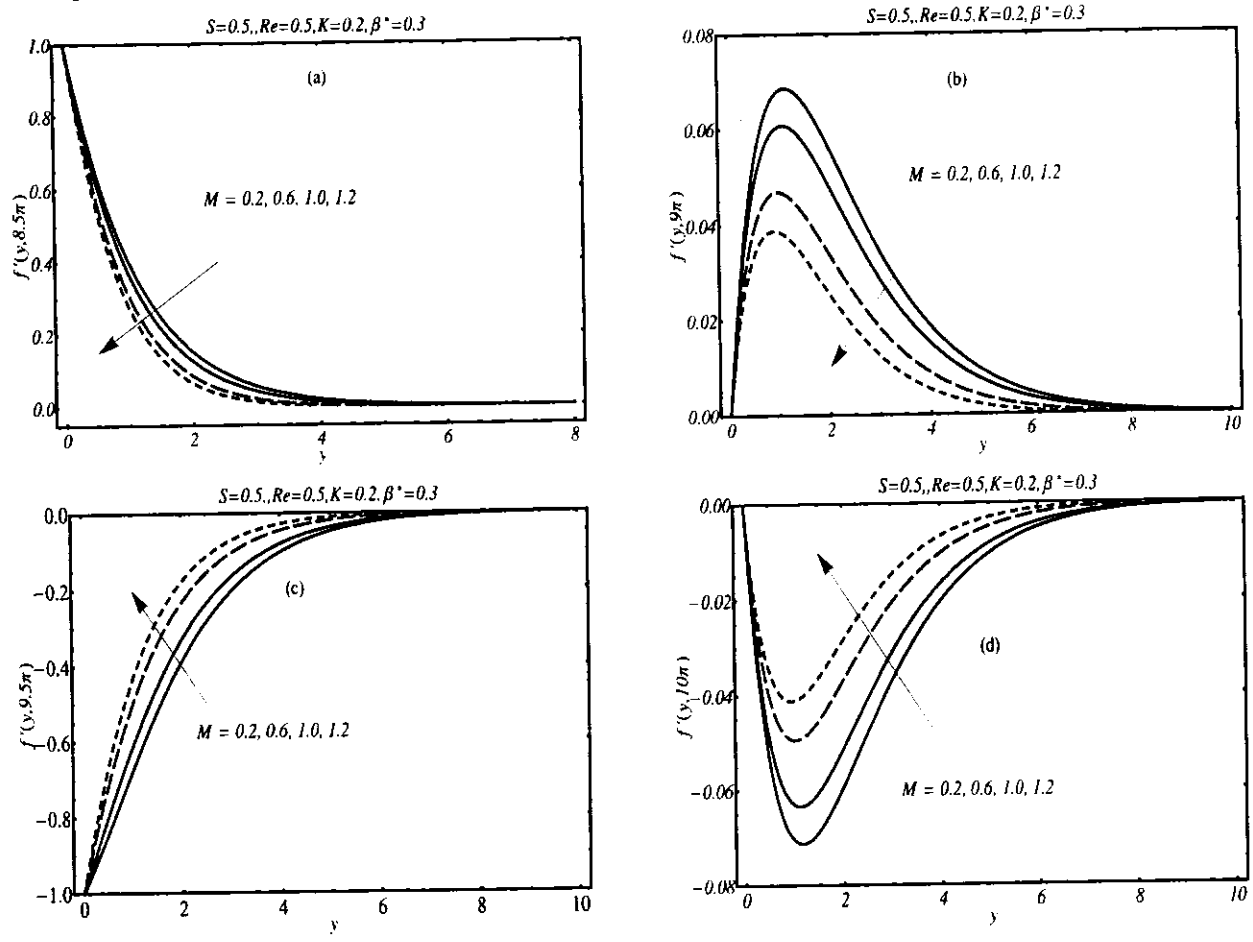

Fig. 5.5: Effects of M on velocity profile.

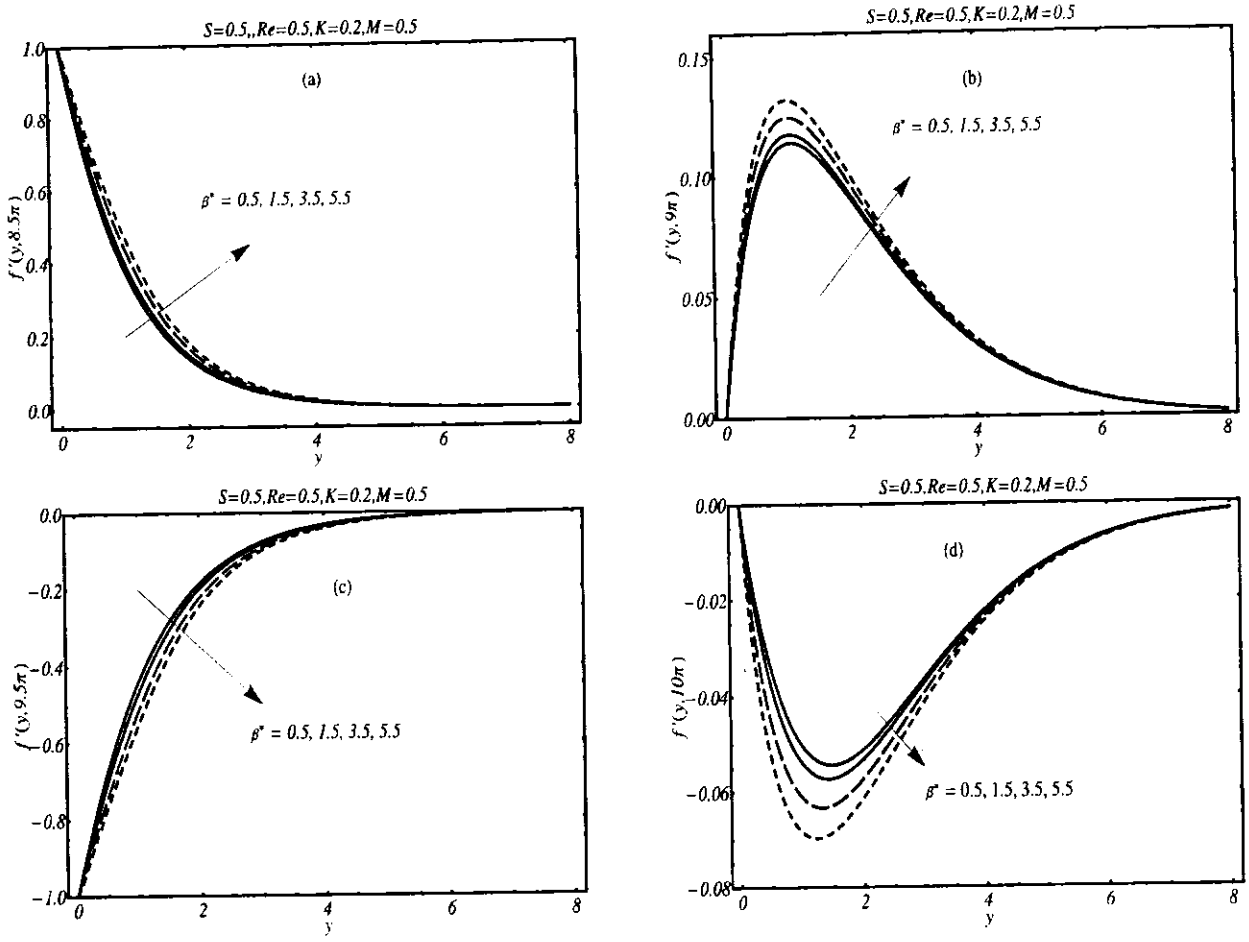

Fig. 5.6: Effects of β^* on velocity profile.

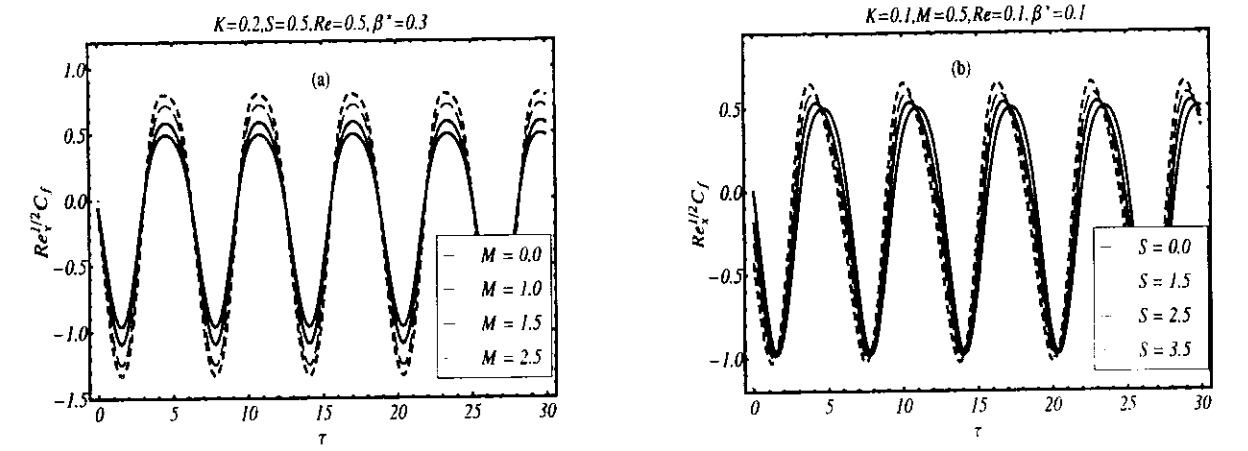

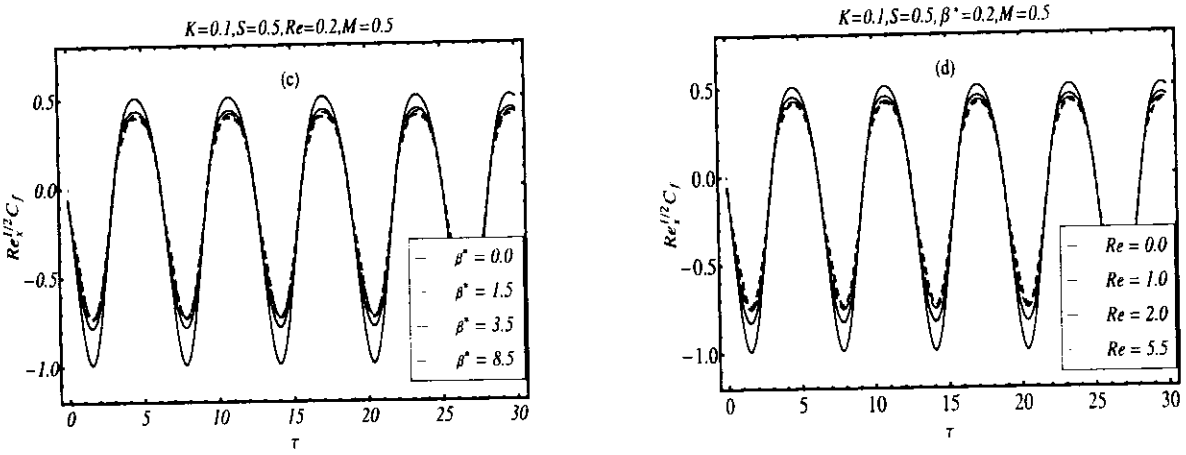

Fig. 5.7: Distribution of skin friction coefficient with time for (a) Hartman number M (b) ratio parameter S (c) third grade parameter β^* (d) Renolds number Re.

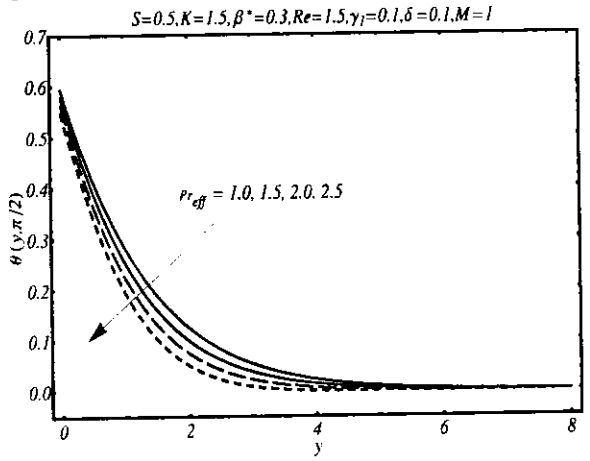

Fig. 5.8: Effects of Pr_{eff} on temperature.

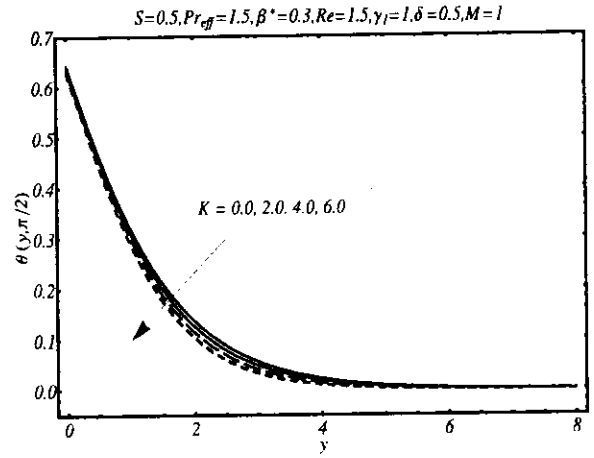

Fig. 5.9: Effects of K on temperature.

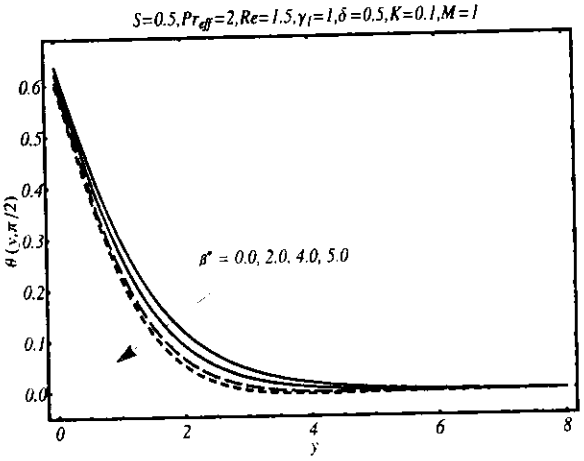

Fig. 5.10: Effects of β^* on temperature.

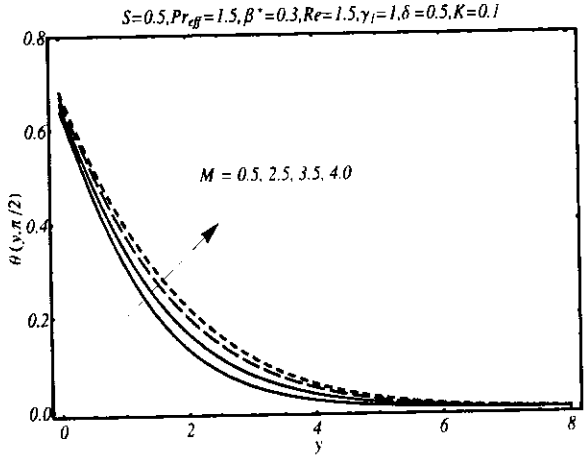

Fig. 5.11: Effects of M on temperature.

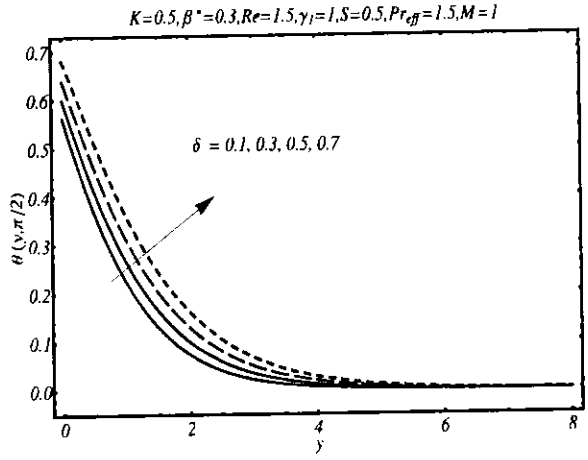

Fig. 5.12: Effects of heat source δ on temperature.

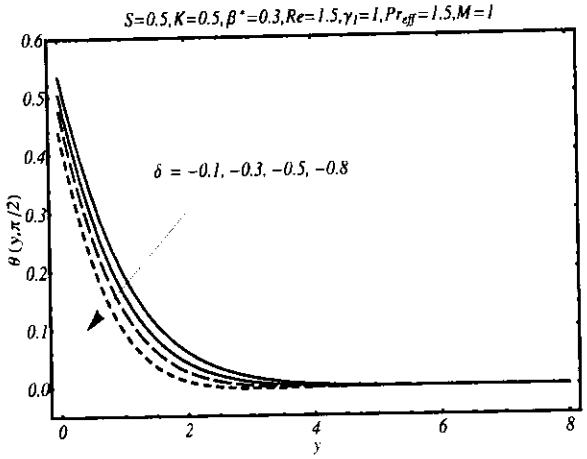

Fig. 5.13: Effects of heat sink δ on temperature.

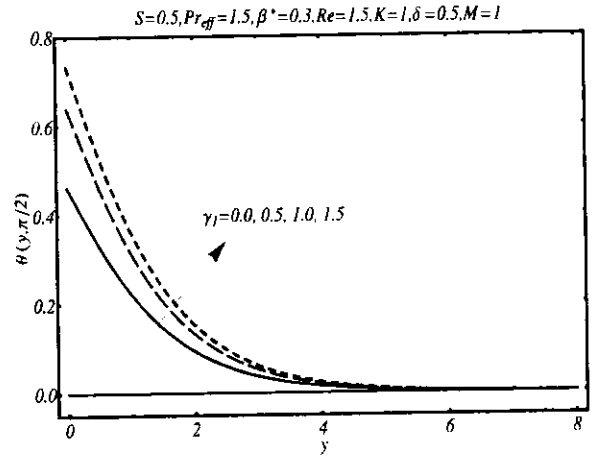

Fig. 5.14: Effects of γ_1 on temperature.

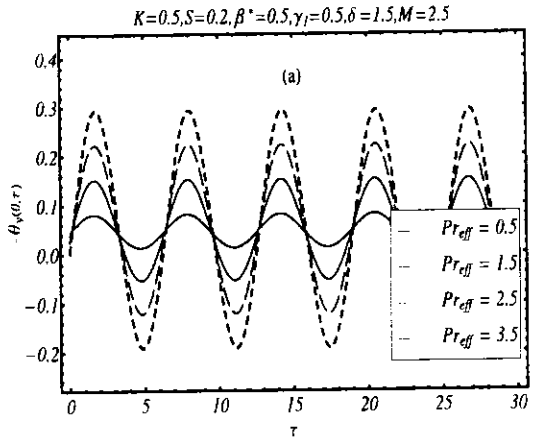

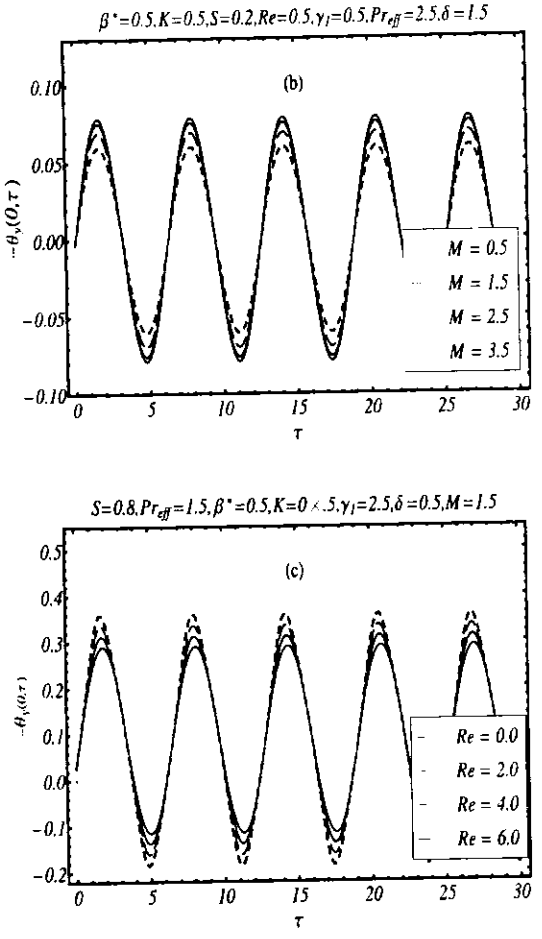

Fig. 5.15: Variation of effective local Nusselt number $\mathrm{Re}_x^{-1/2} Nu_x^*$ with time for (a) effects of Pr_{eff} (b) effects of M (c) effects of Re.

Table 5.1: Numerical values of effective local Nusselt number $-\theta_y(0,\tau)$ for various values of Pr_{eff}, M, β^*, δ and γ when $S = 0.5$, $\mathrm{Re} = 0.5$ and $\tau = \pi/2$.

Pr_{eff}	γ_1	M	K	β^*	δ	$-\theta_y(0,\tau)$
0.1	1.0	0.5	0.2	0.2	0.1	0.476203
0.3						0.477359
0.5						0.478519
0.2	0.0					0.0
	1.0					0.476781
	1.5					0.566646
	1	0.5				0.476781
		1.0				0.476770
		2.5				0.476697
		0.5	0.2			0.476781
			0.6			0.476786
			0.9			0.476790
			0.2	0.5		0.476784
				1.5		0.476797
				3.5		0.476822
				0.2	0.5	0.474780
					1.5	0.469744
					2.5	0.464658

Chapter 6

Hydromagnetic flow and heat transfer of a Jeffrey fluid over an oscillatory stretching surface

The theme of this chapter is to investigate the flow of a Jeffrey fluid over an oscillatory stretching sheet. The heat transfer analysis has also been performed. The system of dimensionless partial differential equations has been solved analytically by using homotopy analysis method (HAM) and numerically by a finite difference scheme. A comparison of both solutions is also provided. The effects of involved parameters are illustrated through graphs and discussed in detail.

6.1 Flow analysis

We consider the unsteady, two-dimensional and magnetohydrodynamics (MHD) flow of an incompressible Jeffrey fluid over an oscillatory stretching surface. The geometry of the flow and heat transfer problem is already discussed in **Fig. 3.1**. Instead of electrically conducting second grade fluid, here the analysis is carried out for a magnetohydrodynamic Jeffrey fluid. Thus the governing equation (1.30) in presence of magnetic field under boundary layer assumptions takes the form

$$\frac{\partial u}{\partial t}+u\frac{\partial u}{\partial x}+v\frac{\partial u}{\partial y}=\frac{\nu}{1+\lambda}\left[\frac{\partial^2 u}{\partial y^2}+\lambda_1\left(\frac{\partial^3 u}{\partial y^2\partial t}+u\frac{\partial^3 u}{\partial x\partial y^2}-\frac{\partial u}{\partial x}\frac{\partial^2 u}{\partial y^2}+\frac{\partial u}{\partial y}\frac{\partial^2 u}{\partial x\partial y}+v\frac{\partial^3 u}{\partial y^3}\right)\right]-\frac{\sigma B_0^2}{\rho}u, \tag{6.1}$$

The energy equation for the flow under consideration is given by Eq. (3.2). The boundary conditions to be satisfied by the velocity components and temperature are also defined in Eqs. (3.3) and (3.4) of chapter 3.

Transformation of variables in Eq. (6.1) using Eqs. (2.6) and (3.5) yields the following system

$$(1+\lambda)\left(Sf_{y\tau}+f_y^2-ff_{yy}+M^2f_y\right)=f_{yyy}+De\left[Sf_{yyy\tau}+f_{yy}^2-ff_{yyyy}\right], \tag{6.2}$$

$$\theta_{yy}+\Pr\left(f\theta_y-S\theta_\tau\right)=0, \tag{6.3}$$

$$f_y(y,\tau)=\sin\tau,\quad f(y,\tau)=0,\quad \theta(y,\tau)=1 \text{ at } y=0, \tag{6.4}$$

$$f_y(y,\tau)=0,\quad f_{yy}(y,\tau)=0,\qquad \theta(y,\tau)=0 \text{ as } y\to\infty \tag{6.5}$$

where $De = \lambda_1 b$ is the Deborah number.

The skin-friction coefficient C_f is given as

$$\mathrm{Re}_x^{1/2} C_f = \frac{1}{1+\lambda}\left[f_{yy} + De\left(S f_{yyt} + f_y f_{yy} - f f_{yyy} \right) \right]_{y=0}. \tag{6.6}$$

The expression for local Nusselt number remains same as given in (3.12).

6.2 Solution of the problem

We have employed two methods for obtaining the solutions of Eqs. (6.2) and (6.3) subject to boundary conditions (6.4) and (6.5). Firstly, we have used homotopy analysis method to solve nonlinear partial differential equations. The method has been already explained in previous chapters. However, for further details we refer the reader to the book by Liao [112]. Secondly, a numerical method based on an implicit finite difference scheme is used. The details of the numerical method are also explained in previous chapters (see section 2.3 and 3.2).

For the sake of completeness, we provide here the transformed version of Eqs. (6.2)-(6.5) in the bounded computational domain. With the help of coordinate transformation $\eta = 1/(y+1)$, Eq. (6.2)-(6.5) can be transformed to

$$\begin{aligned} &S\left((1+\lambda)-6(De)\eta^2\right)\frac{\partial^2 f}{\partial \eta \partial \tau} - S(De)\eta^4 \frac{\partial^4 f}{\partial \eta^3 \partial \tau} - 6S(De)\eta^3 \frac{\partial^3 f}{\partial \eta^2 \partial \tau} = \left((1+\lambda)\eta^2 - 4(De)\eta^4\right)\left(\frac{\partial f}{\partial \eta}\right)^2 \\ &+\left(6\eta^2 + 24(De)\eta^3 f - (1+\lambda)M^2 - 2(1+\lambda)\eta f\right)\frac{\partial f}{\partial \eta} + \left(6\eta^3 - (1+\lambda)\eta^2 f + 36(De)\eta^4 f\right)\frac{\partial^2 f}{\partial \eta^2} \\ &+\eta^4 \frac{\partial^3 f}{\partial \eta^3} - 4(De)\eta^5 \frac{\partial f}{\partial \eta}\frac{\partial^2 f}{\partial \eta^2} - (De)\eta^6\left(\frac{\partial^2 f}{\partial \eta^2}\right)^2 + 12(De)\eta^5 f \frac{\partial^3 f}{\partial \eta^3} + (De)\eta^6 f \frac{\partial^4 f}{\partial \eta^4}, \end{aligned} \tag{6.7}$$

$$\eta^4 \frac{\partial^2 \theta}{\partial \eta^2} + 2\eta^3 \frac{\partial \theta}{\partial \eta} - \mathrm{Pr}\left(f\eta^2 \frac{\partial \theta}{\partial \eta} + S\frac{\partial \theta}{\partial \tau} \right) = 0, \tag{6.8}$$

$$f_\eta = 0,\ f_{\eta\eta} = 0, \quad \theta = 0 \quad \text{at} \quad \eta = 0, \tag{6.9}$$

$$f = 0, \quad f_\eta = -\sin\tau, \quad \theta = 1 \ \text{at} \ \eta = 1. \tag{6.10}$$

The implicit-time difference schemes for f and θ are

$$S\left((1+\lambda)-6(De)\eta^2\right)\frac{1}{\Delta t}\left(\frac{\partial f^{(n+1)}}{\partial \eta}-\frac{\partial f^{(n)}}{\partial \eta}\right)-S(De)\eta^4\frac{1}{\Delta t}\left(\frac{\partial^3 f^{(n+1)}}{\partial \eta^3}-\frac{\partial^3 f^{(n)}}{\partial \eta^3}\right)$$

$$-6S(De)\eta^3\frac{1}{\Delta t}\left(\frac{\partial^2 f^{(n+1)}}{\partial \eta^2}-\frac{\partial^2 f^{(n)}}{\partial \eta^2}\right)=\left((1+\lambda)\eta^2-4(De)\eta^4\right)\left(\frac{\partial f^{(n)}}{\partial \eta}\right)^2$$

$$+\left(6\eta^2-(1+\lambda)M^2\right)\frac{\partial f^{(n+1)}}{\partial \eta}+\left(24(De)\eta^3-2(1+\lambda)\eta\right)f^{(n)}\frac{\partial f^{(n)}}{\partial \eta}+6\eta^3\frac{\partial^2 f^{(n+1)}}{\partial \eta^2} \tag{6.11}$$

$$+\left(36(De)\eta^4-(1+\lambda)\eta^2\right)f^{(n)}\frac{\partial^2 f^{(n)}}{\partial \eta^2}-4(De)\eta^5\frac{\partial f^{(n)}}{\partial \eta}\frac{\partial^2 f^{(n)}}{\partial \eta^2}-(De)\eta^6\left(\frac{\partial^2 f^{(n)}}{\partial \eta^2}\right)^2$$

$$+\eta^4\frac{\partial^3 f^{(n+1)}}{\partial \eta^3}+12(De)\eta^5 f^{(n)}\frac{\partial^3 f^{(n)}}{\partial \eta^3}+(De)\eta^6 f^{(n)}\frac{\partial^4 f^{(n)}}{\partial \eta^4},$$

$$S\,\mathrm{Pr}\frac{\left(\theta^{(n+1)}-\theta^{(n)}\right)}{\Delta t}=\eta^4\frac{\partial^2\theta^{(n+1)}}{\partial \eta^2}+2\eta^3\frac{\partial\theta^{(n+1)}}{\partial \eta}-\mathrm{Pr}\,f^{(n)}\eta^2\frac{\partial\theta^{(n+1)}}{\partial \eta}. \tag{6.12}$$

6.4 Convergence of HAM solution and its comparison with the numerical solution

It is well established fact that convergence of the HAM solution is strongly dependent on the proper values of the auxiliary parameters $\hbar_f$ and $\hbar_\theta$. **Figs. 6.1(a-b)** present two such curves showing the plausible values of $\hbar_f$ and $\hbar_\theta$. These figures indicate that for a convergent solution $-1.1\le\hbar_f<0$ and $-1.7\le\hbar_\theta<-0.2$. Numerical values of $f''(0,\tau)$ at different order of approximations in shown in **Table 1**. It is observed that the convergent values of $f''(0,\tau)$ are obtained at $10th$ order of approximation. A comparison of the HAM solution with the numerical solution is also presented in **Figs. 6.2** and **6.3**. These figures show an excellent agreement between the numerical solution and the higher order HAM solution. The values of $f''(0,\tau)$ obtained by HAM and numerical solution for a Newtonian fluid are also compared with the corresponding values in Refs. [103] and [105]. **Table 6.2** shows the comparison of such values. It can be seen that present results are in excellent agreement with those presented in Ref. [103] and Ref. [105].

6.5 Discussion

The results of velocity f', skin friction coefficient, temperature profile θ and Nusselt number are illustrated through various plots in **Figs. 6.4-6.9**. **Fig. 6.4** illustrates the effects of Deborah number β and ratio of relaxation to retardation parameter λ on the dimensionless velocity at $y = 0.25$. In **Fig. 6.4 (a)** the effects of Deborah number De are illustrated. This figure shows an increase in the amplitude of velocity f' by increasing Deborah number De. Moreover, a phase difference occur for non-zero value of De. Thus viscoelastic fluid with larger retardation time oscillates in time at fixed location from the sheet with different amplitude and phase than that of the Newtonian fluid. **Fig. 6.4(b)** depicts suppression in amplitude of f' with increasing λ.

The transverse profiles of the velocity f' for various values of De at four different time instants in the fifth period are shown in **Figs. 6.5(a-d)**. **Fig. 6.5(a)** shows that at $\tau = 8.5\pi$, the velocity f' increases by increasing De. Moreover at this time instant there are no oscillations in the velocity profile f'. At time instant $\tau = 9\pi$ (**Fig. 6.5(b)**), the velocity f' oscillates near the wall and the amplitude of oscillations increases by increasing De. **Fig. 6.6(c)** elucidates that at $\tau = 9.5\pi$, f' decreases by increasing De. When $\tau = 10\pi$, f' again oscillates near the oscillating sheet and its amplitude increases with De.

Fig. 6.6 shows the effects of ratio of relaxation to retardation time λ on the transverse profiles of velocity different instants $\tau = 8.5\pi - 10\pi$. It is observed from this figure that for $\tau = 8.5\pi$ velocity f' and corresponding boundary layer thickness decrease with λ. At time instants $\tau = 9\pi$ and 10π f' attain zero value both at the sheet and far away from the surface. Furthermore, it oscillates near the wall and amplitude of oscillation decreases by increasing λ. Morever, at $\tau = 9.5\pi$, the magnitude of f' decreases by increasing λ.

The variation of the skin friction coefficient $\mathrm{Re}_x^{1/2} C_f$ with time for different values of De and λ is depicted in **Fig. 6.7**. It is observed from this figure that similar to the velocity profile f', skin friction coefficient also oscillates with time and amplitude of oscillations increases by increasing De and λ. Further like velocity profile f', the oscillations in the skin friction coefficient for $De = 0$ are not in phase with the oscillations for non-zero value of De. In fact a phase shift is observed in the skin friction coefficient for non-zero values of De.

The temperature θ for different values of Pr, De, M and λ is plotted in **Fig. 6.8**. It is observed through this figure that the temperature θ of the fluid decreases by increasing Pr and De. However, it increases by increasing M and λ. The variation of local Nusselt number with time for different values of Pr, De, M and λ is displayed in **Figs. 6.9(a-d)**. **Fig. 6.9(a)** illustrates the effects of Prandtl number on local Nusselt number $\mathrm{Re}_x^{-1/2} Nu_x$. It is noted that the local Nusselt number increases with the increase in Pr. In **Figs. 6.9(b)** the effects of Deborah number De are illustrated. This figure predicts an increase in the local Nusselt number by increasing the Deborah number De. The profiles of the local Nusselt number follow a reverse trend in **Figs. 6.9(c)** and **6.9(d)**. These figures indicate that the local Nusselt number decreases by increasing ratio parameter λ and Hartmann number M.

6.6 Concluding remarks

In this chapter, we have studied the unsteady flow and heat transfer of a Jeffrey fluid over an oscillatory stretching surface which is maintained at a constant temperature. The resulting nonlinear partial differential equations are solved by using homotopy analysis method (HAM) and finite difference scheme. The main conclusions of the present study are:

- The amplitude of the flow velocity increases by increasing the Deborah number De while it decreases with an increase in the ratio of relaxation to retardation time λ. Moreover a phase shift is observed for non-zero values of the Deborah number De.
- The amplitude of the skin friction coefficient increases by increasing Deborah number De and ratio of relaxation to retardation time λ.
- An increase in temperature is found by increasing Hartmann number M and ratio of relaxation to retardation time λ. However, it decreases by increasing Deborah number and Prandtl number Pr. Moreover, the rate of heat transfer increases by increasing Prandtl number Pr and Deborah number De.
- The solution presented in this chapter is more general and includes the solution corresponding to radiative problem as a special case. This conclusion is also supported by recent papers by Magyari and Pantokratoras [38], Fetecau et al. [39] and Vieru et al. [40] where it is explicitly shown that an evaluation of the effect of thermal radiation in the linearized Rosseland approximation does not require any additional research effort. Once the

problem has been solved for a comprehensive set of values of the Prandtl number in the absence of radiation, it has been automatically solved for radiative case too. In view of above argument the solution of problem with radiative effects can be obtained by replacing the Prandtl number in our solution by the effective Prandtl number $\Pr_{eff} = \Pr(1+N_r)$ where N_r is the radiation parameter.

Table 6.1: Convergence of HAM solution of $f''(0,\tau)$ with $S = 0.5, M = 3,\ De = 0.1$ and $\lambda = 0.1$.

Order of approximations	$\tau = 0$	$\tau = \pi$	$\tau = 1.5$
3	-0.002304	0.002304	0.944448
5	-0.002632	0.002574	0.943124
10	-0.002670	0.002588	0.943017
15	-0.002670	0.002588	0.943017
20	-0.002670	0.002588	0.943017
30	-0.002670	0.002588	0.943017

Table 6.2: Comparison of values of $f''(0,\tau)$ for $\lambda = De = 0$ with Refs. [103] and [105].

S	M	τ	Ref. [103] with $K = 0$	Ref. [105]	Present results	
					Numerical solution	HAM solution
1.0	12.0	$\tau = 1.5\pi$	11.678656	11. 678565	11. 678656	11. 6785657
		$\tau = 5.5\pi$	11.678707	11.678706	11.678707	11.6787065
		$\tau = 9.5\pi$	11.678656	11.678656	11.678656	11.6786561

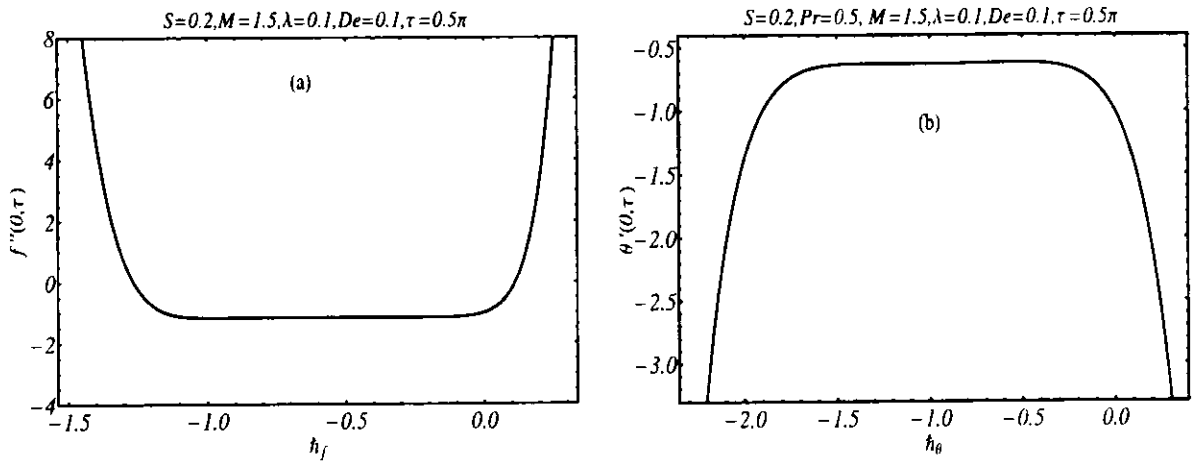

Fig. 6.1: The $\hbar$-curves at 10^{th}-order of approximation (a) for velocity (b) temperature profile.

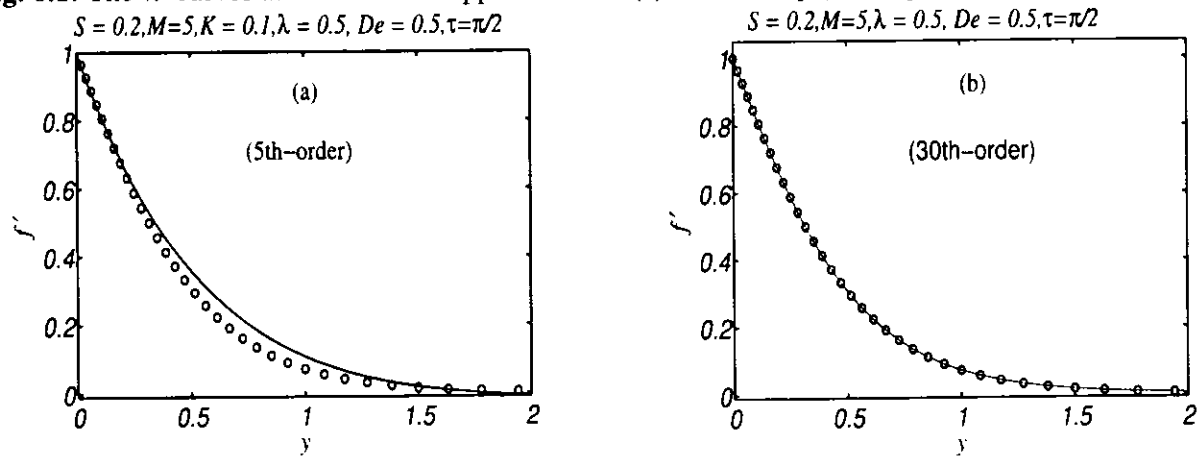

Fig. 6.2. Comparison of HAM solution (solid lines) with numerical solution (open circles) for velocity.

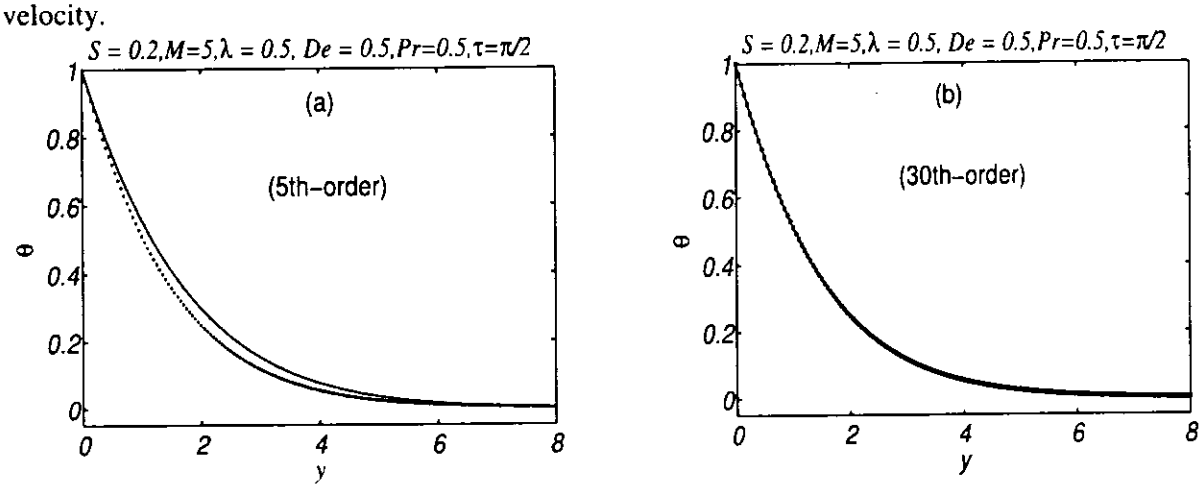

Fig. 6.3. Comparison of HAM solution (solid lines) with numerical solution (open circles) for temperature.

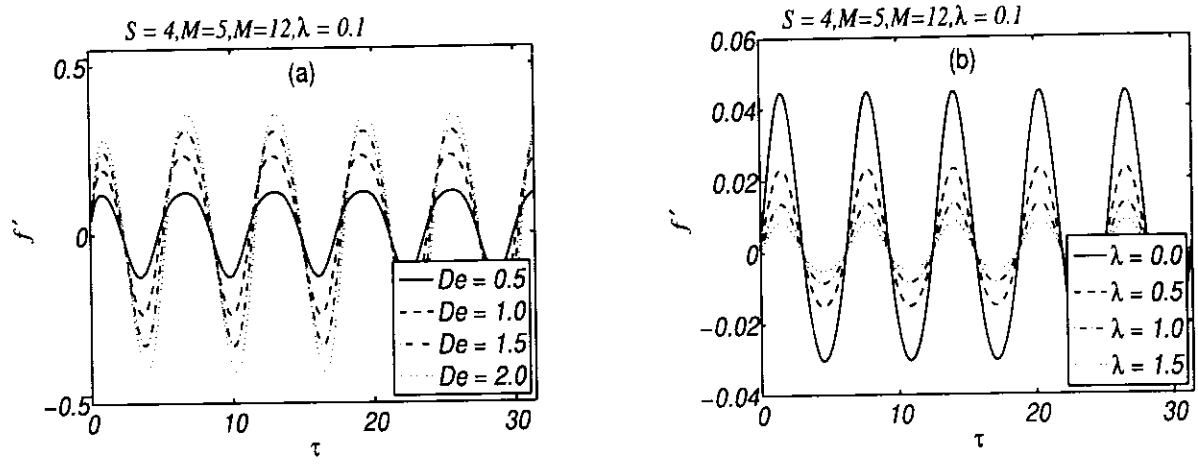

Fig. 6.4: Velocity as function of time (a) effects of De (b) effects of λ.

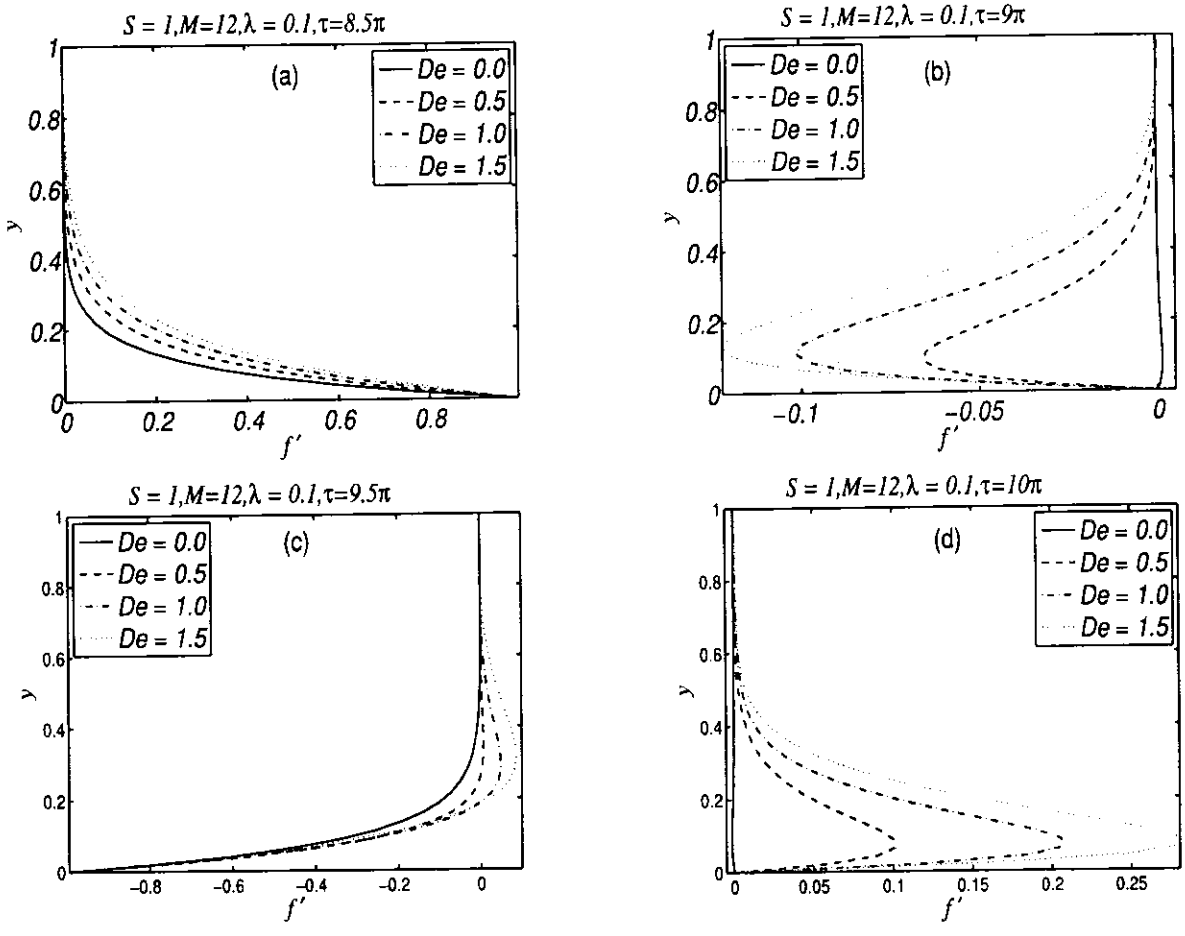

Fig. 6.5: Effects of De on velocity.

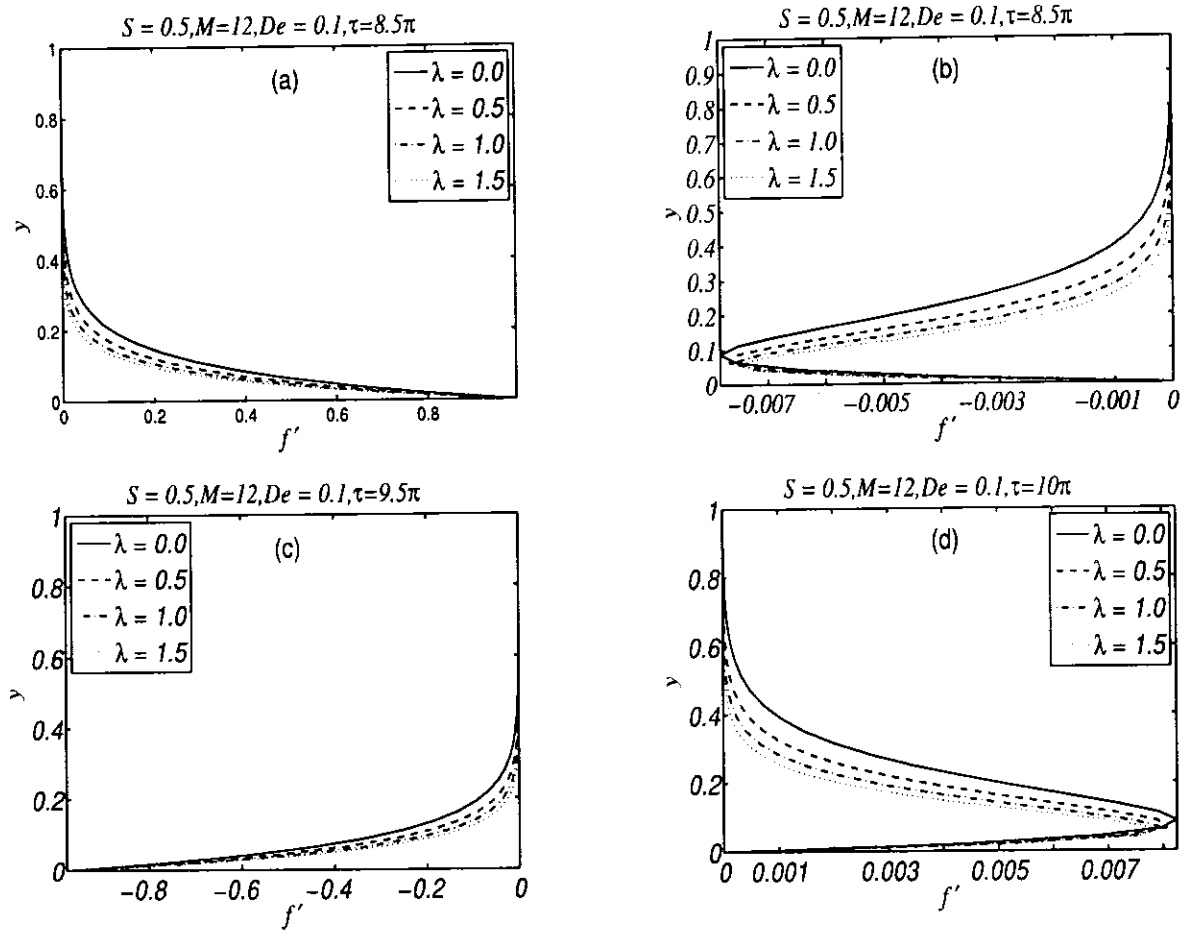

Fig. 6.6: Effects of λ on velocity.

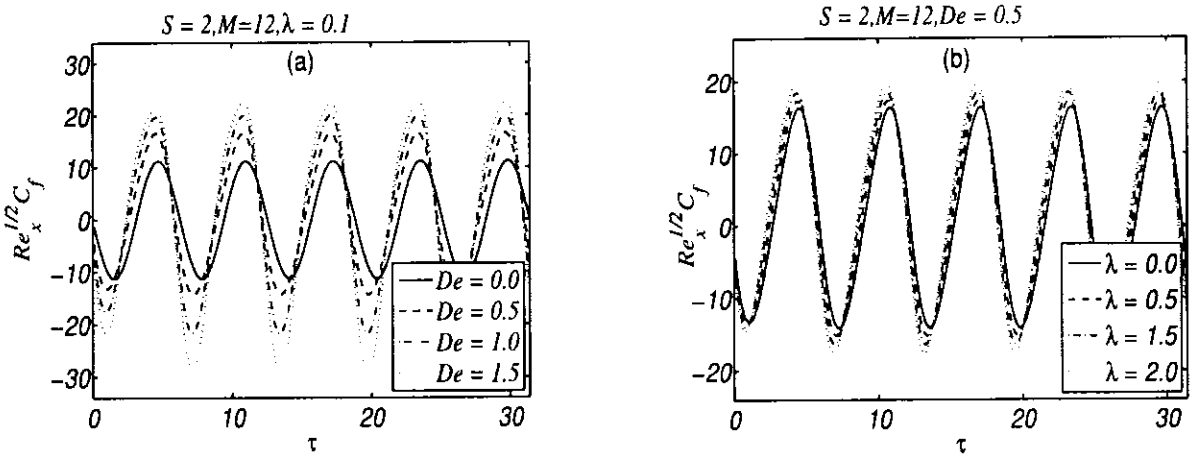

Fig. 6.7: Skin-friction coefficient $\mathrm{Re}_x^{1/2} C_f$ with time (a) effects of *De*, (b) effects of λ.

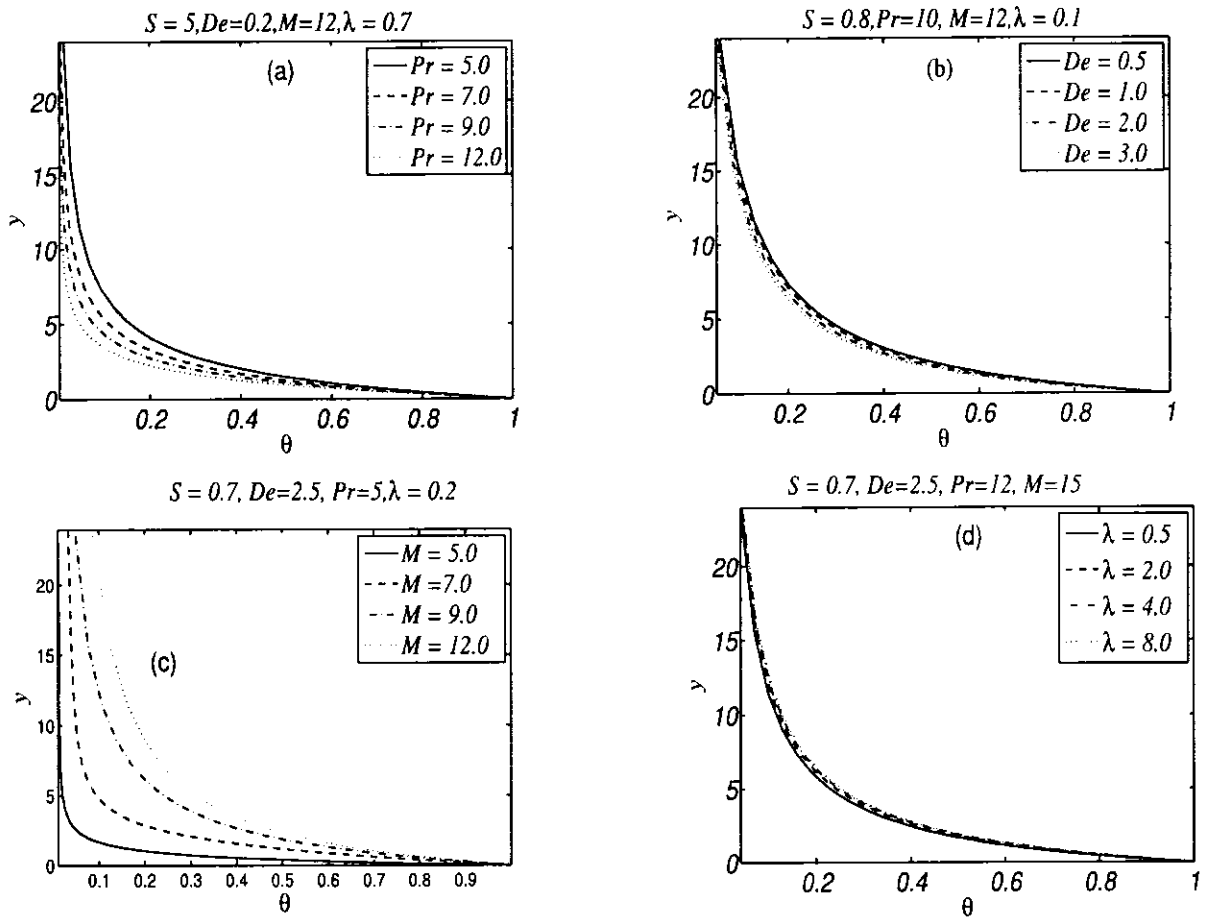

Fig. 6.8: Temperature profile (a) effects of Pr (b) effects of De (c) effects of M (d) effects of λ.

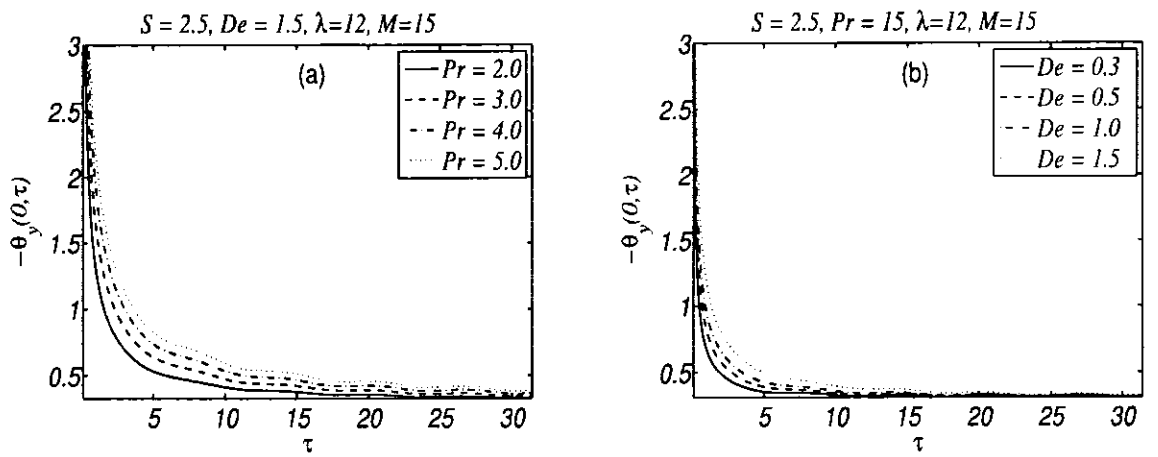

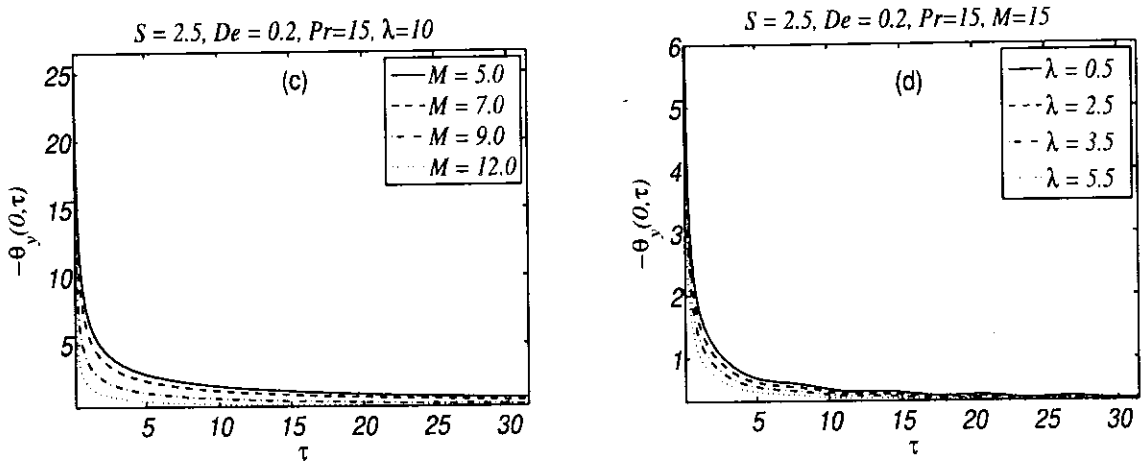

Figure 6.9: Local Nusselt number $\mathrm{Re}_x^{-1/2} C_f$ with time (a) effects of Pr (b) effects of De (c) effects of M and (d) effects of λ.

Chapter 7

MHD flow and heat transfer of Couple Stress fluid over an oscillatory stretching sheet with heat source/sink in porous medium

This chapter presents the MHD flow and heat transfer of a couple stress fluid over oscillatory stretching sheet embedded in a porous medium in the presence of heat source/sink. The unsteady flow problem is reduced to two coupled partial differential equations using dimensionless variables. Homotopy analysis method is employed to obtain the solution of these equations. An extensive analysis is performed to investigate the effects of various flow parameters on the velocity and temperature distributions, skin friction coefficient and Nusselt number.

7.1 Flow Analysis

Let us consider two-dimensional flow of an incompressible fluid over an oscillatory stretching sheet. In contrast to chapter 3, here the fluid in the semi-infinite space is assumed to obey constitutive equation of couple stress fluid. The momentum equation under boundary layer approximation becomes [49]

$$\frac{\partial u}{\partial t}+u\frac{\partial u}{\partial \bar{x}}+v\frac{\partial u}{\partial \bar{y}}=\nu\frac{\partial^2 u}{\partial \bar{y}^2}-\frac{\xi}{\rho}\left[\frac{\partial^4 u}{\partial \bar{y}^4}\right]-\frac{\sigma B_0^2}{\rho}u-\frac{\nu\varphi}{k^*}u, \tag{7.1}$$

where ξ is the material constant for the couple stress fluid. The energy equation for the problem under consideration is also modified slightly due to inclusion of heat absorption/generation term in the balance law. Therefore, energy equation takes the form

$$\frac{\partial T}{\partial t}+u\frac{\partial T}{\partial \bar{x}}+v\frac{\partial T}{\partial \bar{y}}=\frac{k_1}{\rho c_p}\frac{\partial^2 T}{\partial \bar{y}^2}+\frac{Q}{\rho c_p}(T-T_\infty), \tag{7.2}$$

Due to increase in the order of governing equation (7.1), the already available boundary conditions given in (3.3) and (3.4) are not sufficient for the unique solution. The extra boundary condition arises as a consequence of the assumption $\frac{\partial^2 u}{\partial \bar{y}^2}\to 0$ at $\bar{y}=0$. The energy equation is subject to the same boundary conditions as given in (3.3) and (3.4).

Utilizing the dimensionless variables (2.6) and (3.5), Eqs. (7.1) and (7.4) are transformed into

$$f_{yyy} - Sf_{y\tau} - f_y^2 + ff_{yy} - \beta f_y - K^* f_{yyyyy} = 0, \tag{7.3}$$

$$\theta_{yy} + \Pr\left(f\theta_y - S\theta_\tau + \delta\theta\right) = 0. \tag{7.4}$$

The boundary conditions take following form

$$f_y(0,\tau) = \sin\tau, \quad f(0,\tau) = 0, \quad f_{yy}(0,\tau) = 0, \quad \theta(0,\tau) = 1, \tag{7.5}$$

$$f_y(\infty,\tau) = 0, \quad f_{yy}(\infty,\tau) = 0, \quad \theta(\infty,\tau) = 0. \tag{7.6}$$

In above equations $K^* = \eta_0 b/\rho\nu^2$ is couple stress parameter. It has been pointed out by Stokes [122] that the effects of couple stress are quite large for large values of $K^* = l^2 b\rho/\mu$, where $b\rho/\mu$ is a typical length scale associated with the flow and $l = \sqrt{\eta/\mu}$ is a material coefficient which is a function of molecular dimensions of the liquid. The parameter l varies for different liquids. For instant, the length of polymer chain may be a million time the diameter of a water molecule. This is the size dependent effect associated with the couple stress fluid. For small values of K^* the effects of couple stresses diminish and fluid behaves like a Newtonian fluid. The shear stress for couple stress fluid is

$$\tau_w = \mu\left(\frac{\partial u}{\partial \bar{y}}\right)_{\bar{y}=0} - \frac{\xi}{\rho}\left(\frac{\partial^3 u}{\partial \bar{y}^3}\right)_{\bar{y}=0} \tag{7.7}$$

Thus the skin friction coefficient and the local Nusselt number defined in Eq. (3.10) become

$$\mathrm{Re}_x^{1/2} C_f = f_{yy}(0,\tau) - K^* f_{yyyy}(0,\tau), \tag{7.8}$$

$$\mathrm{Re}_x^{-1/2} Nu_x = -\theta_y(0,\tau). \tag{7.9}$$

7.2 Solution by homotopy analysis method

For the series solution of Eqs. (7.3) and (7.4), we employ homotopy analysis method (HAM). According to HAM the velocity and temperature fields can be represented as

$$f(y,\tau) = a_{0.0}^0 + \sum_{n=0}^{\infty}\sum_{k=0}^{\infty}\sum_{j=0}^{\infty} a_{n.k}^j y^k \sin(j\tau)\exp(-ny), \tag{7.10}$$

$$\theta(y,\tau) = b_{0.0}^0 + \sum_{n=0}^{\infty}\sum_{k=0}^{\infty}\sum_{j=0}^{\infty} b_{n.k}^j y^k \sin(j\tau)\exp(-ny), \tag{7.11}$$

where $a_{n.k}^j$ and $b_{n.k}^j$ are the coefficients to be determined. The appropriate initial guesses for

$f(y,\tau)$ and $\theta(y)$ are

$$f_0(y,\tau)=\frac{1}{2}\sin\tau\left(3-3\exp(-y)-y\exp(-y)\right), \tag{7.12}$$

$$\theta_0(y)=\exp(-y). \tag{7.13}$$

Further we choose

$$\pounds_f(f)=\frac{\partial^3 f}{\partial y^3}-\frac{\partial f}{\partial y},\pounds_\theta(f)=\frac{\partial^2 f}{\partial y^2}-f, \tag{7.14}$$

as auxiliary linear operators satisfying following relations

$$\pounds_f\left[C_1+C_2\exp(-y)+C_3\exp(y)\right]=0, \tag{7.15}$$

$$\pounds_\theta\left[C_4\exp(y)+C_5\exp(-y)\right]=0, \tag{7.16}$$

The zeroth order deformation problems are

$$(1-p)\pounds_f\left[\hat{f}(y,\tau;p)-f_0(y,\tau)\right]=p\hbar_f N_f\left[\hat{f}(y,\tau;p)\right], \tag{7.17}$$

$$(1-p)\pounds_f[\left[\hat{\theta}(y,\tau;p)-\theta_0(y,\tau)\right]=p\hbar_\theta N_\theta\left[\hat{\theta}(y,\tau;p),\hat{f}(y,\tau;p)\right], \tag{7.18}$$

$$\hat{f}(0,\tau;p)=0,\frac{\partial\hat{f}(y,\tau;p)}{\partial y}=\sin\tau,\frac{\partial\hat{f}(y,\tau;p)}{\partial y}=0,\frac{\partial^2\hat{f}(y,\tau;p)}{\partial y^2}=0, \tag{7.19}$$

$$\hat{\theta}(0,\tau;p)=1,\hat{\theta}(\infty,\tau;p)=0, \tag{7.20}$$

where nonlinear operators N_f and N_θ are

$$N_f\left[\hat{f}(y,\tau;p)\right]=-K^*\frac{\partial^5\hat{f}(y,\tau;p)}{\partial y^5}+\frac{\partial^3\hat{f}(y,\tau;p)}{\partial y^3}-S\frac{\partial^2\hat{f}(y,\tau;p)}{\partial y\partial\tau}+\hat{f}(y,\tau;p)\frac{\partial^2\hat{f}(y,\tau;p)}{\partial y^2}$$
$$-\left(\frac{\partial\hat{f}(y,\tau;p)}{\partial y}\right)^2-\beta\frac{\partial\hat{f}(y,\tau;p)}{\partial y}, \tag{7.21}$$

$$N_\theta\left[\hat{\theta}(y,\tau;p),\hat{f}(y,\tau;p)\right]=\frac{\partial^2\hat{\theta}(y,\tau;p)}{\partial y^2}+\Pr\left(\hat{f}(y,\tau;p)\frac{\partial\hat{\theta}(y,\tau;p)}{\partial y}-S\frac{\partial\hat{\theta}(y,\tau;p)}{\partial\tau}+\delta\hat{\theta}(y,\tau;p)\right). \tag{7.22}$$

The solutions for zeroth-order deformation problems associated to $p=0$ and $p=1$

$$\hat{f}(y,\tau;0)=f_0(y,\tau),\hat{f}(y,\tau;1)=f(y,\tau), \tag{7.23}$$

$$\hat{\theta}(y,\tau;0)=\theta_0(y,\tau),\hat{\theta}(y,\tau;1)=\theta(y,\tau). \tag{7.24}$$

By using Taylor's expansion with respect to variable p, we can write $\hat{f}(y,\tau;p)$ and $\hat{\theta}(y,\tau;p)$ as

$$\hat{f}(y,\tau;p)=f_0(y,\tau)+\sum_{m=1}^{\infty}f_m(y,\tau)\,p^m, \tag{7.25}$$

$$\hat{\theta}(y,\tau;p)=\hat{\theta}_0(y,\tau)+\sum_{m=1}^{\infty}\theta_m(y,\tau)\,p^m, \tag{7.26}$$

$$f_m(y,\tau)=\frac{1}{m!}\frac{\partial^m\hat{f}(y,\tau;p)}{\partial p^m},\theta_m(y,\tau)=\frac{1}{m!}\frac{\partial^m\hat{\theta}(y,\tau;p)}{\partial p^m}, \tag{7.27}$$

Differentiating zeroth order deformations equations (7.17) and (7.18) m-times with respect to p, then setting $p=0$ and finally dividing by $m!$, we get the following mth -order deformation problem

$$\pounds_f\left[\hat{f}_m(y,\tau)-\chi_m f_{m-1}(y,\tau)\right]=\hbar_f R_m^f(y,\tau), \tag{7.28}$$

$$\pounds_f\hat{\theta}\left[{}_m(y,\tau)-\chi_m\theta_{m-1}(y,\tau)\right]=\hbar_\theta R_m^\theta(y,\tau), \tag{7.29}$$

$$f_m(0,\tau;p)=0,\left.\frac{\partial f_m(y,\tau;0)}{\partial y}\right|_{y=0}=\left.\frac{\partial f_m(y,\tau;0)}{\partial y}\right|_{y=\infty}=\left.\frac{\partial f_m^2(y,\tau;0)}{\partial y^2}\right|_{y=\infty}=0, \tag{7.30}$$

$$\theta_m(0)=0,\theta_m((\infty)=0,$$

$$R_m^f(y,\tau)=-K^*\frac{\partial^5 f_{m-1}}{\partial y^5}+\frac{\partial^3 f_{m-1}}{\partial y^3}-S\frac{\partial^2 f_{m-1}}{\partial y\partial\tau}-\beta\frac{\partial f_{m-1}}{\partial y}+\sum_{k=0}^{m-1}\left(f_{m-1-k}\frac{\partial^2 f_k}{\partial y^2}-\frac{f_{m-k-1}}{\partial y}\frac{\partial f_k}{\partial y}\right), \tag{7.31}$$

$$R_m^\theta(y,\tau)=\frac{\partial^2\theta_{m-1}}{\partial y^2}-\Pr(S)\frac{\partial\theta_{m-1}}{\partial\tau}+\Pr\left(\sum_{k=0}^{m-1}\left[f_k\frac{\partial\theta_{m-1-k}}{\partial y}\right]+\delta\theta_{m-1}\right), \tag{7.32}$$

$$\chi_m=\begin{cases}0,m\le 1,\\ 1,m>1.\end{cases} \tag{7.33}$$

7.3 Convergence of HAM solution

It is well established fact that the convergence of HAM solution is strongly dependent on auxiliary parameters $\hbar_f$ and $\hbar_\theta$. The convergence of series solution can be controlled by proper choice of these auxiliary parameters. **Figs. 7.1** and **7.2** presents two such curves showing the plausible values of h_f and h_θ for particular parameters. We note from these figures that for

convergent solution $-1.2 \leq \hbar_f < -0.2$ and $-1.5 \leq \hbar_\theta < -0.2$. The purpose of showing such curves is just to emphasize that in principle for any physical choice of parameters of the problem, a convergent solution can be obtained. The values of $f''(0,\tau)$ obtained by HAM in the present case are also compared with the corresponding values reported in Refs. [80,81,103,105] in **Tables 7.1** and **7.2**. Both tables show that our results are in excellent agreement with the existing results in the literature.

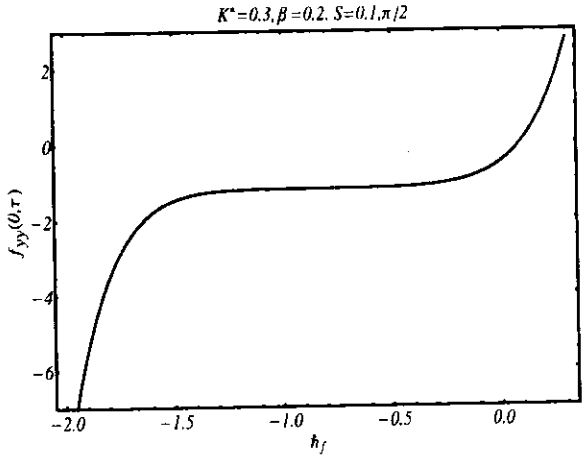

Fig. 7.1: $\hbar$-curve for velocity.

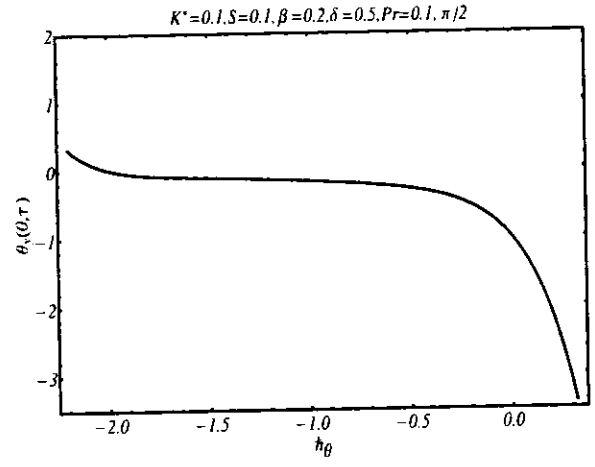

Fig. 7.2: $\hbar$-curve for temperature.

Table 7.1: Comparison $f''(0,\tau)$ for various values of β with $K=0$, $S=0$ and $\tau=\pi/2$.

β	Hayat et al. [80]	Turkyilmazoglu [81]	Present results
0.0	-1.00000000	-1.00000000	-1.00000000
0.5	-1.224747	-1.22474487	-1.224747
1.0	-1.414217	-1.41421356	-1.414217
1.5	-1.581147	-1.58113883	-1.581147
2.0	-1.732057	-1.73205081	-1.732057

Table 7.2: Comparison of values of $f''(0,\tau)$ with Refs. [103] with $K^* = 0$ and [105].

S	β	Zheng et al. [105]	Abbas et al. [105]	Present results
1.0	12.0	11.678565	11.678656	11.678565
		11.678706	11.678707	11.678706
		11.678656	11.678656	11.678656

7.4 Results and discussion

The homotopy analysis method is a power full technique to solve nonlinear partial and ordinary differential equations with initial and boundary conditions. The set of nonlinear partial differential (7.3) and (7.4) with boundary conditions (7.5) and (7.6) are solved analytically by means of homotopy analysis method and the effects of involved parameters are illustrated through graphs. In this section, we are going to present the detailed analysis of flow and heat transfer of couple stress fluid over an oscillating stretching surface in the presence of heat source and sink.

The variation of velocity versus time for various values of couple stress parameter K^* and combined parameter β in studied is **Figs. 7.3 (a-b).** In **Fig. 7.3 (a)** the effects of the couple stress parameter K^* are illustrated by keeping $S = 1$ and $\beta = 0.2$. From this figure we observe that an increase in the couple stress parameter K^* results in an increase of the amplitude of velocity. This is perhaps due to the fact that for large values of K^* the size dependent effects become strong resulting in the enhancement of the velocity amplitude. **Fig. 7.3(b)** describes the effects of combined β by keeping other parameters constant. This figure shows that an increase in combined parameter β results in a decrease of the amplitude.

Figs. 7.4(a)-(d) demonstrate the effects of couple stress parameter K^* on the velocity profile f' at four different time instants $\tau = 8.5\pi$, $\tau = 9\pi, \tau = 9.5\pi$ and $\tau = 10\pi$. **Fig. 7.4(a)** characterizes the effects of the couple stress parameter K^* on the velocity profile f' at $\tau = 8.5\pi$. This figure depicts that the velocity f' decrease as we increase K^*. This decrease in velocity results in decrease of momentum boundary layer thickness. In **Fig. 7.4(b)**, the influence of couple stress parameter K^* on f' is shown for $\tau = 9\pi$. This figure shows an increase in the magnitude of velocity at this instant. The effects of K^* at $\tau = 9.5\pi$ and $\tau = 10\pi$ are illustrated in **Figs. 7.4(c)** and **7.4(d)**, respectively. It is observed from these figures that at $\tau = 9.5\pi$ and $\tau = 10\pi$, the velocity f' decreases with K^*. It is interesting to note that the effects of couple stresses is to the increase the amplitude of the velocity when $f' = 1$ at the surface. For other instants when $f' = -1$ or 0, the magnitude of the velocity decreases due to the presence of couple stresses.

The effects of combined parameter β on the velocity are illustrated in **Figs. 7.5(a)-(d)** at four different times. In **Fig. 7.5(a)** the effects of combined parameter β are shown at $\tau = 8.5\pi$. From this figure it is readily observed that velocity decreases with an increase in β. The effects of magneto-porous parameter on velocity at other three time instants are illustrated in **Figs. 7.5(b)-(d)**. These figures also highlight the decreasing trend in the magnitude of f' with increasing β.

The variation of the skin friction coefficient with couple stress parameter K^* and combined parameter β is shown in **Figs. 7.6(a)-(b)**, respectively. **Fig. 7.6(a)** shows the time series of the skin friction coefficient for different values of couple stress parameter K^* when $S = 0.1$ and $\beta = 0.1$. From this figure we observe that skin friction coefficient varies periodically due to periodic motion of the surface and its amplitude increases with couple stress parameter K^*. This observation reflects that the skin friction coefficient for a Newtonian fluid flowing over an oscillatory stretching sheet is less in comparison with its value for a couple stress fluids performing the same motion. The effects of combined parameter β on skin friction coefficient are illustrated in **Fig. 7.6(b)**. This figure depicts that amplitude of the skin friction coefficient increases by increasing magneto-porous parameter β. Such effects of β and M are expected due to the fact that magnetic force and drag force offered by the porous medium acts as a resistance to the flow.

Fig. 7.7-7.11 presents the effects of Prandtl number Pr, combined parameter β, couple stress parameter K^* and heat source/sink parameter λ on the temperature field. **Fig. 7.7** reveals the graphical behavior of temperature with varying Prandtl number Pr for both heat source and sink cases. It is seen that the temperature is a decreasing function of Pr in both cases. The fact is that the increase of Prandtl number results in lower conductivity, as a result conduction as well as the thermal boundary layer thickness decrease and hence we observe a decrease in the temperature. It is observed that presence of heat sink enhances the decrease of temperature by increasing Prandtl number. In **Fig. 7.8**, the influence of combined parameter β on the temperature is explained graphically by keeping other parameters fixed. This figure shows that temperature increases with magneto-porous parameter β. The influence of couple stress parameter K^* on the temperature is shown in **Fig. 7.9**, which depicts that increase of couple stress parameter results in the increase of temperature. The effects of heat source/sink parameter are illustrated in **Fig. 7.10** and **Fig. 7.11** by keeping $\mathrm{Pr}=0.4$, $\beta=0.5$, $K^*=0.1$, $S=0.1$. It is noted from **Fig. 7.10** that as we increase the strength of the heat source, the temperature increases. This is due to the fact that heat source can add more heat to the stretching sheet which increases its temperature and thus the temperature of the fluid rises. It is also observed out that an increase in the strength of heat source results in increase of thermal boundary layer thickness. **Fig. 7.11** is plotted to observe the effects of heat sink by keeping other parameters constant. This figure shows opposite results i.e., the temperature decreases by increasing the strength of heat sink. This result is of key importance for the flows where heat transfer is of prime importance. The numerical values of Nusselt number are shown in **Table. 7.3**. It is found that the Nusselt number an increases with Prandtl number while it decreases with the increase of heat source, couple stress and combined parameter.

7.5 Concluding remarks

Flow and heat transfer of a couple stress fluid over an oscillatory stretching sheet in the presence of heat source/sink is investigated using HAM. It is observed that flow and heat transfer characteristics are greatly influenced by the presence of couple stress and heat source/sink. In fact, the skin friction coefficient increases by increasing couple stress and combined parameter. It is also interesting to note that rate of heat transfer is enhanced by increasing combined

parameter, heat source and couple stress parameters, while it decreases for large values of Prandtl number and heat sink parameter. Such observations may have interesting implications where it is desired to reduce skin friction and enhance heat transfer.

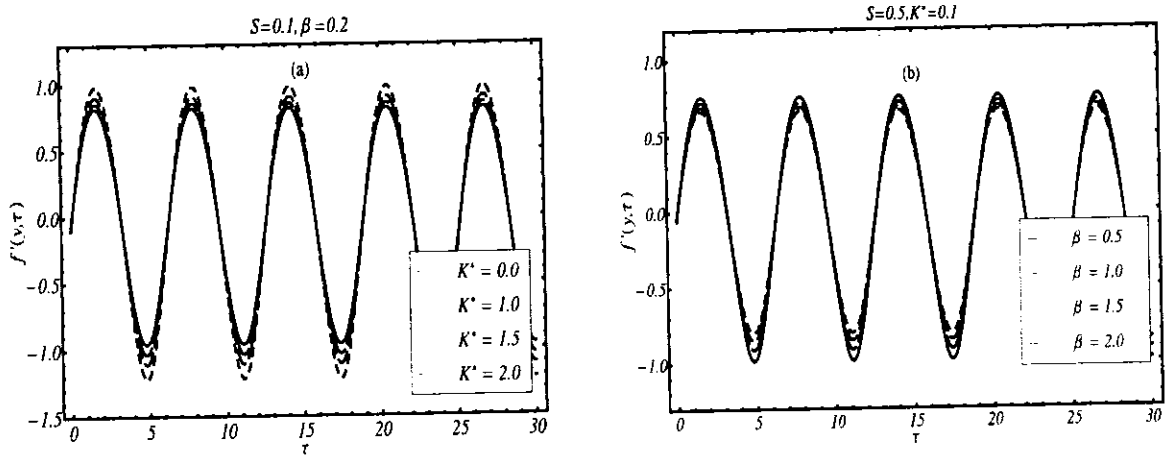

Fig. 7.3: Velocity profile as function of time (a) effects of couple stress parameter K^* (b) effects of magneto-porous parameter β.

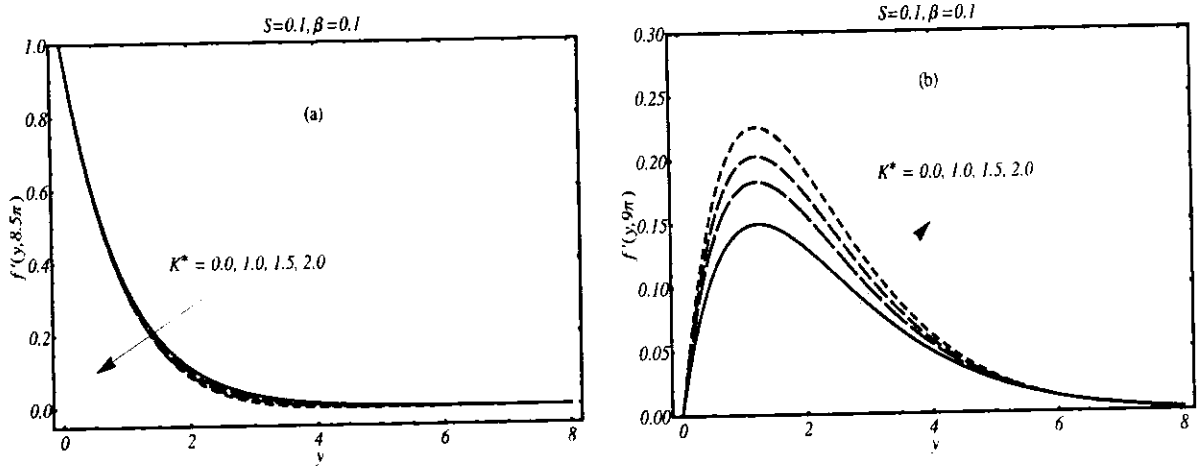

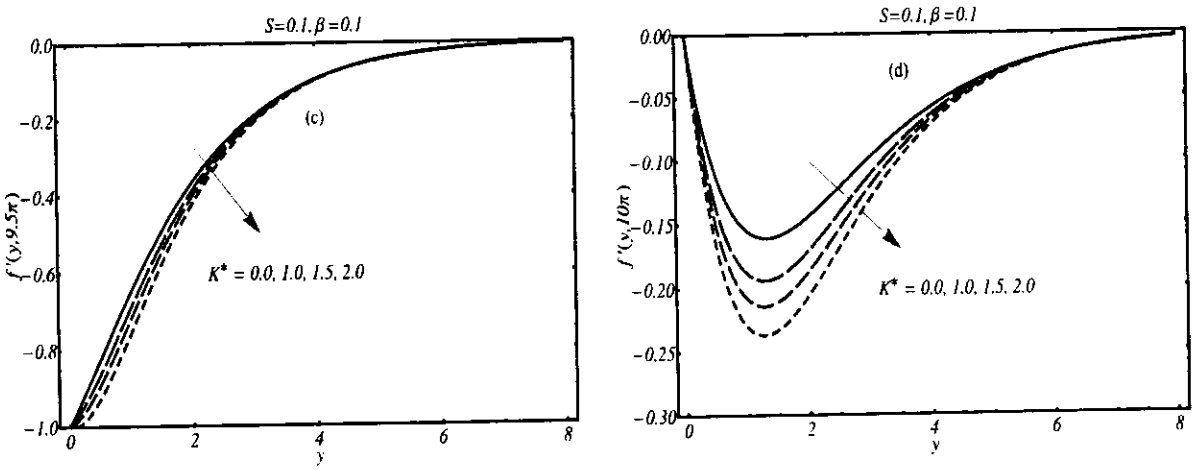

Fig. 7.4: Effects of couple stress parameter K^* on velocity.

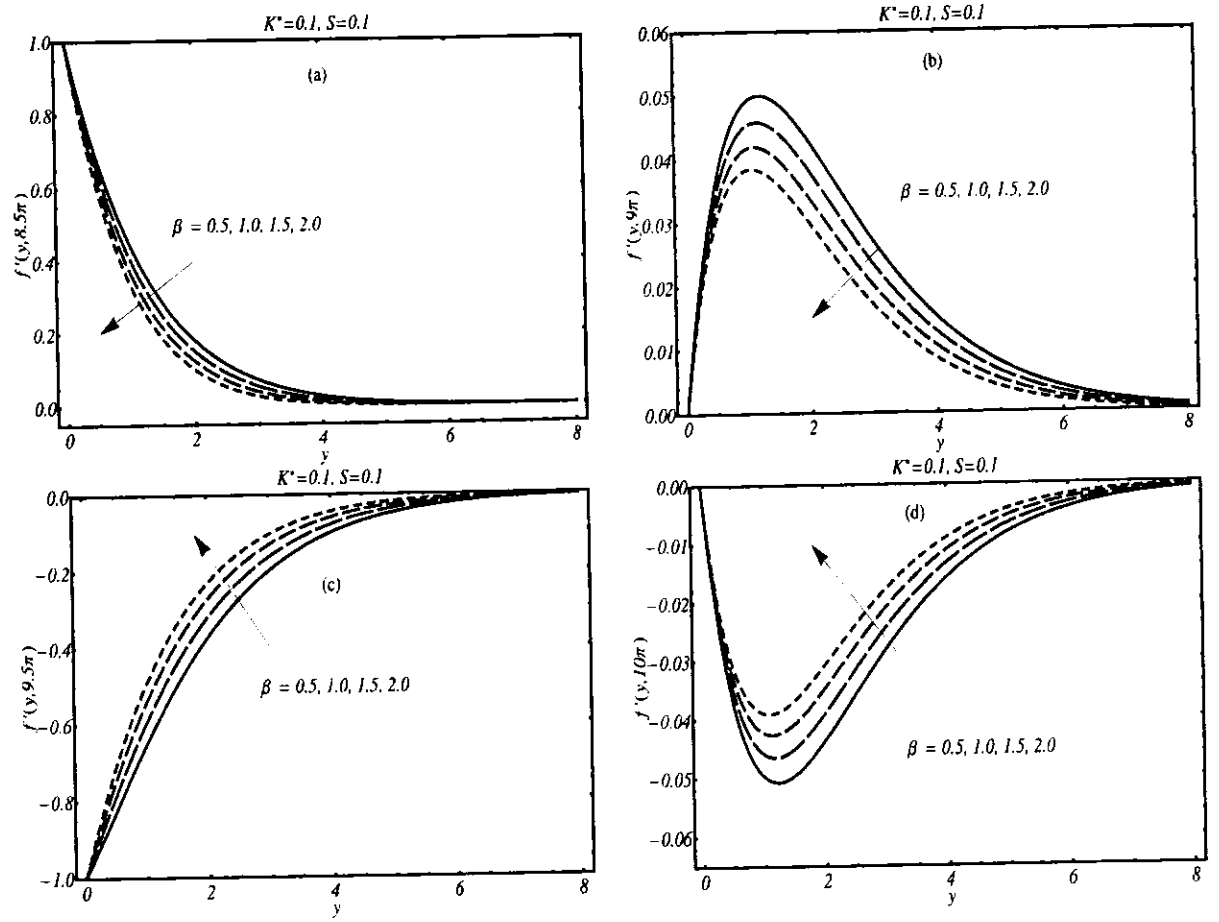

Fig. 7.5: Effects of combined parameter β on velocity.

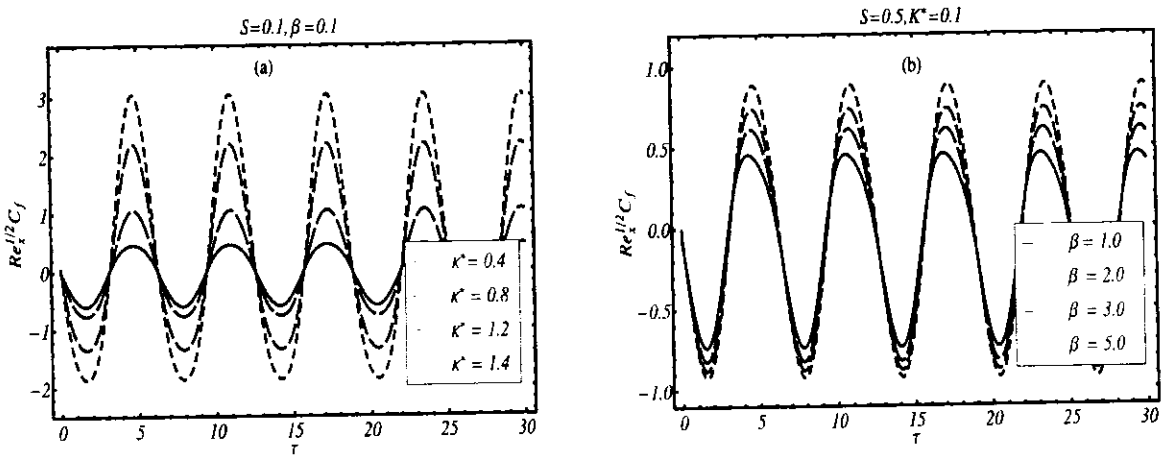

Fig. 7.6: Distribution of skin-friction coefficient $\mathrm{Re}_x^{1/2} C_f$ with time: (a) effects of couple stress parameter K^* and (b) effects of magneto-porous parameter β .

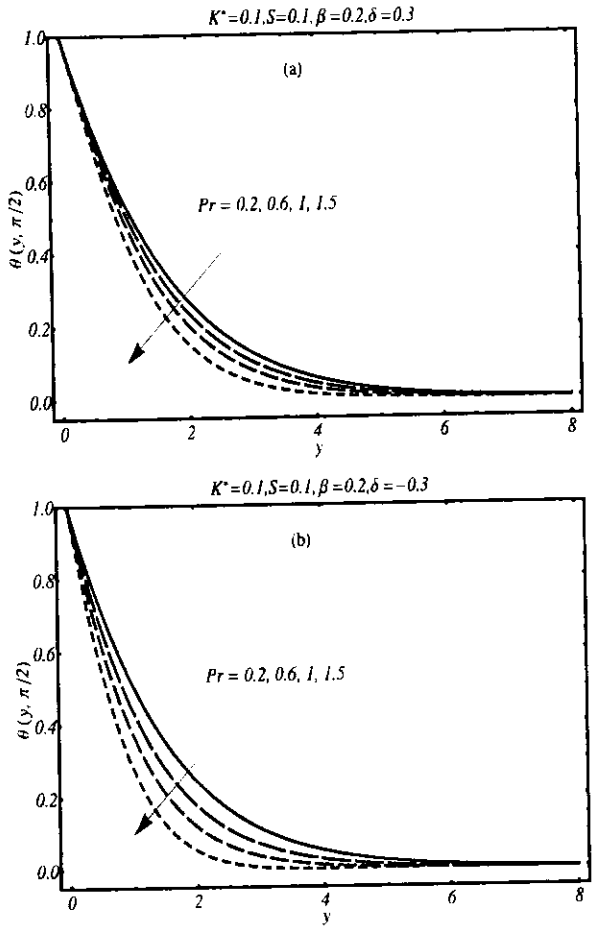

Fig. 7.7: The effects of Prandtl number Pr on temperature field θ.

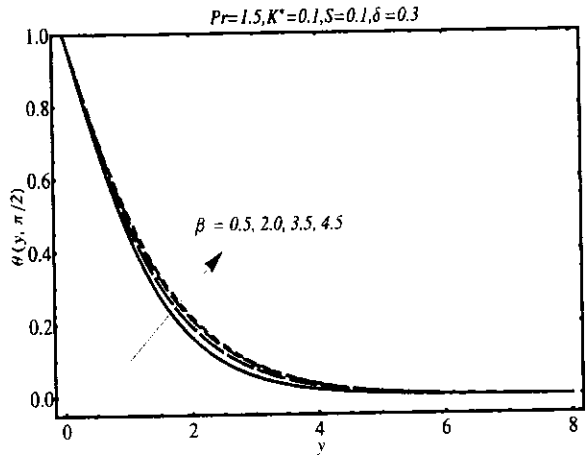

Fig. 7.8: The effects of combined parameter β on temperature field θ.

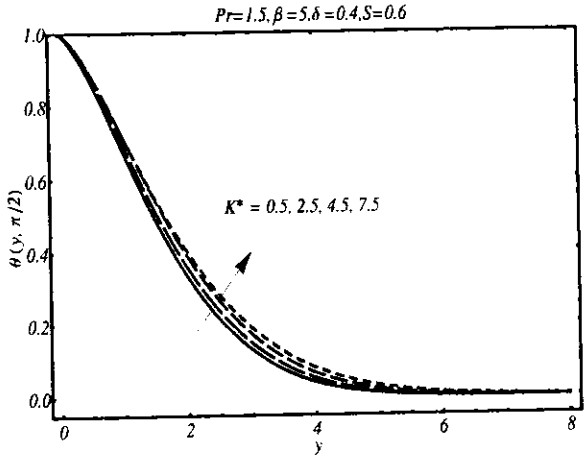

Fig. 7.9: The effects of couple stress number K^* on temperature field θ.

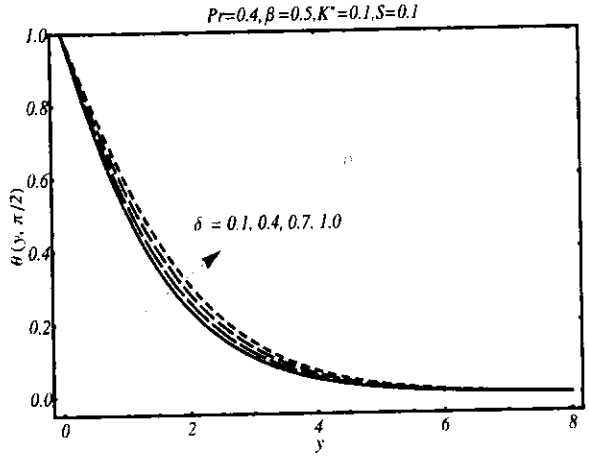

Fig. 7.10: The effects of heat source parameter δ on temperature field θ.

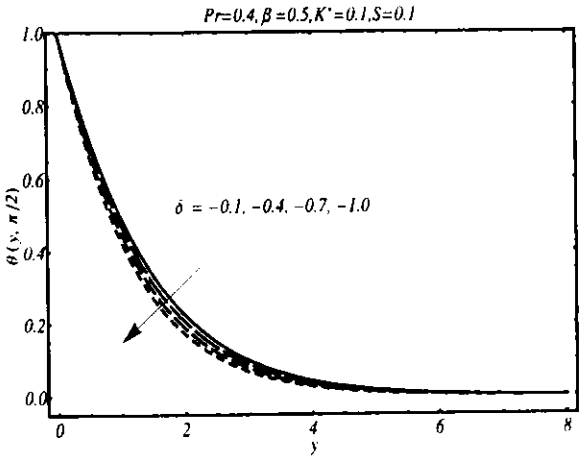

Fig. 7.11: The effects of heat sink parameter δ on temperature field θ.

Table 7.3: Local Nusselt number for Prandtl number Pr, couple stress parameter K^*, combined parameter β and heat source parameter δ at time $\tau = \pi/2$ with $S = 1$.

Pr	δ	K^*	β	$Re_x^{-1/2} Nu_x$
0.5	0.2	5.0	5.0	0.596791
1.0				0.634885
1.5				0.671806
2.0				0.705075
0.5	0.2			0.596791
	0.4			0.547204
	0.6			0.496478
	0.8			0.444590
	0.2	0.2		0.573683
		0.4		0.573021
		0.8		0.572122
		1.0		0.571885
		5.0	0.5	0.643221
			1.5	0.630873
			2.5	0.619684
			3.5	0.609657

Chapter 8

Soret and Dufour effects on hydromagnetic flow of Eyring-Powell fluid over oscillatory stretching surface with heat generation/ absorption and chemical reaction

In this chapter, we have investigated thermal-diffusion and diffusion-thermo effects on unsteady flow of electrically conducting Eyring-Powell fluid over an oscillatory stretching sheet by using convective boundary conditions. Series solution is computed using homotopy analysis method. The effects of various parameters of interest on the velocity filed, temperature profile, concentration profile, skin friction, local Nusselt number and local Sherwood number are illustrated graphically and discussed in detail.

8.1 Flow Analysis

Consider time-dependent laminar boundary layer flow of incompressible electrically conducting Eyring-Powell fluid over an oscillatory stretching sheet. The flow configuration is already explained in **Fig. 4.1**. The boundary layer equation (1.38) in presence of external magnetic field

$$\frac{\partial u}{\partial t}+u\frac{\partial u}{\partial \bar{x}}+v\frac{\partial v}{\partial \bar{y}}=\left(\nu+\frac{1}{\rho B_1 c}\right)\frac{\partial^2 u}{\partial \bar{y}^2}-\frac{1}{2\rho B_1 c^3}\left(\frac{\partial u}{\partial \bar{y}}\right)^2\frac{\partial^2 u}{\partial \bar{y}^2}-\frac{\sigma B_0^2 u}{\rho}. \tag{8.1}$$

The energy and concentration equations (4.2) and (4.3) in the presence of heat source/sink and chemical reaction are

$$\frac{\partial T}{\partial t}+u\frac{\partial T}{\partial \bar{x}}+v\frac{\partial T}{\partial \bar{y}}=\alpha\frac{\partial^2 T}{\partial \bar{y}^2}+\frac{D_m k_T}{c_s c_p}\frac{\partial^2 C}{\partial \bar{y}^2}+\frac{Q}{\rho c_p}(T-T_\infty), \tag{8.2}$$

$$\frac{\partial C}{\partial t}+u\frac{\partial C}{\partial \bar{x}}+v\frac{\partial C}{\partial \bar{y}}=D_m\frac{\partial^2 C}{\partial \bar{y}^2}+\frac{D_m k_T}{T_m}\frac{\partial^2 T}{\partial \bar{y}^2}-k_n(C-C_\infty). \tag{8.3}$$

where k_w is the reaction rate constant. The flow phenomenon is subject to same boundary conditions as given in chapter 3. The boundary conditions on energy and concentration are

$$-k_1\frac{\partial T}{\partial \bar{y}}=h_m(T_f-T),\quad C=C_w,\quad \text{at}\quad \bar{y}=0,\ t>0, \tag{8.4}$$

$$T\to T_\infty,\ C\to C_\infty\ \text{as}\quad \bar{y}\to\infty, \tag{8.5}$$

Using dimensionless variables given in Eq. (2.6), (5.5) (4.9), Eqs. (8.1-8.4) transform to

$$(1+\Gamma) f_{yyy} - S f_{y\tau} - f_y^2 + f f_{yy} - M^2 f_y - \Gamma A f_{yy}^2 f_{yyy} = 0, \tag{8.6}$$

$$\theta_{yy} + \Pr\left(Du\phi_{yy} + f\theta_y - S\theta_\tau\right) + \Pr \delta\theta = 0, \tag{8.7}$$

$$\phi_{yy} + Sc\left(Sr\theta_{yy} + f\phi_y - S\theta_\tau\right) - Kr(Sc)\phi = 0, \tag{8.8}$$

with boundary conditions

$$f_y(0,\tau) = \sin\tau, \quad f(0,\tau) = \gamma, \quad \theta_y(0,\tau) = -\gamma_1\left[1-\theta(0,\tau)\right], \quad \phi(0,\tau) = 1, \tag{8.9}$$

$$f_y(\infty,\tau) = 0, \quad \theta(\infty,\tau) = 0, \quad \phi(\infty,\tau) = 0, \tag{8.10}$$

In above equations $\Gamma = 1/\mu B_1 c$ and $A = \bar{x}^2 b^3 / 2\nu c^2$ are the dimensionless Eyring-Powell fluid parameters. The parameter A is the local non-Newtonian parameter because of its dependence on the length scale $\bar{x}$. Due to this dependence A varies along the flow direction and thus the solution of Eq. (8.6) is locally similar [21]. The graphical results for particular value of A represent the variation in flow along the vertical direction at a specific longitudinal position $\bar{x}$. Morevoer, $Kr = k_w / b$ is the chemical reaction parameter.

The mathematical expression for the skin-friction coefficient is

$$\mathrm{Re}_x^{1/2} C_f = \left[(1+\Gamma) f_{yy} - \frac{\Gamma}{3} A f_{yy}^3\right]_{y=0}, \tag{8.11}$$

The problem defined by Eqs. (8.6)-(8.10) is solved by HAM. The method is already explained and therefore we shall proceed to the graphical results and their interpretation.

8.2. Result and discussion

It is well established fact that the auxiliary parameters play an important role within the framework of the homotopy analysis method. The rate of convergence depends upon the proper choice of these parameters. To highlight convergence region, we draw the $\hbar$-curves in **Fig. 8.1(a-c)**. We see that these curves predict that convergent solution for temperature, velocity and concentration fields can be obtained when $-1.1 \le \hbar_f \le -0.1$, $-1.5 \le \hbar_\theta \le 0.5$ and $-1.3 \le \hbar_\phi \le -0.4$.

Fig. 8.2(a-b) displays the variation of velocity with time under influence of two important parameters namely, Eyring fluid parameter Γ and suction/injection γ. From **Fig. 8.2(a)**, we

observe that velocity shows oscillatory behavior and its amplitude increases with increasing Γ. **Fig. 8.2(b)** elucidates the effects of suction/blowing parameter γ on dimensionless velocity profile f'. It is noticed that a phase shift occurs and amplitude of velocity decreases with increasing suction/blowing parameter γ.

The effects of Eyring Powell fluid parameter, Hartmann number and suction/injection parameter on transverse distribution of velocity at a time $\tau = \pi/2$ are shown in **Fig. 8.3**. **Fig. 8.3(a)** depicts that velocity increase with increasing the Eyring-Powell fluid parameter Γ. **Fig. 8.3(b)** depicts that the velocity profile decreases rapidly with increasing the Hartmann number. Moreover, the boundary layer thickness also decreases in this case. From **Fig. 8.3(c)**, it has been noticed that increase in suction/blowing parameter γ causes the thinning of the boundary layer and velocity profile decreases with increasing suction/blowing parameter γ.

The influence of Γ on both temperature and concentration profiles at $\tau = \pi/2$ is shown in **Fig. 8.4(a-b)**. A significant decreasing effect in temperature is seen near the wall. Similar effects are observed in **Fig. 8.4(b)**. However, the change in concentration field with increasing Γ is smaller as compared to the corresponding change in temperature field.

Fig. 8.5 illustrates the effects of M on temperature and concentration profiles at $\tau = \pi/2$. The temperature inside the thermal boundary layer is found to be enhanced with increasing M. The variation of concentration for different values of M is shown in **Fig. 8.5(b)**. It is observed that concentration profile slightly increases with increasing M.

Fig. 8.6 shows the variation of suction /blowing parameter γ on temperature and concentration profiles at $\tau = \pi/2$ by keeping other parameters constant. The dimensionless temperature inside the thermal boundary layer is found to decrease in the case of suction. However, an increase in temperature and corresponding thermal boundary layer thickness is noted for the injection case and corresponding thermal boundary layer thickness increases. Similar observations are made through the examination of concentration profiles (**Fig. 8.6(b)**)

Fig. 8.7 is sketched to see the temperature profiles for various values of Pr, Du, γ_1 and δ at $\tau = \pi/2$. **Fig. 8.7(a)** indicates that an increase of Pr reduce the thickness of thermal boundary layer. The effect of Dufour number on temperature field is shown in **Fig. 8.7(b)**. An increase in Dufour number leads to an increase in the temperature. The thermal boundary layer is also found

to increase for larger values of Dufour number. In fact, increase in Dufour number causes increase in energy flux due to concentration gradient which is responsible for the increases of temperature. **Fig. 8.7(c)** predicts the behavior of thermal Biot number γ_1 on temperature θ. With an increase in γ_1, the heat transfer coefficient increases and as a result temperature of fluid rises. **Fig. 8.7(d)** depicts that temperature increases with increasing the strength of the heat generation parameter. In contrast, the temperature decreases with an increase in heat absorption parameter. This result is of key importance for the flows where heat transfer is of prime importance. The effects of Schmidt number Sc, Soret number Sr and chemical reaction parameter Kr on concentration field ϕ are shown in **Fig. 8.8**. **Fig. 8.8(a)** illustrates that as we increase Schmidt number Sc, mass diffusion reduces and thus the concentration field decreases. **Fig. 8.8(b)** depicts that increase in Soret number Sr results in increase in concentration field. The concentration decreases with chemical reaction parameter Kr (**Fig. 8.8(c)**). Physically, larger values of Kr correspond to larger interfacial mass transfer rate and as a result concentration decreases.

Fig. 8.9 illustrates the variation of wall shear stress with time for different values of Hartmann number M and Eyring Powell fluid parameter Γ. From **Fig. 8.9(a)**, it is observed that skin friction oscillates periodically due to the oscillatory surface and amplitude of oscillation increases with increasing Hartmann number M. The effects of fluid parameter Γ on wall shear stress are quite opposite. Here, amplitude of skin friction decreases by increasing fluid parameter Γ (**Fig. 8.9(b)**). **Fig. 8.10(a)** depicts the effects of Prandtl number on time-series of local Nusselt number examined by keeping other parameters constant. It is interesting to note that amplitude of local Nusselt number increases with an increase in Prandtl number. **Fig. 8.10(b)** shows the on time-series of local Sherwood number for various values of Schmidt number. Here it is noted that amplitude of oscillations in local Nusselt number increases with an increase in Schmidt number.

The velocity, temperature and concentration profiles for various time instants are shown graphically in **Fig. 8.11(a-c)**. **Fig. 8.11(a)** shows that velocity component oscillates periodically between -1 to 1 because of the oscillatory nature of the sheet. **Fig. 8.11(b)** and **8.11(c)** shows that temperature and concentration profiles decrease as time increases from $\pi/6$ to $2\pi/3$.

8.3. Concluding remarks

This paper highlights the Soret and Dufour effects in two-dimensional flow of Eyring-Powell fluid over an oscillatory stretching sheet. Furthermore, heat transfer analysis is carried out in the presence of chemical reaction and convective boundary conditions. The impact of various parameters of interest is discussed graphically. The larger values of Eyring Powell fluid parameter enhance the amplitude of velocity and boundary layer thickness. However, opposite effects are observed in temperature and concentration profiles. Moreover, the temperature is found to decrease with increasing values of suction while it increases in the case of injection. It is also observed that the temperature and concentration field are increasing functions of Hartmann number. Similarly, temperature inside the thermal boundary layer increases with an increase in Dufour and Biot numbers. Finally, concentration and concentration boundary layer thickness decrease by increasing dimensionless Schmidt number and reaction rate parameter.

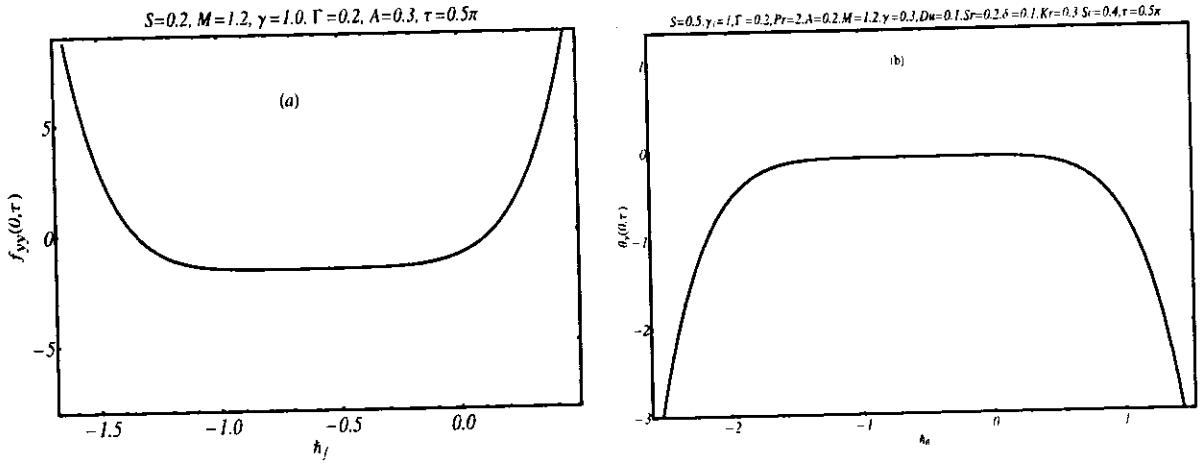

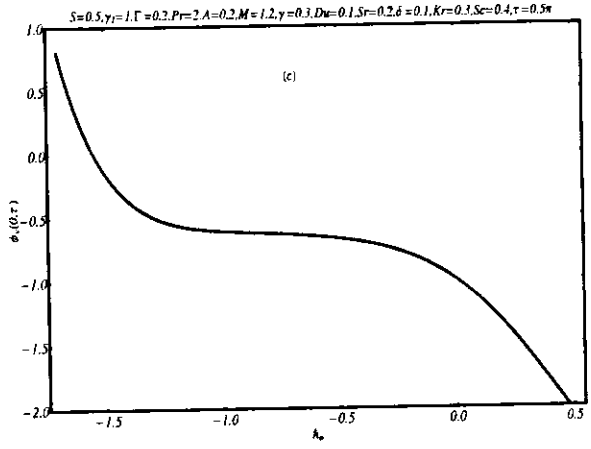

Fig. 8.1. $\hbar$-curves at 6^{th} order of approximation for(a) velocity (b) temperature and (c) concentration profiles.

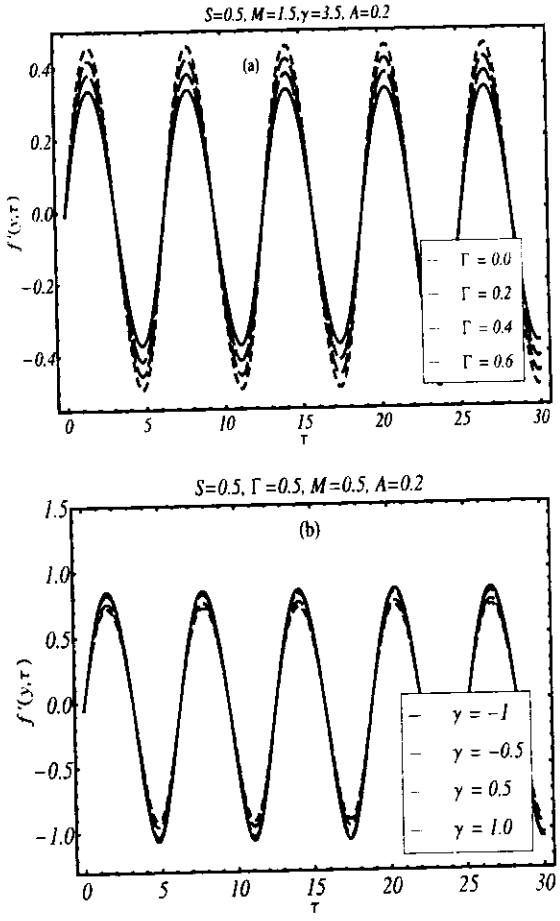

Fig. 8.2. Velocity as function of time for various values of (a) fluid parameter Γ and (b) suction/injection parameter γ.

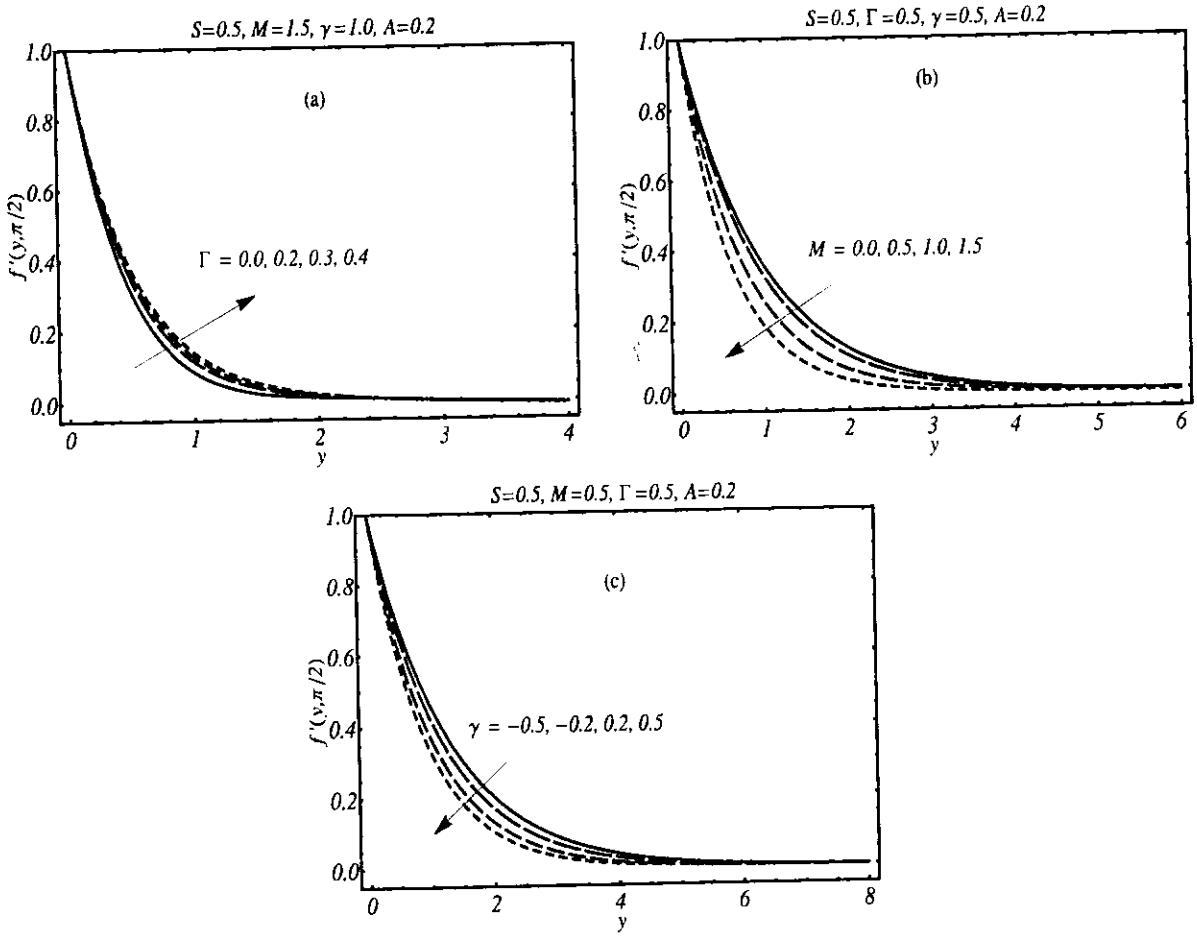

Fig. 8.3: Velocity profile for (a) effects of Γ (b) effects of M (c) effects of γ.

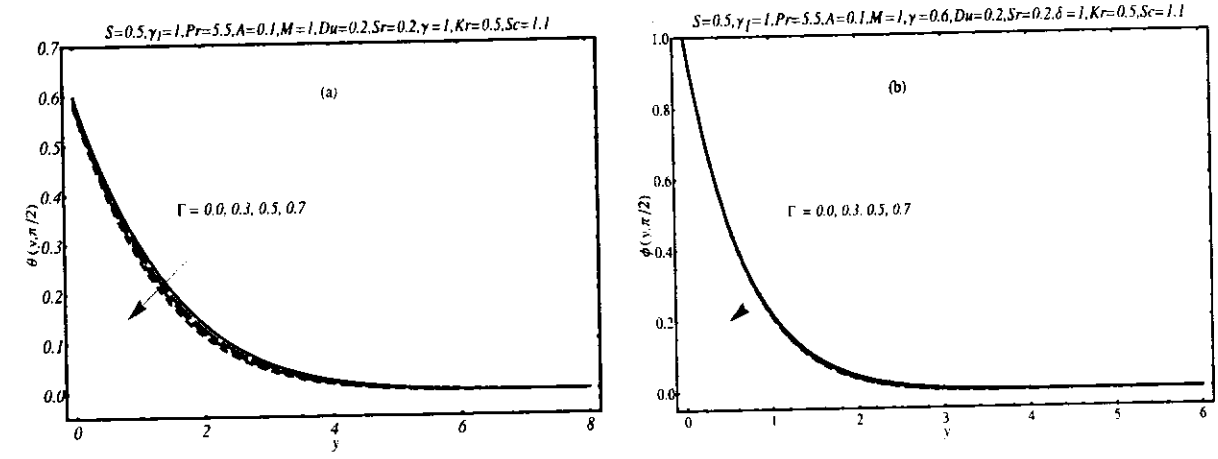

Fig. 8.4: Effects of Γ on (a) temperature and (b) concentration profiles.

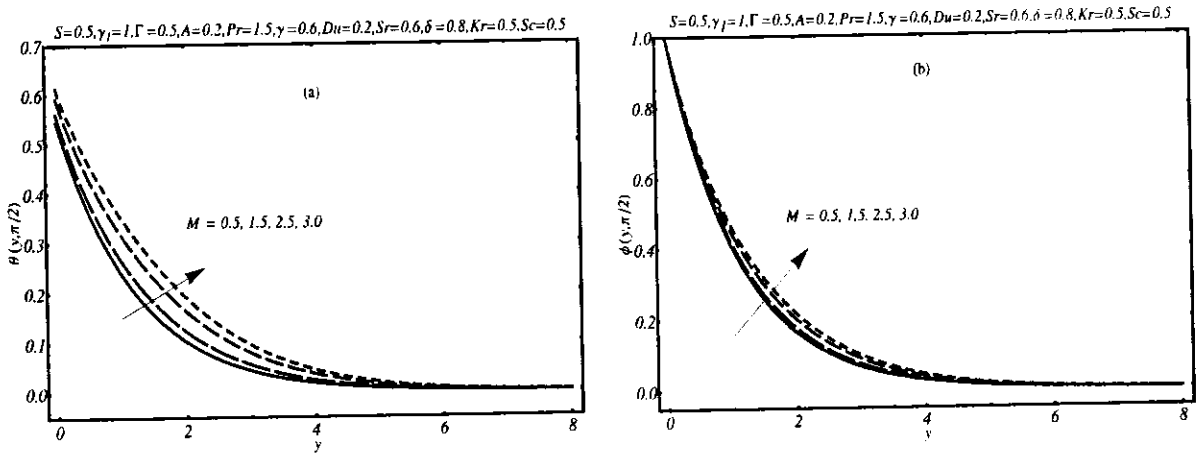

Fig. 8.5: Effects of M on (a) temperature and (b) concentration profiles.

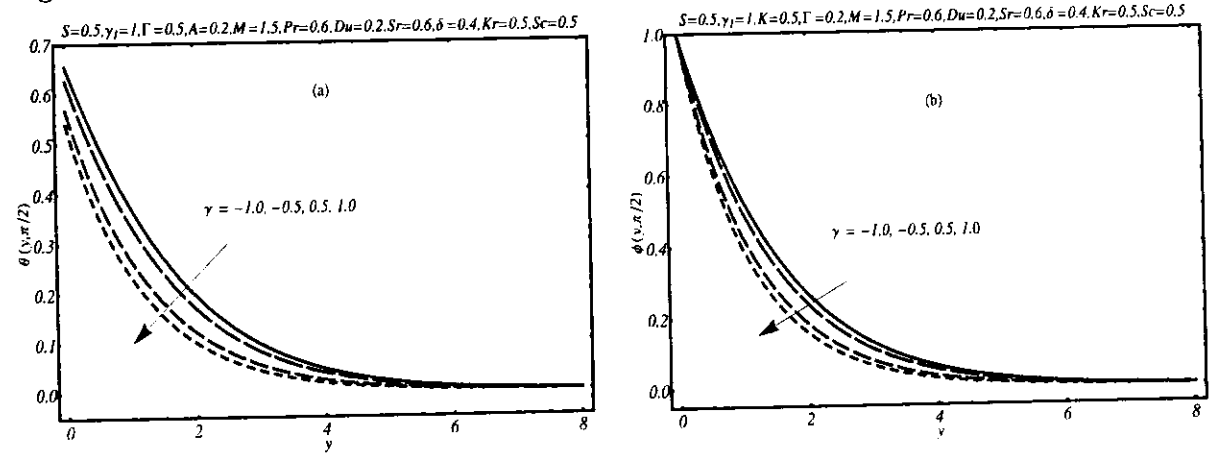

Fig. 8.6: Effects of γ for (a) temperature and (b) concentration profile.

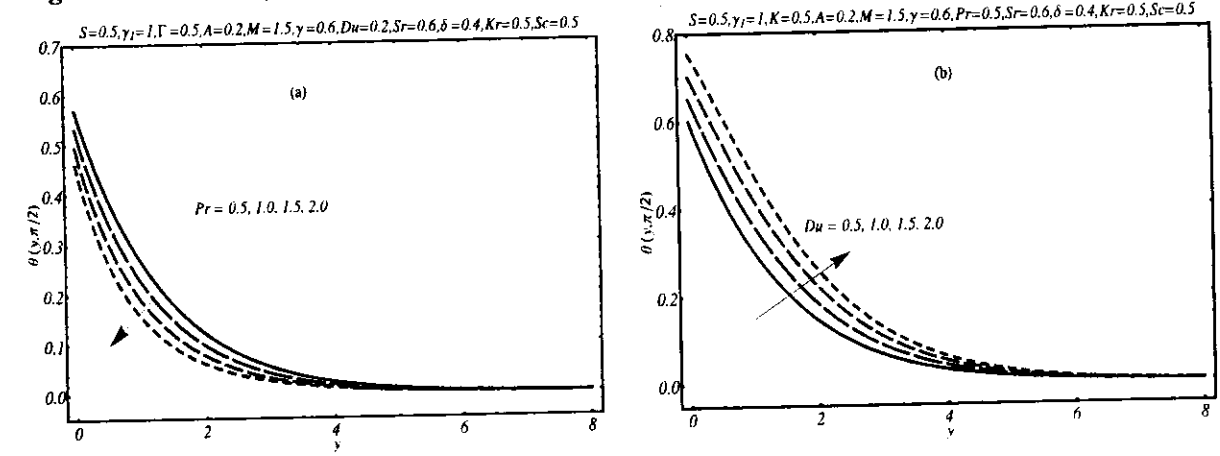

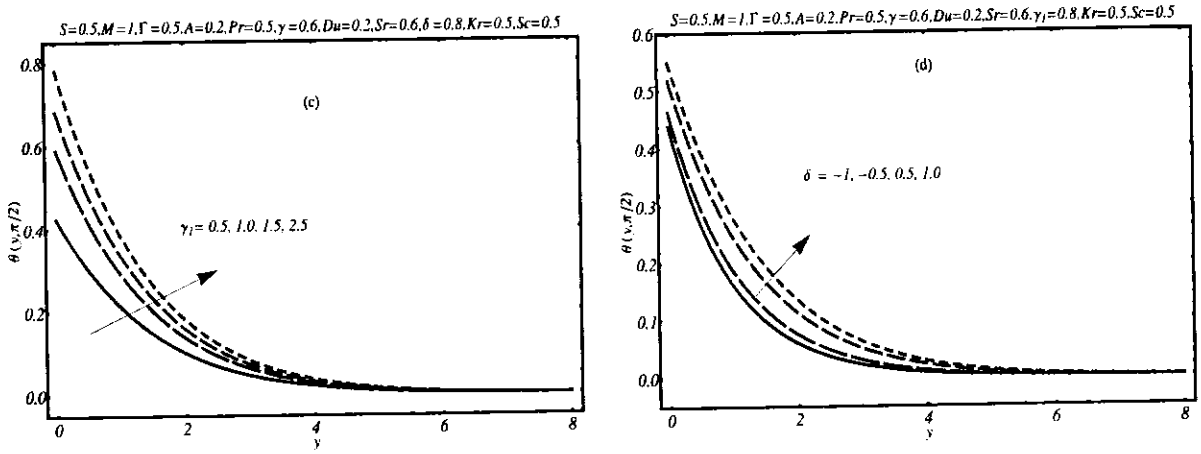

Fig. 8.7: Temperature field (a) effects of Pr (b) effects of Du (c) effects of γ_1 (d) effects of δ

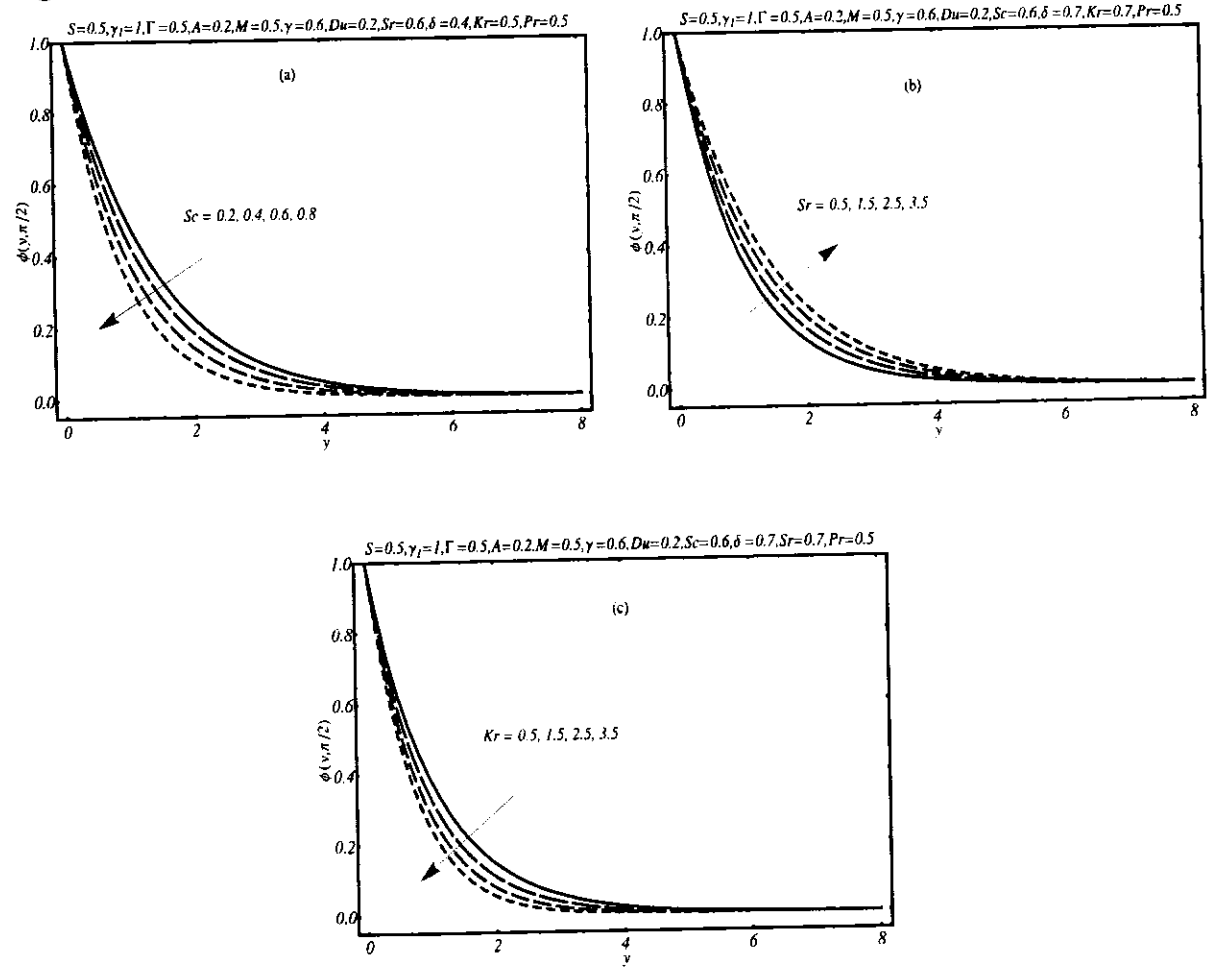

Fig. 8.8: Concentration field with (a) effects of Sc (b) effects of Sr (c) effects of Kr.

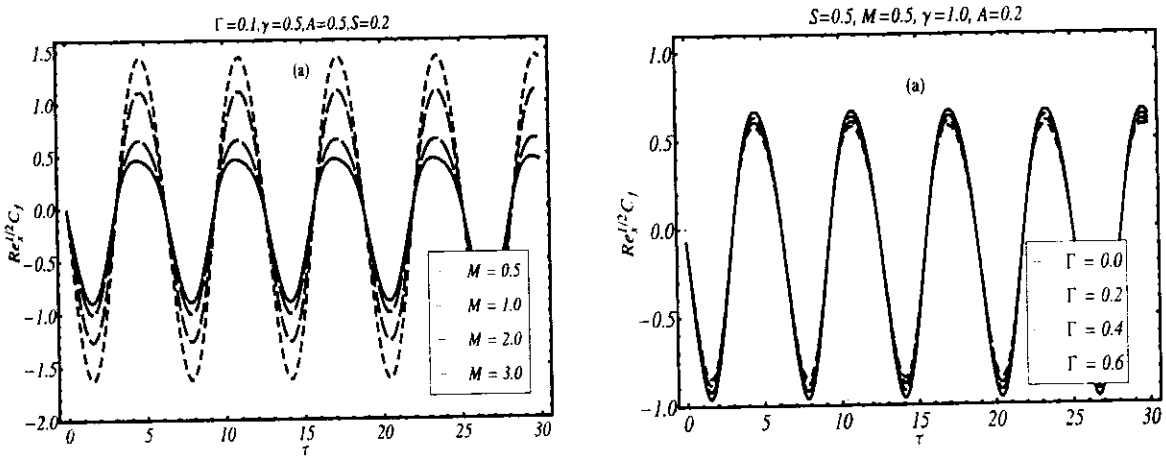

Fig. 8.9: Time-series of the skin friction $\mathrm{Re}_x^{1/2} C_f$ (a) effects of M (b) effects of Γ.

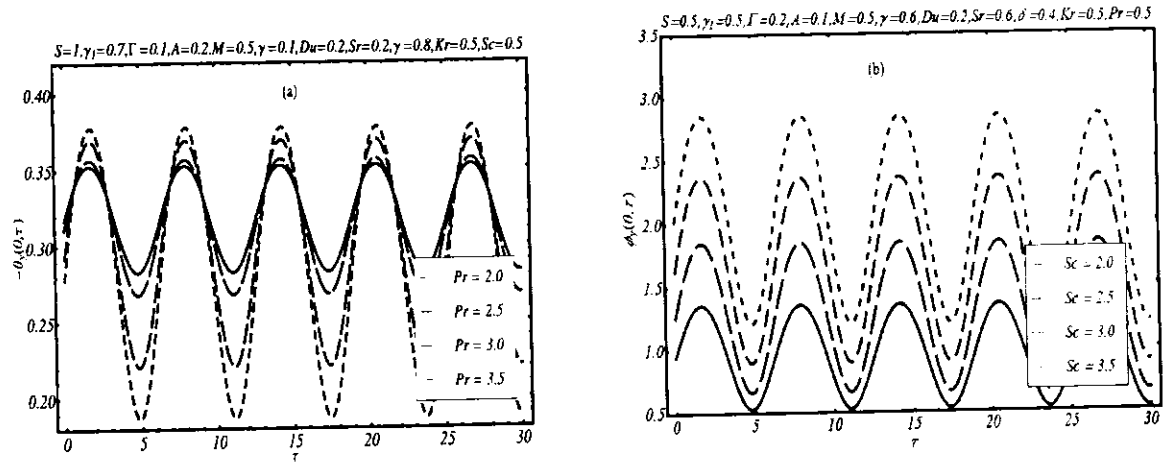

Fig. 8.10. (a) Effects of Pr on local Nusselt number $\mathrm{Re}_x^{-1/2} Nu$ (b) effects of Sc on local Sherwood number $\mathrm{Re}_x^{-1/2} Sh$.

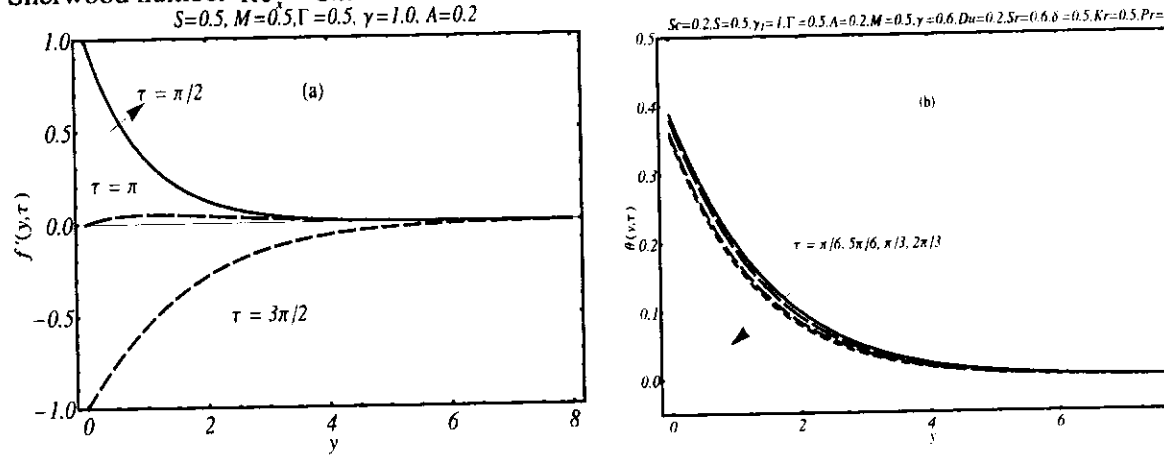

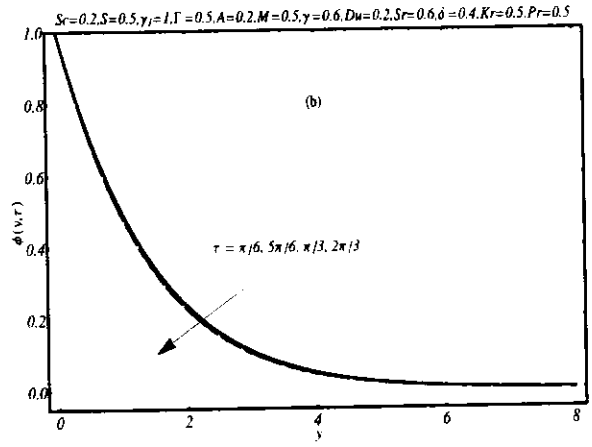

Fig. 8.11: Effects of time τ on (a) Velocity profile (b) Temperature profile (c) Concentration profile.

Chapter 9

Influence of heat source/sink and convective conditions in unsteady stretching flow of Walters' B nanofluid

In this chapter investigates the magnetohydrodynamic (MHD) boundary layer flow of Walters' B nanofluid over an oscillatory stretching surface. The convective boundary conditions are imposed on the temperature and nanoparticles concentration. The effects of heat generation/absorption are also considered in the heat transfer process. The periodic motion of elastic sheet induces the flow. With help of dimensionless variables, series solution is obtained by using HAM. Graphical results illustrating the effects of pertinent parameters like viscoelastic parameter, the ratio of angular velocity to stretching rate, thermophoresis parameter, thermal Biot number, concentration Biot number, Hartmann number, Prandtl number, heat source/sink parameter, Schmidt number on various quantities of interest are discussed.

9.1 Flow Analysis

Let us observe two-dimensional, laminar flow of Walters' B nanofluid over an oscillatory stretching surface. **(Fig. 4.1)**. The modeled momentum, energy and concentration equations under boundary layer approximations for flow phenomenon of Walters' B fluid can be expressed as

$$\frac{\partial u}{\partial t}+u\frac{\partial u}{\partial \bar{x}}+v\frac{\partial u}{\partial \bar{y}}=\nu\frac{\partial^2 u}{\partial \bar{y}^2}-\frac{\alpha_1}{\rho_f}\left[\frac{\partial^3 u}{\partial t\partial \bar{y}^2}+u\frac{\partial^3 u}{\partial \bar{x}\partial \bar{y}^2}+v\frac{\partial^3 u}{\partial \bar{y}^3}+\frac{\partial u}{\partial \bar{x}}\frac{\partial^2 u}{\partial \bar{y}^2}-\frac{\partial u}{\partial \bar{y}}\frac{\partial^2 u}{\partial x\partial \bar{y}}\right]-\frac{\sigma B_0^2}{\rho_f}u, \tag{9.1}$$

$$\frac{\partial T}{\partial t}+u\frac{\partial T}{\partial \bar{x}}+v\frac{\partial T}{\partial \bar{y}}=\alpha\frac{\partial^2 T}{\partial \bar{y}^2}+\tau\left[D_B\frac{\partial C}{\partial \bar{y}}\frac{\partial T}{\partial \bar{y}}+\frac{D_T}{T_\infty}\left(\frac{\partial T}{\partial \bar{y}}\right)^2\right]+\frac{Q}{(\rho c)_f}(T-T_\infty), \tag{9.2}$$

$$\frac{\partial C}{\partial t}+u\frac{\partial C}{\partial \bar{x}}+v\frac{\partial C}{\partial \bar{y}}=D_B\frac{\partial^2 C}{\partial \bar{y}^2}+\frac{D_T}{T_\infty}\frac{\partial^2 T}{\partial \bar{y}^2}, \tag{9.3}$$

where ρ_f is the density of the base fluid, $\tau'\left(=(\rho c)_p/(\rho c)_f\right)$ is the ratio between heat capacity of nanoparticle material to the heat capacity of base fluid, $\alpha\left(=k/(\rho c)_f\right)$ is the thermal

diffusivity of nanofluid, D_B and D_T denotes Brownian diffusion coefficient and thermophoretic diffusion coefficient, respectively.

Eqs. (9.1)-(9.2) are subject to the same boundary conditions as given in chapter 5. However, the concentration is assumed to satisfy following convective type boundary conditions

$$-D_m \frac{\partial C}{\partial \bar{y}} = k_m \left(C_f - C\right), \quad \bar{y} = 0, \ t > 0, \tag{9.4}$$

$$C \to C_\infty \quad \text{as} \quad \bar{y} \to \infty, \tag{9.5}$$

where C_f and C_∞ are the concentration of fluid at the surface and ambient concentration, respectively, D_m is the molecular diffusivity of the species concentration, k_m is the wall mass transfer coefficient. Now using the dimensionless variables used in (2.6) along with

$$\theta(y,\tau) = \frac{T - T_\infty}{T_f - T_\infty} \quad \phi(y,\tau) = \frac{C - C_\infty}{C_f - C_\infty} \tag{9.6}$$

Eqs. (9.1)-(9.3) are transformed as

$$f_{yyy} - Sf_{y\tau} - f_y^2 + ff_{yy} - M^2 f_y - K\left(Sf_{yyy\tau} + 2f_y f_{yyy} - ff_{yyyy} - f_{yy}^2\right), \tag{9.7}$$

$$\frac{1}{\Pr}\theta_{yy} - S\phi_\tau + f\phi_y + Nb\theta_y\phi_y + Nt\left(\theta_y\right)^2 + \gamma\theta = 0, \tag{9.8}$$

$$\phi_{yy} - S\left(Sc\right)\phi_\tau + \left(Sc\right) f\phi_y + \frac{Nt}{Nb}\theta_{yy} = 0, \tag{9.9}$$

The boundary conditions in dimensionless form become

$$f_y\left(0,\tau\right) = \sin\tau, \ \ f\left(0,\tau\right) = 0, \ \ \theta_y(0,\tau) = -\gamma_1\left[1 - \theta(0,\tau)\right], \ \ \phi_y(0,\tau) = -\gamma_2\left[1 - \phi(0,\tau)\right], \tag{9.10}$$

$$f_y\left(\infty,\tau\right) = 0, \ f_{yy}\left(\infty,\tau\right) = 0, \ \ \theta(\infty,\tau) = 0, \qquad \phi(\infty,\tau) = 0. \tag{9.11}$$

The Schmidt number Sc, the concentration Biot number γ_2, Brownian motion parameter Nb, and thermophoresis parameter Nt are, respectively, defined below:

$$\gamma_2 = (k_m / D_m)\sqrt{\nu / b}, Nb = \frac{\left(\rho c\right)_p D_B\left(C_f - C_\infty\right)}{\left(\rho c\right)_f \nu}, Nt = \frac{\left(\rho c\right)_p D_T\left(T_f - T_\infty\right)}{\left(\rho c\right)_f T_\infty \nu}.$$

The expression of skin friction takes form

$$\mathrm{Re}_x^{1/2} C_f = \left[f_{yy} - K\left(3f_y f_{yy} + Sf_{yy\tau} - ff_{yyy}\right)\right]_{y=0}. \tag{9.12}$$

The solution of Eqs. (9.7)-(9.9) subject to boundary conditions (9.10) and (9.11) is computed using HAM. The method is already explained in the previous chapters. Therefore we shall not described it here and proceed only with graphical results and discussion in the next section.

9.3 Convergence of the HAM Solution

In order to locate the convergence region, the $\hbar$-curves are plotted in **Fig. 9.1(a-c)** for a particular set of involved parameters. From these figures it clear that for this choice of parameter values a convergent solution can be obtained when $-1.3 \leq \hbar_f < -0.3$, $\leq -1.4 \leq \hbar_\theta < 0.2$ and $-2 \leq \hbar_\phi < -0.2$.

9.4 Results and discussion

The dimensionless nonlinear partial differential equations (9.7)-(9.9) are solved analytically using homotopy analysis method. **Fig. 9.2** presents the effects of the viscoelastic parameter K, Hartmann number M and ratio of oscillation frequency to stretching sheet S on velocity as function of time from a fix distance $y = 0.25$, respectively. **Fig. 9.2(a)** demonstrates the influence of viscoelastic parameter K on velocity f'. The amplitude of velocity shows a decreasing trend with increase of K. **Fig. 9.2(b)** elucidates the behavior of Hartmann number M f' by keeping other physical parameters fixed. Here suppression in velocity amplitude is observed which is due to the fact that the magnetic field introduces a retarding force known as Lorentz force which acts as a resistance to the flow.

Figs. 9.3(a-c) are prepared to see the effects of K, M and S on f' when $\tau = 0.5\pi$. The study reveals that the dimensionless velocity profile f' decreases by increasing the viscoelastic parameter K. **Fig. 9.3(b)** shows that an increase in Hartmann number reduces the velocity and consequently the thickness of momentum boundary layer also reduces. **Fig. 9.3(c)** exhibits similar effects as observed in **Fig. 9.3(b)**. **Fig. 9.4(a)** shows the physical impact of Prandtl number Pr on temperature field θ while **Fig. 9.4(b)** illustrates the variation of concentration profile with Prandtl number. It is observed that temperature inside the thermal boundary layer decreases with increasing Pr. This can be justified physically because an increase in Prandtl number Pr is due to increase of momentum diffusivity and decrease of thermal diffusivity. This decrease in thermal diffusivity is responsible for decrease in the temperature. The effects of Pr

on ϕ are marginal. The influence of K on temperature and concentration fields is disdplayed in **Figs. 9.5**. **Fig. 9.5(a)**. illustrates the influence of viscoelastic parameter K on the dimensionless temperature θ. It is noted that an increase in viscoelastic parameter K results in an increase in the temperature because viscoelastic normal stress results in thickening of the thermal boundary layer. The concentration field also seems to increase with increasing viscoelastic parameter K **(Fig. 9.5(b))**.

In order to see the impact of Hartmann number on temperature and concentration profiles, **Fig. 9.6** is plotted. It is observed that temperature increases with increasing values of Hartmann number M. **Fig. 9.6(b)** shows that increase in concentration by increasing Hartmann number is smaller in comparison with corresponding increase in the temperature. **Fig. 9.7(a)** presents the temperature profile for different values of thermophoresis parameter Nt. It is clearly seen from this figure that the temperature increases with increasing the value of thermophoresis parameter Nt. Similar results are observed in **Fig. 9.7(b)** where it is found that the concentration increases by increasing thermophoresis parameter Nt.

The effects of Brownian parameter Nb on temperature and concentration fields are portrayed in **Figs. 9.8(a)** and **9.8(b)**, respectively. These figures elucidate that the Brownian parameter Nb is responsible for increase in the fluid temperature. However, concentration profile follow a reverse trend with increasing the Brownian parameter Nb.

Fig. 9.9(a) illustrates the effects of thermal Biot number γ_1 on the temperature θ. This figure predicts an increase in the temperature by increasing γ_1. This is expected because the expression of thermal Biot number depends upon heat transfer coefficient h, so higher values of Biot number means greater rate of heat transfer from wall to the fluid. The concentration profile also increases with increase of the concentration Biot number γ_2 **(Fig. 9.9(b))**.

In **Fig. 9.10(a),** variation of the temperature profiles for various values of heat source/sink parameter δ. From this figure, it is noted that the temperature increases by increasing δ. It is expected because more heat is added to the system with increasing the strength of the heat source which results in the rise of the fluid temperature and the thermal boundary layer thickness. **Fig. 9.10(b)** depicts the effects of Schmidt number on the concentration ϕ. The concentration boundary layer thickness decreases by increasing Schmidt number.

Fig. 9.11(a-c) shows the transverse distribution of the velocity, temperature and concentration profiles at different time instants. It is found that the velocity oscillates periodically between -1 to 1, because in present study the sheet is assumed to be oscillatory. Moreover, the boundary layer thickness is found to increase in the time interval $[\pi/2, 3\pi/2]$. On contrary, a decrease in the temperature and concentration is found as time increases from $\pi/6$ to $2\pi/3$.

Fig. 9.12(a-b) is sketched to discuss the effects of Hartmann number M and viscoelastic parameter K on the time-series of the shear stress at the wall $\mathrm{Re}_x^{1/2} C_f$. From these figures we observe that the skin friction coefficient shows oscillatory behavior with time and its amplitude increases monotonically for larger values of M and viscoelastic parameter K. **Fig. 9.13(a) is** sketched to discuss the effect of Prandtl number Pr on local Nusselt number $\mathrm{Re}_x^{1/2} Nu_x$. From this figure we observe that amplitude of the Nusselt number increases by increasing Prandtl number. The response of local Sherwood number $\mathrm{Re}_x^{1/2} Sh$ with time for various values of Schmidt number is shown in **Fig. 9.13(b)**. It is observed that the local Sherwood number oscillates periodically with time and its amplitude increases for larger values of Schmidt number Sc.

9.5 Summary

In present chapter, we have discussed unsteady boundary layer flow of Walters' B fluid in presence of nanoparticles by using HAM. From the obtained results it is observed that the boundary layer thickness decreases by increasing viscoelastic parameter, ratio of oscillating frequency to stretching rate and Hartmann number. Further, it is found that the temperature profile is increasing functions of thermal Biot number, Hartmann number, Brownian force parameter, thermophoresis parameter and heat source parameter. Increase in Schmidt number and Brownian force parameter leads to decrease the concentration profile. The effect of Prandtl number on the concentration profile is marginal. The amplitude of the wall shear stress increases by increasing viscoelastic parameter and Hartmann number.

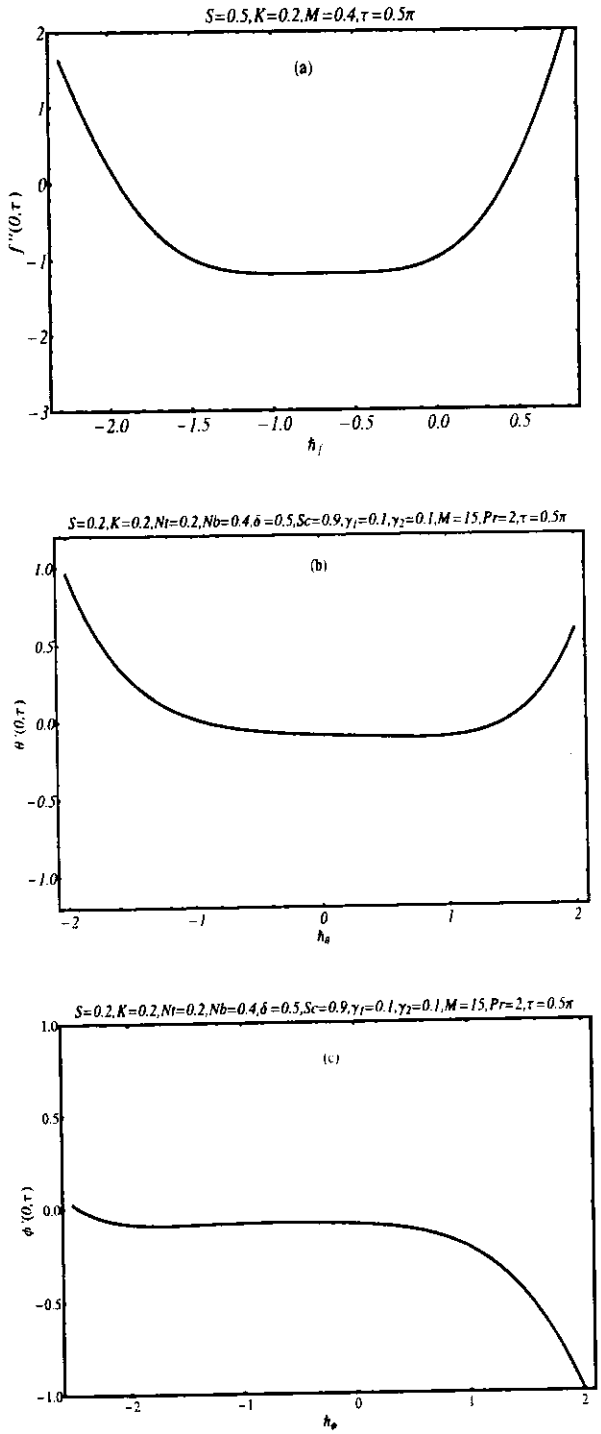

Fig. 9.1: $\hbar$-curves for (a) velocity (b) temperature and (c) concentration profiles.

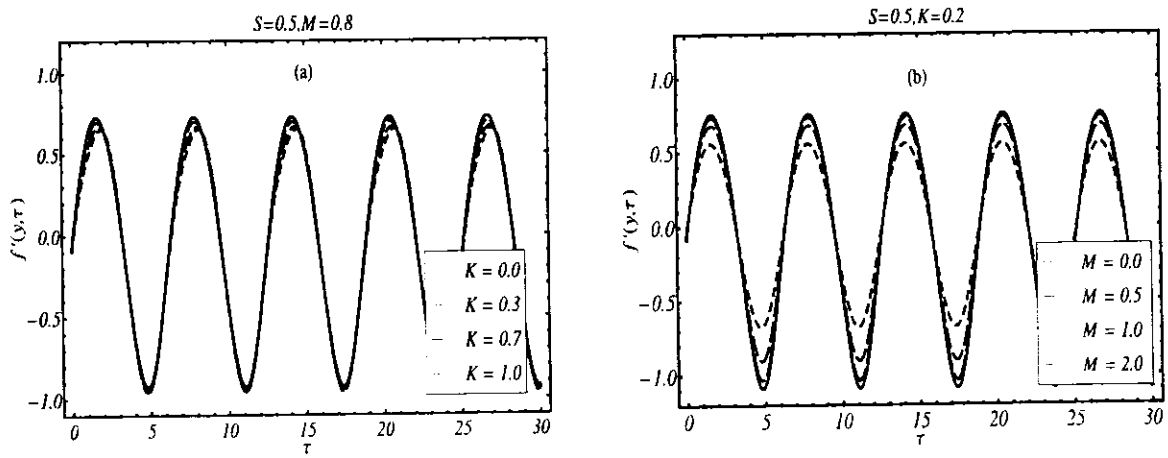

Fig. 9.2 Velocity as a function of time of (a) effects of K (b) effects of M.

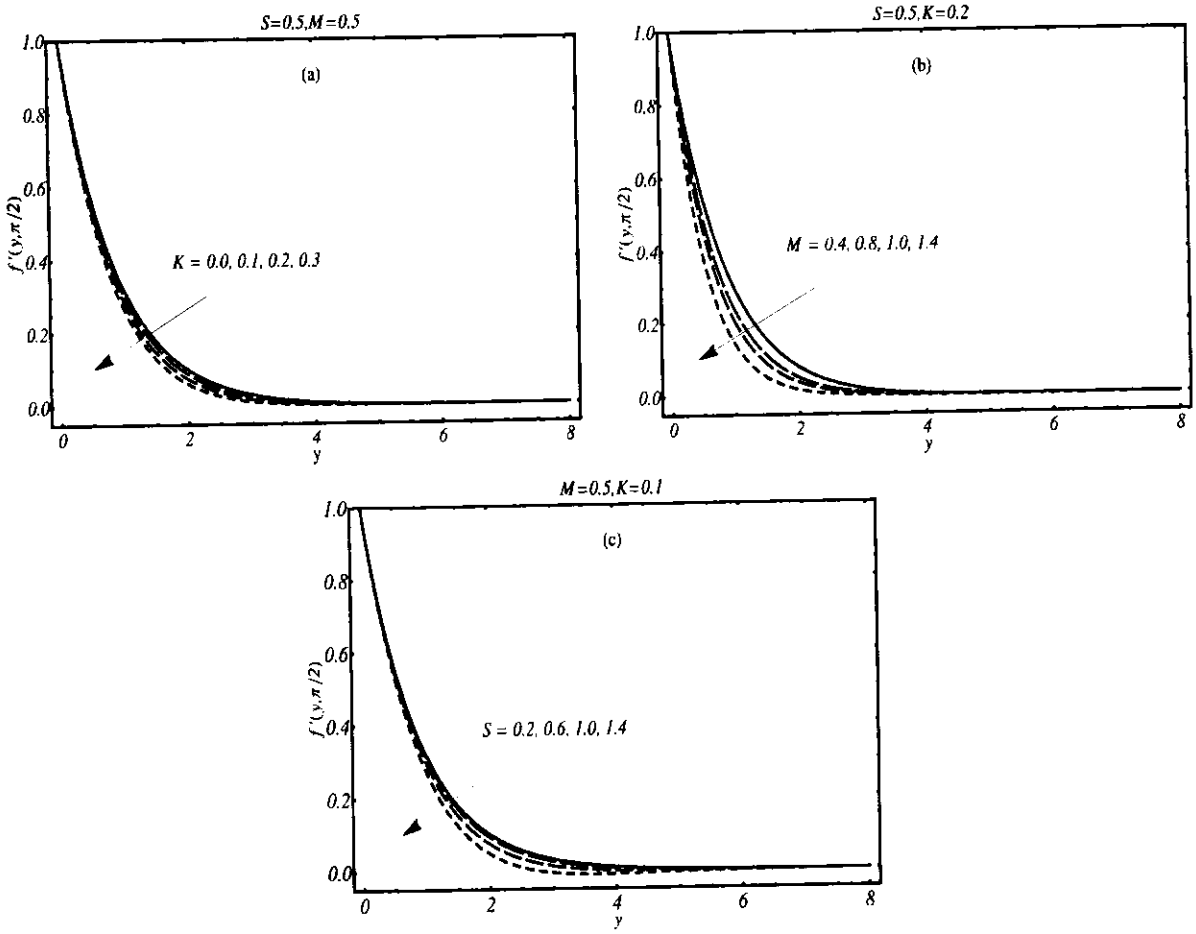

Fig. 9.3: The response of velocity with increasing (a) K (b) M c) S.

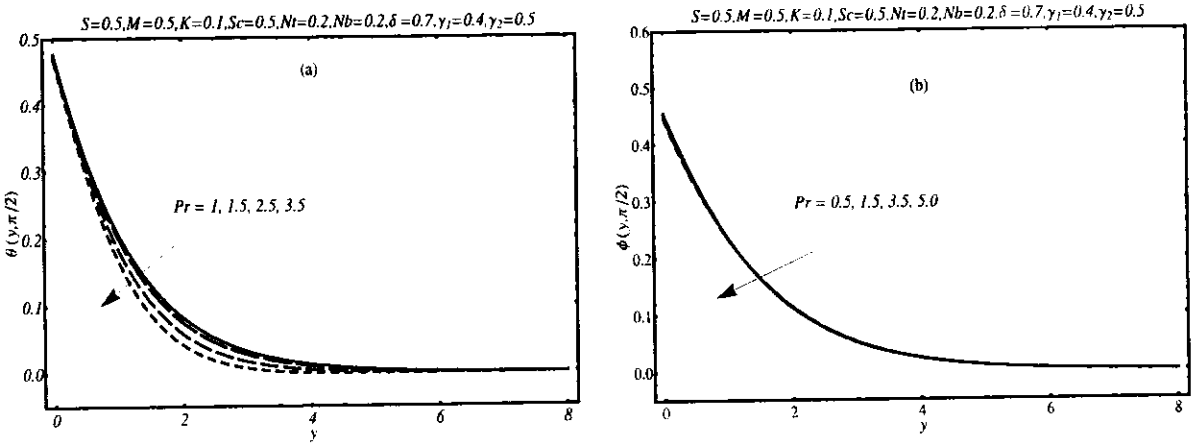

Fig. 9.4: The effects of Pr on (a) temperature profile (b) concentration profile.

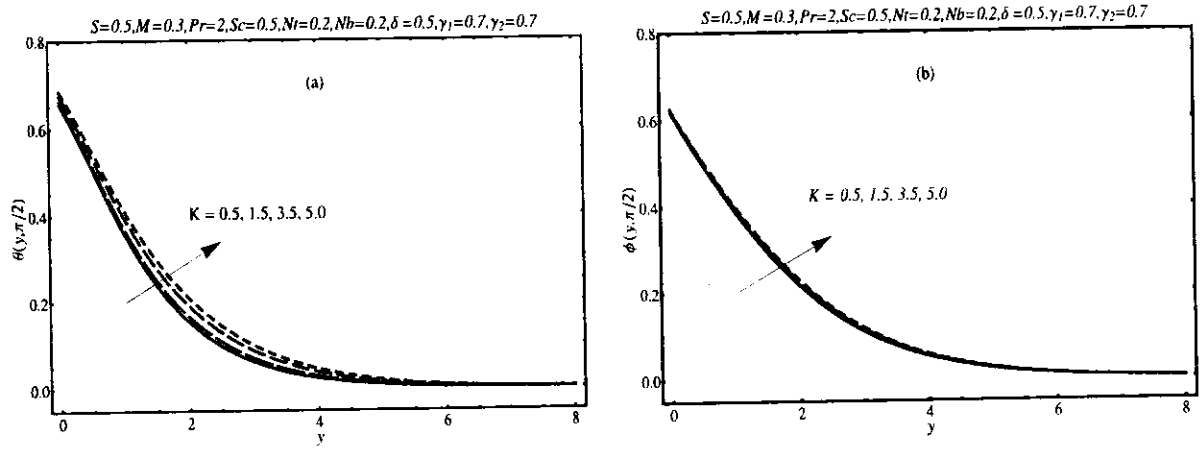

Fig. 9.5: The influence of K for (a) temperature profile (b) concentration profile.

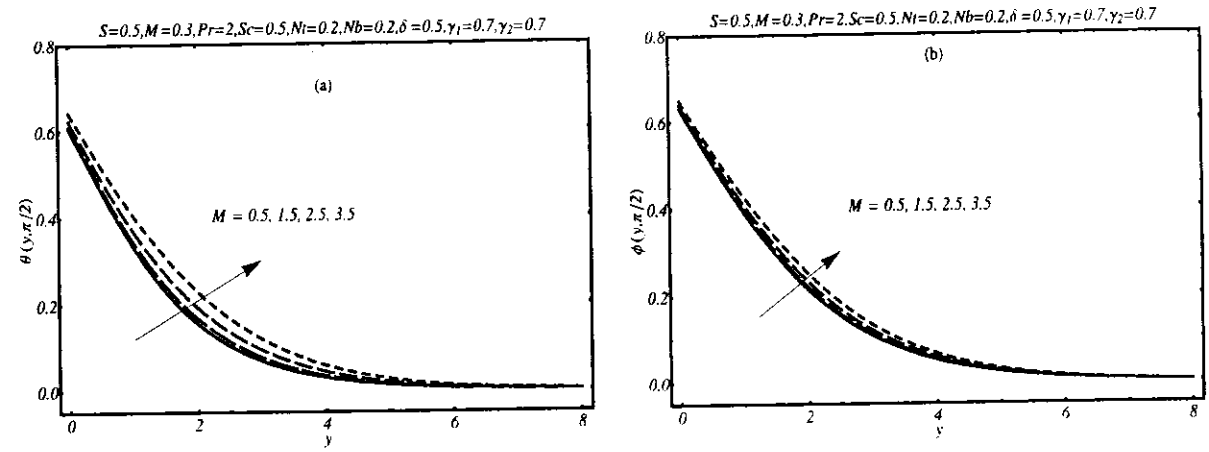

Fig. 9.6: (a) Temperature profile (b) concentration profile for different values of M.

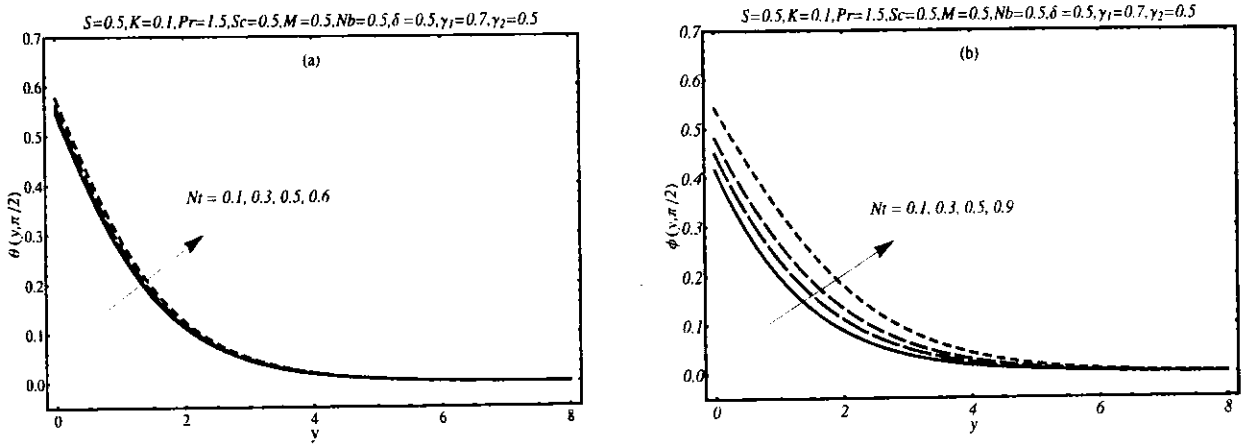

Fig. 9.7: (a) Temperature profile (b) concentration profile for different values of Nt.

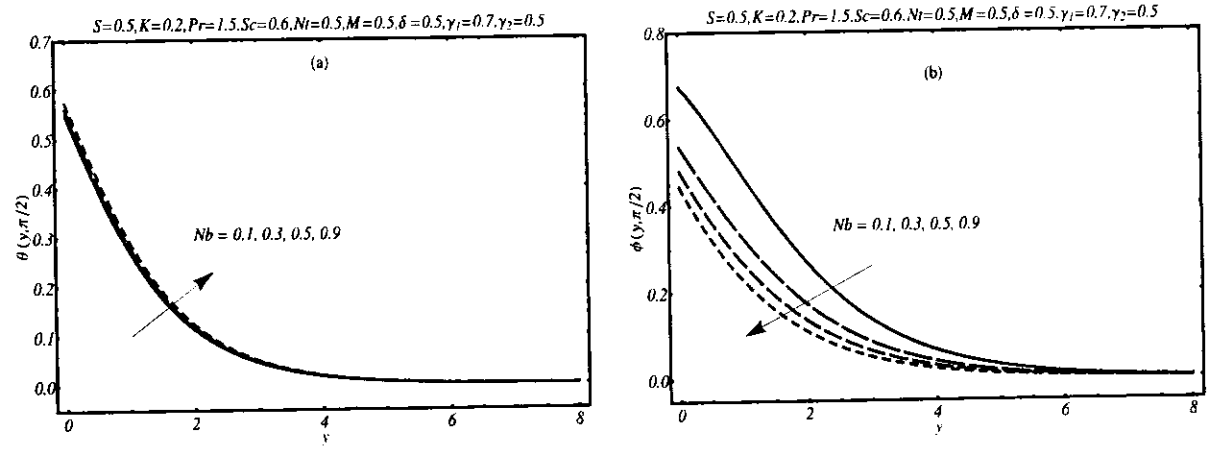

Fig. 9.8: (a) Temperature profile (b) concentration profile for different values of Nb.

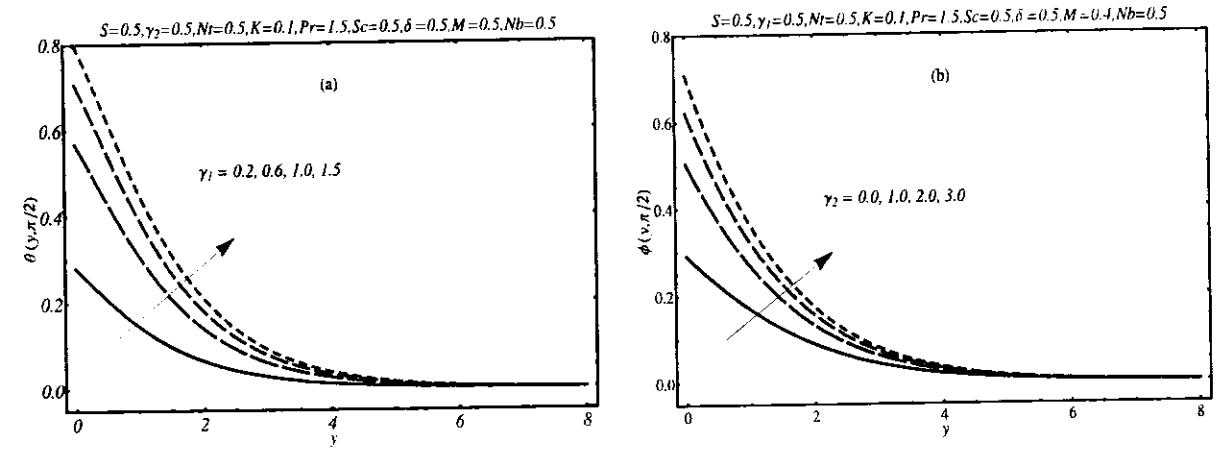

Fig. 9.9: Effects of γ_1 on temperature profile (b) effects of γ_2 on concentration profile.

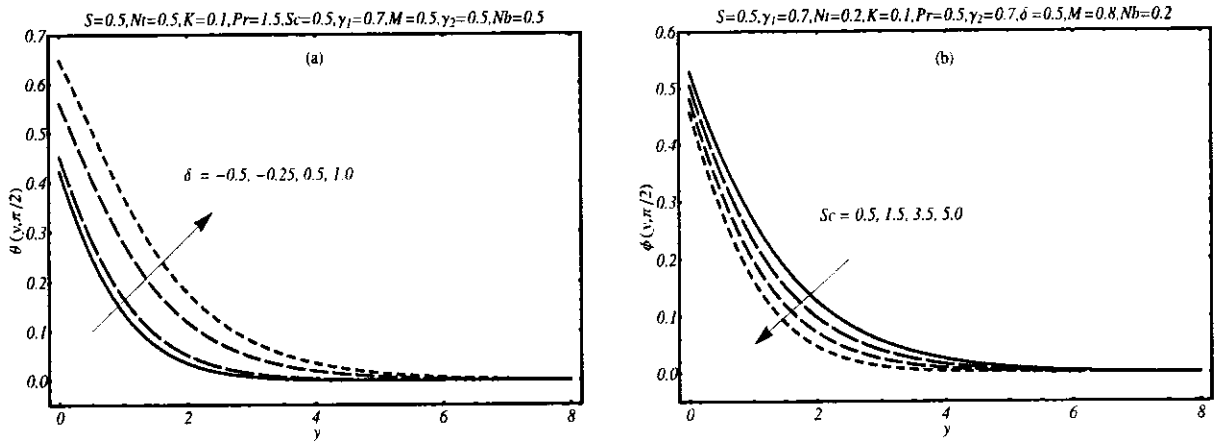

Fig. 9.10: Effects of δ on temperature profile (b) effects of Sc on concentration.

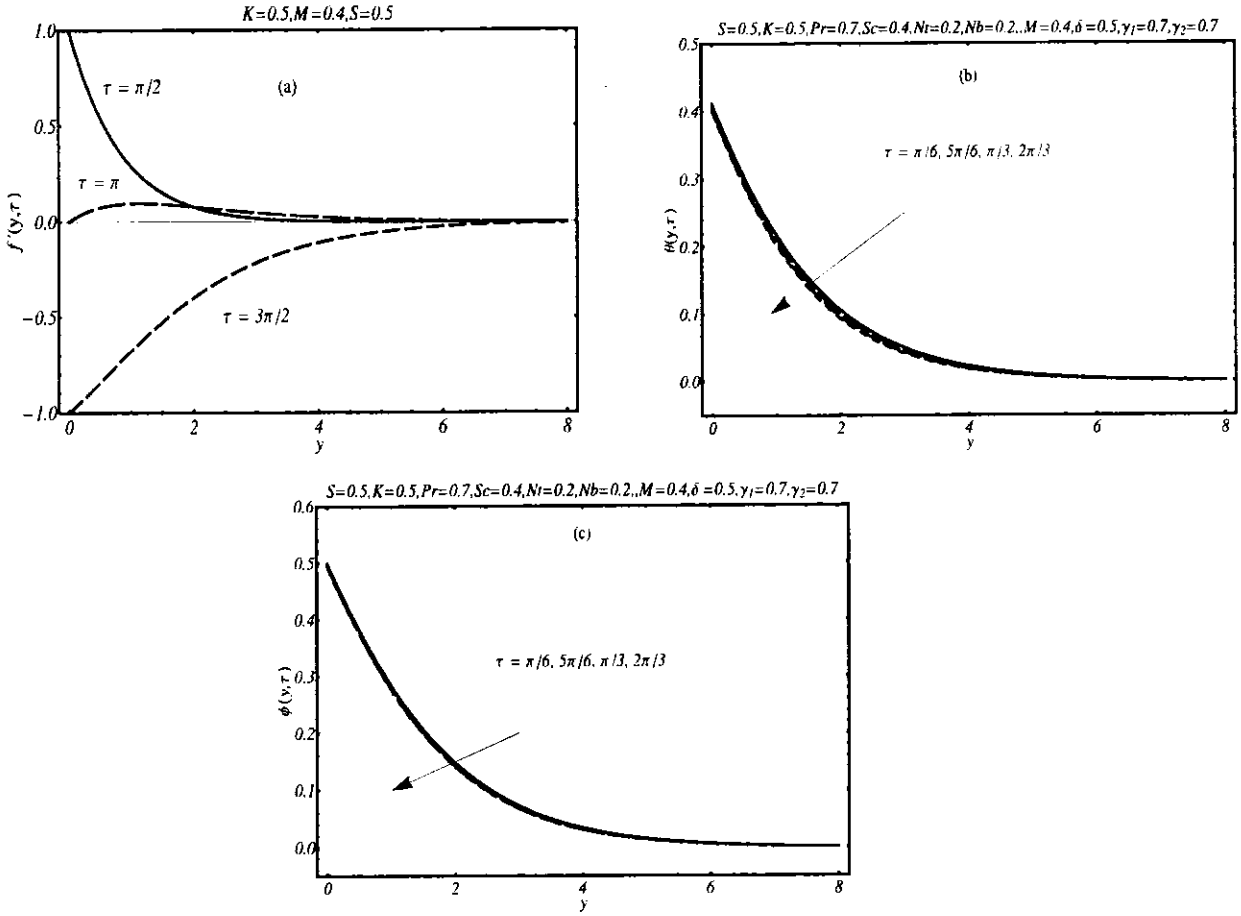

Fig. 9.11: Effects of increasing time on (a) velocity profile (b) temperature profile (c) concentration profile.

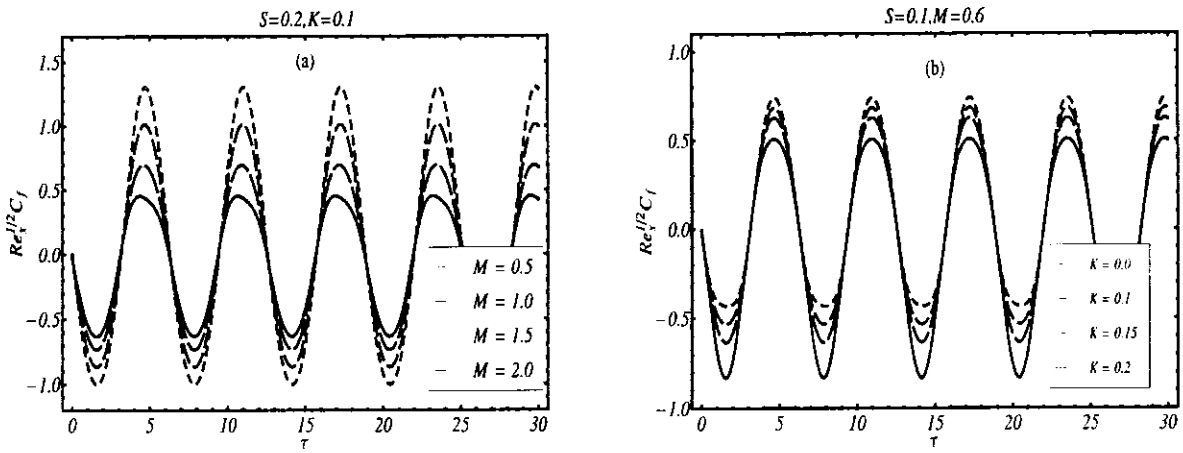

Fig. 9.12: Skin friction as a function of time (a) effects of K (b) effects of M.

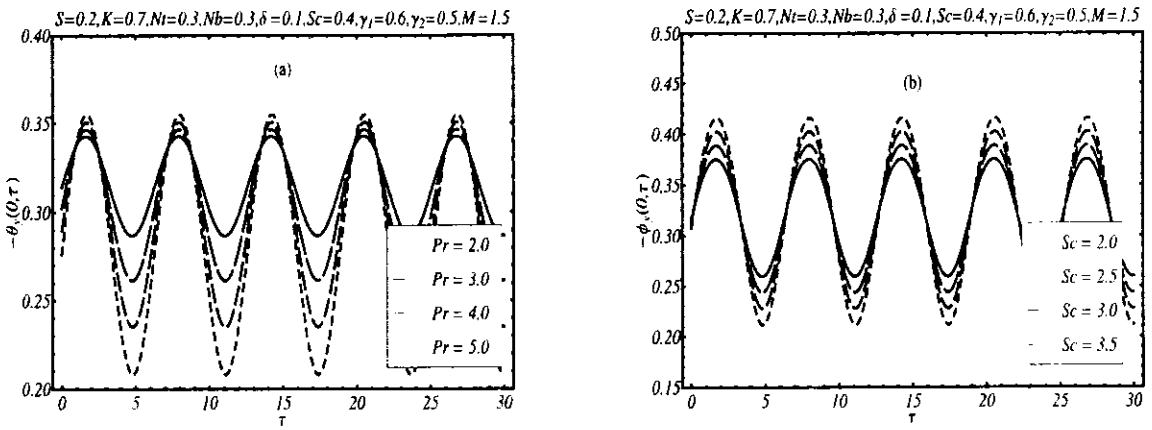

Fig. 9.13. (a) Nusselt number as a function of time for different values of (a) Pr (b) Sc.

Chapter 10

Heat transfer characteristics in oscillatory hydromagnetic channel flow of Maxwell fluid using Cattaneo-Christov model

This chapter presents the analysis of hydromagnetic flow and heat transfer of Maxwell fluid in channel with oscillatory stretching walls. Unlike typical heat transfer studies, here Cattaneo-Christov heat flux model is used. The transformed dimensionless nonlinear partial differential equations are solved by means of the homotopy analysis method (HAM). The convergent series solutions are utilized to discuss the main effects of emerging parameters on velocity and temperature. The obtained results illustrate that Hartmann and Deborah numbers suppress the velocity. However, an increase in ratio of oscillation frequency to stretching rate increases the velocity. A reverse flow occurs in the central region of the channel which is found to decrease by increasing Hartmann and Deborah numbers. Moreover, for the Cattaneo-Christov model fluid temperature inside the channel is less when compared with temperature obtained using heat flux based on Fourier's law.

10.1 Flow Analysis

Consider two-dimensional, unsteady flow of a Maxwell fluid between two oscillatory stretching sheets in planes $y=\pm h$. The flow geometry is displayed in **Fig. 10.1**. The sheets are stretched along x -axis with velocity $u=bxe^{i\omega t}$. A constant magnetic field B_0 is imposed in $y-$ direction. Based on low magnetic Reynolds number assumption, the effects of induced magnetic field are neglected. The continuity equation for flow is defined in Eq. (2.1). The governing boundary layer equations for two-dimensional Maxwell fluid are

$$\frac{\partial u}{\partial t}+u\frac{\partial u}{\partial x}+v\frac{\partial u}{\partial y}=\nu\frac{\partial^2 u}{\partial y^2}-\lambda_1\left(\begin{array}{l}\dfrac{\partial^2 u}{\partial t^2}+2\left(u\dfrac{\partial^2 u}{\partial x\partial t}+v\dfrac{\partial^2 u}{\partial y\partial t}\right)+u^2\dfrac{\partial^2 u}{\partial x^2}\\ +2uv\dfrac{\partial^2 u}{\partial x\partial y}+v^2\dfrac{\partial^2 u}{\partial y^2}\end{array}\right)-\frac{\sigma B_0^2}{\rho}\left(u+\lambda_1 v\frac{\partial u}{\partial y}+\lambda_1\frac{\partial u}{\partial t}\right). \quad (10.1)$$

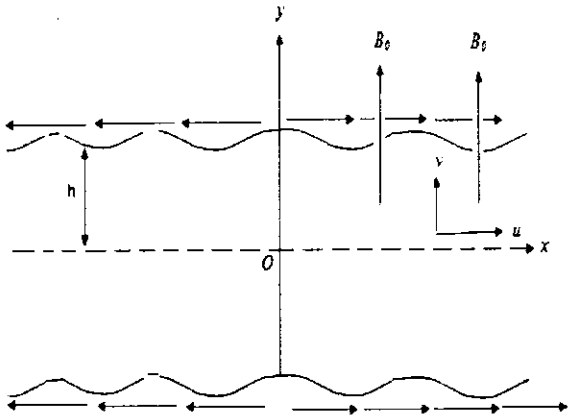

Fig. 10.1: Geometry of problem

The flow problem is subjected to the following boundary conditions [106]

$$u = u_w = bxe^{i\omega t}, \quad v = 0, \quad \text{at} \quad y = h, \; t > 0, \tag{10.2}$$

$$\frac{\partial u}{\partial y} = 0, \quad v = 0, \quad \text{at} \quad y = 0. \tag{10.3}$$

10.2 Heat Transfer Analysis

In present study, we discuss the effects of heat transfer using Cattaneo-Christov heat flux model [57]. According to this model the heat flux and temperature gradient are related through following expression

$$\mathbf{q} + \lambda_2 \left[\frac{\partial \mathbf{q}}{\partial t} + \mathbf{V}.\nabla \mathbf{q} - \mathbf{q}.\nabla \mathbf{V} + (\nabla.\mathbf{V})\mathbf{q} \right] = -k_1 \nabla T, \tag{10.4}$$

where $\mathbf{q}$ is heat flux, λ_2 the relaxation time of the heat flux, T is the Maxwell fluid temperature and k_1 is the thermal conductivity. It is clear that when $\lambda_2 = 0$, above equation represents the well known Fourier's law. For incompressible fluid $\nabla.\mathbf{V} = \mathbf{0}$ and Eq. (10.4) reduce to

$$\mathbf{q} + \lambda_2 \left[\frac{\partial \mathbf{q}}{\partial t} + \mathbf{V}.\nabla \mathbf{q} - \mathbf{q}.\nabla \mathbf{V} \right] = -k_1 \nabla T. \tag{10.5}$$

The energy equation for incompressible fluid in the absence of viscous dissipation effects is

$$\rho c_p \left[\frac{\partial T}{\partial t} + \mathbf{V}.\nabla T \right] = -\nabla.\mathbf{q}. \tag{10.6}$$

Elimination of $\mathbf{q}$ from (10.5) and (10.6) yields to the following single equation for the

temperature field

$$\frac{\partial T}{\partial t}+u\frac{\partial T}{\partial x}+v\frac{\partial T}{\partial y}+\lambda_2\left(\begin{array}{l}\dfrac{\partial^2 T}{\partial t^2}+2u\dfrac{\partial^2 T}{\partial x\partial t}+2v\dfrac{\partial^2 T}{\partial y\partial t}+\dfrac{\partial v}{\partial t}\dfrac{\partial T}{\partial y}+u\dfrac{\partial u}{\partial x}\dfrac{\partial T}{\partial x}+v\dfrac{\partial v}{\partial y}\dfrac{\partial T}{\partial y}\\ +u\dfrac{\partial v}{\partial x}\dfrac{\partial T}{\partial y}+v\dfrac{\partial u}{\partial y}\dfrac{\partial T}{\partial x}+2uv\dfrac{\partial^2 T}{\partial x\partial y}+u^2\dfrac{\partial^2 T}{\partial x^2}+v^2\dfrac{\partial^2 T}{\partial y^2}\end{array}\right)=\alpha\frac{\partial^2 T}{\partial y^2}, \quad (10.7)$$

The imposed boundary conditions are

$$T=T_w \qquad y=h, \quad t>0, \quad \frac{\partial T}{\partial y}=0 \quad \text{at} \quad y=0. \quad (10.8)$$

10.3 Dimensionless formulation

Eqs. (10.1) and (10.7) can be written in the terms of dimensionless variables by defining [106]

$$x^*=\frac{x}{h}, \qquad \zeta=\frac{y}{h}, \qquad u^*=\frac{u}{hb}, \qquad v^*=\frac{v}{hb}, \qquad \tau=t\omega. \quad (10.9)$$

The transformed equations in new variable can further be reduced through following equations

$$u^*=x^*e^{i\omega t}f'(\zeta), \qquad v^*=-e^{i\omega t}f(\zeta), \qquad \theta(\zeta,\tau)=\frac{T}{T_w}. \quad (10.10)$$

It is pointed out that in view of (10.9) the continuity equation is identically satisfied and Eqs. (10.2) and (10.8) takes the following forms

$$\begin{aligned}&\frac{\partial^3 f}{\partial\zeta^3}-De\left[-S^2\frac{\partial f}{\partial\zeta}-2S(Sin\tau)\left(\left(\frac{\partial f}{\partial\zeta}\right)^2-f\frac{\partial^2 f}{\partial\zeta^2}\right)+Cos2\tau\left(f^2\frac{\partial^3 f}{\partial\zeta^3}-2f\frac{\partial f}{\partial\zeta}\frac{\partial^2 f}{\partial\zeta^2}\right)\right]\\ &+Cos\tau\left[f\frac{\partial^2 f}{\partial\zeta^2}-\left(\frac{\partial f}{\partial\zeta}\right)^2\right]-M^2\left(\frac{\partial f}{\partial\zeta}-De(Cos\tau)f\frac{\partial^2 f}{\partial\zeta^2}\right)=0,\end{aligned} \quad (10.11)$$

$$\frac{1}{\Pr}\frac{\partial^2\theta}{\partial\zeta^2}-S\frac{\partial\theta}{\partial\tau}+Cos\tau f\frac{\partial\theta}{\partial\zeta}-\gamma^*\left[\begin{array}{l}S^2\dfrac{\partial^2\theta}{\partial\tau^2}-2SCos\tau f\dfrac{\partial^2\theta}{\partial\varpi\zeta}+S(Sin\tau)f\dfrac{\partial\theta}{\partial\zeta}\\ +Cos2\tau\left(f\dfrac{\partial f}{\partial\zeta}\dfrac{\partial\theta}{\partial\zeta}+f^2\dfrac{\partial^2\theta}{\partial\zeta^2}\right)\end{array}\right]=0. \quad (10.12)$$

The boundary conditions of problem under consideration reduce to

$$\frac{\partial f}{\partial\zeta}=1, f(\zeta)=0, \quad \theta(\zeta)=1 \ \ at \ \ \zeta=1, \quad (10.13)$$

$$\frac{\partial^2 f}{\partial \zeta^2} = f(\zeta) = 0, \ \frac{\partial \theta}{\partial \zeta} = 0 \ \ at \ \zeta = 0. \tag{10.14}$$

where $De = \lambda_1 b$ is the Deborah number and $\gamma^* = \lambda_2 b$ is the dimensionless relaxation time of heat flux.

10.4 Homotopy analysis method

To discuss the influence of emerging parameters appearing in Eq. (10.11) and (10.12), we have solved the set of these nonlinear differential equations analytically by means of homotopy analysis method. The procedure of HAM is same as described in the previous chapters therefore it would be redundant to reproduce it here.

10.5 Results and discussion

The solution obtained by HAM contains the convergence-contral parameters $\hbar_f$ and $\hbar_\theta$. In the present case the convergence region is identified by plotting the so-called $\hbar$ -curves in **Figs. 10.2** and **10.3**. It is found that the plausible values of $\hbar_f$ and $\hbar_\theta$ must be in the range $-2 \le \hbar_f < 0$ and $-2 \le \hbar_\theta < 0$, respectively. The values of $\hbar_f$ and $\hbar_\theta$ in subsequent figures are also chosen through a similar methodology.

Once convergence of the solution is guaranteed, the next step is to examine the effects of Hartmann number M, ratio parameter S, Deborah number De, dimensionless relaxation time of the heat flux γ and Prandtl number Pr on transverse velocity component $f(\zeta)$, longitudinal velocity component $f'(\zeta)$ and temperature $\theta(\zeta)$. For this purpose, **Figs. 10.4-10.14** have been plotted. **Fig. 10.4** shows that the effects of M on the transverse velocity $f(\zeta)$. Here, velocity component $f(\zeta)$ decreases with the increase of Hartmann number M. **Fig. 10.5** reflects the influence of Hartmann number M on longitudinal component $f'(\zeta)$ of the velocity. The flow region can be divided into two parts on the basis of behavior of the velocity component $f'(\zeta)$. For $0 \le \zeta \le 0.5$ the magnitude of $f'(\zeta)$ shows decreasing trend by increasing M while for $0.5 < \zeta < 1$ the opposite trend is observed. The negative values of $f'(\zeta)$ in the region

$0 \le \zeta < 0.5$ are the indicator of the flow reversal. It is also observed from **Fig. 10.5** that flow reversal decreases by increasing M. Moreover, the vertical location ζ_c at which the velocity component $f'(\zeta)$ becomes zero shifts towards the channel wall by increasing M. The graph illustrating the effects of De on transverse component of the velocity $f(\zeta)$ is shown in **Fig. 10.6**. A decrease in magnitude of $f(\zeta)$ is observed by increasing the Deborah number. The longitudinal component of the velocity shows similar behavior by increasing De as observed by increasing M. However, the ratio parameter S affects the transverse and the longitudinal velocity components in a manner different from De and M. In fact the magnitude of the transverse component of velocity is enhanced by increasing S (**Fig. 10.8**). Moreover, the flow reversal increases by increasing S (**Fig. 10.9**). It is evident from **Fig. 10.9** that ζ_c shifts away from the boundary by increasing S. The effects of Pr on $\theta(\zeta)$ are shown in **Fig. 10.10**. As expected, the temperature inside the channel decreases by increasing Prandtl number. Fig. **10.11** reveals that temperature inside the channel is an increasing function of Hartmann number M. The effects of dimensionless relaxation time of heat flux γ^* are illustrated in **Fig. 10.12**. The curve $\gamma^* = 0$ in **Fig. 10.12** represents the temperature profile inside the channel obtained on the basis of Fourier law. It is interesting to note that temperature decreases by increasing γ^*. **Fig. 10.13** depicts an increase in temperature by increasing Deborah number De. **Fig. 10.14** shows the plots of $\theta(\zeta)$ for various values of S. It is noted that the effects of ratio parameter S on $\theta(\zeta)$ are similar to the effects of γ^* and Pr.

10.6 Concluding remarks

In this chapter Cattaneo-Christov heat flux model is used to analyze the heat transfer characteristics of unsteady flow of Maxwell fluid in a channel with oscillatory walls. The nonlinear differential equations are solved analytically by homotopy analysis method. The main points of analysis are summarized as:

- The effects of Deborah number De and Hartmann number M are similar on the longitudinal velocity component are similar.

- The reversal flow take place near the central line of the channel which is found to increase by increasing ratio parameter. However, it is suppressed by increasing Hartmann number M and Deborah number De.
- The temperature decreases by increasing Prandtl number $\Pr$ while it increases by increasing Hartmann number M and ratio parameter S.
- The values of temprature inside the channel obtained by Fourier law are in excess of those predicted by Cattaneo-Christov heat flux model.

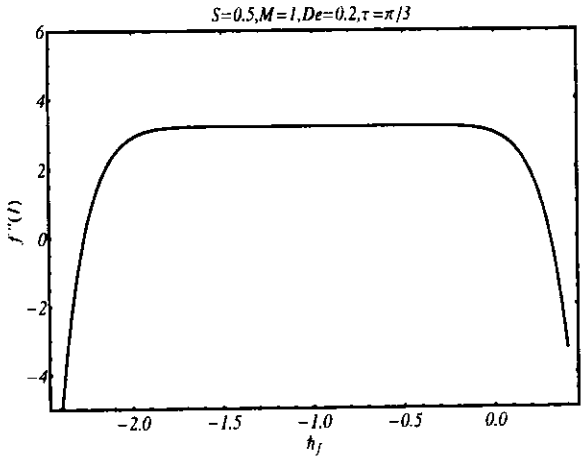

Fig. 10.2: $\hbar$-curve for velocity profile.

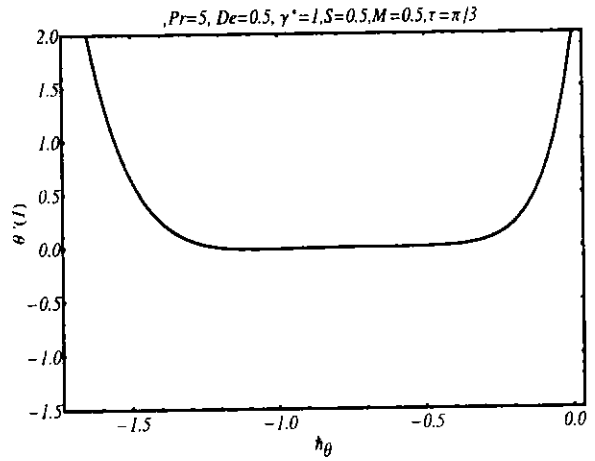

Fig. 10.3: $\hbar$-curve for temperature profile.

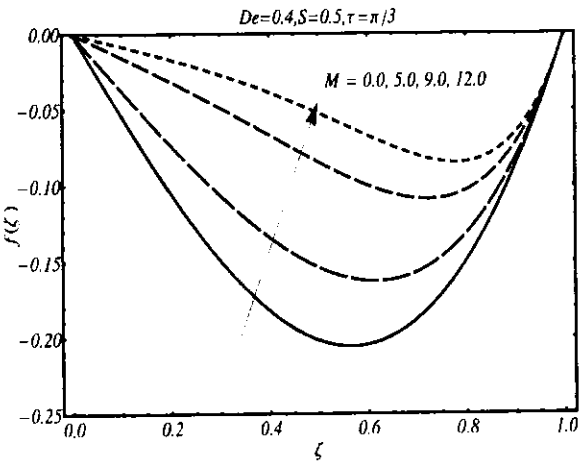

Fig. 10.4: The effects of M on f.

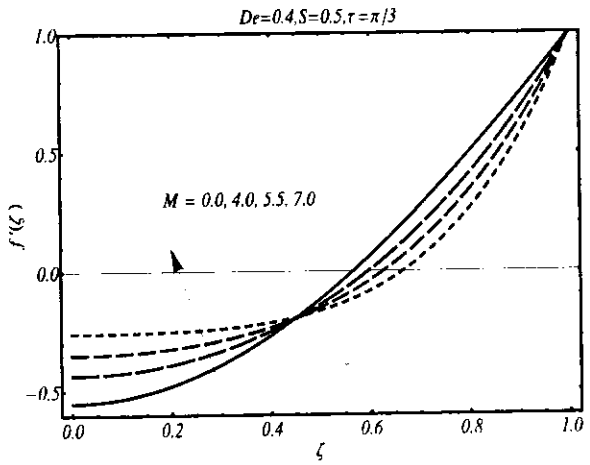

Fig. 10.5: The effects of M on f'.

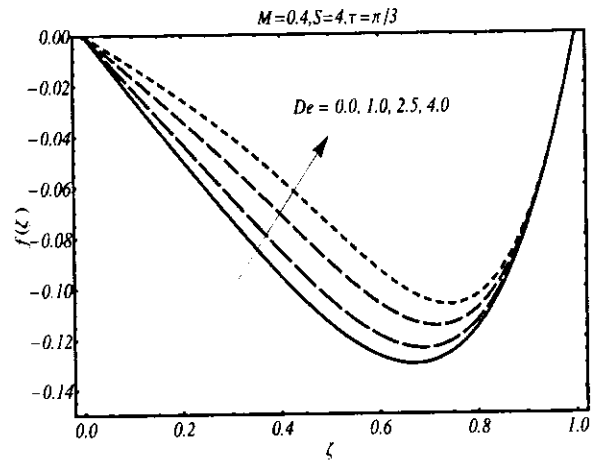

Fig. 10.6: The effects of De on f.

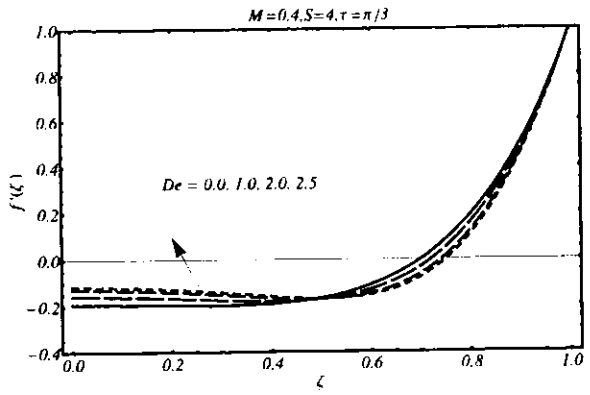

Fig. 10.7: The effects of De on f'.

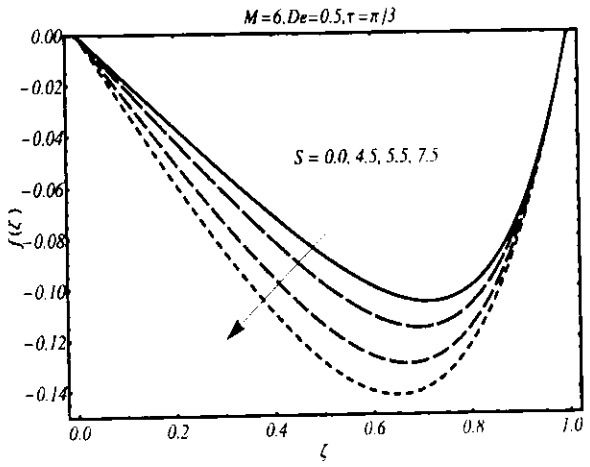

Fig. 10.8: The effects of S on f.

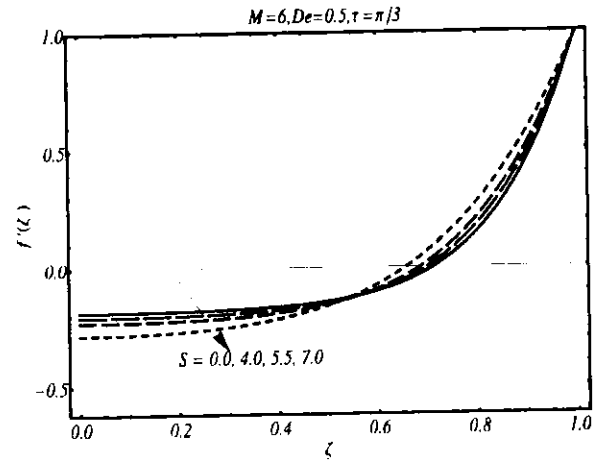

Fig. 10.9: The effects of S on f'.

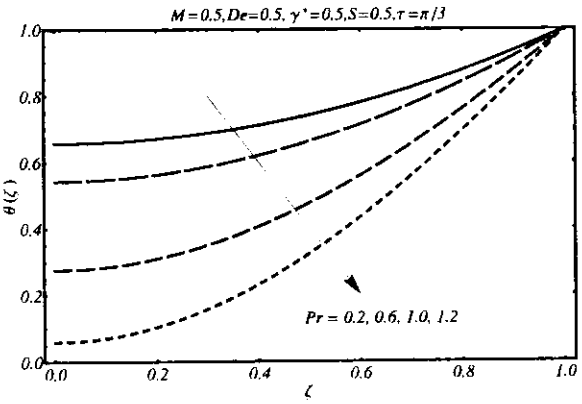

Fig. 10.10: The effects of Pr on temperature θ.

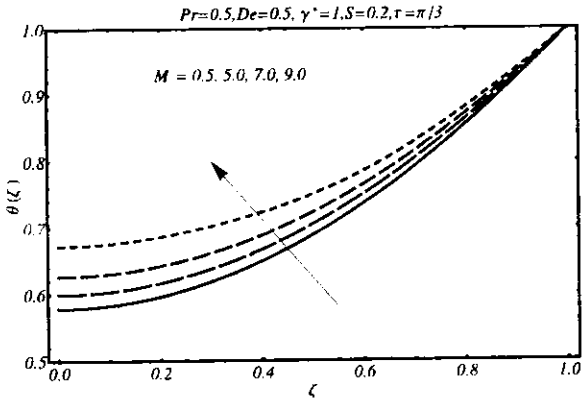

Fig. 10.11: The effects of M on temperature θ.

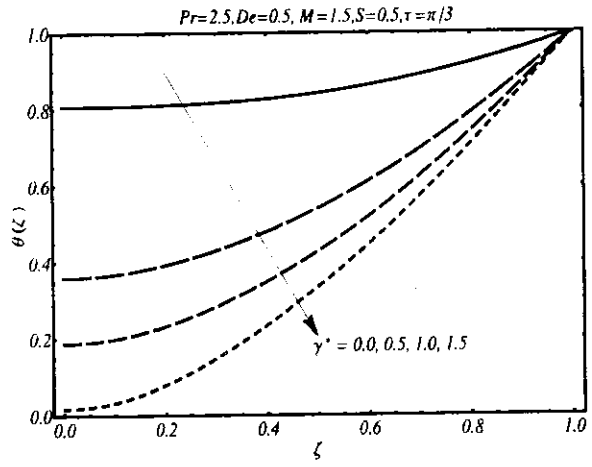

Fig. 10.12: The effects of γ^* on temperature θ.

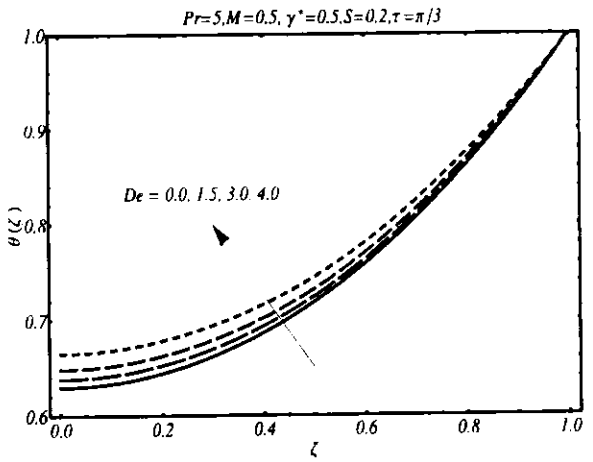

Fig. 10.13: The effects of De on temperature θ.

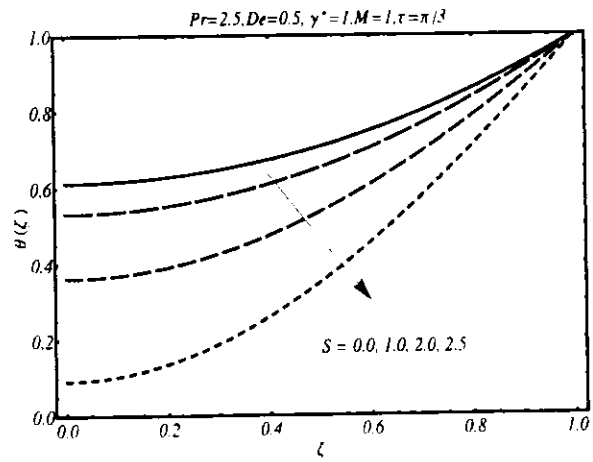

Fig. 10.14: The effects of S on temperature θ.

References

[1] K.R. Rajagopal, T Y Na, and A.S. Gupta, Flow of viscoelastic fluid over stretching sheet, Rheol. Acta, 23 **(1984)** 213-215.

[2] F. Talay Akyildiz, Hamid Bellou and K. Vajravelu, Exact solutions of nonlinear differential equations arising in third grade fluid flows, Int. J. Nonlinear Mech., 39 **(2004)** 1571–1578.

[3] T. Hayat and N. Ali, Peristaltic motion of a Jeffrey fluid under the effect of a magnetic field in a tube, Commun. Nonlinear Sci. Numer. Simul. 13 **(2008)** 1343–1352.

[4] N. Ali, T. Hayat and S. Asghar, Peristaltic flow of a Maxwell fluid in a channel with compliant walls, Chaos Soliton Fract. 39 **(2009)** 407–416.

[5] R. E. Powell and H. Eyring, Mechanisms for the relaxation theory of viscosity, Nature, 154, **(1944)** 427–428.

[6] C. Fetecau, C. Fetecau, M. Khan and D. Vieru, Decay of potential vortex in a generalized Oldroyd-B fluid. Appl. Math. Comput. 205 **(2008)** 497–506.

[7] R. K. Dash, K. N. Mehta and G. Jayaraman, Casson fluid flow in a pipe filled with a homogeneous porous medium. Int.J. Eng. Sci., 34(10) **(1996)** 1145–1156.

[8] R. V. Williamson, The flow of pseudoplastic materials. Int. Eng. Chem. Res., 21, **(1929)** 1108.

[9] W. R. Schowalter, The application of boundary-layer theory to power-law pseudoplastic fluids: Similar solutions. AICHE J 6 **(1960)** 24-28.

[10] A. M. Siddiqui, A. R. Ansari, A. Ahmad and N. Ahmad, On Taylor's scraping problem and flow of a Sisko fluid, Math. Model. Anal. 14 **(2009)** 515–529.

[11] H. Schlichting, Boundary Layer theory, McGraw-Hill, New York,**(1964).**

[12] H. Blasius, Grenzschiechten in flüssigkeiten mit kleiner reibung, Z. Angew. Math. Phys., 56 **(1908)** 1–37.

[13] B. C. Sakiadis, Boundary layer behavior on continuous solid surfaces: I boundary layer equations for two dimentional and axisymetric flow, AIChE J. 7 **(1961)** 26-28.

[14] B. C. Sakiadis , Boundary layer behavior on continuous solid surface. II boundary layer equations for two dimensional and axisymmetric flow, AIChE. J. 7 **(1961)** 221–225.

[15] L. J. Crane, Flow past a stretching plate. Z Angew Math Phys. (ZAMP), 21 **(1970)** 645-47

[16] C. Y. Wang, The three dimensional flow due to stretching surface, Phys. Fluids 27 **(1984)** 1915-1917.

[17] V. Rajeswari and G. Nath, Unsteady flow over a stretching surface in a rotating fluid, Int. J. Eng. Sci. 30 **(1992)** 747-756.

[18] P. D. Ariel, Axisymmetric flow of a second grade fluid past a stretching sheet. Int. J. Eng. Sci. 39, **(2001)** 529-553.

[19] M. Sajid and T. Hayat, Non-similar series solution for boundary layer flow of a third-order fluid over a stretching sheet, Appl. Math. Comput. 189(2) **(2007)** 1576-1585.

[20] T. R. Mahapatra, S. Dholey and A. S. Gupta, Oblique stagnation-point flow of an incompressible visco-elastic fluid towards a stretching surface, Int. J. Nonlinear Mech. 42 **(2007)** 484-499.

[21] T. Javed, N. Ali, Z. Abbas and M. Sajid, Flow of an Eyring-Powell non-Newtonian over a stretching sheet, Chem. Eng. Commun., 200, **(2012)** 327-336

[22] M. Sajid, Z. Abbas, T. Javed and N. Ali, Boundary layer flow of an Oldroyd-B fluid in the region of stagnation point over a stretching sheet, Can. J Phys., 88 **(2010)**, 9, pp. 635-640

[23] S. Nadeem, S. T. Hussain and C. Lee, Flow of a Williamson fluid over a stretching Sheet, Braz. J. Chem. Eng., 30, **(2013)**. 619-625.

[24] K. Bhattacharyya, T. Hayat and A. Alsaedi, Exact solution for boundary layer flow of Casson fluid over a permeable stretching/shrinking sheet, ZAMM. Angew. Math. Mech. 94, **(2014)** 522–528

[25] M. Awais, T. Hayat, A. Alsaedi and S. Asghar, Time-dependent three-dimensional boundary layer flow of a Maxwell Fluid, Comput. Fluids 91 **(2014)** 21–27.

[26] P. D. Ariel, MHD flow of a viscoelastic fluid past a stretching sheet with suction, ACTA MECH. 105 (1994) 49.

[27] H. I. Anderson, MHD flow of a viscoelastic fluid past a stretching surface, Acta Mech. 95 **(1992)** 227.

[28] M. Kumari and G. Nath, MHD boundary layer flow of non-Newtonian fluid over continuously moving surface with a parallel free stream, Acta Mech. 146, **(2001)** 138-150.

[29] T. Hayat, K. Hutter, S. Asghar and A. M. Siddiqui, MHD flows of an Oldroyd-B fluid Math Comput. Model, 36 **(2002)** 987-995

[30] N. F. M. Noor a, S. Awang Kechil and I. Hashim, Simple non-perturbative solution for MHD viscous flow due to a shrinking sheet, Commun Nonlinear Sci Numer Simulat 15 **(2010)** 144–148.

[31] S. S. Motsa, P. Sibanda, F.G. Awad and S. Shateyi, A new spectral-homotopy analysis method for the MHD Jeffery–Hamel problem, Comput. Fluids 39 **(2010)** 1219–1225.

[32] M. Sajid, T. Javed and T. Hayat, MHD rotating flow of a viscous fluid over a shrinking surface. NONLINEAR DYNAM, 51 **(2008)** 259–65.

[33] Y. Taamneh and R. Omari, Slip-flow and heat transfer in a porous microchannel saturated with Power-Law fluid, J. Fluids, 9 **(2013)**.

[34] D.S. Chauhan and R. Agrawal, MHD flow through a porous medium adjacent to a stretching sheet: Numerical and an approximate solution, Eur. Phys. J. Plus **(2011)** 126: 47.

[35] A. Ishak and R Nazar, Steady and unsteady boundary layers due to stretching vertical sheet in a porous medium using Darcy-Brinkman equation model, Int. J. App. Mech. Engineering 11(3) **(2006)** 623-637.

[36] V.Kumaran and Tamizharasi Brinkman Flow past a stretching sheet, Transport Porous Med., 87(2) **(2011)** 541-560.

[37] S. Nadeem , Rizwan Ul Haq, Noreen Sher Akbar, Z.H. Khan, MHD three-dimensional Casson fluid flow past a porous linearly stretching sheet, Alexandria Eng. J. 52 **(2013)** 577–582.

[38] M. Sajid, Z. Abbas, N. Ali and T. Javed, Stretching a surface having a layer of porous medium in a viscous fluid, Appl. Appl. Math.,7(2) **(2012)** 609-618.

[39] K. Vajravelu and D. Rollins, Heat transfer in a viscoelastic fluid over a stretching sheet, J. Math. Anal. Appl. 158 **(1991)** 241-255.

[40] A. M. Subhas and P. H. Veena, Visco-elastic fluid flow and heat transfer in a porous medium over a stretching sheet, Int. J. Nonlinear Mech.,33 **(1998)** 531.

[41] M. Massoudi and C. E. Maneschy, Numerical solution to the flow of a second grade fluid over a stretching sheet using the method of quasi-linearization, Appl. Math. Comput. 149 **(2004)** 165-173.

[42] R. Cortell, Flow and heat transfer of an electrically conducting fluid of second grade over a stretching sheet subject to suction and a transverse magnetic field, Int. J. Heat Mass Tran. 49 **(2006)** 1851-1856.

[43] M. S. Abel, M. M. Nandeppanavar and S. B. Malipatil, Heat transfer in a second grade fluid through a porous medium from a permeable stretching sheet with non-uniform heat source/sink, Int J. Heat Mass Tran. 53 **(2010)** 1788–1795.

[44] T. Hayat, Z. Iqbal, M. Mustafa, and A. Alsaedi ,Unsteady flow and heat transfer of Jeffrey fluid over a stretching sheet, Therm. Sci., 18(4) **(2014)** 1069-1078.

[45] W. Ibrahim and B. Shanker, Unsteady MHD boundary-layer flow and heat transfer due to stretching sheet in the presence of heat source or sink, Comput. Fluids 70 **(2012)** 21–28.

[46] Hayat, T., Javed, T. and Abbas Z., Slip flow and heat transfer of second grade fluid past a stretching sheet through a porous space, Int. J. Heat Mass Tran., 51 **(2008)** 4528-4534.

[47] K. Bhattacharyya, S. Mukhopadhyay and G. C. Layek, Slip effects on an unsteady boundary layer stagnation-point flow and heat transfer towards a stretching sheet, Chinese Phys. Lett. 28 **(2011)** 9.

[48] E. M. A. Elbashbeshy and A. A. Bazid, Heat transfer over an unsteady stretching surface, Heat Mass Transfer 41, **(2004)** 1–4.

[49] T. Hayat, M. Mustafa, Z. Iqbal and A. Alsaedi, Stagnation-point flow of couple stress fluid with melting heat transfer, Appl. Math. Mech. -Engl. Ed., 34(2) **(2013)**167–176

[50] A. Raptis, C. Perdikis and H. S. Takhar, Effect of thermal radiation on MHD flow, Appl Math Comput. 153 **(2004)** 645–649.

[51] R. Cortell, Viscoelastic fluid flow and heat transfer over a stretching sheet under the effect of a non-uniform heat source, viscous dissipation and thermal radiation, Int. J. Heat Mass Tran. 50 **(2007)** 3152–3162.

[52] M. Sajid and T. Hayat, Influence of thermal radiation on the boundary layer flow due to an exponentially stretching sheet, Int. Commun. Heat Mass 35 **(2008)** 347–356.

[53] V. Aliakbar, A. Alizadeh-Pahlavan and K. Sadeghy, The influence of thermal radiation on MHD flow of Maxwellian fluids above stretching sheets, Comm. Nonlinear Sci. Num. Simulation 14 **(2009)** 779–794.

[54] D. Pal and H.Mondal, Hydromagnetic non-Darcy flow and heat transfer over a stretching sheet in the presence of thermal radiation and Ohmic dissipation, Comm. Nonlinear Sci. Num. Simulation 15 **(2010)** 1197–1209

[55] E. Magyari and A. Pantokratoras, Note on the effect of thermal radiation in the linearized Rosseland approximation on the heat transfer characteristics of various boundary layer flows, Int. Commun. Heat Mass 38 **(2011)** 554–556.

[56] J. B. J. Fourier, Théorie Analytique De La Chaleur, Paris, **(1822)**.

[57] C. Cattaneo, Sulla conduzione del calore, Atti Semin. Mat. Fis. Univ. Modena Reggio Emilia 3 **(1948)** 83-101.

[58] C. I. Christov, On frame indifferent formulation of the Maxwell-Cattaneo model of finite-speed heat conduction, Mech. Res. Commun. 36 **(2009)** 481-486.

[59] J. G. Oldroyd, On the formulation of rheological equations of state, Proc. R. Soc. Lond. Ser. A Math. Phys. Eng. Sci. 200 **(1949)** 523-541.

[60] S. Pranesh and R. V. Kiran, Study of Rayleigh-Bénard magneto convection in a micropolar fluid with Maxwell-Cattaneo law, Appl. Math., 1 **(2010)**, 470-480

[61] V. Tibullo and V. Zampoli, A uniqueness result for the Cattaneo-Christov heat conduction model applied to incompressible fluids, Mech. Res. Commun. 38 **(2011)** 77-79.

[62] B. Straughan, Thermal convection with the Cattaneo-Christov model, Int. J Heat Mass Tran. 53 **(2010)** 95-98.

[63] S. A. M. Haddad, Thermal instability in Brinkman porous media with Cattaneo-Christov heat flux, Int. J. Heat Mass Tran. 68 **(2014)** 659-668.

[64] S. Han, L. Zheng, C. Li and X. X. Zhang, Coupled flow and heat transfer in viscoelastic fluid with Cattaneo-Christov heat flux model, Appl. Math. Lett. 38 **(2014)** 87-93

[65] E. Sanjayanand and S. K. Khan, On heat and mass transfer in a viscoelastic boundary layer flow over an exponentially stretching sheet, In.t J. Therm. Sci. 45 **(2006)** 819–828

[66] S. M. Alharbi, M. A. A. Bazid and M. S. E. Gendy, Heat and mass transfer in MHD viscoelastic fluid flow through a porous medium over a stretching sheet with chemical reaction, App. Math. 1 **(2010)** 446-455.

[67] T. Hayat, Z. Abbas and M. Sajid, Heat and mass transfer analysis on the flow of a second grade fluid in presence of chemical reaction, Phys Lett. A, 372 **(2008)** 2400-2408.

[68] P. H. Veena, V. K. Pravin, S. M.Shahjahan and V. B. Hippargi, , Non-similar solutions for heat and mass transfer fow in an electrically conducting visco-elastic Fluid Over a stretching sheet embedded in a porous medium, Int. J. Mod. Math., 2 (1) **(2007)** 9-26.

[69] M. Turkyilmazoglu, Multiple solutions of heat and mass transfer of MHD slip flow for the viscoelastic fluid over a stretching sheet, Int. J. Therm. Sci, 50, **(2011)** 2264-2276

[70] G. C. Layek, S. Mukhopadhyay and S. A Samad, Heat and mass transfer analysis for boundary layer stagnation-point flow towards a heated porous stretching sheet with heat absorption/generation and suction/blowing, Int. Commun. Heat Mass, 34(3) **(2007)** 347-356.

[71] M. Anghel, H.S. Takhar and I. Pop, Dufour and soret effects on free convection boundary layer over a vertical surface embedded in a porous medium, Studia Universitatis Babes-Bolyai, Mathematica,Vol. XLV(4) **(2000)** 11-21

[72] A. Postelnicu, Influence of a magnetic field on heat and mass transfer by natural convection from vertical surfaces in porous media considering Soret and Dufour effects, Int. Commun. Heat Mass, 47 **(2004)** 1467-1472.

[73] D. Srinivasacharya and Ch. Reddy, Soret and Dufour Effects on mixed convection from an exponentially stretching surface. Int. J. Nonlinear Sci., 12 **(2011)** 60-68.

[74] O.A. Beg, A. Y. Bakier, and V. R. Prasad, Numerical study of free convection magnetohydrodynamic heat and mass transfer from a stretching surface to a saturated porous medium with Soret and Dufour effects, Comp. Materials Science, 46 **(2009)** 57-65.

[75] R. Tsai and J. S. Huang, Heat and mass transfer for a Soret and Dufour's effects on Hiemenz flow through porous medium onto a stretching surface. Int. J. Heat Mass Tran.,

52 (**2009**) 2399-2406.

[76] A. A. Ahmed, Simlarty solution in MHD effects of thermal diffusion and diffusion thermo on free convective heat and mass transfer over a stretching surface considering suction and injuction, Commun Nonlinear Sci Numer Simulat, 14 (**2009**) 2202-2214.

[77] M. A. A. Bazid, Z. M. Gharsseldien, M. A. Seddeek and M. Alharbi, Soret and Dufour numbers effect on heat and mass transfer in stagnation point flow twards a stretching surface in the presence of Buoyancy force and variable thermal conductivity, J. Comp. and modeling ,2 (**2012**) 25

[78] D. Pal and H. Mondal, Soret and Dufour effects on MHD non-Darcian mixed convection heat and mass transfer over a stretching sheet with non-uniform heat source/sink, PHYS REV B, 407 (**2012**) 642-651.

[79] A. Nayak, S. Panda and D. K Phukan, Soret and Dufour effects on mixed convective unsteady MHD boundary layer flow over stretching sheet in porous medium with chemical spacies, App. Math. Mechanics, 35 (**2014**) 849-862.

[80] T. Hayat, M. Mustafa and I. Pop, Heat and mass transfer for Soret and Dufour's effect on mixed convection boundary layer flow over a stretching vertical surface in a porous medium filled with a viscoelastic fluid, Commun Nonlinear Sci. Numer. Simulat 15 (**2010**) 1183-1196.

[81] M. Turkyilmazoglu, The analytical solution of mixed convection heat transfer and fluid flow of a MHD viscoelastic fluid over a permeable stretching surface, Int. J. Mech. Sci. 77 (**2013**) 263-268.

[82] R. Saidur, K. Y. Leong and H. A. Mohammad, A review on applications and challenges of nanofluids, Renewable and Sustainable, Energy Reviews 15 (**2011**) 1646–1668.

[83] O. Mahian, A. Kianifar, S. A. Kalogirou, I. Pop and S. Wongwises, A review of the applications of nanofluids in solar energy, Int. J. Heat Mass Tran., 57 (**2013**) 582–594.

[84] S. Choi, Enhancing thermal conductivity of fluids with nanoparticle. In: Development and applications of non-Newtonian flow. ASME, FED-66 (**1995**) 99–105.

[85] A. V. Kuznetsov and D. A. Nield, Natural convective boundary-layer flow of a nanofluid past a vertical plate. Int. J. Therm Sci. 49 (**2010**) 243–247.

[86] W. A. Khan and I. Pop, Boundary-layer flow of a nanofluid past a stretching sheet. Int J Heat Mass Tran. 53 **(2010)** 2477–2483.

[87] M. Mustafa, T. Hayat and S. Obaidat, Boundary layer flow of a nanofluid over an exponentially stretching sheet with convective boundary conditions, Int. J. Numer. Method H. 23 **(2013)** 945–959.

[88] M. Turkyilmazoglu, Exact analytical solutions for heat and mass transfer of MHD slip flow in nanofluids, Chem. Eng. Sci. 84 **(2012)** 182–187.

[89] T. Hayat, T. Muhammad, S. A. Shehzad and A. Alsaedi, Three-dimensional boundary layer flow of Maxwell nanofluid: mathematical model, Appl. Math. Mech. -Engl. Ed., 36(6), **(2015)** 747–762

[90] S. A. Shehzad, T. Hayat, and A. Alsaedi, Influence of convective heat and mass conditions in MHD flow of nanofluid, Bull. Polish Acad. Sci. Tech. Sciences, 63, **(2015)** 465-474.

[91] K. Das, P. R. Duari and P. K. Kundu, Nanofluid flow over an unsteady stretching surface in presence of thermal radiation, Alexandria Eng. J. 53 **(2014)** 737–745.

[92] R. Nazar, M. Jaradat, M. Arifin and I. Pop, Stagnation-point flow past a shrinking sheet in a nanofluid, Cent. Eur. J. Phys. 9 (5) **(2011)** 1195–1202.

[93] W. Ibrahim and B. Shankar, MHD boundary layer flow and heat transfer of a nanofluid past a permeable stretching sheet with velocity, thermal and solutal slip boundary conditions, Comput Fluids 75 **(2013)** 1–10.

[94] P. K. Kameswaran, S. Shaw, P. Sibanda and P. V. S. N. Murthy, Homogeneous-hetrogeneous reactions in a nanofluid flow due to a porous stretching sheet, Int. J. Heat Mass Tran. 57 **(2013)** 465-472.

[95] M. Goyal and R. Bhargava, Boundary layer flow and heat transfer of viscoelastic nanofluids past a stretching sheet with partial slip conditions Appl. Nanosci., 4 **(2014)** 761–767

[96] M. A. Hamad, I. Pop and A. I. Ismali, Magnetic field effects on free convection flow of a nanofluid past a vertical semi-infinite flat plate. NonLinear Anal: Real World Appl, 12 **(2011)** 1338–46.

[97] M. J. Uddin, M. Ferdows and O. A. Beg, Group analysis and numerical computation of magneto-convective non-Newtonian nanofluid slip flow from a permeable stretching sheet, App. Nanoscience, October 4, **(2014)** 897-910.

[98] W. N. Mutuku-Njane and O.D. Makinde, Combined effect of buoyancy force and Navier slip on MHD flow of nanofluid over a convectively heated vertical porous plate, Scientific Worrld J. **(2013)** 8.

[99] D. Pal, G. Mandal and K. Vajravalu, Mixed convection stagnation-point flow of nanofluids over a stretching/shrinking sheet in a porous medium with internal heat generation/absorption, Comm. Num. Analysis 2015(1) **(2015)** 30-50

[100] C. Y Wang, Nonlinear streaming due to the oscillatory stretching of a sheet in a Viscous fluid, Acta Mech. 72 **(1988)** 261-268.

[101] B. Siddappa and M. S. Abel, non-Newtonian flow past a stretching plate, Z Angew Math. Phys. 36 **(1985)** 890.

[102] K. Rajagopal, P. H. Veena and V. K. Pravin, Oscillatory motion of an electrically conducting viscoelastic fluid over a stretching sheet in a saturated porous medium with suction/blowing, Math. Probl. Eng., 2006 **(2006)** 14.

[103] Z. Abbas, Y. Wang, T. Hayat and M.Oberlack. Hydromagnetic flow in a viscoelastic fuid due to the oscillatory stretching surface. Int. J. Nonlinear Mech. 43 **(2008)** 783–793.

[104] Z. Abbas, Y. Wang, T. Hayat and M. Oberlack, Slip effects and heat transfer analysis in a viscous fluid over an oscillatory stretching surface, Int. J. Numer. Meth. Fl., 59 **(2009)** 443–448.

[105] L.C. Zheng, X. Jin, X. X. Zhang and J. H. Zhang, Unsteady heat and mass transfer in MHD flow over an oscillatory stretching surface with Soret and Dufour effects, Acta Mech. Sinica., 29(5) **(2013)** 667-675.

[106] J. C. Misra, G. C. Shit and S. Chandra, Hydromagnetic flow and heat transfer of a second-grade viscoelastic .uid in a channel with oscillatory stretching walls: application to the dynamics of blood flow. J. Eng. Math., 69 **(2011)** 91-100.

[107] H. Schhchting, *Boundary layer Theory*, McGraw-Hill, New York, **(1964).**

[108] S. J. Liao, A Second-Order Approximate Analytical solution of a smple pendulum by the process analysis method, ASME. J. Appl. Mech. 59 **(1992)** 970.

[109] Liao, S.J., *Advances in the Homotopy Analysis Method*, World Scientific Publishing, 5 Toh Tuck Link, Singapore (**2014**).

[110] M. Turkyilmazoglu, Analytic Approximate Solutions of rotating disk boundary layer flow subject to a uniform suction or injection, Int. J. Mech. Sci. 52 (**2010**), 1735-1744

[111] B. Raftari and K. Vajravelu, Homotopy analysis method for MHD viscoelastic fluid flow and heat transfer in a channel with a stretching wall, Commun. Nonlinear. Sci. Numer. Simulat. 17 (**2012**) 41-49.

[112] S. J. Liao, Advance in the Homotopy Analysis Method, World Scientific Publishing, 5 Toh Tuck Link, Singapore (**2014**).

[113] S. J. Liao, An explicit, totally analytic approximation of Blasius' viscous flow problems. Int. J. Nonlinear Mech., 34(4) (**1999**) 759-778.

[114] S. J. Liao, On the analytic solution of magnetohydrodynamic flows of non-Newtonian Fluids over a stretching sheet. J. Fluid Mech., 488 (**2003**) 189-212.

[115] M. Turkyilmazoglu, Solution of the Thomas-Fermi Equation with a Convergent Approach, 2012, Comm. Nonlinear Sci. Num. Simulation, 17 (**2012**) 4097-4103.

[116] Sankara K. Rao, *Numerical Methods for Scientists and Engineers*, PHI Learning Pvt. Ltd (**2014**).

[117] T. Hayat, H. M. Mamboudou and F. M. Mahmed, Unsteady solutions in a third grade fluid filling the porous space, Math. Probl. Eng., (**2008**) 1-13.

[118] Y. Wang, T. Hayat, N. Ali, M. Oberlack, Magnetohydrodynamic peristaltic motion of a Sisko fluid in a symmetric or asymmetric channel, Physica A 387 (**2008**) 347–362.

[119] Y. Wang, T. Hayat, Fluctuating flow of a Maxwell fluid past a porous plate with variable suction, Nonlinear Anal.: Real World Applications 9 (**2008**) 1269–1282.

[120] Y. Wang, W. Wu, Unsteady flow of a fourth-grade fluid due to an oscillating plate, Int J nonlinear Mech 42 (**2007**) 432–441.

[121] N. Ali, Y. Wang, T. Hayat, M. Oberlack, Long wavelength approximation to peristaltic motion of an Oldroyd 4-constant fluid in a planar channel, Biorheology 45 (5) (**2008**) 611-628.

[122] V. K. Stokes, Couple Stress in Fluids, 9 (**1966**) 1709-1715.